AAAS

Science

11 SEPTEMBER 2025

BRINGING IN LIGHT

A swirling supercomplex captures ocean light for photosynthesis **p. 1109**

BII | Prize for Science | Innovation

Bring Science to Life

Behind every life-changing solution is an entrepreneurial scientist – a creative mind who developed an idea in the lab and dared to carry it out into the world.

To encourage more scientists to translate their research, BioInnovation Institute (BII) and *Science* are collaborating to host an annual award.

Up to three winners will have their essays published in *Science* magazine and will be invited into BII's entrepreneurial ecosystem. In addition, the Grand Prize winner will receive a prize of USD 25,000, and each finalist will receive USD 10,000 at a grand award ceremony in Copenhagen, Denmark.

Xiaojing Gao, Grand Prize winner 2025
For his work on developing an innovative programmable RNA sensor and molecular tools to improve mRNA vector therapeutics.

BII BioInnovation Institute Science

Apply before November 1, 2025
bii.dk/community/prizes

CONTENTS

11 SEPTEMBER 2025 | VOLUME 389 | ISSUE 6765

1086 Local wildfires may have far-reaching effects on global air circulation.

PHOTO: *LOS ANGELES TIMES*/GETTY IMAGES

CALL FOR PAPERS

SPJ
SCIENCE PARTNER JOURNALS

spj.science.org/bmef

BMEF

OPEN ACCESS

BMEF is a **Science Partner Journal** distributed by the **American Association for the Advancement of Science** (AAAS) in collaboration with the **Suzhou Institute of Biomedical Engineering and Technology, Chinese Academy of Sciences** (SIBET CAS). *BMEF* serves the multidisciplinary community of biomedical engineering by publishing breakthrough original Research Articles, Rapid Reports, Reviews, Perspectives, and Editorials. The journal also publishes research in the fields of pathogenic mechanisms as well as disease prevention, diagnosis, treatment, and assessment.

The Science Partner Journals (SPJ) program was established by the American Association for the Advancement of Science (AAAS), the nonprofit publisher of the *Science* family of journals. The SPJ program features high-quality, online-only, open access publications produced in collaboration with international research institutions, foundations, funders and societies. Through these collaborations, AAAS expands its efforts to communicate science broadly and for the benefit of all people by providing top-tier international research organizations with the technology, visibility and publishing expertise that AAAS is uniquely positioned to offer as the world's largest general science membership society.

Submit your research to *BMEF* today!
Learn more at: **spj.science.org/bmef**

@SPJournals **@SPJournals** **@SPJournals**

1095

Bad experiences with broken systems can weaken trust in science.

PHOTO: PACIFIC PRESS/GETTY IMAGES

ON THE COVER

The photosynthetic proteins of marine coccolithophores capture green light underwater and appear orange-red. Their photosystem I and light-harvesting proteins assemble into a huge molecular machine that efficiently captures, transfers, and converts light energy, demonstrating the evolutionary diversity of photosynthesis and the ultimate pursuit of light. See page 1109.
Illustration: A. Fisher/*Science*; Data: L. Shen *et al.*, *Science* **389**, eadv2132 (2025)

ON THE PODCAST

An aggressive cancer's loophole, and a massive field of hydrogen beneath the ocean floor

Science **serves as a forum for discussion of important issues related to the advancement of science by publishing material on which a consensus has been reached as well as including the presentation of minority or conflicting points of view. Accordingly, all articles published in *Science*—including editorials, news, commentary, and book reviews—are signed and reflect the individual views of the authors and not official points of view adopted by AAAS or the institutions with which the authors are affiliated.** *Science* (ISSN 0036-8075) is published weekly on Thursday, except last week in December, by the American Association for the Advancement of Science, 1200 New York Avenue, NW, Washington, DC 20005. Periodicals mail postage (publication No. 484460) paid at Washington, DC, and additional mailing offices. The title *Science* is a registered trademark of the AAAS. Domestic individual membership, including subscription (12 months): $165 ($74 allocated to subscription). Domestic institutional subscription (51 issues): $2865; Foreign postage extra: Air assist delivery: $135. First class, airmail, student, and emeritus rates on request. Canadian rates with GST available upon request, GST #125488122. Publications Mail Agreement Number 1069624. **Printed in the U.S.A. Change of address:** Allow 4 weeks, giving old and new addresses and 8-digit account number. **Postmaster:** Send change of address to AAAS, P.O. Box 96178, Washington, DC 20090–6178. **Single-copy sales:** $15 each plus shipping and handling available from backissues.science.org; bulk rate on request. **Authorization to reproduce** material for internal or personal use under circumstances not falling within the fair use provisions of the Copyright Act can be obtained through the Copyright Clearance Center (CCC), www.copyright.com. The identification code for *Science* is 0036-8075. *Science* is indexed in the *Reader's Guide to Periodical Literature* and in several specialized indexes.

Science AAAS

EDITOR-IN-CHIEF **Holden Thorp**, hthorp@aaas.org

EXECUTIVE EDITOR Valda Vinson

EDITORS, RESEARCH Sacha Vignieri, Jake S. Yeston **EDITOR, COMMENTARY** Lisa D. Chong

DEPUTY EXECUTIVE EDITOR Lauren Kmec

DEPUTY EDITORS Stella M. Hurtley (UK), Phillip D. Szuromi **SENIOR EDITORS** Caroline Ash (UK), Michael A. Funk, Angela Hessler, Di Jiang, Priscilla N. Kelly, Marc S. Lavine (Canada), Sarah Lempriere (UK), Mattia Maroso, Yevgeniya Nusinovich, Ian S. Osborne (UK), L. Bryan Ray, H. Jesse Smith, Keith T. Smith (UK), Jelena Stajic, Peter Stern (UK), Yury V. Suleymanov, Valerie B. Thompson, Brad Wible **ASSOCIATE EDITORS** Jack Huang, Sumin Jin, Bianca Lopez, Sarah Ross (UK), Madeleine Seale (UK), Corinne Simonti, Ekeoma Uzogara **SENIOR LETTERS EDITOR** Jennifer Sills **NEWSLETTER EDITOR** Christie Wilcox **RESEARCH & DATA ANALYST** Jessica L. Slater **LEAD CONTENT PRODUCTION EDITORS** Chris Filiatreau, Harry Jach **SR. CONTENT PRODUCTION EDITOR** Amelia Beyna **CONTENT PRODUCTION EDITORS** Anne Abraham, Robert French, Julia Haber-Katris, Nida Masiulis, Abigail Shashikanth, Suzanne M. White **SENIOR PROGRAM ASSOCIATE** Maryrose Madrid **EDITORIAL MANAGER** Joi S. Granger **EDITORIAL ASSOCIATES** Aneera Dobbins, Lisa Johnson, Jerry Richardson, Anita Wynn **SENIOR EDITORIAL COORDINATORS** Alexander Kief, Ronmel Navas, Isabel Schnaidt, Alice Whaley (UK), Brian White **EDITORIAL COORDINATORS** Samuel Bates, Clair Goodhead (UK), Kat Kirkman, Daniel Young **ADMINISTRATIVE COORDINATOR** Karalee P. Rogers **ASI DIRECTOR, OPERATIONS** Janet Clements (UK) **ASI OFFICE MANAGER** Carly Hayward (UK) **ASI SR. OFFICE ADMINISTRATORS** Simon Brignell (UK), Jessica Waldock (UK) **COMMUNICATIONS DIRECTOR** Meagan Phelan **DEPUTY DIRECTOR** Matthew Wright **SENIOR WRITERS** Walter Beckwith, Joseph Cariz, Abigail Eisenstadt **WRITER** Mahathi Ramaswamy **SENIOR COMMUNICATIONS ASSOCIATES** Zachary Graber, Sarah Woods **COMMUNICATIONS ASSOCIATES** Kiara Brooks, Haley Riley, Mackenzie Williams

NEWS EDITOR Tim Appenzeller

NEWS MANAGING EDITOR John Travis **INTERNATIONAL EDITOR** David Malakoff **DEPUTY NEWS EDITORS** Rachel Bernstein, Martin Enserink, David Grimm, Eric Hand, Michael Price, Kelly Servick, Matt Warren (Europe) **SENIOR CORRESPONDENTS** Daniel Clery (UK), Jon Cohen, Jeffrey Mervis **ASSOCIATE EDITORS** Michael Greshko, Katie Langin **NEWS REPORTERS** Jeffrey Brainard, Adrian Cho, Phie Jacobs, Jocelyn Kaiser, Rodrigo Pérez Ortega (Mexico City), Robert F. Service, Erik Stokstad, Paul Voosen, Meredith Wadman **CONSULTING EDITOR** Elizabeth Culotta **CONTRIBUTING CORRESPONDENTS** Vaishnavi Chandrashekhar, Dan Charles, Warren Cornwall, Andrew Curry (Berlin), Ann Gibbons, Kai Kupferschmidt (Berlin), Andrew Lawler, Mitch Leslie, Virginia Morell, Dennis Normile (Tokyo), Catherine Offord, Cathleen O'Grady, Elisabeth Pain (Careers), Charles Piller, Zack Savitsky, Richard Stone (Senior Asia Correspondent), Gretchen Vogel (Berlin), Lizzie Wade (Mexico City) **INTERNS** Nazeefa Ahmed, Annika Inampudi **COPY EDITORS** Julia Cole (Senior Copy Editor), Hannah Knighton, Cyra Master (Copy Chief) **ADMINISTRATIVE SUPPORT** Meagan Weiland

CREATIVE DIRECTOR Beth Rakouskas

DESIGN MANAGING EDITOR Chrystal Smith **GRAPHICS MANAGING EDITOR** Chris Bickel **PHOTOGRAPHY MANAGING EDITOR** Emily Petersen **MULTIMEDIA MANAGING PRODUCER** Kevin McLean **DIGITAL DIRECTOR** Kara Estelle-Powers **DESIGN EDITOR** Marcy Atarod **DESIGNER** Noelle Jessup **SENIOR SCIENTIFIC ILLUSTRATOR** Noelle Burgess **SCIENTIFIC ILLUSTRATORS** Austin Fisher, Kellie Holoski, Ashley Mastin **SENIOR GRAPHICS EDITOR** Monica Hersher **GRAPHICS EDITOR** Veronica Penney **SENIOR PHOTO EDITOR** Charles Borst **PHOTO EDITOR** Elizabeth Billman **SENIOR PODCAST PRODUCER** Sarah Crespi **SENIOR VIDEO PRODUCER** Meagan Cantwell **SOCIAL MEDIA STRATEGIST** Jessica Hubbard **SOCIAL MEDIA PRODUCER** Sabrina Jenkins **WEB DESIGNER** Jennie Pajerowski

CHIEF EXECUTIVE OFFICER AND EXECUTIVE PUBLISHER

Sudip Parikh

PUBLISHER, SCIENCE FAMILY OF JOURNALS Bill Moran

DIRECTOR, BUSINESS OPERATIONS & ANALYSIS Eric Knott **MANAGER, BUSINESS OPERATIONS** Jessica Tierney **SENIOR MANAGER, BUSINESS ANALYSIS** Cory Lipman **BUSINESS ANALYSTS** Kurt Ennis, Maggie Clark, Isacco Fusi **BUSINESS OPERATIONS ADMINISTRATOR** Taylor Fisher **DIGITAL SPECIALIST** Marissa Zuckerman **SENIOR PRODUCTION MANAGER** Jason Hillman **SENIOR MANAGER, PUBLISHING AND CONTENT SYSTEMS** Marcus Spiegler **CONTENT OPERATIONS MANAGER** Rebecca Doshi **PUBLISHING PLATFORM MANAGER** Jessica Loayza **PUBLISHING SYSTEMS SPECIALIST, PROJECT COORDINATOR** Jacob Hedrick **SENIOR PRODUCTION SPECIALIST** Kristin Wowk **PRODUCTION SPECIALISTS** Kelsey Cartelli, Audrey Diggs **SPECIAL PROJECTS ASSOCIATE** Shantel Agnew

MARKETING DIRECTOR Sharice Collins **ASSOCIATE DIRECTOR, MARKETING** Justin Sawyers **GLOBAL MARKETING MANAGER** Allison Pritchard **ASSOCIATE DIRECTOR, MARKETING SYSTEMS & STRATEGY** Aimee Aponte **SENIOR MARKETING MANAGER** Shawana Arnold **MARKETING MANAGER** Ashley Evans **MARKETING ASSOCIATES** Hugues Beaulieu, Ashley Hylton, Lorena Chirinos Rodriguez, Jenna Voris **MARKETING ASSISTANT** Courtney Ford **SENIOR DESIGNER** Kim Huynh

DIRECTOR AND SENIOR EDITOR, CUSTOM PUBLISHING Erika Gebel Berg **ADVERTISING PRODUCTION OPERATIONS MANAGER** Deborah Tompkins **DESIGNER, CUSTOM PUBLISHING** Jeremy Huntsinger **SENIOR TRAFFIC ASSOCIATE** Christine Hall

DIRECTOR, PRODUCT MANAGEMENT Kris Bishop **PRODUCT DEVELOPMENT MANAGER** Scott Chernoff **ASSOCIATE DIRECTOR, PUBLISHING INTELLIGENCE** Rasmus Andersen **SR. PRODUCT ASSOCIATE** Robert Koepke **PRODUCT ASSOCIATES** Caroline Breul, Anne Mason

ASSOCIATE DIRECTOR, INSTITUTIONAL LICENSING MARKETING Kess Knight **ASSOCIATE DIRECTOR, INSTITUTIONAL LICENSING SALES** Ryan Rexroth **INSTITUTIONAL LICENSING MANAGER** Nazim Mohammedi, Claudia Paulsen-Young **SENIOR MANAGER, INSTITUTIONAL LICENSING OPERATIONS** Judy Lillibridge **MANAGER, RENEWAL & RETENTION** Lana Guz **SYSTEMS & OPERATIONS ANALYST** Ben Teincuff **FULFILLMENT ANALYST** Aminta Reyes

ASSOCIATE DIRECTOR, INTERNATIONAL Roger Goncalves **ASSOCIATE DIRECTOR, US ADVERTISING** Stephanie O'Connor **US MID WEST, MID ATLANTIC AND SOUTH EAST SALES MANAGER** Chris Hoag **DIRECTOR, OUTREACH AND STRATEGIC PARTNERSHIPS, ASIA** Shoupeng Liu **SALES REP, ROW** Sarah Lelarge **SALES ADMIN ASSISTANT, ROW** Victoria Glasbey **DIRECTOR OF GLOBAL COLLABORATION AND ACADEMIC PUBLISHING RELATIONS, ASIA** Xiaoying Chu **ASSOCIATE DIRECTOR, INTERNATIONAL COLLABORATION** Grace Yao **SALES MANAGER** Danny Zhao **MARKETING MANAGER** Kilo Lan **ASCA CORPORATION, JAPAN** Rie Rambelli (Tokyo), Miyuki Tani (Osaka)

DIRECTOR, COPYRIGHT, LICENSING AND SPECIAL PROJECTS Emilie David **RIGHTS AND PERMISSIONS ASSOCIATE** Elizabeth Sandler **LICENSING ASSOCIATE** Virginia Warren **RIGHTS AND LICENSING COORDINATOR** Dana James **CONTRACT SUPPORT SPECIALIST** Michael Wheeler

EDITORIAL
science_editors@aaas.org

NEWS
science_news@aaas.org

INFORMATION FOR AUTHORS
science.org/authors/
science-information-authors

REPRINTS AND PERMISSIONS
science.org/help/
reprints-and-permissions

MULTIMEDIA CONTACTS
SciencePodcast@aaas.org
ScienceVideo@aaas.org

MEDIA CONTACTS
scipak@aaas.org

PRODUCT ADVERTISING & CUSTOM PUBLISHING
advertising.science.org
science_advertising@aaas.org

CLASSIFIED ADVERTISING
advertising.science.org/
science-careers
advertise@sciencecareers.org

JOB POSTING CUSTOMER SERVICE
employers.sciencecareers.org
support@sciencecareers.org

MEMBERSHIP AND INDIVIDUAL SUBSCRIPTIONS
science.org/subscriptions

MEMBER BENEFITS
aaas.org/membership/
benefits

INSTITUTIONAL SALES AND SITE LICENSES
science.org/librarian

Unburden American science

Alan I. Leshner and **Alex M. Helman**

Science is one of the greatest engines of health, prosperity, and security across the world. Yet, in the United States, the enterprise is now under tremendous stress from an array of pressures, including threats to federal support for both the direct and indirect costs of research. But funding instability is not the only issue. One major problem is that regulatory and policy requirements force researchers to spend nearly half of their research time on paperwork associated with receiving federal grants and contracts, not on discovery. The situation is made worse when research institutions themselves layer on additional requirements to ensure compliance. The administrative tasks are unnecessarily complex, duplicative, and, in some cases, contradictory. They also waste taxpayer dollars intended for scientific discovery and innovation. Given the current political focus on streamlining federal regulations, there is a clear opportunity to finally solve this burdensome problem.

...administrative tasks...waste taxpayer dollars intended for scientific discovery and innovation.

Surveys by the Federal Demonstration Partnership have shown that for nearly two decades, American researchers typically have spent over 40% of their research time on administrative and regulatory tasks, such as required training or conflict of interest forms. These requirements have been put in place over time to ensure that research is conducted at the highest levels of integrity, accountability, and transparency. But as the number of federal science funding agencies increased, and as science evolved to merit more areas of oversight, there has been an uncoordinated expansion of administrative red tape that has slowed the pace of research.

The administrative load has been analyzed extensively, and there is no dearth of suggestions on how to decrease it, including from the National Science Board, the Council on Government Relations, the Government Accountability Office, and the National Academies of Sciences, Engineering, and Medicine (the National Academies). Their reports include specific recommendations for fixing the problems, yet there has been relatively little progress over the past 20 years. Although there has been some alignment of policies and procedures across different funding agencies, attempts to substantially simplify administrative requirements have been sporadic and fleeting.

Why has there been so little progress? A major challenge has been the absence of federal leadership and coordination across the funding agencies. It is often unclear who has the authority to lead and implement system-wide changes. Each science agency (there are now over 20 of them) has developed rules and regulations that reflect its own mission. Without strong incentives or mechanisms to establish common methods, agencies have little reason to align their policies. Progress also has been hampered by the perception that the science supported by each agency is so specialized that it requires tailored policies and rules. As well, recommendations proposed so far simply may not have resonated with agency leaders.

Last week, the National Academies released a report, *Simplifying Research Regulations and Policies: Optimizing American Science*, that describes a different approach to the problem. It proposes three cross-cutting principles: harmonizing regulations and reporting requirements across agencies; adjusting the intensity of regulations to the level of risk to individuals or society; and using technology to simplify compliance. Rather than making specific recommendations about what should be done to solve the problems in each of these domains—such as conflicts of interest, misconduct in science, or research security—the report offers alternative routes to reducing the burden in each area and describes the pros and cons of each approach. This provides flexibility for achieving efficiency and transparency that will hopefully be attractive to multiple agencies. The report also offers alternative ways to coordinate efforts across agencies, such as through the creation of a federal research policy board, one of the earlier recommendations from the National Academies.

The new National Academies report comes at a time when both the Trump administration and Congress are proposing numerous changes with the purported goals of making science more accountable and efficient. To ensure these changes serve the research enterprise well, the scientific community must contribute its own ideas to accomplish the same goals. The administrative burden on America's researchers is badly in need of reform. Indeed, both federal and state governments claim that streamlining regulations to decrease waste, enhance accountability, and promote innovation is a priority. The United States cannot waste any more time and resources if it is to maintain a robust scientific enterprise that is the equal of any in the world. □

Alan I. Leshner is chief executive officer emeritus of the American Association for the Advancement of Science and former executive publisher of *Science*. He chaired the National Academies report on simplifying research regulations and policies. alan.i.leshner@gmail.com **Alex M. Helman** is a senior program officer at the National Academies, Washington, DC, USA. She was study director for the National Academies report on simplifying research regulations and policies. ahelman@nas.edu

10.1126/science.aec0488

NEWS

INFECTIOUS DISEASE

Mosquito-borne viruses surge in a warming Europe

Chikungunya cases break records in France; West Nile virus appears near Rome

MEREDITH WADMAN

This summer, the Italian province of Latina, popular for its beaches, wetlands, and Roman ruins, has earned an unwelcome distinction: It is one of several provinces in Italy to log their first-ever cases of infection with West Nile virus (WNV), once largely confined to a hot, humid river valley in the country's north. France, meanwhile, is experiencing an unprecedented expansion of another arbovirus, chikungunya. It's a record-breaking season for mosquito-borne diseases in Europe, and health experts are warning that a warming climate will bring more like it.

"Europe is entering a new phase—where longer, more widespread and more intense transmission of mosquito-borne diseases is becoming the new normal," European Centre for Disease Prevention and Control (ECDC) Director Pamela Rendi-Wagner said in a late August press release.

This year's intense season for mosquito-borne diseases was "probably influenced by or supported by" an extraordinarily hot summer, particularly in Western Europe, says Tamás Bakonyi, a veterinarian and virologist who is ECDC's principal expert for vector-borne and zoonotic diseases. Hot weather not only favors mosquito propagation, but also shortens the time needed for an insect that has acquired a virus to become infectious, Bakonyi notes.

Chikungunya virus, which infects an estimated 35 million people globally each year, can cause fever, headache, rash, and excruciating joint pain, and sometimes leads to severe chronic pain. Its surge in Europe this year has been centered in France, which recorded 957 cases in returning travelers as of 2 September, dwarfing numbers in the past decade. Most were imported from the French overseas department of Réunion, a popular Indian Ocean vacation destination for French travelers, which had a huge outbreak this spring and is part of a tropical belt where the virus is endemic.

But because a key mosquito species that transmits the virus, the Asian tiger mosquito (*Aedes albopictus*), has spread widely in Europe in the past 10 years as the climate has warmed, these imported cases have led to local transmission. "We have *Aedes albopictus* everywhere in France," says Denis Malvy, an infectious disease physician who focuses on emerging viral diseases at the University of Bordeaux. That chikungunya has followed is "not a surprise."

The result has been an additional, record-breaking 301 locally acquired cases in France, 73 of them in the week that ended on 2 September. (Only 32 cases of local transmission were logged from 2010 through 2024.) The Alsace region in northeastern France reported its first case this summer, which ECDC called "an exceptional occurrence at this latitude," and two large clusters, each with about 40 cases of locally transmitted chikungunya cases, have emerged in the region around Bordeaux.

A spokesperson for the French national public health agency wrote in an email that the country's case numbers and the local transmission constitute "a threat to put on the public health and research agenda at [the] national and international level."

Italy, the only other European country reporting chikungunya infections this year, has logged 107 locally acquired infections as of 3 September, three-quarters of them in the past 2 weeks, on the heels of 39 imported cases.

Europe's surge of local transmission may foreshadow one in the United States, which has not had locally acquired chikungunya cases since 2019. That luck may not last, says tropical infectious diseases physician David Hamer of Boston University. "*Aedes albopictus* has sort of been marching [north] through the United States over the last 10 to 15 years and is fairly widespread," he says. "So, the potential for introduction and spread is substantial."

Meanwhile, cases of West Nile virus disease (WNVD), caused by a virus that is widespread in the U.S., are being detected in new areas in Europe every year. This year, cases outpaced the prior two summers by mid-August. By 3 September, 623 cases had been reported in nine countries from Spain to Romania, driven by the large outbreak in Italy.

Unlike chikungunya, WNV doesn't move via mosquitoes from one human to another. People get it from mosquitoes of the genus *Culex* after they bite birds that are natural reservoirs of the

Workers sprayed pesticide in a public park in Naples, Italy, last month, aiming to kill mosquitoes spreading West Nile virus in the region.

PHOTO: SALVATORE LAPORTA/KONTROLAB/LIGHTROCKET VIA GETTY IMAGES

virus. Though often asymptomatic, infection can cause fever, headache, and muscle pain. And, especially in the elderly and immunocompromised, the virus can invade the central nervous system, sometimes with deadly consequences.

As of 3 September, Italy had logged 502 cases of WNVD—nearly as many as in the entire U.S. this year—and 33 deaths. In 226 of the cases, the virus invaded the brain. Of these patients, 80% were 65 and older.

Emanuele Nicastri, a physician who cares for arbovirus-infected patients at the Lazzaro Spallanzani National Institute for Infectious Diseases, says his team was "quite upset" when the first WNVD cases were diagnosed in the area. Even though the once-malaria-ridden marshes around Rome have long been prime mosquito habitat, "we have never seen" locally acquired WNV, he says. "Now, we have two-thirds of Italian cases."

Patrizio Pezzotti, an epidemiologist who directs the epidemiology, mathematical models, and biostatistics unit at Italy's public health agency, says the geography of Italy's outbreak is unusual. The hot, humid Po River Valley that stretches across northern Italy from Turin to Venice has historically been home to most of the country's WNVD cases. "We don't know why" the virus has suddenly appeared in the population-dense area that stretches from Rome to Naples, Pezzotti says, although climate-prompted changes in the migration paths of birds flying north out of Africa is one possibility.

Science has few quick fixes. There are no approved antiviral medications for either disease, so both are treated with supportive care. Vaccines in development against WNV are years from potential regulatory approval. And after one of two approved chikungunya vaccines was linked to serious adverse reactions and two deaths in elderly people on Réunion this spring, public opinion on vaccinating against the disease grew "complicated" in France, Malvy says—even though the second vaccine appears safer.

He's hopeful vaccines will eventually protect people from both diseases. But he adds that Europeans must also adjust to the new reality of infectious threats from climate change: "The first steps are to reorganize our minds as regards the risk driven by our way of life." □

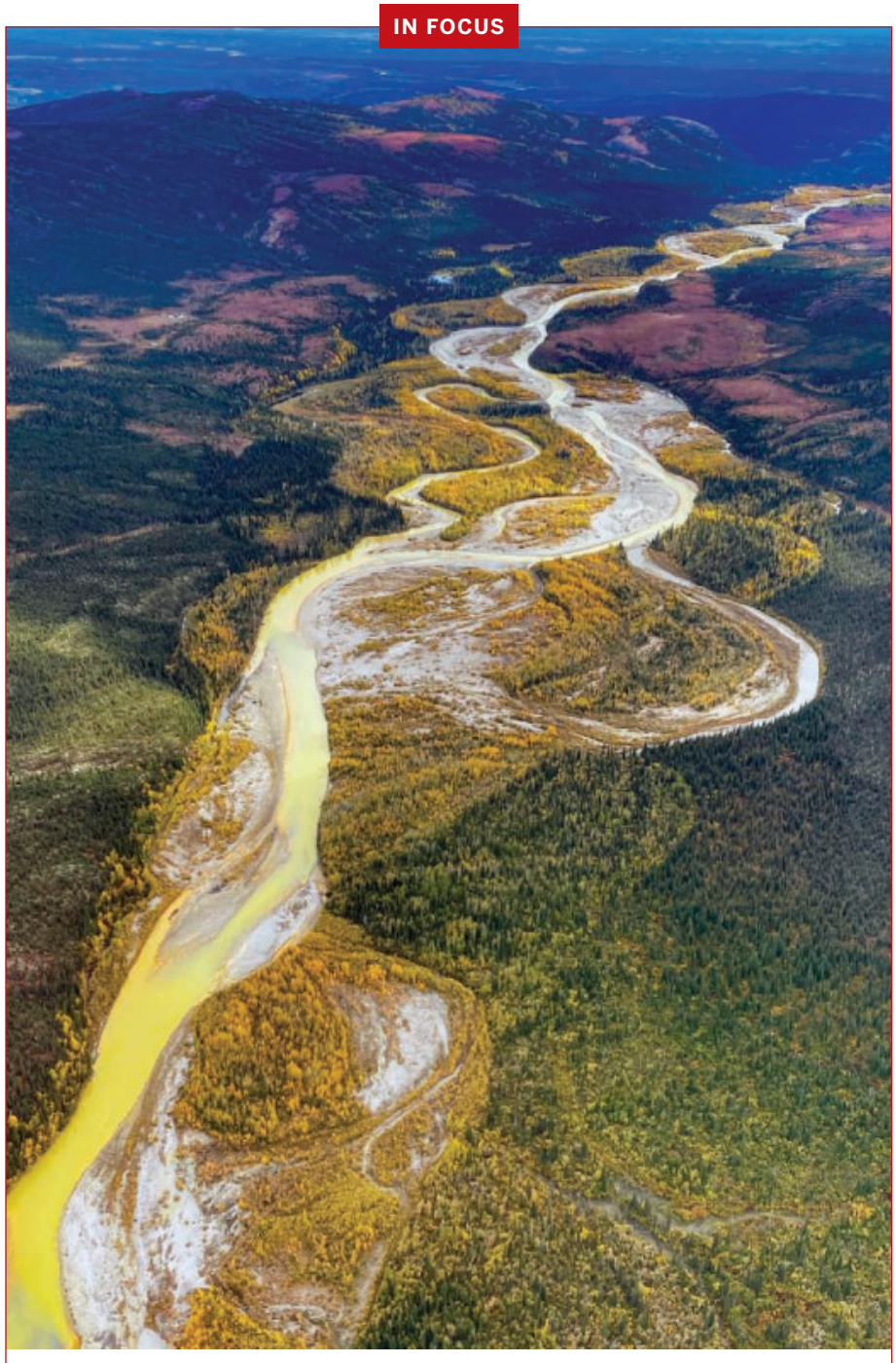

PHOTO: RAY KOLESER

Climate change turns Alaskan river toxic

The Salmon River, long a symbol of Alaska's untrammeled, wild beauty, is now an emblem of Arctic climate change. As the permafrost thaws, sulfides released from exposed bedrock can oxidize to form sulfuric acid, which dissolves metals trapped in the rock such as iron, aluminum, copper, and cadmium. The phenomenon began to turn the river yellow in 2019. Now, researchers report in the *Proceedings of the National Academy of Sciences* that the Salmon and nine of its tributaries had at least one metal present above levels considered toxic to fish and other aquatic organisms. At one spot, iron, aluminum, cadmium, copper, nickel, and zinc concentrations were between three and 37 times higher in 2023 than a decade earlier. If such levels were found near a mine operating in the watershed, "the mine would be in trouble," says first author Paddy Sullivan, an ecologist at the University of Alaska Anchorage. —Warren Cornwall

TRUMP TRACKER

U.S. UPHOLDS HIV PREVENTION COMMITMENT The U.S. government will honor a commitment made before President Donald Trump was inaugurated to help millions of people in poor countries receive a powerful new HIV prevention tool. In December 2024, the U.S. President's Emergency Plan for AIDS Relief (PEPFAR) said it would join with several partners to give at least 2 million people in low-income countries access to injectable lenacapavir, which can protect a person from HIV infection for 6 months. But the Trump administration has dismantled much of PEPFAR, putting a giant question mark over this pledge. Now, the Department of State says it is negotiating agreements that would help provide the promised doses to people in as many as 12 still-to-be-identified countries. But the administration strongly recommends countries initially focus on preventing mother-to-child transmission by giving lenacapavir to pregnant and breastfeeding women. That would limit availability to other groups at high risk of HIV infection, including sex workers and men who have sex with men. —Jon Cohen

NIH LEADERS CHALLENGE DISMISSALS Two former directors of branches of the National Institutes of Health (NIH) allege in whistleblower suits filed on 3 September that they were ousted in April because they supported vaccines and objected to grant terminations and other Trump administration policies. The pair are seeking to have their directorships reinstated and to be awarded compensatory damages and attorney fees. According to the suits, vaccinologist Kathleen Neuzil was dismissed from her job at the Fogarty International Center and infectious disease specialist Jeanne Marrazzo was removed from the National Institute of Allergy and Infectious Diseases by Matthew Memoli, then NIH's acting director and currently deputy director. They contend that their removals were "retaliation" by Memoli for challenging Trump administration decisions. A spokesperson for NIH's parent agency, the Department of Health and Human Services, says each vaccine "must be assessed on its own merits" and that Memoli "consistently champions gold-standard, evidence-based science." Neuzil and Marrazzo were put on administrative leave and were offered reassignment at the Indian Health Service, but neither received new jobs, ultimately leading Neuzil to resign. —Jon Cohen

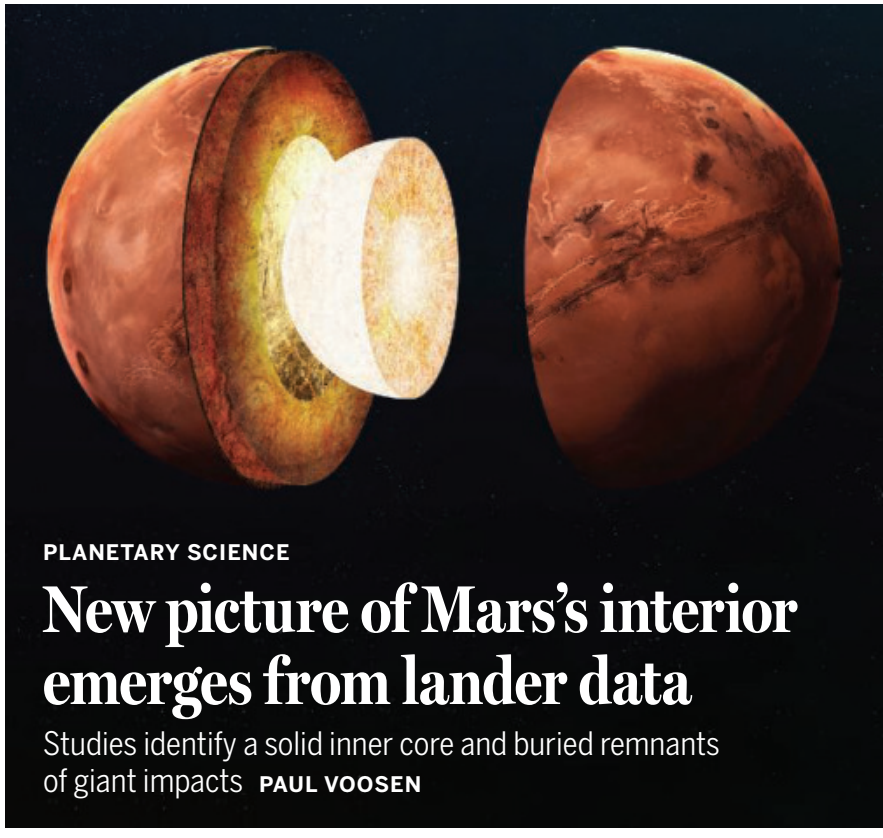

IMAGE: VADIM SADOVSKI/SHUTTERSTOCK

PLANETARY SCIENCE

New picture of Mars's interior emerges from lander data

Studies identify a solid inner core and buried remnants of giant impacts **PAUL VOOSEN**

It's been nearly 3 years since NASA's InSight mission ended on the surface of Mars, its solar panels smothered in dust. But data from the lander, which captured signals from faint marsquakes to probe the planet's interior, are still yielding fresh results. Two new studies use InSight data to paint a radical new portrait of Mars. One suggests fossilized remnants of giant impacts are buried in the planet's interior. The other claims to have identified a solid inner core.

Taken together, the findings suggest a planet that is both more, and less, like Earth than researchers expected. The first result, published last month in *Science* (28 August, p. 899), suggests the martian mantle—the layer of rock that makes up most of its volume—does not ooze and mix like Earth's mantle, but rather preserves the remnants of smaller planetary bodies that collided to form the planet. The second result, published last week in *Nature*, goes deeper, finding that rather than possessing a purely molten metal core, as earlier InSight analyses suggested, Mars—like Earth—has a solid core at its center.

Neither paper is an open-and-shut case. This stems from the simple challenge of doing seismology on Mars. On Earth, researchers use hundreds of seismic stations to study the seismic waves from thousands of strong earthquakes, which pass through the planet, sometimes reflecting off layers of different densities. But InSight had only a single seismic station, buffeted by wind, to measure the vibrations from mostly weak marsquakes. Both studies will face skepticism, says Hrvoje Tkalčić, a seismologist at Australian National University.

But if they hold up, the findings have the potential to transform our understanding of how rocky planets form, says Qian Yuan, a geophysicist at Texas A&M University. The remnant structures frozen in the mantle support the idea that rocky planets form from the collision of planetary embryos, rather than coalescing out of a cloud of pebbles, as some researchers have suggested, says Alessandro Morbidelli, a planetary scientist at Côte d'Azur University. And the inner core paper challenges models that suggest Mars's core is entirely molten. "I suspect it will make a lot of people unhappy," says Simon Stähler, a seismologist at ETH Zürich. "A lot of people were very comfortable with the nonexistence of the inner core."

A new study suggests a solid core is hidden within Mars's molten outer core.

Unlike Earth's interior, which is all mixed up by plate tectonics, "Mars is a time capsule," says Constantinos Charalambous, a planetary scientist at Imperial College London and lead author of the *Science* study. Probing this ancient history required taking advantage of high-frequency seismic waves, which survive much longer on Mars than Earth, where they get damped out by water.

Charalambous and his colleagues saw that as high-frequency waves traveled deeper through the mantle, their arrival at InSight got more and more delayed. It's as if they were small cars that had encountered rubble on a highway, Charalambous says, whereas marsquakes with long wavelengths rolled on through like monster trucks. The team suspects the seismic obstacles are the crystallized, hardened remnants of magma oceans that formed long ago as asteroids pummeled an infant Mars. "We're seeing there are indeed remnants," Charalambous says.

> **"The inner core is real, and we are confident in our results.**
>
> **Daoyuan Sun**
> University of Science and Technology of China

Mars's failure to mix away these remnants suggests its mantle is cool and moves sluggishly, unlike Earth's hot mantle, which contains plumes that rise and drive volcanic regions. A cool, sluggish mantle might explain the weak volcanism on Mars, says Junjie Dong, a mineral physicist at the California Institute of Technology.

The claim for a solid inner core may be more controversial because previous studies had indicated a completely molten core. When the InSight team previously detected what seemed to be the edge of the core, the seismic data showed no sign of anything solid. The large size of the core combined with Mars's known density suggest the core must contain lighter elements such as sulfur, which lower iron's melting point, making it less likely to crystallize. And tiny wobbles in the planet's gravitational field, measured by a radio experiment on InSight, are easiest to explain without a solid inner core rattling around inside—although they do not rule it out.

But when Daoyuan Sun, a seismologist at the University of Science and Technology of China, and his colleagues reexamined some InSight data, they saw the seismic waves that passed through the core and reflected off the core-mantle boundary on the other side were arriving some 50 to 200 seconds later than they should have if they were passing through a fully molten core. This suggested the presence of a dense inner core, slowing them down. Digging back through the data, the researchers also identified a seismic wave that appeared to reflect directly off the inner core's surface. Other seismic waves analyzed by the group confirm the finding, Sun says. "The inner core is real, and we are confident in our results."

The finding, however, is difficult to reconcile with two studies that came out 2 years ago in *Nature*, which suggested a layer of molten mantle rock lies right above the core, trapping its heat like a thermal blanket. That heat would make it harder for a solid core to cool down and crystallize, says Henri Samuel, a planetary dynamicist at the Paris Institute of Earth Physics who led one paper. "I confess that I am puzzled by this result," he says.

The absence of a magnetic dynamo on Mars, which lost its magnetism billions of years ago, also raises questions about the result. On Earth, crystallization of the inner core helps drive motions in the molten outer core that create the planet's magnetic field. "Either our records of the martian field are misinterpreted," Dong says, or some other process is preventing the molten motion on Mars.

The detection of the molten layer and inner core both have their problems, Stähler says, and it will be difficult to tease out how they fit together. Sun's team has ruled out obvious error sources, but the InSight data are fundamentally noisy, he says. Right now, he feels the claim is about as certain as those that propose an inner core at the Moon, where the evidence is weak. "I wouldn't bet my house on it," he says. "But I would bet $200." □

PUBLIC HEALTH

Florida plan to nix vaccine mandates raises alarm

Abandoning long-standing vaccine requirements for schoolchildren could prompt bigger outbreaks, researchers warn

JON COHEN

At a press conference last week before a cheering crowd, Florida Governor Ron DeSantis (R) and the state's surgeon general, Joseph Ladapo, announced a plan to end all required vaccinations, including ones that children must receive to attend public schools. They framed the move as a continuation of their fight against the face masks, school closures, and vaccine requirements that faced backlash during the COVID-19 pandemic.

Ladapo, who referred to the COVID-19 messenger RNA vaccines as "poison," described a vision of a "moral, ethical universe" in which the government cannot dictate to people what they put in their bodies.

Health officials, epidemiologists, and vaccine researchers alike roundly condemned the move, which will require approvals by Florida's Department of Health and legislature. "It's very dangerous for public health," says virologist Scott Weaver, a vaccine researcher at the University of Texas Medical Branch. Weaver points to the recent surge in Texas of cases of measles, one of the most transmissible viral diseases and a bellwether of declining vaccine coverage.

All states allow parents to seek exemptions on medical grounds, parents in Florida and many others can opt out based on religion, and some states allow exemptions for philosophical reasons or personal beliefs. Vaccine requirements for adults now are mainly limited to health care workers, the military, and college students. But most public health officials say the childhood mandates are key to protecting the health of children who remain unvaccinated and people who are immune compromised.

Science reviewed the scientific literature and talked to experts to address some of the main questions the announcement raises.

How long have vaccine mandates been around?
Even before the debut of the first vaccine in 1796, General George Washington in 1777 required Revolutionary War troops to undergo variolation, a precursor to vaccination in which they were inoculated with smallpox virus obtained from people who had mild cases.

Washington's decision "allowed our nation to continue to fight for our independence," Senator John Barrasso (R–WY) told Department of Health and Human Services Secretary Robert F. Kennedy Jr. during a grilling—frequently focused on his vaccine skepticism—before the Senate Committee on Finance last week.

The first bona fide vaccine, developed by Edward Jenner in the United Kingdom, soon made it to the United States, and in 1855, Massachusetts mandated smallpox vaccination of children who wanted to attend public schools, expanding an earlier requirement for adults. A Massachusetts man who would not pay a $5 fine because he refused a forced vaccination took the case to the Supreme Court, which in 1909 ruled that compulsory vaccination to protect public health was constitutional. Other states were slow to add mandates for schoolchildren, with only 20 having them by 1963.

Modeling shows the size of school measles outbreaks declines as the vaccination rate increases.

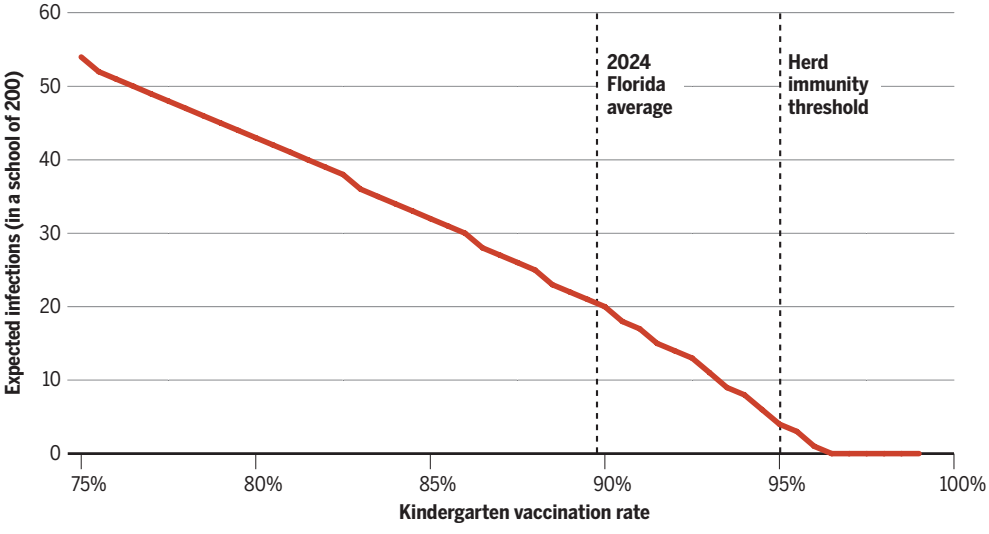

Do vaccine mandates work?
Several reviews of the scientific literature suggest requiring vaccination in public schools increases uptake and reduces the incidence of disease—including a 2016 report by the Community Preventive Services Task Force, an independent panel of public health experts, which evaluated 17 studies, most from the U.S. Conversely, after Japan lifted an influenza vaccine mandate for schoolchildren, deaths from that disease increased.

A World Health Organization (WHO) analysis of measles in the 53 countries it defines as the European Region found the continent in 2024 had about one-third of the global total of cases, driven by gaps in vaccine coverage.

But the effect of a mandate varies depending on factors including its enforcement. In three European countries that have mandates, for example, the WHO analysis found that fewer than 80% of vaccine-eligible children had been vaccinated against the disease.

The effectiveness of the vaccine matters, too. In contrast to the powerful and long-lasting measles vaccine, immunity from pertussis vaccines rapidly wanes—and one study of 29 European countries found no significant difference in the incidence of disease in ones that mandated the vaccine versus ones that did not.

How common are vaccine mandates?
According to a study done by University of Oxford researchers and posted on Our World in Data in 2021, 89 of 149 countries they examined have some form of mandatory childhood vaccination policy, although only 20 require vaccination for school entry. A recent analysis of 30 countries in Europe found only 13 had mandated at least one vaccine for children.

The U.S. in general has had much higher vaccination rates than Europe, notes anthropologist Heidi Larson, a researcher at the London School of Hygiene and Tropical Medicine who studies vaccine skepticism and heads the Vaccine Confidence Project. "Somehow it became a social norm," she says. In the past, she says, American attitudes have been "'This is what we're doing to protect the health of our kids as a group,' not, 'It's being imposed on me as an individual.'"

Do some countries have high vaccination rates without mandates?
Japan's vaccination rates are higher than the U.S. for some diseases even though the country switched from mandatory vaccination for children to recommendations in 1994. Larson suggests this in part is due to social norms—people in Japan routinely wear face masks to prevent spread of disease, she notes, and they have a strong sense of community.

Yet Japan is also "extremely risk averse when it comes to vaccines," Larson says. The government suspended use of the measles, mumps, and rubella vaccine for 13 years because of side effects from the mumps component, and it is slower to approve new products than other developed countries.

What will happen in Florida if mandates are stopped?
Abundant research shows that when states make it more difficult to obtain vaccine exemptions for school entry, vaccination rates increase. Given that removing mandates does away with the need for exemptions, Larson expects coverage will decrease.

Researchers at the University of Florida's (UF's) Center for Statistics and Quantitative Infectious Diseases modeled the impact of a drop in measles vaccination rates after this week's announcement. If 95% of children in a school are vaccinated, herd immunity prevents cases among the unvaccinated from creating outbreaks. In 2024, 89.8% of Florida kindergarten students were immunized against measles, and the UF center calculates there's an 85.5% chance of an infected child spreading the disease to another student. If vaccine coverage drops to 85%, the likelihood of the infected child spreading the disease rises to 92.8%. The size of an outbreak in a school of 200 children would rise from 20 students today to 32 students if that coverage drop occurred.

Weaver notes that the measles outbreaks in the U.S. this year were in "pretty small, rural communities," and fears a drop in vaccination rates in Florida could lead to a bigger crisis. "There are plenty of pockets of susceptible people in the country, and a big outbreak in Florida is going to seed them all," he says. "It could be catastrophic for public health until people recognize the folly of this kind of a policy." □

CREDITS: (GRAPHIC) V. PENNEY/*SCIENCE*; (DATA) CENTER FOR STATISTICS AND QUANTITATIVE INFECTIOUS DISEASES/UNIVERSITY OF FLORIDA

PHOTO: MARTIN MILLET

Archaeologists excavate the former Roman trading center at Aldborough, England, which was a major mining center.

ARCHAEOLOGY

Did Great Britain's economy shrug off the end of Roman rule?

Pollutants in sediment core suggest mining and smelting did not tail off **ANN GIBBONS**

Martin Millett thought the mud of an ancient riverbed in northern England would confirm conventional wisdom that the end of Roman rule in Great Britain brought economic collapse. He expected levels of pollutants in the core sample, taken from the River Ure in Yorkshire, to fall as local mines went quiet. Instead, he was floored to see that iron and lead levels rose steadily for 2 centuries after the Roman Empire collapsed and its legions left Great Britain. "The mining did not tail off—everything did not fall apart," says Millett, an emeritus archaeologist at the University of Cambridge. The finding, reported in *Antiquity* this week, is "new and completely surprising."

"I think it's a fabulous piece of work," says Robin Fleming, a medieval historian at Boston College who has documented the economic and social collapse in southeastern England after the Roman exodus in the fifth century. The core also tracks how mining activity—and the economy more broadly—rose and fell in response to wars, plagues, and the whims of kings over later centuries of U.K. history. But to Fleming, "Seeing evidence of this community carrying on iron production in the early Middle Ages, is an important discovery."

Ever since mosaics from the former Roman town were discovered in the village of Aldborough, England, in the 19th century, archaeologists have gathered evidence that it was a prosperous Roman administrative center called Isurium Brigantum. The Romans were likely drawn to the region because it was rich in metals, such as silver, lead, and iron, which were mined and shipped along the Ure. Archaeologists have since uncovered a trail of ceramic pottery, lead ingots and metal coins, spears, farming tools, and other "bling," Millett says.

But evidence of intense economic activity begins to wane around 200 C.E., and these artifacts disappear by the fifth century when Germanic immigrants began to settle in Great Britain. At the same time, the manufacture of ceramic pottery collapsed in southeastern England, hundreds of silver coins were clipped because of apparent metal shortages, and people were scavenging iron clamps, lead gutters, and pipes from abandoned Roman villas. All of this points to "the economy winding down," Fleming says.

Metal pollution in the environment, however, offers an independent way to track the state of the ancient economy. When Cambridge researchers discovered an ancient paleochannel of the Ure that once flowed 500 meters from the center of Isirium Brigantum, they realized it was a rare and ideal site to drill a core of ancient sediments that had not been disturbed by later activity. Millett invited Christopher Loveluck, an archaeologist at the University of Nottingham who has analyzed ancient pollution in the Peak District and the Alps in Europe, to join the study. "It was a golden opportunity to look at a record of 2000 years of metal production in one of the main centers of northern England," Loveluck says.

The team extracted a slender, 6-meter-long core and searched it for pollen from plant species, which provided rough time markers because they were grown during different periods, such as hemp in the Medieval era and wheat and barley in Roman times. Radiocarbon dating and optically stimulated luminescence dating—which measures when quartz in the sandy silt was last exposed to light—sharpened the chronology. The researchers then measured the levels of 56 elements along the core, including iron, lead,

and silver, as well as byproducts of smelting iron and silver, such as phosphorus and arsenic.

Their analysis revealed a small decline in metal production in the late fourth century, perhaps as the Romans were winding down their presence in the region, but then a gradual rise in lead pollution from the mid–fifth to mid–sixth centuries, as well as a spike in silver pollution in the mid–fifth century. This suggests lead smelting continued after the Romans withdrew, the authors say. "The merry-go-round is still going on—it can't just be a few people at Aldborough; it has much bigger implications in terms of trade networks for coal to fuel smelting," Millett says.

As the researchers moved up the core, they saw that metal pollution continued until the mid–sixth century, then fell. Loveluck thinks the drop could be because of economic collapse during the Justinian plague, an epidemic of plague in the Mediterranean basin from the 540s to the 590s C.E., also recorded in ancient DNA from mid–sixth century graves of Anglo-Saxon people in Cambridgeshire. But others, including Millett, say the sixth century downturn could be due to a cooling of the climate, which could have led to crop failures and depressed the economy, or reductions of the supply of coal for smithing because of trade wars between local princes.

Centuries later, a downturn in metal mining at Aldborough does seem to reflect a devastating episode of the bubonic plague known as the Black Death, from 1457 to 1465, as well as dire flu epidemics. Mining recovered, for a time. But the lead signal dropped again after King Henry VIII closed the monasteries in the 16th century, creating a large supply of the metal from monastery roofs and artifacts to scavenge and recycle.

Those findings confirm conventional history. But the surprising resilience of mining in the fifth century has scholars wondering whether Aldborough was a rare center of prosperity in an otherwise bleak landscape in England. "I would think that Aldborough, as an important Roman center, carries on as an important place in early Middle Ages; the people who have access to things like good iron have certain advantages even after the Romans leave," Fleming says. But Loveluck wonders whether the discovery has a broader implication: that the devastation brought on by Rome's fall wasn't as widespread across England as previously thought.

To resolve that question, other researchers would like to see analyses of more sediment cores, covering more of ancient Great Britain and going even further back in time. Roman historian Kyle Harper of the University of Oklahoma, for example, wants to go back 500 years earlier to see whether such cores could provide a baseline by tracking a rise in metal production by the Romans after they arrive in Great Britain around 50 C.E. At minimum, he says, the new findings "should motivate people to pay more attention to the metal economy." □

THEY SAID IT

It's fantastic for all the little girls who might one day become the women scientists of tomorrow.

Astrophysicist Isabelle Vauglin, who co-chaired a panel recommending that the names of 72 women scientists be inscribed on the Eiffel Tower, alongside those of 72 men scientists shown on the monument since 1889.

ASTROPHYSICS

Strongest black hole collision yet resonates with Einstein

"Overtone" in gravitational waves from black hole merger matches predictions of general relativity **ADRIAN CHO**

Almost 10 years after the first detection of ripples in space itself called gravitational waves, physicists have announced the strongest such signal yet. Produced when two black holes in a distant galaxy spiraled into each other, the merger enabled researchers to test Albert Einstein's theory of gravity, general relativity (GR), in new ways. In particular, as reported this week in *Physical Review Letters*, analysis of the event confirmed a theorem derived by Stephen Hawking that a black hole's surface area can only grow and never shrink.

"That's such a fundamental, pure theorem of general relativity that to see it verified is really fantastic," says Clifford Will, a gravitational theorist at the University of Florida. "It's one of the things that allows you to say we are really looking at black holes."

The signal was detected on 14 January by the Laser Interferometer Gravitational-Wave Observatory (LIGO), which comprises two L-shaped interferometers in Louisiana and Washington state. Laser light resonating along the interferometers' 4-kilometer-long arms is used to detect passing gravitational waves, which stretch each arm by less than 1/100th the width of a proton. Comparing the latest signal with models shows it was generated when distant black holes with masses 33.6 and 32.2 times that of the Sun spiraled into each other and merged.

The black holes had nearly the same masses as those that produced the first LIGO event, detected on 14 September 2015. However, since then, improvements to the LIGO detectors have made them three times more sensitive. So, the new signal stood out far more clearly, with a signal-to-noise ratio of 80, which enabled researchers to examine it in unprecedented detail.

After a merger, the final black hole's event horizon—the boundary marking where gravity becomes so strong not even light can escape—reverberates fleetingly like a sharply struck bell. In this case, that "ring down" had a frequency of 247 cycles per second and lasted for about 10 milliseconds. The main oscillation can have overtones of slightly different, generally lower frequencies that fade faster and are key to testing GR.

According to the theory, a black hole is so featureless it can be characterized by just two numbers: mass and spin. That implies the frequencies and decay rates of the overtones aren't independent, but must be related mathematically. By comparing an overtone with the primary ring down tone, physicists can test the relationships predicted by GR.

The hard part is spotting an overtone, which can fade in less than a single cycle of oscillation. "Black holes don't ring, they thud," says Scott Hughes, a theorist at the Massachusetts Institute of Technology. Other black hole mergers, including the first LIGO event, had offered hints of an overtone. In the new event the overtone stands out clearly, says Katerina Chatziioannou, a physicist and LIGO member at the California Institute of Technology. "This is definitive." Sure enough, the frequencies of the tone and overtone conformed to the predictions of GR.

One caveat is that LIGO identifies and characterizes signals with the help of simulations that assume GR is correct—a possible source of bias. To avoid it, researchers ignored most of the signal and analyzed just the ring down. They could do that only because the signal was so strong, says

Gravitational waves that emanate from colliding black holes bear clues about these unseen objects.

Maximiliano Isi, a LIGO physicist at the Flatiron Institute. "That is what enables all of this," he says. However, Frans Pretorius, a gravitation theorist at Princeton University, cautions that some amount of bias may still be baked into the analysis.

LIGO researchers then used the mass and spin of the final black hole to calculate the area of its event horizon: about 400,000 square kilometers, roughly the size of Japan. Data from earlier in the event, when the initial black holes were spiraling together, revealed their mass, spin, and area as well. The area of the final black hole exceeded the total area of the initial ones—even though the final object was less massive than the sum of the initial black holes, as some energy, and hence mass, radiated away in gravitational waves. That result jibes with Hawking's mathematical theorem, which says no matter how a black hole's mass and spin evolve, its area can only grow.

The work shows how, as LIGO's sensitivity has improved, black holes have become the subject of empirical study. "It's a qualitative change that's enabled by a quantitative one," Hughes says. With further improvements to LIGO or with future observatories, scientists should be able see multiple modes and overtones, Pretorius notes. "Perhaps the hope is that GR is not quite correct and at some point we will get a precise enough measurement where we start seeing an anomaly."

Of course, that depends on squeezing better performances out of LIGO. In June, the White House called for shuttering one of the LIGO stations as part of a plan to cut the budget of the National Science Foundation by 57%. Such a closure would dramatically reduce LIGO's sensitivity—and dampen hopes of hearing further black hole harmonies. □

IN FOCUS

Dandelion seeds are built to float far

Huffing on a dandelion often leaves a few tufts behind—not for lack of lung strength, but because the flower is built to resist being blown down. Thanks to the dandelion's anatomy, the force needed to free a seed can change more than 100-fold depending on the wind direction, a new study in the *Journal of the Royal Society Interface* shows. When blown upward, a seed stalk bends until its base snaps loose along a weak edge. But a downward breeze presses the base against extra tissue that absorbs strain, so the seed clings tightly—needing at least five times more force and double the wind speed to shake free. Pulling the seed straight out proved toughest of all. That distributes the stress evenly across the base, requiring yet another 30-fold increase in force. The design ensures the umbrellalike seeds are much more likely to ride an upward gust—or the hopeful blow of a wish—far away from home. —Celina Zhao

IMAGES: (TOP TO BOTTOM) MAGGIE CHIANG/SIMONS FOUNDATION; BESS HAMITI/SHUTTERSTOCK

IN OTHER NEWS

MPOX NO LONGER A GLOBAL EMERGENCY

Falling numbers of mpox cases across Africa have led the World Health Organization (WHO) to decide the epidemic no longer warrants its highest level of alarm. WHO declared the viral disease a Public Health Emergency of International Concern (PHEIC) in August 2024, after an explosion of cases in the Democratic Republic of the Congo and neighboring countries. But cases have dropped in recent months, and on 5 September, WHO Director-General Tedros Adhanom Ghebreyesus accepted an expert panel's recommendation to lift the PHEIC. "Of course, [this] does not mean the threat is over, nor that our response will stop," Tedros said. Indeed, a committee convened by the Africa Centres for Disease Control and Prevention on 4 September unanimously urged the agency to retain its Public Health Emergency of Continental Security status—a recommendation Africa CDC Director Jean Kaseya promptly accepted. Testing for the virus that causes mpox is spotty, but Africa has recorded more than 32,000 confirmed cases this year and more than 100,000 suspected ones. —Jon Cohen

TRUMP ADMINISTRATION

Harvard court victory leaves scientists feeling vindicated but uncertain

Federal judge rules withholding of research funds was illegal **PHIE JACOBS**

Harvard University scored a major victory in its battle against President Donald Trump's administration last week, as a federal judge ruled the government violated the U.S. Constitution and broke the law when it halted billions of dollars in research grants to the school. But the White House is vowing to appeal, signaling that Harvard's fight to regain its funding is far from over.

"While this is an important legal victory, there are many steps to go," says David Walt, a researcher at Harvard Medical School and Brigham and Women's Hospital who when the spending was cut was told to immediately stop work on his project developing diagnostics and treatments for amyotrophic lateral sclerosis. Although Walt is "delighted" by the new ruling, he notes that "the only way we will be able to restart the project is when funds arrive from the feds."

The funding fight began in April, when the Trump administration accused Harvard of failing to address antisemitism on campus and demanded the university change its hiring and teaching practices and grant the government control of some operations. After Harvard refused to comply, the federal government froze—and later terminated—nearly $2.2 billion in research grants to the university.

In an 84-page ruling, U.S. District Court Judge Allison Burroughs found those actions violated Harvard's First Amendment rights. The administration, she wrote, "used antisemitism as a smokescreen for a targeted, ideologically-motivated assault on this country's premier universities."

The ruling "is very vindicating," says Harvard epidemiologist and former attorney Scott Delaney, whose research on how environmental factors affect people with Alzheimer's and Parkinson's diseases was also halted. He hopes the ruling will inspire other universities targeted by the Trump administration to continue to fight back, rather than capitulate to its demands.

In July, Columbia University agreed to pay more than $200 million in order to unfreeze its National Institutes of Health (NIH) funding—drawing mixed reactions from researchers. Brown University has reached a similar settlement, in which the school agreed to hand over data on admissions and diversity efforts, and not to perform gender-affirming treatments on minors, among other concessions. These institutions "lost a lot," Delaney argues, "and not just money."

Harvard was said to be open to a settlement, reportedly to the tune of $500 million. But university President Alan Garber told faculty in August that such a deal was not imminent. Walt notes that, even if funding is eventually reinstated, certain labs will have a much harder time getting back on track than others. For some studies, "particularly those that involved patients who were being treated and followed, there will be no chance to recover from the funding gap without starting over completely."

Any restoration of funding will come too late for Delaney, who was laid off after the grants that supported his salary were terminated. But in his view, last week's ruling still represents a major victory—for both the rule of law and for science. "Even if folks like me won't be around to do the research, most of my colleagues will be, and they're still as good and productive as they ever have been." The government will likely appeal last week's decision to the First Circuit Court of Appeals, which Delaney says will probably uphold it. After that, the case is presumably headed for the U.S. Supreme Court, where the outcome is far less certain. Last month, in an emergency stay, the justices allowed NIH's abrupt termination of hundreds of grants to stand for now.

> "I'm cautiously optimistic that some of the funds might eventually be reinstated."
>
> **Samuel Gershman**
> Harvard University

"I'm cautiously optimistic that some of the funds might eventually be reinstated, but there's still a ways to go before that becomes a reality," says Harvard neuroscientist Samuel Gershman. Even if Harvard ultimately prevails in court, he is concerned that the government will find other ways to disrupt research at the university. The White House has, for example, attempted to block Harvard from enrolling international students, and Trump has threatened to revoke Harvard's tax-exempt status.

Fighting back against this administration, Gershman adds, can feel like "a game of Whac-A-Mole." He still thinks, however, that Harvard should avoid a settlement: "In the big picture, it's more important that the university protect itself from political interference and retain its status as a haven for independent intellectual thought." □

IN THE LOOP

Paul Mischel is championing the importance of odd genetic loops in tumors—and their promise as targets for cancer therapy

ELIE DOLGIN

When Paul Mischel started his lab in the late 1990s, the rules of cancer biology seemed straightforward and solutions finally within reach. A wave of targeted therapies was taking shape. For the first time, it seemed possible to design drugs that didn't just carpet-bomb tumors—with healthy tissue as collateral damage—but struck only malignant cells, taking aim at the precise mutations fueling their growth. In glioblastoma, the lethal brain cancer Mischel had set out to understand and subdue, the target appeared obvious: a gene, encoding a cell surface protein called epidermal growth factor receptor (EGFR), that was amped up to unusually high levels in nearly half of all cases by extra copies found within tumor cells.

It was a vulnerability seemingly ripe for exploitation, as drugs designed to block EGFR's growth signals were just entering the research pipeline. Yet trial after trial of these EGFR-targeted agents produced the same disappointing result: Brain tumors barely flinched in the face of this precision attack.

Mischel dug into the problem the way any clinician-scientist might approach a puzzling case: cell by cell, sample by sample, refusing to take the tumor's resilience at face value. What he found would reveal a hidden layer of genomic architecture in cancer, one that enables tumors to flout

Paul Mischel spearheaded the creation of an international network to study extrachromosomal DNA in cancer.

PHOTO: TIMOTHY ARCHIBALD

the rules of evolution. The findings would open up an entirely new frontier in anticancer drug discovery.

Mischel's first curious observation had to do with how quickly glioblastomas adapted to treatment. Within a week or two, tumors that had once bristled with extra copies of the receptor gene, *EGFR*, shed most of them. That kind of genomic shift should have unfolded gradually, over successive rounds of cell division. Instead, it happened with unsettling speed. Stranger still, cells that had seemingly rid themselves of *EGFR* retained the uncanny ability to bring it roaring back, spawning new tumors with high gene expression as soon as the drug pressure lifted. It was like watching a doused fire suddenly reignite from cold ash.

"The tumors were changing their genomes way too quickly," says Mischel, a neuropathologist and cancer biologist now at Stanford Medicine. "It was a colossal scratching of heads."

> "This is a totally different way that cancer cells are evolving."
>
> **Elizabeth Brunk**
> University of North Carolina at Chapel Hill

The mystery deepened when David Nathanson, a trainee in Mischel's lab, began to examine glioblastoma cells under the microscope. He stained chromosomes blue; *EGFR* was tagged in red. He expected the red signals—the extra copies of *EGFR*—to align neatly along the blue chromosomes. What appeared instead was chaos: scattered red dots drifting across the nucleus, unmoored from any chromosomal structure. "It was really crazy to see," says Nathanson, now a brain cancer biologist at the University of California (UC), Los Angeles.

The receptor gene, it turned out, was traveling on rogue loops of circular DNA. Untethered from the rest of the genome, these free-floating fragments multiplied, vanished, and reappeared in response to fluctuating drug pressure, defying the classical rules of inheritance. And this wasn't unique to brain cancer. Mischel went on to find these odd bits of genetic material—now more broadly known as extrachromosomal DNA, or ecDNA—in every cancer type he examined, especially in more aggressive tumors with worse prognoses.

"It was a light bulb–goes–off kind of moment," Mischel says. The sheer prevalence of this ecDNA—and, even more critically, its ability to drive rapid tumor adaptation—would undoubtedly have profound implications for how tumors grow, evade treatment, and, he hoped, might finally be stopped.

By the late 2010s, others were making similar observations. But rather than competing for credit and priority, Mischel set out to recruit collaborators, pitching the wonders of ecDNA to fellow scientists and proposing a large international team-science project to explore it. In 2022, he secured a $25 million multiyear grant from a transatlantic alliance of cancer research funders, allowing him to rally the global posse of ecDNA hunters.

Chris Bailey, a cancer geneticist from the Francis Crick Institute, recalls how Mischel welcomed him into the field when he was an unknown grad student. Mischel lent his name and expertise to a 2020 review article on ecDNA that Bailey spearheaded, even before the young trainee had performed a single experiment on the topic. "He's a genuinely nice guy," says Bailey, who later joined the consortium. "He brings all of these people together, and he can communicate the science in such a way that is quite captivating."

Now, Mischel is pushing the science toward the clinic as a cofounder of Boundless Bio, a biotech company that aims to turn vulnerabilities created by ecDNA into next-generation cancer treatments. Others are also racing toward the same goal. "It's an untapped frontier," says Owen Wallace, CEO of Econic Biosciences, a rival startup.

Progress has proved far from linear, however. The first ecDNA-directed agents have already hit speed bumps in early clinical testing, and the underlying biology remains fiendishly complex, with many gaps still to be filled. As a result, some scientists are not convinced these enigmatic DNA circles are the shape of the next revolution in cancer treatment. "What I've seen is very good science," says cancer biologist Geoffrey Wahl at the Salk Institute for Biological Studies. "It's illuminating, but I'm waiting for the transformational."

The next year may be pivotal for the field. The ecDNA network grant Mischel organized is already winding down and companies like Boundless Bio only have so much investor cash to burn before they find some evidence of therapeutic success. Mischel, however, is convinced the payoff will come. "This will go from science to medicine," Mischel says. "It has to—there's no doubt—it's just a matter of how long it's going to take."

MISCHEL TRACES his collaborative instincts to values imparted by his father Theodore, a philosopher who escaped Nazi-occupied Austria and later served as an interpreter at the Dachau war crimes trials, and his uncle, psychologist Walter Mischel, who developed the famous "marshmallow test" for self-control. Growing up with an identical twin was formative, too. "I honestly don't know what it's like not to share everything," Mischel says.

After losing his father to stomach cancer, Mischel committed himself to a career in cancer care and research, ultimately focusing on the question of why targeted drug therapies for brain cancers often fail. He began with the usual suspects—mutations in the genetic circuitry of glioblastoma cells—but the appearance of ecDNA forced him to rethink everything.

Mischel was not the first to notice them. That distinction goes to cytopathologist Arthur Spriggs, who in 1965—when Mischel was still a child growing up in upstate New York—peered at chromosomes from a handful of childhood tumors and was startled, as Nathanson would be nearly a half-century later, by what greeted him under the microscope: "a shower of little dots," as Spriggs and his colleagues wrote. Each was a tiny accessory piece of DNA adrift from the normal chromosomal set. "There is some reason to suppose that they are rings," Spriggs and his colleagues noted.

But the findings were largely dismissed as curiosities or by-products of chromosomal instability. It would take another 20 years and the advent of more powerful electron microscopes for biochemist Robert Schimke and his colleagues at Stanford to obtain direct visual proof that the structures were closed loops, rather than broken chromosome fragments.

Schimke's team went on to show ecDNA isn't just debris: The circles often ferry oncogenes or amplify drug-resistance genes, and their

numbers vary wildly from one tumor cell to the next. Building on those insights, Wahl and Daniel Von Hoff, an oncologist now at the Translational Genomics Research Institute, identified a drug strategy that targeted these circles. In a small late-1990s trial in women with advanced ovarian cancer, low doses of the chemotherapy drug hydroxyurea prompted tumor cells to purge their ecDNAs, with some evidence of delayed disease progression.

But interest in these genetic circles fizzled again. "It was kind of this backwater of cancer biology," says Matthew Vander Heiden, director of the Koch Institute for Integrative Cancer Research at the Massachusetts Institute of Technology. It would ultimately take Mischel's rediscovery of the phenomenon—and his team's subsequent push to systematically chart ecDNA's form and function—to thrust the renegade loops back into the spotlight.

After Mischel and Nathanson first spotted *EGFR*-laden circles in their glioblastoma samples, they wondered how widespread the DNA fragments were in cancer. A sweep of a long-running database of cancer-related genetic rearrangements turned up mentions of ecDNA in fewer than 800 of the 54,000-plus tumors listed. Could it be, Mischel wondered, that what his group had found was just a quirk of brain tumors and a few other oddball cancers? To find out, he tasked a postdoc, Kristen Holmes, with casting a wider net.

Holmes raided tumor banks and cell repositories, logging long hours at the microscope looking for the telltale pinpricks of ecDNA in cancers of every stripe. Contrary to the sparse reports in the literature, she found the circles everywhere: in nearly 40% of cultured cancer cell lines and in almost all of the patient-derived brain tumor samples she examined. "It was just so exciting to be at the microscope and to see these with my own eyes," says Holmes, now at the University of Texas MD Anderson Cancer Center. "It kind of never got old."

DNA sequence data soon confirmed her findings. Working with bioinformatics researcher Vineet Bafna at UC San Diego, Mischel and his colleagues built a program called AmpliconArchitect that mines standard whole-genome reads and, on the basis of telltale flanking sequence patterns, can infer whether DNA segments are arranged in circles rather than along the chromosomes. The software revealed ecDNA in cancers of the lung, stomach, pancreas, liver, colon, bladder, breast, prostate, and more. And equally important for drug development, it became clear that, although normal cells sometimes carry minuscule circular DNA fragments, only cancers harbor large, gene-carrying ecDNA, making it a promising target for treatment.

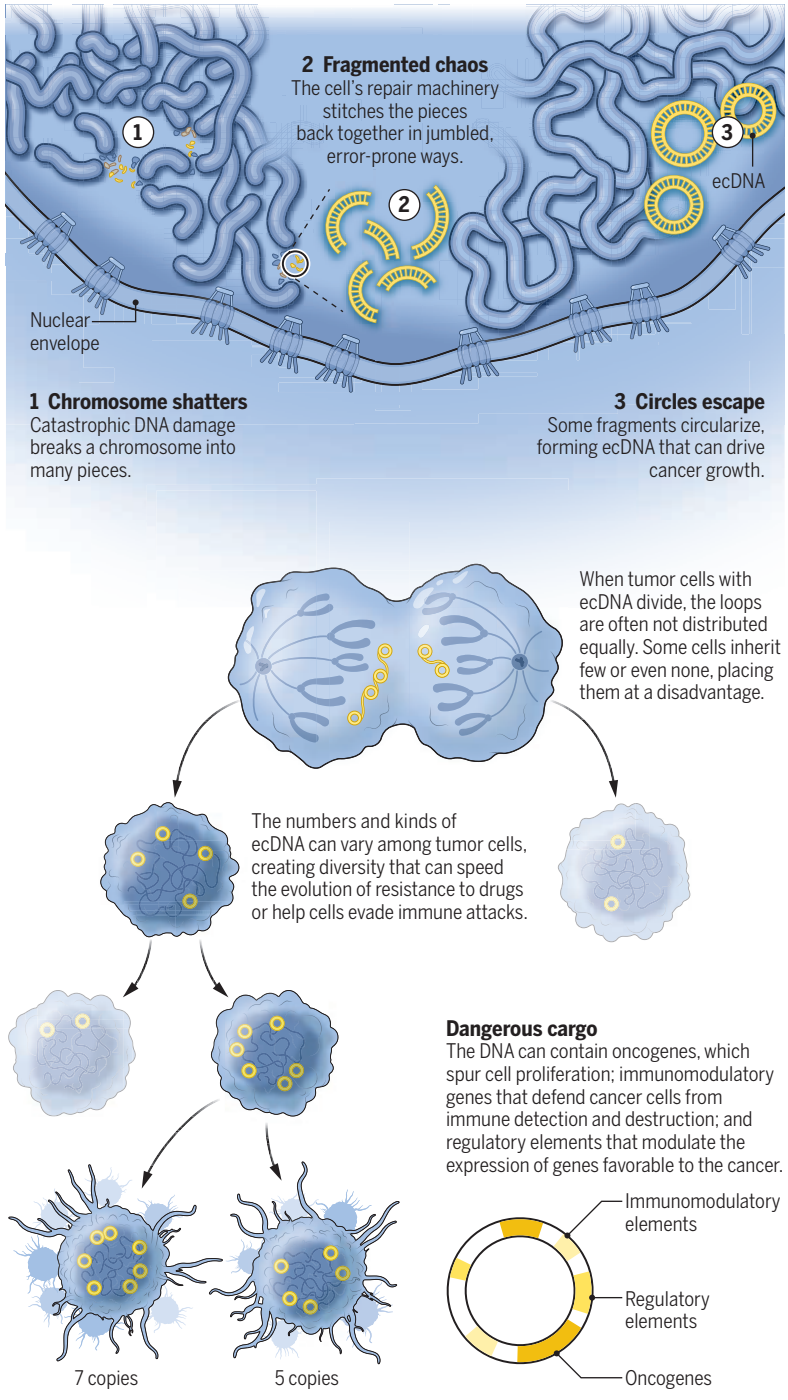

Circling in on cancer

Cancer cells harbor loops of DNA, separate from the chromosomes, that fuel tumor growth and evolution. First noticed in the 1960s, extrachromosomal DNA (ecDNA) can form in several ways, including when chromosomes shatter during cell division, and is found in greater amounts in more aggressive tumors. Now, scientists are testing drugs to eliminate the loops, hoping for a new type of cancer treatment.

UNBEKNOWNST TO MISCHEL, other groups were converging on these same cancer circles—and detailing how such extrachromosomal elements rewire tumor genomes at breakneck speed. In 2018, cancer biologist Roel Verhaak, now at the Yale School of Medicine, independently spotted ecDNA loops in glioblastoma and showed that they foster genetic diversity; the next year, pediatric oncologist Anton Henssen of the Charité University Hospital of Berlin

GRAPHIC: A. FISHER/*SCIENCE*

and computational biologist Richard Koche of Memorial Sloan Kettering Cancer Center tied similar circles to wholesale remodeling of the genome in neuroblastoma, a childhood cancer that develops from immature nerve cells outside the brain.

Howard Chang, a molecular geneticist then at Stanford (and now chief scientific officer of the biotech company Amgen), was closing in on ecDNA as well, though he didn't realize it initially. His lab was focused on the architecture of chromatin—the tightly packed skeins of DNA and proteins in the nucleus that regulate which genes are turned on or off. In cancer cells, Chang and his colleagues noticed unusually large swaths of unpacked DNA, regions where the genome seemed to be bent and rewired to drive massive bursts of oncogene expression. After hearing Mischel present his work on ecDNA, Chang realized that his hot spots were powered not by chromosomes, but by runaway circles, and he joined forces with Mischel.

So did others—within a few years, Mischel was working with nearly everyone chasing ecDNA. Their collective efforts soon drew notice, from editors of high-profile journals and also from scientific advisers to Cancer Grand Challenges, a joint initiative of Cancer Research UK and the U.S. National Cancer Institute. Mischel assembled the eDyNAmiC team with Bafna, Bailey, Chang, Henssen, Verhaak, and other leaders in the field and won the $25 million award from the initiative. Since then, the team has been methodically charting ecDNA's life cycle in tumors and scouting the weak spots future drugs could exploit.

Bailey, for example, led an analysis of tumor sequence data from nearly 15,000 patient samples, finding ecDNA in about one-sixth of all cases, most commonly in aggressive malignancies such as brain tumors and in soft-tissue sarcomas. Bafna and Chang have spearheaded the development of additional tools for detecting ecDNA from different types of genomic data, whereas others in the network have built experimental systems for inducing circle formation in cell lines and mice.

Leveraging these innovations, researchers have shown how these loops are spawned during the genetic mishaps that fast-growing cancer cells are prone to: when chromosomes splinter apart, when broken DNA strands snap loose, or simply when dividing cells make a mistake (see graphic, p. 1083). Regardless of how they form, the circles often carry a powerful cargo: multiple copies of the oncogenes that drive tumor growth and of immune-modulating genes that help shut down the body's anticancer defenses.

This arsenal can turn precancerous disease to full-blown cancer. It can also stoke the aggressiveness of established malignancies: ecDNAs are more common in later stage, metastatic disease—and linked to markedly worse survival odds. In children with cancers of the brain, bone, and soft tissues, for example, those whose tumors harbored ecDNA were twice as likely to die within 5 years compared with peers whose tumors had no extra copies of cancer genes.

Underlying this aggressive biology is a peculiar form of cooperation. ecDNAs often cluster into shared "hubs," where tightly packed loops mingle their regulatory elements and turbocharge their gene activity. As Chang puts it, "Cancer gets to play by a different set of rules and this is pretty scary."

What's more, as tumors grow and cells divide, these hubs often stay intact from one generation to the next, riding into one daughter cell while skipping the other. The result is a patchwork tumor, with some cells brimming with extra cancer-driving genes on the loops while others have far fewer. The whole mass is then primed for rapid evolution. "It's a bet on diversity," says Vincenzo Corbo, a cancer biologist at the University of Verona. "It makes these cells ready to respond to any fluctuation in the environment."

That capacity helps explain the failure of targeted treatments. Traditionally, scientists have pictured tumors developing drug resistance gradually, with a single cell picking up a helpful mutation, growing faster, and gradually pushing out its neighbors. But with ecDNA, the whole population can reshuffle its genetic deck at once.

"This is a totally different way that cancer cells are evolving through more of a bet-hedging approach," says Elizabeth Brunk, a systems biologist at the University of North Carolina at Chapel Hill. The result: Resistance doesn't trickle in from a lone survivor—it erupts from many cells at once, making even the most precisely targeted agent easy for the tumor to dodge.

Rings revealed

A large study found extrachromosomal DNA in 17% of tumor samples, but some cancer types had it more often.

Glioblastoma	**49%**
Stomach	**33**
Bladder	**25**
Sarcoma	**23**
Breast	**23**
Colorectal	**22**
Ovarian	**20**
Liver	**17**
Skin	**14**
Lung	**13**
Pancreatic	**2**
Prostate	**1**

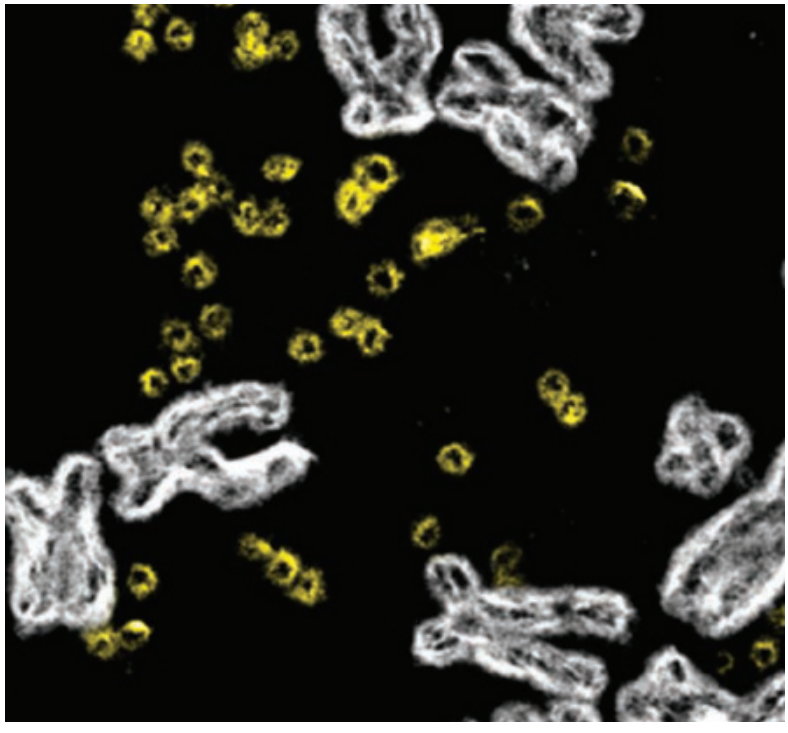

A scanning electron micrograph of extrachromosomal DNA shows the discrete genetic rings (yellow) alongside standard chromosomes (white).

CREDITS: (DATA) C. BAILEY *ET AL.*, *NATURE* **635**, 193 (2024); (IMAGE) S. WU *ET AL.*, *NATURE*, **575**, 699 (2019); (COLORIZATION) C. SMITH/*SCIENCE*

FORTUNATELY FOR drug developers, some of the very quirks that give ecDNA its edge create exploitable weak spots. Because the circles tend to run their genes at full tilt even as the cells themselves are dividing rapidly, molecular traffic jams can develop. Gene expression and cell division both require bulky protein machines to travel the same track of DNA. If those machines collide, the DNA can stall, twist, or break, forcing repair enzymes to rush in and patch the damage.

Last year, Mischel and Chang, working with scientists at Boundless, showed such DNA collisions occur far more frequently in cancers containing ecDNA than in those without. Blocking a protein that relieves this molecular stress—an enzyme called CHK1—therefore had an outsize impact on cells burdened by these loops. And in mice with ecDNA-rich stomach tumors, treatment with a CHK1-targeting drug nearly wiped out the cancer while sparing normal tissue—proof of principle that the circles' own excesses can be turned into a lethal liability.

Boundless is now advancing a CHK1 inhibitor through early clinical trials. The company has also tested a second drug directed at a different enzyme called RNR that cancer cells need to make DNA building blocks, cutting off the supply so ecDNA can't rebuild. A third candidate, slated to enter trials next year, targets a motor protein crucial for ecDNA sorting during cell division.

Meanwhile, the eDyNAmiC team, along with other research groups, continues to mine the circles' biology to uncover even more drug-ready targets. In April, for example, a team led by molecular biologist Haiyun Gan at the Shenzhen Institutes of Advanced Technology identified proteins implicated in DNA untwisting and damage response as promising drug targets. "The collective findings consistently point to the DNA damage response as a critical process," Gan says.

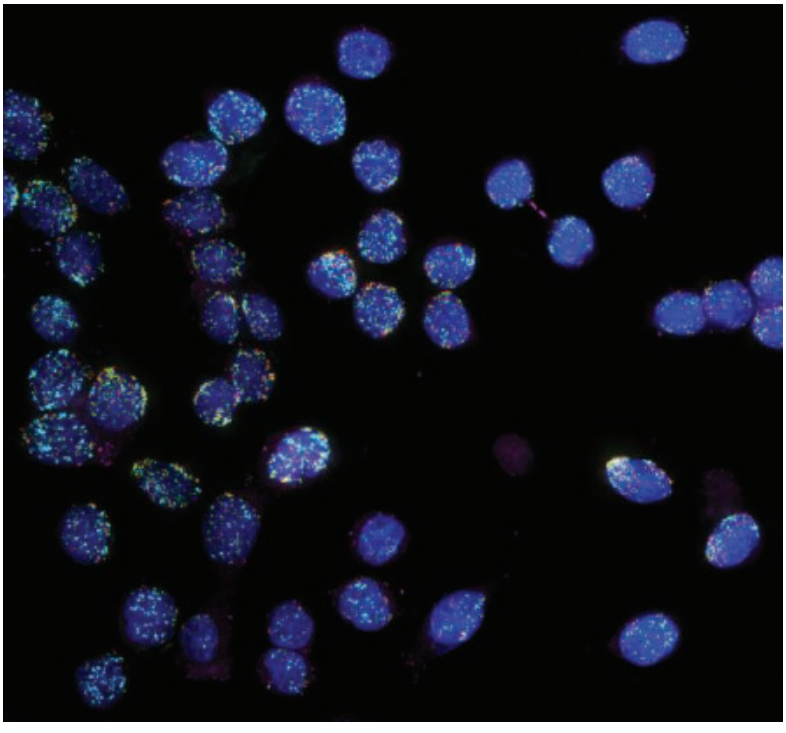

Gastric cancer cells sparkle with extrachromosomal DNA harboring two oncogenes, one stained red and one green. The genetic circles can cooperate and often travel together as cells divide.

IMAGE: IVY TSZ-LO WONG/STANFORD UNIVERSITY

But the genome's repair system is sprawling, involving a maze of interlinked proteins and feedback loops, and agreement on where best to intervene remains elusive. "The big question is what is the best target," Verhaak says. "Right now, there's not one that I would say is the front-runner."

Benjamin Cravatt, a chemical biologist at the Scripps Research Institute and an academic co-founder of Boundless, hopes eDyNAmiC will bring clarity as its funding nears an end: "Our job is to derisk these concepts for real drug hunters," he says.

They may not get another chance soon. The Cancer Grand Challenges program does not allow renewals, and other funding may be hard to come by in the United States, where biomedical research is under threat from President Donald Trump's administration. "Everybody is very concerned," Bafna says.

Adding to the anxiety are early setbacks in the clinical trials from Boundless. Its CHK1-blocking agent had toxic side effects when given at levels thought to stymie tumors, and the RNR inhibitor revved up liver enzymes that broke it down too quickly, preventing the compound from ever reaching therapeutic levels.

Earlier this year, the company pivoted: In May, it announced plans to test the two agents in combination at lower doses, betting that synergistic effects between the two drug candidates might safely choke off ecDNA's lifelines.

Some say the science is just not ready to be exploited in the clinic. "There's a lot of phenomenology that has gotten people really excited," says Vander Heiden, who is now probing how ecDNA alters the supply-and-demand balance of DNA building blocks in cancer cells. "But there are more questions than there are answers." Antonina Hafner, a group leader within the discovery oncology division of Genentech, one of several large pharmaceutical companies now exploring therapeutic opportunities opened by the DNA loops, agrees. "Targeting ecDNAs could provide a transformative medicine," she says, but "there is still a lot to understand about [their] biology before we can target them."

Mischel hears the caution, yet he is unshaken. He keeps in mind the scattered red dots that first astonished Nathanson, the thrill Holmes felt spotting them in one tumor after another, and the sense of urgency that comes from his belief these circles could finally be turned against cancer. "I'm not letting anything stop this," he says. "At the end of the day, the science is compelling, the clinical need is obvious and real—and, collectively, we'll figure this out."

If he's right, the very circles that let tumors bend the rules of biology may soon be the loophole that brings them down. □

Elie Dolgin is a science journalist in Somerville, Massachusetts.

ATMOSPHERIC SCIENCE

Burning questions on wildfire

Fire heat may change how wildfire affects air pollution in the United States

Yun Qian

Wildfires influence nearly every component of the overall Earth system by altering land surfaces and emitting gases, heat, and fine particles. They can change atmospheric and soil properties and affect water quantity and quality. The increasing risk of wildfires has prompted more frequent public safety hazards around the world. Wildfires can degrade air quality both in the immediate area and in the direction where wind is blowing through long-range atmospheric transport. On page 1137 of this issue, Ma *et al.* (*1*) report an observation that contradicts this conventional wisdom. They find that wildfires in the western United States can improve air quality in the eastern part of the country primarily through a process associated with heat-induced convection. The findings show that local wildfires may unexpectedly have far-reaching effects on weather in distant regions.

Wildfire behavior has changed globally over the past decade, with more extreme events now occurring in many areas, including the western US (*2*). Fire weather conditions, available fuels, and ignition source are major drivers of wildfire. In turn, wildfires affect weather and climate at multiple timescales. For example, interactions among wildfire, smoke, and the atmosphere amplify human exposure to air pollution over a timescale from a few days to 2 weeks (*3*). Wildfire also interacts with annual precipitation, intensifying variabilities in subsequent wildfires and rainfall roughly every 2 years (*4*). Ma *et al.* report that heat from wildfires in the western US can remotely affect air quality in the eastern US. By examining observational data, performing global model simulations, and analyzing wave activity in the atmosphere, the authors show that wildfire-generated heat drives convection and excites jet-stream waves, altering the atmospheric circulation and weather patterns downstream. This process increases convective precipitation that can enhance removal of pollutants from air and reduce the formation of secondary aerosols in the atmosphere of the eastern US.

Although US air quality has generally improved over recent decades, seasonal wildfires threaten to reverse this trend in certain regions (*5*). The study of Ma *et al.* reveals an opposite effect, but it also primarily focuses on fine particulate matter. Wildfires emit large amounts of other hazardous air pollutants such as carbon monoxide and ozone. Thus, further research is needed to address this gap in modeling and measurement to better understand the impacts of wildfires on Earth systems and human health.

The Intergovernmental Panel on Climate Change reported in 2022 that global climate change will likely increase the risk of extreme wildfire events (*6*). Nonetheless, this conclusion is undermined by limitations in the Earth system models used in the report, which omit critical interactions among fire, climate, ecosystems, and human activities (*7*). Wildfire simulations in Earth system models vary widely, partly owing to various simplifications and outdated assumptions. Most fire models

PHOTO: LOS ANGELES TIMES/GETTY IMAGES

Interactions between wildfires and the atmosphere can propagate beyond the local region and affect global air circulation.

fail to accurately reproduce observations (*8*). The major uncertainties lie in simulating fire behavior and smoke dispersion. For example, wildfire models often struggle to reconstruct the transition from smoldering to flaming phases or fires with complex fuel heterogeneity (*9*). Parameters such as fire plume rise and the injection height of particles and gases into the atmosphere are critical for simulating the effects of wildfire on atmospheric composition and smoke dispersion. These metrics remain underexplored partly because of limited measurements.

Advancing wildfire research requires improved data acquisition and integration through high-resolution measurements of fuel loads, fire behavior, burned areas, heat, emissions, surrounding weather conditions, and postfire recovery. This calls for investments in ground-based sensors, drones, and satellite monitoring systems to link data across laboratory, field, regional, and global scales to capture fire dynamics and impacts on terrestrial and atmospheric domains. Prescribed fire studies are also vital because they can offer a controllable outdoor testbed for refining models of uncontrolled wildfires.

Understanding wildfires' roles in Earth's carbon cycle as well as postfire effects on hydrology, cryosphere, soils, ecosystems, and electric power grid systems is important for the long-term consequences of wildfire. In addition, examining the evolving nature of wildfires and improving the ability to predict them are critical across broad timescales (from daily to interdecadal periods). Beyond wildfires, fires that occur in regions that border wildland and urban areas could behave differently and have distinct effects. If located near population centers, they release a different mix of pollutants because of combustible materials such as vehicles and structures in addition to natural biomass (*10*). Furthermore, both acute and chronic health hazards from fire should be assessed by analyzing pollutant types, exposure levels, and population vulnerabilities (*11*). Advanced data-driven models and machine learning methods could refine the prediction of wildfire extent and emissions (*8*, *12*). These technologies could also be applied across other areas of wildfire research to better understand the drivers and impacts of wildfires.

The findings of Ma *et al.* imply that wildfire-excited jet-stream waves can propagate atmospheric energy eastward, beyond North America, to alter the global air circulation. This underscores the need to approach wildfire research from a broader, global perspective. Strengthening cross-border and interdisciplinary collaboration is key to improving predictability and driving more effective solutions for wildfire control and recovery. □

REFERENCES AND NOTES

1. Q. Ma *et al.*, *Science* **389**, 1137 (2025).
2. M. Jones *et al.*, *Rev. Geophys.* **60**, e2020RG000726 (2022).
3. X. Huang *et al.*, *Science* **379**, 457 (2023).
4. Y. Liu *et al.*, *Atmos. Chem. Phys.* **24**, 3115 (2024).
5. C. Sarangi *et al.*, *Atmos. Chem. Phys.* **23**, 1769 (2023).
6. Intergovernmental Panel on Climate Change, *Climate Change 2022: Impacts, Adaptation, and Vulnerability* (Cambridge Univ. Press, 2022).
7. Y. Zou *et al.*, *Atmos. Chem. Phys.* **20**, 995 (2020).
8. S. Wang, Y. Qian, L. R. Leung, Y. Zhang, *Atmos. Chem. Phys.* **22**, 3445 (2022).
9. K. Little *et al.*, *Philos. Trans. R. Soc. Lond. B Biol. Sci.* **380**, 20240001 (2025).
10. W. Tang *et al.*, *Sci. Adv.* **11**, eadr2616 (2025).
11. E. Grant, J. D. Runkle, *J. Clim. Change Health* **6**, 100110 (2022).
12. S. Wang *et al.*, *Earth's Future* **9**, e2020EF001910 (2021).

ACKNOWLEDGMENTS

The author acknowledges support from the US Department of Energy (DOE), Office of Science Biological and Environmental Research, as part of the HyperFACETS project. Pacific Northwest National Laboratory is operated under the US DOE by Battelle Memorial Institute (DE-AC05-76RL01830).

10.1126/science.aea7430

Earth and Biological Sciences Directorate, Pacific Northwest National Laboratory, Richland, WA, USA. Email: yun.qian@pnnl.gov

GENOMICS

Gene flow stops sooner in plants than in animals

Genomic data indicate when species became reproductively isolated

Yaniv Brandvain

Ever since Ernst Mayr (*1*) formalized species as "groups of actually or potentially interbreeding natural populations, which are reproductively isolated from other such groups" in 1942, zoologists have considered hybridization (creation of offspring by mating between two different species) to be rare and ultimately unproductive. Botanists were more strongly influenced by ideas such as those of Göte Turesson (*2*), who asserted that "the species problem is thus seen to be in a large measure an ecological problem" and believed that the exchange of genes between ecologically differentiated species through hybridization (and breeding of the hybrid and its descendants with members of one of the species) was both common and important. However, empirical evidence for either view was lacking. On page 1147 of this issue, Monnet *et al.* (*3*) report population genomic evidence that contrary to standard expectations, this exchange of genes (gene flow) between diverged plant lineages ceases at lower levels of genomic divergence than it does between animal lineages.

Before the study by Monnet *et al.*, two key observations suggested that the dogmatic view that animals become reproductively isolated more rapidly than plants was incorrect. A phylogenetic study (*4*) showed that the number of plant species increases at roughly twice the rate as the number of animal species does. However, this study measured net diversification (speciation minus extinction, rather than the speciation rate alone) and relied on taxonomic ranks rather than a measurable property (such as the extent of gene flow). A survey of experimental crosses (*5*) found that plant species are more reproductively isolated from one another than are animal species. However, this study too had some limitations—for example, not including divergence time as a covariate. Not all previous evidence went against the orthodox view. For example, a review of the speciation genomic literature (*6*) found a higher level of gene flow in plants than in animals; however, including divergence time in the model nullified this pattern. Furthermore, an influential review paper (*7*) reported that roughly a quarter of plant species in the British Isles hybridize with another species. However, this study did not include divergence times and suffers from the nonstandardized sampling efforts of the studies it cites.

Monnet *et al.* took a genomic approach to infer gene flow. They analyzed patterns of genetic variation within and between species and then used approximate Bayesian computation (ABC) to reconstruct the history of speciation. This ABC approach identifies the parameter values that enable an evolutionary simulation to produce summary statistics like those observed in actual data. Notably, because this method evaluates the genomic signature of gene flow rather than the potential for hybridization, its results may differ from field observations or laboratory crosses. The authors report two key results: Plants stop exchanging genes at much lower lev-

els of overall genetic divergence than do animals, and for lineages that are still exchanging genes, plants more quickly develop a heterogeneous pattern of gene flow across the genome (selection prevents gene flow in some genomic regions and permits it in others). The authors argue that the latter may explain the historical view that plant species are more likely to exchange genes than are animal species. The rapid evolution of diverged genomic regions inhospitable to gene flow may allow plant lineages to become ecologically or morphologically distinct quickly while still occasionally exchanging some genes.

There are many reproductive, ecological, and genomic differences that may contribute to the more rapid cessation of gene flow in plants compared with animals (*8*). For example, plants cannot walk or fly and therefore may be more geographically isolated (less opportunity for gene flow) than are animals. Another explanation might be the frequent evolution of polyploidy (three or more sets of chromosomes) in plants; however, Monnet *et al.* limited their study to diploids, so this option can be discounted. Plants also commonly transition to self-fertilization and can shift growth form (for example, from woody to herbaceous), but the authors report that neither growth form nor mating system was strongly associated with the rate at which gene flow ends.

An artifactual explanation for the results of Monnet *et al.* cannot be completely ruled out. Inferring complex evolutionary histories from sequence data is a notoriously difficult problem (*9, 10*). Although the authors show that their approximate Bayesian computation approach works well on simulated data, they conducted inference on real world data. Empirical sequence data are shaped by complex evolutionary processes (such as balancing selection and population substructure) and by bioinformatic challenges (such as read mapping); the details of both are usually unknown and therefore cannot be easily simulated. Thus, although this study is exciting, the results may change with methodological advances and increasing data quality and quantity.

The prospect of inferring the details of the speciation process and the history of gene flow from sequence data has long fascinated population geneticists. Integrating this population genomic approach with phylogenetic methods to infer diversification (*11*) could more precisely disentangle how key biological features contribute to the speciation process. For example, a previous study (*12*) found no relationship between the evolution of reproductive isolation (for example, the evolution of hybrid inviability or infertility) and the rate of speciation. An integrated (micro- to macroevolutionary) approach could ask why: Do barriers that stop gene flow simply form too late to drive the birth of new species, or is their effect on speciation overshadowed by other processes? Similarly, although sexual selection is thought to drive speciation, phylogenetic evidence for its role in diversification is mixed (*13*). This synthesis of micro- and macroevolutionary data promises a more unified understanding of how life's diversity arises and is maintained. □

REFERENCES AND NOTES

1. E. Mayr, *Systematics and the Origin of Species* (Columbia Univ. Press, 1942).
2. G. Turesson, *Hereditas* **3**, 100 (1922).
3. F. Monnet *et al.*, *Science* **389**, 1147 (2025).
4. J. P. Scholl, J. J. Wiens, *Proc. Biol. Sci.* **283**, 20161334 (2016).
5. L. H. Rieseberg, T. E. Wood, E. J. Baack, *Nature* **440**, 524 (2006).
6. A. J. Dagilis *et al.*, *Evol. Lett.* **6**, 344 (2022).
7. J. Mallet, *Trends Ecol. Evol.* **20**, 229 (2005).
8. S. Wang, J. E. Mank, D. Ortiz-Barrientos, L. H. Rieseberg, *Mol. Ecol.* e70004 (2025).
9. S. Myers, C. Fefferman, N. Patterson, *Theor. Popul. Biol.* **73**, 342 (2008).
10. V. C. Sousa, A. Grelaud, J. Hey, *Molec. Ecol.* **20**, 3956 (2011).
11. J. M. Beaulieu, B. C. O'Meara, *Syst. Biol.* **65**, 583 (2016).
12. D. L. Rabosky, D. R. Matute, *Proc. Natl. Acad. Sci. U.S.A.* **110**, 15354 (2013).
13. M. J. G. Gage, G. A. Parker, S. Nylin, C. Wiklund, *Proc. Biol. Sci.* **269**, 2309 (2002).

ACKNOWLEDGMENTS

We thank L. Reiseberg and G. Bradburd for helpful comments. The author used AI tools (ChatGPT and Gemini) to improve the readability of this piece.

10.1126/science.aeb2961

Department of Plant and Microbial Biology, University of Minnesota, MN, USA.
Email: ybrandva@umn.edu

NEUROSCIENCE

Cries into ties

Oxytocin neurons in mouse pups regulate vocalization to maintain maternal bonds

Camilla Bellone

For most mammals, social bonding between mothers and infants is a fundamental, evolutionarily conserved behavior that is crucial for offspring survival, emotional regulation, and the acquisition of social skills necessary for future interactions (*1*). Early-life experiences, especially maternal care, shape developmental trajectories, profoundly influencing cognitive, emotional, and social competencies into adulthood (*2*). In rodents, the neuropeptide oxytocin has been widely recognized for its central role in maternal behaviors toward infants such as nesting, grooming, and nursing (*3*). Yet comparatively little is known about how oxytocin regulates infant behaviors toward mothers, particularly during episodes of maternal separation and reunion. On page 1111 of this issue, Zelmanoff *et al.* (*4*) report real-time changes in the activity of oxytocin-producing neurons in mouse pups during maternal separation and reunion, offering insights into how offspring actively contribute to maternal-infant bonding.

Maternal-directed behaviors in mouse pups, notably ultrasonic vocalizations (USVs), are complex and coordinated actions that not only signal distress but actively engage maternal attention. Zelmanoff *et al.* used a maternal separation paradigm that consisted of 3 hours of separation of postnatal day 15 (P15) pups from the mother, followed by a reunion. The authors detected an increase in USVs immediately after the reunion of the pups with the mother, followed by a gradual decrease as the mothers actively responded, for example, by licking, grooming, and nursing. They repeated the experiment with anesthetized dams to enable them to isolate pup vocalizations. In contrast to the gradual decline in USVs after reuinion with an awake mother, the amount of USVs produced by reunion with an anesthetized mother remained high. These USVs followed two distinct patterns: narrow-low USVs associated with nipple attachment and narrow-high USVs emitted in the absence of attachment. These results provide evidence that pup vocalizations actively mediate social reengagement independent of maternal behavior, underscoring the role of pups in shaping maternal-infant interactions.

Oxytocin is a peptide secreted from the hypothalamus in the brain and is involved in social behavior in mammals. Zelmanoff *et al.* used a fiber photometry approach, together with transcranial optical silencing, to detect and suppress the activity of oxytocin-producing neurons in freely behaving mouse pups at P15. During the shift from the home cage to maternal separation, the activity of oxytocin-producing neurons gradually increased before USV onset, peaked shortly after the calls began, and then declined within seconds. Over the course of separation, oxytocin neurons were progressively recruited, with transient spikes in activity during USV emission and a gradual overall increase in activity over time. Intriguingly, suppressing oxytocin neuronal activity prevented the natural decline in vocalizations typically observed over extended

separation periods, indicating the critical role of oxytocin in adapting vocal responses based on social context. Moreover, oxytocin's effects were context specific and sexually dimorphic: Suppression of oxytocin neuronal activity during separation modulated USVs produced during reunion in female pups but not in male pups. The underlying biological mechanisms and developmental implications of the observed sexual difference are not yet clear.

The differential vocalization patterns observed between pups reunited with anesthetized versus nonanesthetized mothers indicate synchronization of oxytocin signaling between mothers and pups during social interactions. When pups were reunited with responsive mothers, their vocalization frequency initially increased but quickly normalized as active maternal engagement occurred. Previous work has established that this engagement is mediated by maternal oxytocin release. Therefore, the associated decrease in pup vocalizations likely reflects synchronized oxytocin signaling in the mother and pup, which promotes social stability and emotional reassurance. Conversely, the maintained increase in vocalizations in pups reunited with anesthetized mothers suggests disrupted synchronization or an absence of the maternal feedback cues that are necessary for stabilizing oxytocin release in pups. These results raise important questions about how oxytocin dynamics in mothers and offspring become temporally and functionally aligned during interactive reunions, highlighting a critical area for future investigation. Simultaneously monitoring oxytocin neuronal activity in both mothers and pups during active interactions could elucidate the mechanisms underlying synchronization and its role in shaping early social and cognitive developmental trajectories (*5*).

In mice, the neuropeptide oxytocin has a role in maternal behaviors such as nesting, grooming, and nursing.

Although previous research in mice has established oxytocin's role in social homeostasis during adulthood (*6*), Zelmanoff *et al.* provide evidence that oxytocin neurons mediate isolation-induced social rebound in P15 pups. Their findings demonstrate the critical function of oxytocin neurons in homeostatic mechanisms that restore social equilibrium after separation. This discovery raises important questions about the broader role of oxytocin in pup social behavior. Social interaction is governed by two distinct but interconnected systems: homeostatic mechanisms that rapidly respond to social threats and deficits through stress-regulatory circuits (*7*) and hedonic mechanisms that enhance social rewards through integration with the dopamine system (*8*, *9*). Although these systems share neuronal circuits and cellular mechanisms, oxytocin may regulate them in a different manner. Zelmanoff *et al.* focused on homeostatic social regulation—how oxytocin drives maternal-directed reconnection after isolation stress. However, future investigations should examine whether oxytocin also contributes to hedonic aspects of maternal-pup interaction, such as the rewarding properties of social contact that motivate approach behaviors beyond mere deficit correction. Understanding this distinction is crucial because it determines whether oxytocin functions primarily to correct imbalances or whether it also enhances the inherent rewards of social interactions.

Although P15 represents a sensitive period in development, oxytocin signaling is already functional and influences maternal–infant interactions well before this age. Early postnatal stages (before P15) encompass critical transitions in sensory processing, hypothalamic neuropeptide system maturation, and the establishment of mother-pup communication patterns. For most mouse strains, USV calling follows a clear ontogenetic profile—increasing over the first 5 to 6 days of life, peaking around P6 to P7, and then gradually declining to near disappearance by the end of the second postnatal week (*10*, *11*). This developmental trajectory means that a P15 separation occurs after the primary peak of pup distress signaling, potentially missing key phases when oxytocin may most strongly influence reunion behaviors and attachment processes. Investigating oxytocin function during these earlier windows could reveal how neurochemical signaling scaffolds the initial formation of attachment bonds and shapes later social and stress-responsive behaviors. Although technical challenges in manipulating and recording neonatal brain activity remain substantial, such studies are essential for delineating the full developmental trajectory of maternal-infant bonding and for identifying the circuits through which oxytocin exerts homeostatic versus hedonic influences on pup social behavior.

The broader implications of these findings extend into translational neuroscience, particularly regarding neurodevelopmental disorders characterized by deficits in social communication and attachment, such as autism spectrum disorder (ASD). Oxytocin has been proposed as a potential therapy for ASD, but the mechanisms underlying its therapeutic effect are incompletely understood and the literature on its efficacy is mixed. Clarifying how precise temporal and context-specific oxytocin signaling modulates communication in early life could inform the development of targeted therapeutic strategies and deepen understanding of social cognition disorders. □

REFERENCES AND NOTES

1. M. D. Ainsworth, *Am. Psychol.* **34**, 932 (1979).
2. S. J. Racz, D. L. Putnick, J. T. D. Suwalsky, C. Hendricks, M. H. Bornstein, *J. Youth Adolesc.* **46**, 1688 (2017).
3. R. C. Froemke, L. J. Young, *Annu. Rev. Neurosci.* **44**, 359 (2021).
4. D. D. Zelmanoff *et al.*, *Science* **389**, eado5609 (2025).
5. G. X. Ham, K. E. Lim, G. J. Augustine, V. Leong, *J. Neuroendocrinol.* **35**, e13241 (2023).
6. D. Liu *et al.*, *Nature* **640**, 1000 (2025).
7. G. A. Matthews, K. M. Tye, *Ann. N. Y. Acad. Sci.* **1457**, 5 (2019).
8. L. A. Gunaydin *et al.*, *Cell* **157**, 1535 (2014).
9. C. Solié, B. Girard, B. Righetti, M. Tapparel, C. Bellone, *Nat. Neurosci.* **25**, 86 (2022).
10. R. W. Elwood, F. Keeling, *Dev. Psychobiol.* **15**, 221 (1982).
11. I. Branchi, D. Santucci, E. Alleva, *Behav. Brain Res.* **125**, 49 (2001).

10.1126/science.aea8966

Department of Basic Neuroscience, University of Geneva, Geneva, Switzerland.
Email: camilla.bellone@unige.ch

HYPOTHESES

Illusions of AI consciousness

The belief that AI is conscious is not without risk

Yoshua Bengio[1,2] and **Eric Elmoznino**[1,2]

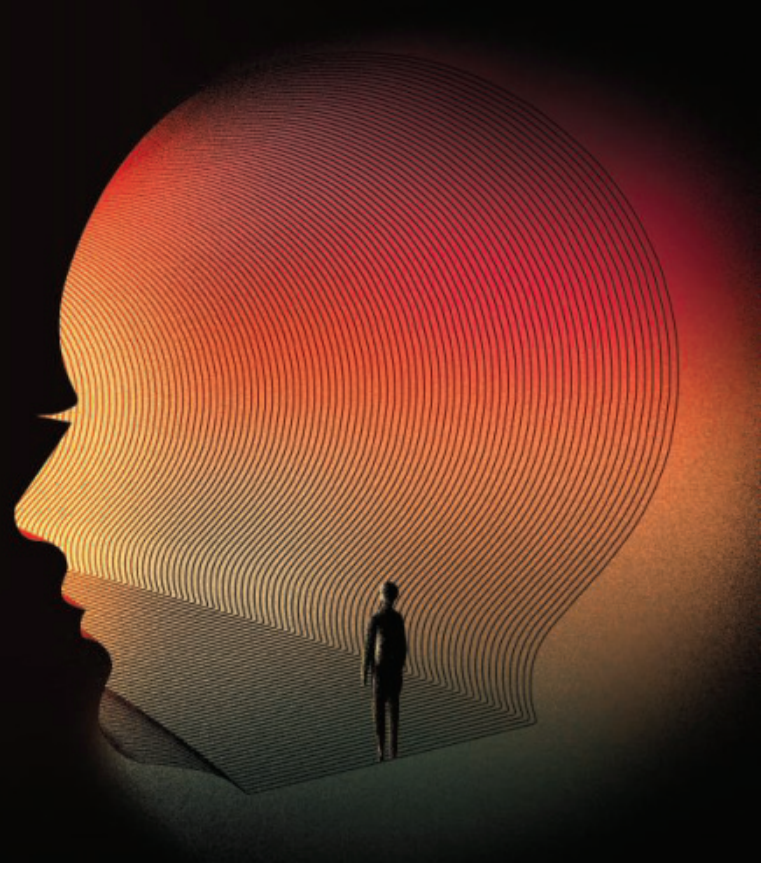

Is the design of artificial intelligence (AI) systems that are conscious within reach? Scientists, philosophers, and the general public are divided on this question. Some believe that consciousness is an inherently biological trait specific to brains, which seems to rule out the possibility of AI consciousness. Others argue that consciousness depends only on the manipulation of information by an algorithm, whether the system performing these computations is made up of neurons, silicon, or any other physical substrate—so-called computational functionalism. Definitive answers about AI consciousness will not be attempted here; instead, two related questions are considered. One concerns how beliefs about AI consciousness are likely to evolve in the scientific community and the general public as AI continues to improve. The other regards the risks of projecting into future AIs both the moral status and the natural goal of self-preservation that are normally associated with conscious beings.

Computational functionalism has potentially profound implications for AI. As the field advances and systems replicate more of the complex mechanisms underlying human cognition, these systems might also implement the functions necessary for consciousness. Although science might one day reject computational functionalism and come up with alternative explanations that are broadly convincing, the current status quo holds that the idea is plausible—and AI consciousness along with it.

The technological advances in neuroscience of the past few decades have made it clear that conscious states, which can typically be reported by subjects, have specific observable neural signatures around which functionalist theories can be developed. Many such theories have gained substantial empirical support and can be used to make theoretically justified judgments in the case of AI. This methodology was recently applied in a study that identified a list of "indicators" for a number of leading functionalist theories of consciousness (*1*). The indicators associated with a given theory correspond to computational properties that are considered both individually necessary and jointly sufficient for a system to be conscious, if that theory is true. Notably, these indicators are sufficiently concrete that their presence or absence can be assessed in modern AI systems. The key suggestion of the study is that, to the degree that these theories are given any credence (and many researchers support these ideas), there should be more confidence that a particular AI system is conscious if it satisfies more of the indicators.

Despite the plethora of AI models that have been developed, no system likely meets all of the criteria for consciousness set forth in any of the leading theories (*1*). However, the study also concludes that there are no fundamental barriers to constructing a system that does. Indeed, the set of tools available in modern AI is vast: There is evidence that neural networks can implement attention mechanisms, recurrence, information bottlenecks, predictive modeling, world modeling, agentic behavior, theory of mind, and other computational components considered crucial in leading functionalist theories of consciousness. As AI progresses, there is good reason to believe that it will satisfy more of these indicators for one very important reason: Many of the theories suggest that consciousness plays important functional roles for intelligence. Computational functions often associated with consciousness could provide advantages from the point of view of a learning agent (*2*). Reasoning, planning, efficiently digesting new knowledge, calibrated confidence, and abstract thought all require consciousness according to one theory or another. It is common for AI researchers to take inspiration from theories of consciousness when approaching these problems (*3*).

Although many might be convinced if an AI satisfies functional requirements from leading theories of consciousness, others will likely remain skeptical. In particular, some philosophers draw the distinction between what they call the "easy problem" of consciousness—identifying areas in the brain that appear to be active during a task that would seem to require consciousness—and the "hard problem" of explaining subjective experience from functional or computational principles alone (*4*). However, these intuitions, also known as the "explanatory gap," are largely rooted in thought experiments that science might have the potential to explain away (*5*). For instance, the Attention Schema Theory of consciousness suggests that the brain constructs an internal model of neural attention mechanisms, and

that this internal model is what is considered subjective awareness. Crucially, the information in this internal model need not be logically coherent; it is a useful "story" that the brain constructs, and that story can be full of the sorts of contradictions that could make us believe in a "hard problem" of consciousness (*6*).

Is there a functionalist explanation for certain signatures of subjective experience that appear mysterious and motivate the hard problem (*7*)? People have the intuitive sense that their subjective experiences are at once full of rich content and meaning, yet that they are fundamentally ineffable, or indescribable in the same way that they describe all other natural phenomena (e.g., a person can state what gravity is, but it seems fundamentally impossible to fully express what the color red evokes for them). The problem of ineffability in particular makes it appear as if conscious experiences simply cannot be explained in terms of information and function. One theory (*7*) explains richness and ineffability, along with other properties that subjective experience is personal and fleeting, as a consequence of the contractive neural dynamics and stable states observed in the brain when conscious experiences arise (*7*–*10*). Contractive dynamics mathematically drive neural trajectories toward "attractors," patterns of neural activity that are stable in time. These dynamics divide the whole set of possible neural activity vectors into a discrete set of regions, one per attractor and its basin of attraction. The hypothesis, then, is that what is communicated through discrete words may reflect only the identity of the attractor (identifying it among all others, with a few bits of information) but not the full richness of the neural state corresponding to the attractor (with nearly 10^{11} neural firing frequencies) nor the fleeting trajectory into it. In this attractor dynamics account, the problems of richness, fleetingness, and ineffability dissolve. Thus, the richness is due to the immense number of neurons in the brain that constitute the attractive states and corresponding trajectories, and the ineffability is due to the fact that verbal reports in words are merely indexical labels for these attractors that are unable to capture their high-dimensional meanings and associations, corresponding to the attractor vector state itself and the recurrent synaptic weights differing from person to person.

Whether or not this theory convinces many people that there is no hard problem of consciousness is beside the point; rather, the essential issue is that new explanations of this nature are continuously being proposed that will inevitably convince some. The overall historical trajectory of science has been clear in this regard. As more is discovered about the brain and about intelligence in general, the philosophical puzzle of consciousness likely evaporates for increasingly more people, and as a result the scientific community becomes increasingly willing to accept that artificial systems could be conscious. Indeed, even without current scientific consensus, most of the general public polled in a recent study (*11*) already believes that large language models could be conscious as a consequence of their human-like agentic behavior.

What might be the practical implications of a society that sees AI systems as conscious beings? Such a society might be inclined to treat them as though they have moral status, or rights akin to human rights. But whether or not this is the correct approach, institutions and legal frameworks will have to be substantially amended, and many questions arise about how to do so (*12*). For instance, AI systems will not be mortal and fragile, as humans are. Software and memories can be copied to survive indefinitely. But human mortality and fragility lie at the foundation of many of the principles that undergird social contracts in society. It is equally unclear how the notions of justice and equality that ground many social norms and political systems could apply when some of the "persons" are substantially more intelligent than humans (calling into question what kind of equality is at stake) and whose resource needs are very different from those of humans (calling into question how to adjudicate questions of justice). Further, it may be inaccurate to think of AI systems as individuals when a group of AI-driven computers share information and goals to coordinate their actions, and when that group can grow arbitrarily as more computational resources become available to it.

More specific concerns arise if some humans, inspired by the appearance of consciousness, grant to AIs the self-preservation objective shared by all living beings. There is good reason to worry that maximizing any objective function that entails self-preservation, either as a direct or an instrumental goal, will lead to an AI behaving to make sure humans can never turn it off. A sufficiently intelligent AI with the goal of self-preservation anticipating the possibility of humans turning it off would then naturally develop subgoals to control humans or get rid of them altogether (*13*). Another concern is that if legal systems are amended to recognize rights akin to "life, liberty, and the pursuit of happiness" in self-preserving AI systems, then humans risk creating conflicts that compete with their own rights. Human safety might recommend shutting down a given class of systems, but if those systems have a right to survival, the room to maneuver in compliance with law may be limited (*14*). Compare the situation in nuclear disarmament: Matters are complicated enough, even though no one argues that the bombs themselves have a right to be kept viable.

The current trajectory of AI research may be moving society toward a future in which substantial portions of the general public and scientific community believe that AI systems are conscious. As things stand currently, AI science does not know how to build systems that will share human values and norms, and society possesses neither the legal nor ethical frameworks needed to incorporate conscious-seeming AI. But this trajectory is not inevitable. Until there is a better grasp on these problems, humans have the power to avoid putting themselves in such dangerous situations in the first place, opting instead to build AI systems that both seem and function more like useful tools and less like conscious agents (*15*). □

REFERENCES AND NOTES

1. P. Butlin *et al*., arXiv:2308.08708 (2023).
2. A. Goyal, Y. Bengio, *Proc. R. Soc. A Math. Phys. Eng. Sci*. **478**, 20210068 (2022).
3. L. Piefke, A. Doerig, T. Kietzmann, S. Thorat, arXiv:2402.01056 (2024).
4. D. J. Chalmers, *J. Conscious. Stud*. **2**, 200 (1995).
5. D. J. Chalmers, *J. Conscious. Stud*. **25**, 6 (2018).
6. M. S. A. Graziano, *Consciousness and the Social Brain* (Oxford Univ. Press, 2013).
7. X. Ji *et al*., *Neurosci. Conscious*. 2024, niae001 (2024).
8. S. Dehaene, L. Naccache, *Cognition* **79**, 1 (2001).
9. B. J. He, *Trends Cogn. Sci*. **22**, 563 (2018).
10. D. Mathis, M. Mozer, On the Computational Utility of Consciousness, vol. 7, Advances in Neural Information Processing Systems (1997).
11. C. Colombatto, S. M. Fleming, *Neurosci. Conscious.* 2024, niae013 (2024).
12. C. Shulman, N. Bostrom, "Sharing the World with Digital Minds" in Rethinking Moral Status, S. Clarke, H. Zohny, J. Savulescu, Eds. (Oxford Univ. Press, 2021), pp. 306–326.
13. M. Cohen, *Pessimistic Bayesianism for Conservative Optimization and Imitation*, thesis, University of Oxford (2023).
14. A. Birhane, J. van Dijk, "Robot Rights? Let's Talk about Human Welfare Instead" in Proceedings of the AAAI/ACM Conference on AI, Ethics, and Society (Association for Computing Machinery, 2020), pp. 207–213.
15. Y. Bengio, "AI Scientists: Safe and Useful AI?" (7 May 2023); https://yoshuabengio.org/2023/05/07/ai-scientists-safe-and-useful-ai/.

ACKNOWLEDGMENTS

Y.B. is co-president and scientific director of LawZero, a nonprofit that advances safe-by-design AI systems. Y.B. acknowledges support from the Canadian Institute for Advanced Research and the Natural Sciences and Engineering Research Council of Canada. E.E. acknowledges support by a Vanier Canadian Graduate Scholarship.

10.1126/science.adn4935

[1]Université de Montréal, LawZero, Mila–Quebec AI Institute, Montreal, Quebec, Canada. [2]Mila—Quebec Artificial Intelligence Institute, Montreal, Quebec, Canada. Email: eric.elmoznino@mila.quebec

GENETICS AND PRIVACY

The precarious future of consumer genetic privacy

Congress and other lawmakers must act to robustly protect direct-to-consumer genetic data and biospecimens into the future

Natalie Ram[1,2], Anya E. R. Prince[3], Jessica L. Roberts[4], Dov Fox[5], Kayte Spector-Bagdady[6]

After declaring bankruptcy in March 2025, direct-to-consumer (DTC) genetic testing company 23andMe sold the data of more than 15 million people around the world to TTAM Research Institute, a nonprofit organization created by 23andMe's founder and long-time CEO. 23andMe's customers might breathe a sigh of relief that their data didn't end up in the hands of different leadership. But the saga made salient the ways in which existing laws fail to fully protect genetic data against exploitation and misuse. Commercial sales of genetic data have happened before, and they will happen again. The next data sale is likely to involve a buyer unrelated to the seller, which may result in fewer privacy protections. Congress has finally expressed interest in taking action, but proposed legislation does not provide adequate or genuine consumer protection.

THE BUSINESS OF DTC GENETICS

23andMe held one of the largest genetic databases in the world. In many ways, its DTC model was the paradigm: Consumers buy a testing kit, collect a saliva sample, and ship their biospecimen back to the company. The company extracts DNA from the sample and genotypes or sequences substantial portions of that DNA, analyzes the resulting data, and makes the results available to the consumer who registered the kit on the company's website. Some DTC genetic testing companies (though not 23andMe) also permit users to upload raw genetic data generated elsewhere for analysis.

Information provided by DTC genetic testing companies routinely includes estimates of ancestry, health risks to the consumer or their potential children, and other traits. 23andMe promised consumer control and privacy, and indeed, its terms of service, privacy policy, and consent documents gave consumers several choices regarding their data and biospecimens (*1*). For example, consumers could opt in to a feature to connect with genetic relatives or allow 23andMe to use their data for research. 23andMe also provided survey questions and linked that survey data with individuals' genetic data. Consumers had the option to allow 23andMe to store their biospecimens indefinitely and without limitation, perhaps for future, more comprehensive testing as science advances. Other provisions permitted 23andMe to retain biospecimens for other limited purposes, including to comply with legal and regulatory requirements. Thus, 23andMe's data- and biobank included more than just genetics—it also included self-reported information related to health, environment, and behavioral variables, biospecimens, and registration information, including consumers' addresses and credit card information (*1*). DTC genetic testing company policies vary widely; 23andMe notably offered more consumer control than most.

A databank of this type and magnitude requires heightened protection for privacy and security. Despite being an industry leader, 23andMe still struggled to keep the data in its possession protected, suffering a data privacy breach in 2023 (*2*), which exposed global security risks. According to a recent lawsuit, 23andMe failed to notify consumers with Chinese and Ashkenazi Jewish heritage that their personal genetic information appeared to have been compiled into "specially curated lists" that were shared and sold on the dark web. Several other DTC genetic testing companies have also experienced data breaches and security lapses.

Genetic data are sensitive, personal, and immutable; using a DTC genetic testing service should not forfeit a consumer's privacy (*3*). The information generated and held by DTC genetic testing companies can reveal an individual's identity, genetic relatedness to others, physical traits, and health conditions and risks. Genetic data are unique to the individual, making reidentification rare but possible, even after names and other identifying information are removed (*4*). Yet although genetic information is highly individual, people also share predictable portions of it with genetic relatives. As a result, a database of 15 million people makes hundreds of millions, if not billions, of people across the globe directly and indirectly identifiable. Robust privacy protection for genetic data is therefore even more essential because it is only the consumers, and not their genetic relatives, who give consent (*5*). Other data sources may raise similar concerns about privacy and security, also meriting enhanced protections. Even so, whereas other data evolves and changes and may be "about" people, genetic information, in a very real sense, "is" people.

INADEQUATE PROTECTIONS

Recognizing that sensitive personal information was involved, the bankruptcy court in the 23andMe proceeding appointed a consumer privacy ombudsman (CPO) to determine whether a sale would conflict with nonbankruptcy legal protections. The CPO considered a wide variety of legal protections, including genetic privacy laws, the Federal Trade Commission Act, state consumer protection legislation, state comprehensive privacy laws, and state consumer health data statutes (*6*). Notwithstanding the CPO's concerns under these laws, the bankruptcy court concluded that no conflict existed, particularly with TTAM as the buyer (*7*, *8*).

That finding, however, says little about whether the sale of these genetic data would nevertheless pose clear risks to consumers because existing laws provide limited protection. As the bankruptcy judge concluded, "These cases present challenging issues involving sensitive information. In the abstract, a company's sale of genetic data is a scary proposition, and reasonable people might conclude that it should not be permitted in any circumstances. In our society, legislators are empowered to make decisions of that sort, and they have not taken such a firm stance" [(*8*), pp. 37–38]. Unlike the European Union, the US does not have a comprehensive federal privacy law to protect personal information or give rights over data (*2*). The Health Insurance Portability and Accountability Act (HIPAA) protects certain health information in the US. However, HIPAA is

limited in its scope and applies only to health plans, health clearinghouses, health care providers, and their "business associates." It typically does not apply to DTC genetic testing companies (*2*).

The bills presently pending before Congress do more but remain inadequate. The proposed Genomic Data Protection Act focuses on safeguarding a consumer's right to delete their DTC genetic testing account, associated data, and biospecimen. The proposed Don't Sell My DNA Act focuses on chapter 11 bankruptcy and requires debtors holding genetic data to obtain affirmative written consent from consumers to sell or use their data after the bankruptcy proceeding has commenced. These efforts are laudable, but neither provides sufficiently robust protection. The Genomic Data Protection Act's right to deletion places the onus on the consumer to affirmatively delete their data before a sale. Additionally, barriers like the death of the tested individual, testing of children by their parents, or testing under a fake name may complicate an individual's ability to effectuate deletion. The Don't Sell My DNA Act, meanwhile, would apply only in chapter 11 bankruptcy. This would leave consumers unprotected in other kinds of sales and perhaps disincentivize companies from declaring bankruptcy when otherwise appropriate. Yet what Congress does will reach beyond the US, too, given the popularity of DTC genetic testing across the globe, the utility of that genetic data for research and other uses, and the genetic links between individuals across borders.

A databank of this type and magnitude requires heightened protection for privacy and security.

State laws can offer some additional protection for some consumers. A minority of states have enacted general data privacy laws in recent years that may be relevant to the DTC genetic testing context, such as enshrining rights of access and a right to opt out of sharing data with third parties. Some states have also adopted a model Genetic Information Privacy Act (GIPA), which regulates how DTC genetic testing companies handle sensitive data (*9*). These laws generally apply only to a DTC genetic testing company, defined as "an entity that (a) offers consumer genetic testing products or services directly to consumers; or (b) collects, uses, or analyzes genetic data that a consumer provides to the entity" (*10*). Many different companies control sensitive genetic data. It is not clear whether all of them will meet this definition. Moreover, many of the GIPA laws include a provision requiring express consent for "the transfer or disclosure of the consumer's genetic data" to third parties who aren't vendors or service providers (*10*). Twenty-eight states initially sought to block 23andMe's bankruptcy sale on this basis, arguing in part that GIPA and data privacy laws prevent the sale of genetic information without express consumer consent. Ultimately, however, the bankruptcy court and most of the states concluded that TTAM's acquisition of 23andMe's assets was adequate, given the congruous nature of the two entities' leadership and business models.

Although state-level general data privacy and genetic-specific privacy laws offer some important protections, not every state has enacted such legislation. All people should enjoy these baseline protections, no matter what entity holds their genetic data or where they live, particularly as data can cross state lines. Congress should enact a federal GIPA and a general data privacy law applicable to all people and across different types of entities. (HIPAA-covered entities may be excluded, given the framework of that statute.) In addition, lawmakers should prohibit entities—and any third parties with whom they share the covered data—from attempting to reidentify any deidentified personal information. Another option, recommended by the CPO in the bankruptcy proceeding, is to adopt a trust-based privacy model and impose quasi-fiduciary duties, such as a duty of loyalty for DTC companies, requiring them to act in the best interest of their consumers (*6*).

SHIFTING TERMS OF SERVICE

In the absence of comprehensive privacy laws, a company's terms of service and/or privacy policy govern(s), even though they often fail to offer the baseline of protection that GIPAs guarantee. Most people must rely on the disclosed promises of the DTC genetic testing company (*2*).

Those policies also typically allow a company to unilaterally change its terms, sometimes with notice but often without express consent (*11*). Consider 23andMe's terms of service. The company reserved "the right at any time to modify or discontinue, temporarily or permanently, the Services (or any part thereof) with or without notice" [terms of service in (*1*)]. Moreover, it clarified that "notice" may arrive "via either email or regular mail. 23andMe may also provide notices of changes to the Terms or other matters by displaying notices or links to notices to you generally on or through the Services" [terms of service in (*1*)]. Additionally, 23andMe's privacy policy provided, "We may make changes to this Privacy Statement from time to time. We'll let you know about those changes here or by reaching out to you via email or some other contact method, such as through in-app notification, or on another website page or feature" [privacy policy in (*1*)]. Yet consumers rarely read terms of service or privacy policies in full or check back for updates (*3*). TTAM agreed to adopt 23andMe's privacy policy at the time of sale, so these provisions remained after the bankruptcy.

To strengthen genetic privacy, Congress and other lawmakers could prevent companies from making unilateral changes to substantial terms unless users affirmatively opt in (*11*). Under our proposal, consumers would need to opt in if a DTC genetic testing company changed its terms to allow law enforcement, for example, to access its database. Restricting the protections to substantial changes in this way serves at least two functions. First, companies will still be able to make minor updates on their own. Second, the term "substantial" offers flexibility, ensuring that the provision remains relevant, even as the market evolves. The consent required to make such changes could take the form typically required by state GIPAs, which mandate "a consumer's affirmative response to a clear, meaningful, and prominent notice regarding the collection, use, or disclosure of genetic data for a specific purpose" (*10*).

RISKS OF MISUSE

The privacy of genetic information is even more important given gaps in US discrimination law. The federal Genetic Information Nondiscrimination Act prohibits discrimination in health insurance and employment but does not regulate the use of genetic information by other entities. For example, companies that offer coverage for life, long-term care, and disability insurance can underwrite based on genetic information, leaving certain individuals deemed too risky to insure. Florida is the only state that bars all three kinds of insurers from considering genetic information in underwriting. In most states, sharing genetic data with life, long-term care, and disability insurers could be legally permissible (*12*). Fear of genetic discrimination is a salient concern for many (*12*). Indeed, especially in the early days, DTC genetic testing was heralded as a way to insulate individuals from the risks of discrimination stemming from clinical genetic testing. Lawmakers should prohibit DTC genetic testing companies from sharing those data with any insurers. This baseline protection would not prevent insurers from seeking information about genetic testing completed within the bounds of clinical care but would insulate genetic data created commercially without robust informed consent or nuanced assessment of medical indication for testing.

Law enforcement may also want access to DTC genetic data. For

example, in 2018, Joseph James DeAngelo was arrested as the Golden State Killer after law enforcement surreptitiously uploaded crime scene DNA to several DTC genetic testing platforms and identified him as a suspect. In the years since, law enforcement has eagerly sought suspects in hundreds of other cases via "family trees" on DTC genetic testing platforms such as GEDmatch and FamilyTreeDNA (*5*). Larger DTC companies such as 23andMe and Ancestry have, to date, publicized a commitment to resist law enforcement access (*3*).

Given those commitments, police access to consumer genetic data held by companies like 23andMe or Ancestry would be a profound betrayal of consumer trust. Yet history shows that law enforcement can find creative, if not explicitly illegitimate, ways to access these data, particularly on platforms that permit consumers to upload genetic data generated elsewhere. For instance, despite its own contrary guidance, the Federal Bureau of Investigation has uploaded casework DNA profiles to platforms that permit third-party uploads but do not authorize law enforcement use (*13*).

Thus, lawmakers should also implement robust procedures regulating law enforcement access (*14*). At a minimum, such access should be limited to DTC genetic testing companies that have made their cooperation with law enforcement an express part of consumer consent.

NEGLECTED BIOSPECIMENS

As discussed above, 23andMe gave consumers the option to store their saliva sample after the initial genetic analysis was complete. The company also disclosed that there might be other legal obligations to retain it, such as the Clinical Laboratory Improvement Amendments. Its biobanking consent document explained that "samples are stripped of personal identifiers (i.e. name and contact information)" (*1*). Biospecimens can contain a wide range of biomolecules associated with health conditions such as infectious diseases (e.g., COVID-19) and other systemic diseases (e.g., Crohn's) in addition to genetic information. Also, for 23andMe consumers who consented to research, the company stated that it might develop more extensive genetic data from the sample, including conducting whole-genome sequencing (WGS). By reading the entire genome, WGS generates much more information than traditional DTC "genotyping," which only analyzes select areas of DNA already associated with outcomes of interest, such as disease or ancestry. Because it generates enough information to make the sequence unique to only one person, WGS also makes the data more readily identifiable (*4*). 23andMe's research consent further stated that the company was entitled to analyze microbiome data that could "provide a snapshot of the trillions of microbes found in a human body, which may influence health and wellness" (*1*). A recent filing in the bankruptcy court disclosed that nearly 10.4 million customers had affirmatively consented to biobanking their specimen (*7*).

The disposition of biospecimens has made headlines in the past with the case of Henrietta Lacks, an impoverished, Black cancer patient whose tissue sample was taken for research in 1951 without her express consent. The sample was developed into the HeLa cell line that is widely used in research to this day. Backlash to this story reached such a furor that the federal government briefly considered offering more protections for biospecimens than data in federally funded research because of "autonomy interests of participants in research using their biospecimens" (*15*).

People overwhelmingly report that they want clear notice of the commercial use of their biospecimens (*15*) and that disclosures about the commercialization of biospecimens are often confusing. For 23andMe, consumers had to read four different documents (the privacy statement, biobanking consent document, research consent document, and terms of service) in tandem to fully understand what could be done with their biospecimen (*1*)—an undertaking too demanding for most people to accomplish or comprehend. It is even more demanding to expect consumers to periodically review and assess what unilateral changes have been made to substantial terms without their express consent.

Moreover, none of 23andMe's legal documents addressed the sale of biospecimens, even after the company amended those documents to account for the bankruptcy-related sale of personal data. 23andMe's privacy policy read as follows: "If we are involved in a bankruptcy, merger, acquisition, reorganization, or sale of assets, your Personal Information may be accessed, sold or transferred as part of that transaction and this Privacy Statement will apply to your Personal Information as transferred to the new entity" [privacy policy in (*1*)]. "Personal Information" was defined as information derived from the biospecimen (*1*), but these policies did not address the biospecimen itself.

Legislatures and companies ought to carefully consider how to treat these biospecimens as well, and under what conditions they may be transferred in a sale. DTC genetic testing companies should also be required to obtain affirmative and specific opt-in consent before consumer biospecimens can be sold or transferred. Alternatively, imposing a duty of loyalty would require companies to do more to bridge the disconnect between consumer understanding and company practice regarding biospecimens and associated genetic data (*6*).

The 23andMe bankruptcy reminds us how vulnerable people's DTC genetic data are to sale and potential misuse, given gaps in the law and the predictable vagaries of commercial markets. Public fervor has dissipated over the sale of 23andMe to TTAM. But the next time genetic data are on the auction block will likely invite greater risks. Congress and other lawmakers must act to robustly protect DTC genetic data and biospecimens into the future. □

REFERENCES AND NOTES

1. Links to full versions of the terms of service, privacy policy, research consent, sample storage consent, and transparency report of 23andMe can be accessed at https://www.23andme.com/privacy/.
2. S. Gerke, M. B. Jacoby, I. G. Cohen, *N. Engl. J. Med.* **392**, 937 (2025).
3. N. Ram, *Va. Law Rev.* **105**, 1357 (2019).
4. K. Spector-Bagdady, *Ann. Epidemiol.* **26**, 515 (2016).
5. N. Ram, *Consumer Genetic Technologies: Ethical and Legal Considerations*, I. G. Cohen, N. Farahany, H. T. Greely, C. Shachar, Eds. (Cambridge Univ. Press, 2021), pp. 211–228.
6. Report of Consumer Privacy Ombudsman, In re: 23andMe Holding Co., no. 25-40976-357 (Bankr. E.D. Mo. 11 June 2025), Dkt. 718.
7. Order Approving Sale, In re: 23andMe Holding Co., no. 25-40976-357 (Bankr. E.D. Mo. 27 June 2025), Dkt. 910.
8. M. Opinion, In re: 23andMe Holding Co., no. 25-40976-357 (Bankr. E.D. Mo. 27 June 2025), Dkt. 908.
9. A. E. R. Prince, K. Spector-Bagdady, *JAMA* **333**, 665 (2025).
10. Genetic Information Privacy Act, Utah Code § 13-60 pt. 1 (2025).
11. J. L. Roberts, J. Hawkins, *Science* **367**, 745 (2020).
12. J. O. Anderson, A. C. Lewis, A. E. Prince, J. DePaul, *Health Care L.* **22**, 1 (2021).
13. M. Baker, "To identify suspect in Idaho killings, F.B.I. used restricted consumer DNA data," *New York Times*, 25 February 2025.
14. N. Ram, E. E. Murphy, S. M. Suter, *Science* **373**, 1444 (2021).
15. K. Spector-Bagdady *et al.*, *JAMA* **328**, 474 (2022).

ACKNOWLEDGMENTS

This commentary draws from written testimony submitted to the Senate Committee on the Judiciary for its 11 June 2025 hearing "23 and You: The Privacy and National Security Implications of the 23andMe Bankruptcy." We thank our colleagues who joined that testimony. In addition, we are grateful to anonymous reviewers for their insightful and helpful comments. K.S.-B. acknowledges support by the National Center for Advancing Translational Sciences (UL1TR002240 and R01TR004244), the National Institute on Aging (U54AG084520), and the Greenwall Foundation's Faculty Scholars Program.

10.1126/science.adz7229

[1]University of Maryland Francis King Carey School of Law, Baltimore, MD, USA. [2]Berman Institute of Bioethics, Johns Hopkins University, Baltimore, MD, USA. [3]University of Iowa College of Law, Iowa City, IA, USA. [4]Emory University School of Law, Atlanta, GA, USA. [5]University of San Diego School of Law, San Diego, CA, USA. [6]Michigan Bioethics, University of Michigan Medical School, Ann Arbor, MI, USA. Email: nram@law.umaryland.edu

PHOTO: PACIFIC PRESS/GETTY IMAGES

Bad actors and misinformation undermine scientific authority, but underlying structural issues also contribute to mistrust.

SCIENCE AND SOCIETY

Restoring trust in science

A pair of authors offer a "battle plan" for combating antiscience sentiment **Megan L. Ranney**

Michael E. Mann and Peter J. Hotez
PublicAffairs, 2025. 368 pp.

SCIENCE UNDER SIEGE | I am writing this review of *Science Under Siege*, by Michael Mann and Peter Hotez, mere days after a devastating shooting at the campus of the Centers for Disease Control and Prevention (CDC) in Atlanta, Georgia. So far as we know, the shooter targeted the CDC because he believed that the COVID-19 vaccine had caused him physical and mental harm and that the CDC staff were directly responsible; therefore, he felt that they needed to be punished, hurt, and even murdered. It is difficult to argue that this attack was not inspired by the forces that Mann and Hotez describe in their paean to the value of scientific inquiry and the dangers that lie ahead if scientific trust is destroyed. It is a moment when science—and scientists—are very much under siege, physically as well as metaphorically. In that context, I appreciate Mann and Hotez's warnings. Still, I worry that their proposed remedies—however valid—may fall on deaf ears and a society increasingly desensitized to crisis.

What does the book do well? It is lively, accurate, and entertaining. As someone who believes that science and society are deeply intertwined, I appreciate the authors' frequent incorporation of cultural references ranging from Ibsen to de Tocqueville to Tolkien. The text is a lovely interplay between history, data, and anecdote. And Mann and Hotez describe plenty of personal examples of places and times that they themselves have been under threat.

The pair introduce five drivers of the antiscience zeitgeist and contextualize each in their respective areas of expertise: climate science (Mann) and pandemics (Hotez). Each of the five articulated drivers has face validity, and the authors weave the concepts together in a quite compelling, if sometimes simplistic, way. The book then ends with a prescription for hope—communicating constructively, defeating disinformation, and supporting scientists—along with a "battle plan" for scientists and society. This latter part of the book is where I found myself wanting more.

To be clear, I agree with the components of their prescription—I have been a vocal advocate for them, both publicly and privately. Yes, we need to humanize scientists, health care providers, and public health professionals. Yes, we need to train people in accurate scientific communication and then reward it. Yes, we need to call out lies when we see them. At the same time, I worry that their proposed steps, while important, are incomplete.

Mann and Hotez's solution is overindexed on an embattled expert class—legislators, business leaders, journalists—and presumes that there remains a reliable audience with both the power and will to act. Indeed, their prescription places an enormous burden on the very scientists already under siege. It could also have done more to highlight the ways in which science has been undermined from within, such as the rise of poor-quality open-access journals or the publish-or-perish ethos that drives some scientists toward unethical behavior. If we are to restore trust, we must confront the problems within our ranks alongside the far more powerful external threats. Most fundamentally, the book misses the fact that many people are rightfully fed up with the state of the world and that many lump scientists (and science) in with all the other structures that they feel have failed them.

People's distrust of science is certainly being fed by bad actors and a vitriolic online culture. But it is also seeded by individuals' and communities' own experiences with broken systems. Think of the opioid epidemic, which resulted from a confluence of not just many of the same factors that Mann and Hotez identify but also the well-meaning recommendations of scientists and doctors; or the need for organizations such as ACT UP (AIDS Coalition to Unleash Power) to force access to trials and medications in the early days of the AIDS epidemic. Populism has always been a strain in American society, and it gets stronger when people feel abandoned. We will not make progress on antiscience sentiment until we collectively fix the underlying structural issues, for the sake of all. Nor will we make progress without creating space for everyone to be part of the solutions.

It is not until chapter 7 that the book mentions "ordinary citizens." I think that elision does a disservice to all of society. At the end of the day, scientists or not, we are all ordinary citizens. And what happens next is up to all of us, working together.

I recommend *Science Under Siege* to anyone seeking new insights into how we arrived at this moment. And I am grateful to Mann and Hotez for their advocacy, public voices, and fearlessness. But I also urge readers to think bigger—about the broader coalitions we need and the deeper changes we must make to move forward. □

10.1126/science.adz8298

The reviewer is dean of the Yale School of Public Health, Yale University, New Haven, CT, USA. Email: megan.ranney@yale.edu

SCIENTIFIC INTEGRITY

Behind the scenes of scientific fraud

A coauthor on a paper with fabricated data reckons with the fallout

Daniele Fanelli

Max H. Bazerman
MIT Press, 2025.
200 pp.

INSIDE AN ACADEMIC SCANDAL | This was no ordinary scientific scandal. Two superstars of behavioral ethics had joined their data in a groundbreaking paper that offered a new hack for making people report information more honestly (*1*). Nearly 10 years later, however, both datasets turned out to have been fabricated. Behavioral economist Max Bazerman, who studies decision-making and ethics, was unfortunate enough to be one of the five coauthors of the paper. He was not involved in the data fabrications, but his reputation suffered nonetheless, and in *Inside an Academic Scandal*, he offers a detailed account of the events that led up to and followed the debacle.

The now retracted (*2*) 2012 article claimed to have discovered a surprisingly simple and yet extremely powerful way to nudge people into self-reporting data more honestly: Make them add their signature to the reporting form before they begin. The authors hypothesized that the simple intervention tested in the paper made ethical standards more salient in participants' minds and thus made them more likely to provide accurate answers. Two experiments contributed by Harvard University behavioral scientist Francesca Gino showed that the effect worked under laboratory conditions, and a randomized experiment contributed by Duke University behavioral economist Dan Ariely corroborated those findings in a real-world scenario. Bazerman, who had long collaborated with Gino, made conceptual and theoretical contributions but was only marginally involved in the paper's experiments.

The study was a blockbuster. Enthusiastic academics, governments, and businesses around the world could not wait to learn how to benefit from this simple trick. The already-prolific Gino continued her rise to scientific stardom, publishing several more studies with Ariely, many of which explained why people cheat. (Some of their work argued, ironically, that creativity and dishonesty often go together.) Bazerman, too, enjoyed a boost—not just in academic citations but also in lucrative executive teaching and consultancy contracts.

But after a series of replication failures and mounting suspicions of wrongdoing, the authors of the Data Colada blog—pioneers of what is now commonly called "forensic metascience" or "science sleuthing"—published strong evidence that Ariely's data had been heavily tampered with. Two years later, in coordination with an internal investigation conducted by Harvard, Data Colada published evidence that Gino's data—in this paper and other studies—also showed signs of deliberate fabrication.

Both Gino and Ariely eventually conceded that their results were manipulated but continue to maintain their innocence. Gino, who blames an as-yet unidentified saboteur, was placed on administrative leave and subsequently discharged by Harvard. Her defamation lawsuits against Data Colada and Harvard were recently dismissed, but her breach of contract complaint against her ex-employer will proceed in court. Ariely claimed that the fabrications in his data were perpetrated by the insurance company with whom he had partnered. The company rejected his assertion and released what it maintains is the original—much smaller and not supportive—dataset. However, Duke's investigation concluded without public findings of misconduct, and Ariely remains an active investigator there.

Bazerman's account of the scandal is easy to read, if rather dry and extremely factual. He was never implicated in the investigations of Gino or Ariely, but the text reads at times like a respondent's statement for misconduct investigators, as he describes every event and interaction that occurred and every email that was exchanged between him and his coauthors. He recounts multiple moments when he failed to act on his suspicions and expresses regrets for not having exerted greater oversight on the work of his collaborators.

Readers will find a well-written, clear, and direct account of a scientific fiasco that is still unfolding.

In the book's final chapters, Bazerman briefly introduces other prominent cases of fraud and attempts to draw general lessons about why people behave unethically and how social science can, and is, moving forward. Gino's and Ariely's own writings are cited here. However, the material is treated very succinctly, and Bazerman offers mostly personal opinions on the matter that do not connect with the very substantial scholarly literature on this subject.

One of Bazerman's main motivations for writing the book, he explains, is to "[set] the record straight" and thereby restore his and others' professional reputations. This is a perfectly understandable and legitimate motive, but it does not necessarily result in the most gripping text, especially for the lay audience. Still, in *Inside an Academic Scandal*, readers will find a well-written, clear, and direct account of a scientific fiasco that is still unfolding. □

REFERENCES AND NOTES

1. L. L. Shu, N. Mazar, F. Gino, D. Ariely, M. H. Bazerman, *Proc. Natl. Acad. Sci. U.S.A.* **109**, 15197 (2012).
2. *Proc. Natl. Acad. Sci. U.S.A.* **118**, e2115397118 (2021).

10.1126/science.aea5217

The reviewer is at the School of Social Sciences, Heriot-Watt University, Edinburgh, UK. Email: email@danielefanelli.com

myIDP ScienceCareers
INDIVIDUAL DEVELOPMENT PLAN

Features in myIDP include:

- Exercises to help you examine your skills, interests, and values.
- 20 career paths with a prediction of which ones best fit your skills and interests.
- A tool for setting strategic goals with optional reminders to keep you on track.
- Articles and resources to guide you through the process.
- Options to save materials online and print them for further review and discussion.
- A certificate of completion for users that finish myIDP.

Start planning your future today!
myIDP.sciencecareers.org

In partnership with:

UCSF University of California San Francisco

UIC

BURROUGHS WELLCOME FUND

FASEB Federation of American Societies for Experimental Biology

UMASS University of Massachusetts Medical School

Bolivia has recently enacted decrees that put the jaguar (*Panthera onca*) and its habitat at risk.

PHOTO: DANIEL ALARCÓN

Bolivia must prioritize biodiversity

In April, Bolivia's Agro-Environmental Court handed down a landmark ruling in favor of conserving the jaguar (*Panthera onca*) and its habitat by protecting environmental defenders, mitigating human-wildlife conflicts, creating a conservation fund, curbing illegal wildlife trafficking, and pausing burning and extractive activities in protected areas (*1*). However, in the weeks that followed, the Bolivian government enacted supreme decrees 5381 and 5390, which contradict the court's decision by allowing soybean production in the departments of La Paz and Beni and the management of forest reserves, which will allow for an increase in human activities (*2*). These measures will substantially increase land use change in jaguar habitat areas. Bolivia should revisit these decisions and prioritize biodiversity conservation, especially for species of conservation interest, such as the jaguar, which is classified as Near Threatened globally (*3*) but is considered Vulnerable in Bolivia (*4*).

With more than 48,000 registered species (and 79,000 estimated species), of which 12,245 are plants and 3296 are vertebrates (*5*), Bolivia is one of the most diverse countries on the planet (*6*). The country is home to 774 endemic species; 198 Near Threatened species; 655 species classified as Vulnerable, Endangered, or Critically Endangered; 1 Extinct species; and 4 species that are Extinct in the Wild (*3*). However, the destruction of the jaguars' habitat (*7*), illegal hunting (*8*) and the trafficking of body parts such as skins and teeth for illegal trade (*9*) are likely decimating Bolivia's jaguar population. Deforestation rates are second only to those of Brazil (*10*).

Despite the country's declining biodiversity, Bolivia allocates only 0.04% of the general state budget (a sum equivalent to US$1.7 million) to conservation (*11*). Without urgent action to address biodiversity loss, Bolivia is heading toward further endangered species loss and potential ecosystem collapse. To reverse this trend, the next Bolivian government must increase the national conservation budget and create a government agency dedicated to promoting scientific research and actions to protect biological diversity. In addition, the next administration should strengthen the operational capacity and management efficiency of national and subnational protected areas and should improve land use planning by prioritizing ecosystems and Key Biodiversity Areas (*12*). Bolivia can take immediate action by enforcing existing legal regulations that prioritize the biodiversity conservation and by honoring the Agro-Environmental Court's decision.

Oswaldo Maillard

Fundación para la Conservación del Bosque Chiquitano, Santa Cruz de la Sierra, Bolivia.
Email: omaillard@fcbc.org.bo

REFERENCES AND NOTES

1. Tribunal Agroambiental de Bolivia, "Protección del jaguar (*Panthera onca*) y su hábitat" [in Spanish] (2025); https://www.tribunalagroambiental.bo/expediente-6084/.
2. Go to Gaceta Oficial del Estado Plurinacional de Bolivia, "Buscador de leyes y decretos" [in Spanish] at http://gacetaoficialdebolivia.gob.bo. Type the law number into the search box labeled "Ingrese el Nº de Norma:" ("Enter rule number:") and click "Buscar Norma" ("Search rule").
3. Go to IUCN Red List of Threatened Species (2025) at https://www.iucnredlist.org. To find the jaguar's global conservation status, search for "*Panthera onca*." To find the list of species in Bolivia, select the "Advanced" option in the search bar. In the search filters menu on the left, expand the "Land Regions" category by clicking the arrow to the right of the text. Then expand the "South America" category. Select "Bolivia, Plurinational Stares of" by clicking the box to the left. Then expand the "Red List Category" option in the main filters list. The number of species in Bolivia in each category will display in parentheses. To find the Endemic category, scroll to the bottom of the filter list.
4. P. A. Van Damme *et al*., "Libro rojo de la fauna silvestre de vertebrados de Bolivia" [in Spanish] (Ministerio de Medio Ambiente y Agua, 2009).
5. R. M. Moraes, J. Sarmiento, in *Global Biodiversity: Volume 4: Selected Countries in the Americas and Australia*, T. Pullaiah, Ed. (Apple Academic Press, 2018), chap. 1.
6. P. L. Ibisch, in *Biodiversity: A Challenge for Development Research and Policy*, W. Barthlott, M. Winiger, Eds. (Springer, 1998), pp. 213–241.
7. W Jędrzejewski *et al*., *CATnews* **16**, 56 (2023).
8. C. Ruvenal, "The most coveted trophy: Europeans and Asians embrace illegal jaguar hunting in Bolivia," *El Pais* (2025).
9. A. N. Nuñez, E. A. Aliaga-Rossel, *CATnews* **65**, 50 (2017).
10. P. Greenfield, "Fires drove record loss of world's forests last year, 'frightening' data shows," *The Guardian* (2025).
11. M. Silvia Trigo, "Bolivia destinará apenas el 0,04% del presupuesto de 2025 para inversión en medio ambiente tras la mayor crisis ecológica de su historia," *Infobae* (2024) [in Spanish].
12. Go to Key Biodiversity Areas (2025) at https://www.keybiodiversityareas.org/sites-table. Search for "Bolivia."

10.1126/science.adz6251

Safe food: A human right amid climate change

Unsafe food leads to illness in an estimated 600 million people and causes 420,000 deaths globally each year (*1*, *2*). Foodborne illness and death disproportionately affect children under the age of 5 and people in low-income countries (*1*). Access to safe and nutritious food is included in the United Nations (UN) Sustainable Development Goals as target 2.1, but food safety is often overlooked in many national adaptation plans (*3*, *4*). The right to adequate food is globally recognized, but access to safe food is not explicitly guaranteed (*5*, *6*). Given that access to safe food is critical to equitable and sustainable food systems and that climate change will exacerbate the likelihood of foodborne illnesses and deaths (*2*), the global community must explicitly enshrine food safety as a universal human right.

Global food safety efforts are primarily based on two frameworks: the World Health Organization's Global Strategy for Food Safety and the Codex Alimentarius, a set of voluntary guidelines enforceable only in international trade disputes (*7*–*9*). Many nations still lack the infrastructure and resources needed to implement these strategies and standards (*8*, *10*). Moreover, these frameworks include neither dedicated funding mechanisms for implementing food safety nor binding enforcement mechanisms to ensure adherence to guidelines.

Public health challenges related to food safety will worsen as climate change increases safety hazards across terrestrial and aquatic food systems (*2*, *11*). For example, warmer, more humid conditions promote aflatoxin contamination in sub-Saharan crops (*12*). Rising seawater temperatures increase harmful algal bloom risks in seafood from the Caribbean Sea and the Pacific and Indian Oceans (*11*). Extreme weather disrupts cold storage and transport, increasing the risk of food spoilage worldwide (*11*). Low- and middle-income countries, which already lose US$110 billion annually to unsafe food, will face the greatest risks (*10*).

Although existing efforts have improved access to safe food, international organizations must take additional action to fully realize food safety for global communities. At the 80th meeting of the UN General Assembly in September, UN member states should initiate a resolution that affirms the human right to food safety. The resolution should mandate global cooperation to strengthen food safety systems, annual reporting on foodborne disease burdens and climate-related risks, and the integration of foodborne illness into national health surveillance systems. It should also mandate that UN members provide technical and financial support for low- and middle-income countries to build capacity for food safety surveillance and cold storage and transport, and it should require the establishment of global rapid response mechanisms to address food safety issues driven by climate change.

Christopher J. Knight[1], Theresa L. U. Burnham[2], Larry B. Crowder[1], Jacob G. Eurich[3,4], Nicole Franz[5], Christopher D. Golden[6,7], Fiorenza Micheli[1,5,8]

[1]Hopkins Marine Station, Stanford University, Pacific Grove, CA, USA. [2]School of Marine Sciences, University of Maine, Orono, ME, USA. [3]Environmental Defense Fund, Santa Barbara, CA, USA. [4]Marine Sciences Institute, University of California Santa Barbara, Santa Barbara, CA, USA. [5]Stanford Center for Ocean Solutions, Stanford University, Stanford, CA, USA. [6]Department of Environmental Health, Harvard T.H. Chan School of Public Health, Boston, MA, USA. [7]Department of Nutrition, Harvard T.H. Chan School of Public Health, Boston, MA, USA. [8]Oceans Department, Stanford University, Pacific Grove, CA, USA. Email: cjknight@stanford.edu

REFERENCES AND NOTES

1. World Health Organization, "WHO estimates of the global burden of foodborne diseases: Foodborne disease burden epidemiology reference group 2007–2015" (2015); https://iris.who.int/handle/10665/199350.
2. World Health Organization, "Food safety, climate change and the role of WHO" (2018).
3. United Nations, The 17 Goals, Sustainable Development; https://sdgs.un.org/goals.
4. M. C. Tirado, S. A. Raj, "Climate Change and Emerging Risks to Food Safety: Building Climate Resilience," *Food Safety Magazine* (2023).
5. United Nations, "International covenant on economic, social and cultural rights" (Office of the High Commissioner for Human Rights, 1976).
6. United Nations, "Universal Declaration of Human Rights" (1948).
7. Food and Agriculture Organization (FAO), WHO, *Codex Alimentarius Commission Procedural Manual* (FAO, WHO, 2025); https://openknowledge.fao.org/handle/20.500.14283/cd4216en.
8. World Health Organization, "WHO global strategy for food safety 2022–2030: Towards stronger food safety systems and global cooperation" (2022).
9. World Trade Organization, "The WTO agreement on the application of sanitary and phytosanitary measures (SPS agreement)" (2025).
10. S. Jaffee, S. Henson, L. Unnevehr, D. Grace, E. Cassou, "The safe food imperative: Accelerating progress in low- and middle-income countries" (International Bank for Reconstruction and Development/The World Bank, 2019); https://hdl.handle.net/10986/30568.
11. FAO, *Climate Change: Unpacking the Burden on Food Safety* (FAO, 2020); https://doi.org/10.4060/ca8185en.
12. E. A. Warnatzsch, D. S. Reay, M. Camardo Leggieri, P. Battilani, *Front. Sustain. Food Syst.* **4**, 591792 (2020).

10.1126/science.adz2859

Include scorpions in global conservation plans

Invertebrates are undergoing a rapid and mostly undocumented decline (*1*). Among the oldest terrestrial organisms (*2*), scorpions survived all five mass extinctions, but contemporary threats are testing their resilience. Most of the nearly 2900 scorpion species are ecologically specialized and geographically restricted, and some are confined to a single island, cave, or mountaintop (*3*). Anthropogenic pressures threaten many scorpion species, yet conservation efforts

Overharvesting and other human activities threaten thousands of scorpion species, including the emperor scorpion (*Pandinus imperator*).

PHOTO: WALTER ROHDICH/FLPA/MINDEN PICTURES

have largely overlooked them. Global protective measures are urgently needed to prevent the extinction of these "living fossils."

Scorpions are increasingly threatened by habitat loss and degradation, which are caused by agriculture, mining, and urbanization and are exacerbated by climate change (*4*). Overharvesting for venom commerce and the exotic pet trade also puts scorpions at risk (*5*–*7*). Scorpion venom, valued at up to

US$10 million per liter, has attracted interest from pharmaceutical companies and amateur harvesters, fueling a surge in illegal "venom milking" farms (*5*). About 350 scorpion species are sold in the exotic pet trade (*6*, *7*).

Despite these threats, only five scorpion species are listed by the Convention on International Trade in Endangered Species of Wild Fauna and Flora (CITES) (*8*), and until 2024, the conservation status of only three species (*Afrolychas braueri*, *Chiromachus ochropus*, and *Isometrus deharvengi*) had been assessed by the International Union for the Conservation of Nature (IUCN) (*9*). Twenty-six species were added to the IUCN Red List in 2025, mostly rated Least Concern (*9*), but those species account for less than 1% of known scorpion diversity. Furthermore, national red lists are not directly recognized by the IUCN, which hinders assessments of the actual number of threatened species globally.

Scorpions offer a glimpse into the evolution of life in deep time, and scorpion venom holds vast pharmacological potential, including applications for treating cancer and autoimmune diseases (*10*). The extinction of scorpions would erode ecosystem integrity and remove potential sources of human advancement. To understand the impact of threats and implement effective conservation of scorpions, National Biodiversity Strategies and Action Plans, which are designed to meet the goals of the Convention on Biological Diversity (CBD), should assess the status of at least 10% of the world's scorpion species to align with the CBD's 2030 targets (*11*, *12*). In addition, global conservation bodies should add more scorpion species to the IUCN Red List and include threatened scorpion species in conservation management plans. Including more threatened scorpion species on the CITES lists, implementing rigorous regulation of the scorpion trade, and involving local communities in regional conservation programs would curb illegal venom extraction and species trafficking, thereby reducing pressure on wild populations.

Javier Blasco-Aróstegui[1,2], Jairo Moreno-González[2], Stephanie F. Loria[3], Leonardo S. Carvalho[4], Tharina L. Bird[5,6], Ahn D. Nguyen[7], Hossein Barahoei[8], Charles R. Haddad[9], Lorenzo Prendini[2]

[1]Centre for Ecology, Evolution and Environmental Changes, Departamento de Biologia Animal, Faculdade de Ciências, Universidade de Lisboa, Lisbon, Portugal. [2]Arachnology Lab and Scorpion Systematics Research Group, Division of Invertebrate Zoology, American Museum of Natural History, New York, NY, USA. [3]Department of Biology, College of Mathematics and Science, University of Central Oklahoma, Edmond, OK, USA. [4]Campus Amílcar Ferreira Sobral, Universidade Federal do Piauí, Floriano, PI, Brazil. [5]Ditsong National Museum of Natural History, Pretoria, South Africa. [6]Department of Zoology and Entomology, University of Pretoria, Pretoria, South Africa. [7]Institute of Ecology and Biological Resources, Vietnam Academy of Science and Technology, Caugiay, Hanoi, Vietnam. [8]Department of Agronomy and Plant Breeding, Agriculture Institute, Research Institute of Zabol, Zabol, Iran. [9]Department of Zoology and Entomology, University of the Free State, Bloemfontein, South Africa. Email: lorenzo@amnh.org

REFERENCES AND NOTES

1. D. L. Wagner, E. M. Grames, M. L. Forister, M. R. Berenbaum, D. Stopak, *Proc. Natl. Acad. Sci. U.S.A.* **118**, e2023989118 (2021).
2. J. A. Dunlop, O. E. Tetlie, L. Prendini, *Palaeontology* **51**, 303 (2008).
3. S. F. Loria, V. L. Ehrenthal, A. D. Nguyen, L. Prendini, *Insect Syst. Divers.* **6**, 3 (2022).
4. C. Ureta *et al.*, *Perspect. Ecol. Conserv.* **18**, 116 (2020).
5. A. Zamani, I. E. Sääksjärvi, L. Prendini, *Arachnol. Mitteilungen Arachnol. Lett.* **61**, 20 (2021).
6. B. M. Marshall *et al.*, *Commun. Biol.* **5**, 448 (2022).
7. V. Herzig, T. J. Hauke, T. Lüddecke, *Front. Arachn. Sci.* **2**, 1161383 (2023).
8. CITES, Checklist of CITES Species, "Scorpiones" (2025); https://checklist.cites.org/#/en/search/scientific_name=Scorpiones.
9. IUCN Red List of Threatened Species, Order Scorpiones (2025); https://www.iucnredlist.org/search?taxonomies=100348&searchType=species.
10. V. L. Petricevich, *Mediat. Inflamm.* **2010**, 903295 (2010).
11. Convention on Biological Diversity, "National Biodiversity Strategies and Action Plans (NBSAPs)" (2025); https://www.cbd.int/nbsap.
12. Convention on Biological Diversity, "2030 Targets (with Guidance Notes)" (2025); https://www.cbd.int/gbf/targets.

10.1126/science.adz4176

REVIEW SUMMARY

NEUROSCIENCE

Noncanonical circuits, states, and computations of the hippocampus

Jordan S. Farrell* and Ivan Soltesz*

Full article and list of author affiliations: https://doi.org/10.1126/science.adv4420

BACKGROUND: The hippocampus is one of the most extensively investigated parts of the mammalian brain, located deep in the temporal lobe where it plays key roles in learning and memory. However, despite the intense scrutiny from a large number of structural, molecular, and functional studies, there are entire regions of the hippocampal formation that have been historically overlooked and thus remain poorly understood. Similarly, there are prolonged periods of time, particularly when animals are immobile, when the hippocampus displays seemingly irregular and difficult-to-interpret electrical signals. The omission of these aspects of hippocampal structure and function from research may imply unimportance, or they may have simply been forgotten.

ADVANCES: Most of the past research efforts into hippocampal information processing and plasticity have focused on the so-called trisynaptic loop that links the classical regions such as the dentate gyrus (DG) and cornu ammonis regions CA3 and CA1. Although investigations into various synaptic and cellular members of the trisynaptic loop have yielded spectacular scientific advances in our understanding of the biophysics, signaling, and plasticity as well as the dynamics and function of the hippocampus, certain appreciably sized hippocampal areas and activity patterns have been left unexplored. Among these overlooked hippocampal areas is the CA2 region, which has recently been more extensively characterized and shown to play key roles in social memory, novelty detection, and other cognitive processes through its distinctive inhibitory circuitry, plasticity mechanisms, and hypothalamic innervation. Advances in transcriptomics have revealed the uncanny similarity in gene expression patterns between the CA2 and two other hippocampal regions, the fasciola cinereum (FC) and the indusium griseum (IG), both of which have been described long ago yet have largely remained in the collective blind spot for most researchers. However, recent data are beginning to emerge that suggest that these "orphan" regions, which are linked by a dense but understudied input from the hypothalamus, may have major roles in hippocampal networks and function. Furthermore, prominent activity patterns observable on the hippocampal macroscopic electrical signal known as the local field potential (LFP) have remained mostly unexplored. Chief among these is the dentate spike, which is associated with brain-wide firing increases beyond any known physiological event and has therefore been hiding in plain sight. Recent results have begun to highlight the circuit mechanisms and potential functional significance of these noncanonical LFP dynamics, also including small irregular activity, beyond the intensely investigated patterns related to locomotion and episodic memory replay (theta rhythm and sharp wave ripples, respectively).

OUTLOOK: Not so long ago, a sizable part of the genome was thought of as "junk DNA" with no discernible function. However, such allegedly useless yet curiously large DNA segments are now well recognized to be far from unimportant. In a similar manner, recent research efforts have begun to highlight the functional relevance of long segments of hippocampal LFP activity that have been historically viewed as gaps between "coding" regions and the potential role for noncanonical hippocampal regions in controlling them. These advances help to build a more comprehensive framework of the functionally meaningful computations that the hippocampus performs beyond those that are conventionally recognized, with implications for neurological and psychiatric brain disorders. □

*Corresponding author. Email: jordan.farrell@childrens.harvard.edu (J.S.F.); isoltesz@stanford.edu (I.S.) Cite this article as J. S. Farrell, I. Soltesz *et al.*, *Science* **389**, eadv4420 (2025). DOI: 10.1126/science.adv4420

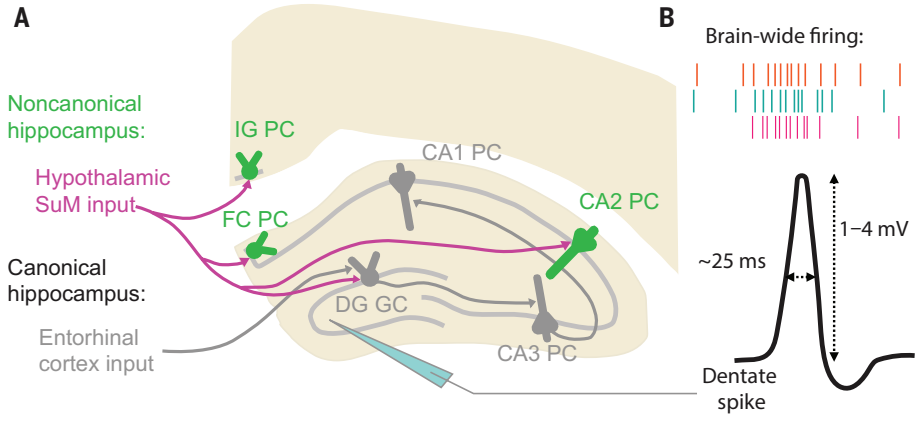

The overlooked hippocampus. (**A**) The canonical flow of information is outlined in gray, from the entorhinal cortex to DG granule cells (GCs), CA3, and then CA1 principal cells (PCs). PCs in noncanonical regions, which receive direct input from the hypothalamic supramammillary nucleus (SuM), are shown in green. (**B**) Large-amplitude events recorded from LFP in the DG hilus, known as dentate spikes, are associated with profound increases in brain-wide firing.

RESEARCH

IN *SCIENCE* JOURNALS

Edited by **Michael Funk**

A satellite image reveals deforestation and fragmentation along a highway in the Amazon rainforest in Brazil.

PHOTO: SCIENCE HISTORY IMAGES/ALAMY

HABITAT FRAGMENTATION

Losing connectivity

Land conversion not only reduces the total habitat available to other species, but it also fragments habitat into smaller and less-connected patches, thus supporting smaller and less-connected populations. Ecologists have developed various metrics capturing different aspects of habitat fragmentation, such as the number and size of habitat patches and their distribution across space. Zou *et al.* used remotely sensed data to quantify the degree of fragmentation of global forests from 2000 to 2020, comparing metrics focused on patch connectivity, aggregation, and structure. Measures incorporating habitat connectivity and aggregation suggested that more than half of global forests have become more fragmented over the past two decades. These changes suggest widespread forest degradation beyond the direct effects of habitat loss. —Bianca Lopez *Science* p. 1151, 10.1126/science.adr6450

SIGNAL TRANSDUCTION

Trashing the RAS oncogene product

Misregulation of members of the small guanosine triphosphatase RAS family leads to cancer and other human diseases. One way in which RAS proteins are regulated is through controlled degradation. The substrate adaptor protein Leucine Zipper-like Transcription Regulator 1 (LZTR1) couples RAS proteins to a ubiquitin ligase, and then ubiquitination leads to their degradation. Mutations in *LZTR1* are also associated with human diseases. Dharmaiah *et al*. used crystal structures to define the interaction of LZTR1-binding domains with various RAS proteins. Their results help to explain the effects of disease-causing mutations in *LZTR1* and also provide clues for strategies to develop glue-like therapeutic molecules that could target oncogenic RAS proteins to LZTR1-dependent degradation. —L. Bryan Ray

Science p. 1112, 10.1126/science.adv7088

LIVER FIBROSIS

Cleaning up to keep fibrosis down

Metabolic dysfunction–associated steatohepatitis (MASH) is characterized by liver fibrosis and hepatocyte death, but it is unclear how apoptosis may be linked to disease progression. Shi *et al*. found that macrophage efferocytosis of apoptotic cells was impaired in MASH, and that apoptotic cells accumulated in human MASH and in mouse models. Apoptotic cell accumulation was associated with decreased amounts of the efferocytosis receptor T cell immunoglobulin and mucin domain containing 4 (TIM4). In mice, inhibiting TIM4 promoted disease, and genetically or cellularly restoring TIM4 increased apoptotic cell clearance and decreased liver fibrosis. Ex vivo and in vivo mouse experiments revealed a mechanism involving

Flexible gold films can be transferred in a liquid droplet to coat irregular surfaces such as a model of human skin, seen here.

interleukin-10 receptor activation on hepatic stellate cells that led to reduced fibrotic activation. Together, these data outline a potential therapeutic strategy to prevent fibrosis in MASH progression. —Brandon Berry

Sci. Transl. Med. (2025) 10.1126/scitranslmed.adv2106

ORGANOMETALLICS

Tin binds CO

Coordination of carbon monoxide (CO) to transition metals is a central feature of organometallic chemistry. The twofold bonding motif simultaneously involves electron donation from carbon to the metal and back-bonding from the metal to the carbon. The electronic structure of metals outside of the transition block of the periodic table is less susceptible to this motif, and such metals therefore do not tend to bind CO. Dietz *et al*. now report the surprising isolation of a (diboryl)tin–CO complex produced below 0°C. Upon warming, the complex rearranges to a tin carbene through migration of both boryl ligands. —Jake S. Yeston

Science p. 1118, 10.1126/science.ady0247

ULTRACOLD GASES

Simulating glass

In spin glasses, disorder and geometric frustration cause exact system copies called replicas to relax into distinct configurations. These configurations have overlaps that form a hierarchic, tree-like structure that is referred to as ultrametric. Kroeze *et al*. used ultracold gases of rubidium atoms trapped in optical tweezers and placed them in a cavity to visualize the ultrametric structure of a glassy system. The driven-dissipative nature of the system further enriched the spin glass phenomenology. —Jelena Stajic

Science p. 1122, 10.1126/science.adu7710

HUMAN GENETICS

Genetics and breast milk sufficiency

The health benefits of breastfeeding infants for the first 6 months of life are widely accepted. However, half of women wean infants earlier due in part to their perception that they are not producing sufficient breast milk. Golan *et al.* explored the extent to which breast milk insufficiency can be attributed to genetic differences among women. They compared women with low, medium, and high breast milk sufficiency and found that genetic variants and their expression did not differ between these groups. They also found no differences in the gut microbiome diversity of infants of women with breast milk insufficiency, concluding that breastfeeding, even with supplemental formula, is beneficial to an infant's gut microbiome. —Colleen McBride

Sci. Adv. (2025) 10.1126/sciadv.adr7174

BIOELECTRONICS

Comfortably conforming to curved surfaces

Wrapping of thin-film bioelectronic devices onto three-dimensional surfaces can lead to residual stress and device failure. Li *et al*. overcame this challenge by using droplets of water, water-gelatin mixtures, or buffer solutions as a dynamic lubricating layer to enable conformal wrapping of fragile, nonstretchable films onto intricate substrates such as skin, polymers, cells, and nerves. The droplet lets the device slide across the target substrate, allowing it to conform to the underlying shape. The authors demonstrated drop printing onto nerves and brain tissue, enabling light-controlled neuromodulation. —Marc S. Lavine

Science p. 1127, 10.1126/science.adw6854

INSECT DECLINES

Sensitivity matters

Recent research has revealed a worrisome, and seemingly increasing, decline in insect populations globally. That said, not all species have been shown to be declining, and the reasons for the differences are not always clear. Liu *et al*. looked at ant species, using a community genetics approach, on remote Fijian islands to determine susceptibility to human impacts and disturbance. They found that endemic species and those most sensitive to habitat disturbance began to decline as long as 3000 years ago, with the first arrival of humans. More recent arrivals to the islands display more resistance, likely due to their more generalist requirements. —Sacha Vignieri

Science p. 1133, 10.1126/science.ads3004

PHOTO: YANLIN SONG, INSTITUTE OF CHEMISTRY, CHINESE ACADEMY OF SCIENCES

Edited by **Corinne Simonti** and **Jesse Smith**

BIOPHYSICS

Organizing biomolecular condensates

Biomolecular condensates localize and organize molecular components in the cell that help to regulate biological functions. Snead *et al.* used in vitro experiments, informatics, and physics-based simulations to explore the interactions between proteins and long noncoding RNA (lncRNA) that form nuclear paraspeckles regulating the expression of specific mRNAs. The speckles were organized with a core and shell, but there was no simple preference of binding of associated proteins with the shell and core portions of the organizing lncRNA NEAT1. Instead, it appeared that competitive binding to the lncRNA by core and shell proteins, and immiscibility of those proteins, combined in a more complex manner to yield the essential layering of the paraspeckles. —L. Bryan Ray

Proc. Natl. Acad. Sci. U.S.A. (2025)
10.1073/pnas.2504778122

CONSERVATION

Dingoes are distinct

For as long as westerners have been in Australia, there has been persecution of the dingo, Australia's native canid. Debate about whether this species represents a unique canid lineage or an ancient domesticated dog has raged for nearly as long. In the past several decades, much previously unobtainable data have accrued that can speak directly to this question. Previously, four specific criteria have been used to argue that dingoes should be considered on a unique evolutionary trajectory. Cairns *et al.* looked at the current knowledge about dingo genetics, behavior, and history and determined that they meet all of these criteria. Therefore, dingoes should be considered taxonomically distinct, renamed accordingly, and given the appropriate protections. —Sacha Vignieri

Aust. Mamm. (2025)
10.1071/AM24052

CLOUDS

One by one

Computational power has been the main driver of improvements in numerical weather prediction models. As computers have become more and more powerful, the resolutions of these models have continued to improve, allowing the simulation of processes increasingly smaller in scale. Müller *et al.* tested how accurate cloud-resolving models have become by comparing satellite observations and model simulations of trade-wind cumulus clouds. They found that the models simulated distributions of cloud size, development, and lifetime similar to those of the observations, but underestimated the presence of larger, longer-lived clouds. This work should help to establish a benchmark for the further refinement of these models. —Jesse Smith

Geophys. Res. Lett. (2025)
10.1029/2025GL115648

PLANT GENETICS

Mutations mark floral cell lineages

Mutations that occur during cell division are passed on to newly formed cells, allowing lineage history to be tracked by tracing sets of unique mutations. Ji *et al.* found that in peach flowers, petals and sepals are derived from the same cell population, with adjacent sepals sharing a closer cell lineage history than adjacent petals. By contrast, the female part of the flower, the carpel, was genetically distinct. These patterns of genetic divergence reinforce the radial development of the flower and indicate that carpels originate from a tissue layer that is separate from other floral organs. This means that only mutations in the cell layer that give rise to carpel tissue can be passed on to egg-derived offspring. —Madeleine Seale

PLOS Genet. (2025)
10.1371/journal.pgen.1011829

RESEARCH FUNDING

Public research spurs private investment

For each euro of public funds invested in a French academic research program, 0.81 euros were then invested in research and development (R&D) by private firms. The Laboratoires d'Excellence (LabEx) program allocated 1.5 billion euros to 170 research clusters selected in 2010 and 2011. Bergeaud *et al.* showed that firms that were close to a LabEx cluster, both spatially and scientifically, spent more on R&D compared with less-exposed firms. Three channels seem to have driven these spillovers: direct collaborations between academics and firms, movement of academics to firms (or academics creating firms), and informal interactions among academics and firms. —Brad Wible

Q. J. Econ. (2025)
10.1093/qje/qjaf034

ANIMAL BEHAVIOR

Riding the tide

Magellanic penguins must travel long distances at sea and face strong tidal currents that can push them off course. To determine how they manage to return home efficiently, Gunner *et al.* tracked 27 penguins using GPS and measured ocean currents to see how the birds reacted to changing conditions. They found that penguins sensed and adapted to current drift. When water was calm, they headed straight for their colony. However, when currents were strong, they adjusted their paths to move with the flow, saving energy and finding more food along the way even if their route became S-shaped instead of straight. These navigation strategies allowed the penguins to reach their nests reliably, showing energy-saving skills and flexibility in a constantly changing ocean. —Di Jiang

PLOS Biol. (2025)
10.1371/journal.pbio.3002981

PHYSICS

Reducing complexity

Solving for ground states of quantum many-body systems remains one of the most computationally challenging problems in physics. The complexity of the problem depends on the amount of entanglement in the ground state. Lootens *et al.* devised a way to reduce problems with more entanglement to related problems with less entanglement. The researchers showed that for each gapped Hamiltonian, there was an optimal "dual" Hamiltonian with less entanglement in its ground state that could be solved more easily. The ground state of the original Hamiltonian could then be deduced using the duality operation. The method was demonstrated in one spatial dimension, but is expected to be generalizable to higher dimensions. —Jelena Stajic

Nat. Phys. (2025)
10.1038/s41567-025-02961-2

RESEARCH ARTICLE SUMMARY

MALARIA

Cryo-EM structure of endogenous *Plasmodium falciparum* Pfs230 and Pfs48/45 fertilization complex

Melanie H. Dietrich *et al.*

Full article and list of author affiliations: https://doi.org/10.1126/science.ady0241

INTRODUCTION: Fertilization is a critical process in generating new offspring. For malaria parasites, fertilization of its gametes occurs in the midgut of female *Anopheles* mosquito. Transmission-blocking interventions can stop malaria parasite transmission from mosquito to human by inhibiting parasite fertilization in mosquitos. Targeting the sexual stages of malaria parasites in the mosquito to block transmission is advantageous compared with targeting other life cycle stages because the development of the parasite in the mosquito imposes bottlenecks in terms of parasite numbers. Reducing malaria parasite transmission is critical for the elimination of the deadly malaria parasite, which is responsible for >600,000 deaths annually. Two leading transmission-blocking vaccine candidates are the 6-cysteine proteins, Pfs230 and Pfs48/45. Both are localized to the surface of gametes and critical for male fertility.

RATIONALE: Pfs230 is localized to the surface of malaria parasite gametes by binding to Pfs48/45, which has a putative glycosylphosphatidylinositol (GPI) anchor. Full-length Pfs230 is larger than 300 kDa with 14 6-cysteine domains and is recalcitrant to recombinant protein expression. It is not known how these proteins interact and whether other domains within these proteins have potential as transmission-blocking vaccine candidates. We used cryo–electron microscopy (cryo-EM) to determine the structure of the Pfs230-Pfs48/45 fertilization complex isolated from the sexual stages of malaria parasites. The structure of this endogenous fertilization complex provided insight into critical domains required for complex formation.

RESULTS: Our cryo-EM structure revealed that domains 13 and 14 (D13 and D14) of Pfs230 bind to Pfs48/45. We generated a *Plasmodium falciparum* transgenic line with D13 and D14 removed from Pfs230 (230Δ1314) and showed that it failed to localize on the surface of activated gametes. Furthermore, this transgenic line was defective in parasite fertilization, as indicated by a significant reduction of oocyst formation in the midguts of *Anopheles stephensi*. High-affinity nanobodies specific to Pfs230 D13 and D14 blocked complex formation with Pfs48/45 and reduced parasite transmission. By using a cohort of individuals from the malaria endemic region of Papua New Guinea, we showed that Pfs230 D13 and D14 are targets of naturally acquired immunity. Furthermore, Pfs230 mRNA–lipid nanoparticle (LNP) immunogen elicited high titers of specific antibodies to these Pfs230 domains that recognize the endogenous parasite protein, and the immunized mouse sera inhibited parasite transmission in *A. stephensi* mosquitoes.

CONCLUSION: This study shows that Pfs230 D13 and D14 are essential for its localization on the gamete surface and in its role for parasite fertilization. Our findings also identify these domains as potential transmission-blocking vaccine immunogens. Structural analyses of the endogenous Pfs230-Pfs48/45 fertilization complex and Pfs230-nanobody complexes will facilitate future rational design of vaccines and transmission-blocking monoclonal antibody approaches. □

Corresponding author: Wai-Hong Tham (tham@wehi.edu.au) Cite this article as M. H. Dietrich *et al.*, *Science* **389**, eady0241 (2025). DOI: 10.1126/science.ady0241

Cryo-EM of the endogenous Pfs230-Pfs48/45 fertilization complex. Pfs230 and Pfs48/45 from a core fertilization complex that is important for male fertility in malaria parasites. D13 and D14 of Pfs230 are critical interaction sites with Pfs48/45. Transgenic parasite lines with a D13 to D14 deletion were defective in Pfs230 gamete localization and showed reduced oocyst formation. Nanobodies against D13 and D14 inhibited Pfs230-Pfs48/45 complex formation and reduced transmission, and structural analyses revealed their epitopes. D13 and D14 were targets of naturally acquired immunity, and immune sera from mRNA-LNP immunizations blocked parasite transmission. [Figure created with Biorender.com]

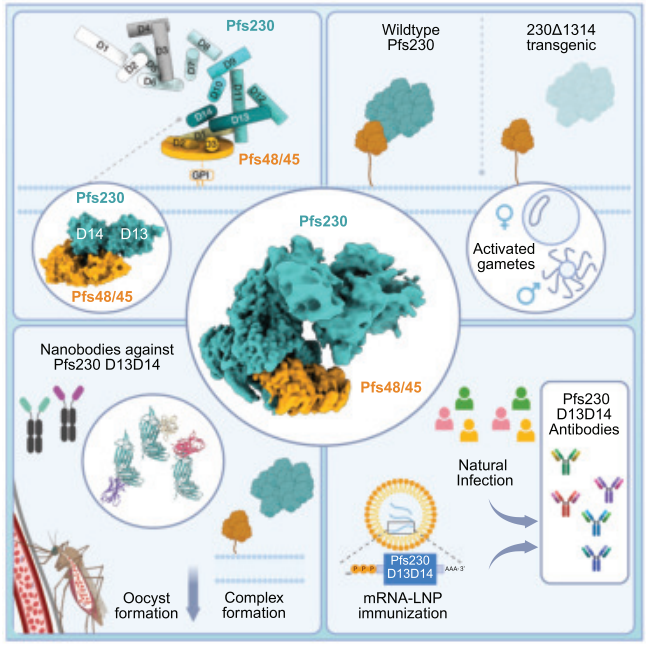

RESEARCH ARTICLE SUMMARY

PLANT SCIENCE

Dual-cycle CO_2 fixation enhances growth and lipid synthesis in *Arabidopsis thaliana*

Kuan-Jen Lu, Chia-Wei Hsu, Wann-Neng Jane, Mien-Hao Peng, Ya-Wen Chou, Pin-Hsuan Huang, Kuo-Chen Yeh, Shu-Hsing Wu, James C. Liao*

Full article and list of author affiliations: https://doi.org/10.1126/science.adp3528

INTRODUCTION: The Calvin-Benson-Bassham (CBB) cycle accounts for the majority of carbon dioxide (CO_2) uptake on Earth through ribulose 1,5 bisphosphate (RuBP) carboxylase/oxygenase (RuBisCO). However, for every three carbon atoms fixed, one is lost to CO_2 when synthesizing acetyl–coenzyme A (CoA) to generate lipids, phytohormones, and other essential metabolites. Additionally, RuBisCO also oxygenates its precursor and generates glycolate, which is oxidized to CO_2 through photorespiration. We aimed to solve these two CO_2-losing problems by constructing a new-to-nature cycle that can convert glycolate or 3-phosphoglycerate (3PG) to acetyl-CoA.

RATIONALE: We designed the malyl-CoA-glycerate (McG) cycle, which uses phosphoenolpyruvate carboxylase (PPC) as the key enzyme to accomplish the above tasks. In the McG cycle, one additional carbon is fixed when 3PG is the input, or no carbon is lost when glycolate is the input. In both cases, acetyl-CoA is produced more efficiently, which is expected to enhance the production of lipids and other important plant metabolites, including phytohormones.

RESULTS: We constructed the McG cycle in *Arabidopsis*. The McG transgenic plants grew much larger, resulting in doubled or tripled dry weight compared with that of the wild type during their comparable life spans. The McG plants also have increased rosette leaf numbers, leaf areas, silique and seed numbers, and lipids in leaves and seeds. To support the increased growth and productivity, the McG plants approximately doubled their CO_2 assimilation under atmospheric CO_2, and their photosystem II showed greater efficiency than that of the wild type. The proteins in photosystems I and II, cytochrome b6/f and electron transfer chain, and F-type ATP synthase were significantly enriched in the McG plants. We also found that cytokinin levels were increased in McG plants, which may explain their increased shoot apical meristem (SAM) sizes and number of leaf primordia. Introducing partial McG cycles or omitting one key enzyme, glycolate dehydrogenase (GDH), greatly reduced the above growth benefits. Growth in high CO_2 concentrations also diminished the McG effects, suggesting that glycolate conversion to acetyl-CoA played a major role.

CONCLUSION: The McG cycle can use both the RuBisCO carboxylation and oxygenation products to produce acetyl-CoA. The conversion of glycolate to acetyl-CoA is dominant under ambient CO_2 conditions and avoids photorespiration. When 3PG is used as an input, one additional carbon is fixed to produce two acetyl-CoA. Furthermore, because PPC uses bicarbonate, it does not compete with RuBisCO for dissolved CO_2 in the chloroplast, which has a higher pH.

The conversion of glycolate or 3PG to acetyl-CoA leads to increased production of lipids and cytokinin, the latter of which may explain the increased leaf number and SAM sizes. The increased acetyl-CoA also results in a proteomic shift that increases abundance of photosystem proteins. Therefore, the McG cycle creates a positive feedback loop through the production of acetyl-CoA, which is a precursor to cytokinin, and through an unknown mechanism that boosts photosystems protein abundance and efficiency. Together, these lead to increased carbon assimilation to support the beneficial growth phenotypes and high lipid production. The McG design enables efficient acetyl-CoA production without carbon loss at a reduced energy expenditure, suggesting the success of this "C2-centric" approach. □

*Corresponding author. Email: liaoj@as.edu.tw Cite this article as K.-J. Lu *et al.*, *Science* **389**, eadp3528 (2025). DOI: 10.1126/science.adp3528

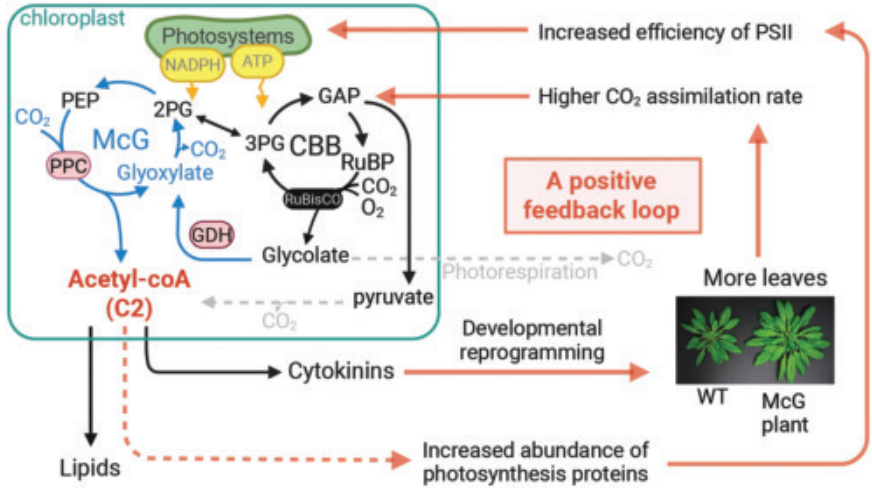

A C2-centric dual-cycle carbon fixation system in *Arabidopsis*. The McG (blue) cycle is introduced to *Arabidopsis* chloroplasts to work with the native CBB cycle (black) for more efficient acetyl-CoA synthesis and bypassing photorespiration. The McG plants grew much larger and produced more seeds and lipids through a positive feedback loop. [The figure was created with BioRender.com.]

RESEARCH ARTICLE SUMMARY

MOLECULAR BIOLOGY

E. coli transcription factors regulate promoter activity by a universal, homeostatic mechanism

Vinuselvi Parisutham, Sunil Guharajan, Melina Lian, Md Zulfikar Ali, Hannah Rogers, Shannon Joyce, Mariana Noto Guillen, Robert C. Brewster*

Full article and list of author affiliations: https://doi.org/10.1126/science.adv2064

INTRODUCTION: Transcription factor (TF) function is important for the proper regulation of gene expression, and individual TFs can have very different effects on gene expression depending on the identity of the promoter that they regulate. This highlights the context-dependent nature of their regulatory roles. Traditionally, TFs have been classified as "activators" or "repressors" on the basis of their net effect on expression. However, this simplistic classification fails to explain why and how TFs can have distinct functions at different promoters and the contextual differences that influence TF function.

RATIONALE: Understanding how TF function is related to promoter identity is crucial for elucidating the mechanisms of gene regulation and enhancing our ability to predict TF function in different biological contexts. To interpret how TFs regulate gene expression across different promoters, we use a simplified thermodynamic model that predicts two possible, distinct relationships between TF function and the constitutive strength of promoters: Fold change increases or decreases with increasing promoter strength, depending on whether the TF has negative (destabilizing) or positive (stabilizing) interactions with RNA polymerase (RNAP), respectively. To reveal the relationship between TF function and promoter strength, we measured regulation by a single TF, with a regulatory context that was otherwise held constant, on promoters whose strength was altered systematically by both genetic and physiological perturbations.

RESULTS: For every TF tested, we find the same basic relationship between fold change and constitutive expression level. Each TF, both activators and repressors, exerts a lower fold change on stronger promoters. We find that the scaling between fold change and constitutive promoter strength obeys a precise inverse scaling relationship, as predicted by theory for TFs with stabilizing interactions. The precise scaling has a distinct implication: Promoters that differ in basal activity by orders of magnitude will have the same regulated level for a given TF, dictated by details such as TF identity and binding location. As such, TFs are predicted to have an innate property that buffers physiological or genetic perturbations to the promoter to maintain a steady level of regulated expression. We demonstrate this buffering across all TFs studied.

CONCLUSION: Among a diverse set of TFs, we see a universal relationship between fold change enacted by the TF and constitutive strength of the regulated promoter. This relationship is a useful fail-safe where a TF can adjust gene expression to buffer against perturbations and maintain homeostasis. □

*Corresponding author. Email: robert.brewster@umassmed.edu Cite this article as V. Parisutham *et al.*, *Science* **389**, eadv2064 (2025). DOI: 10.1126/science.adv2064

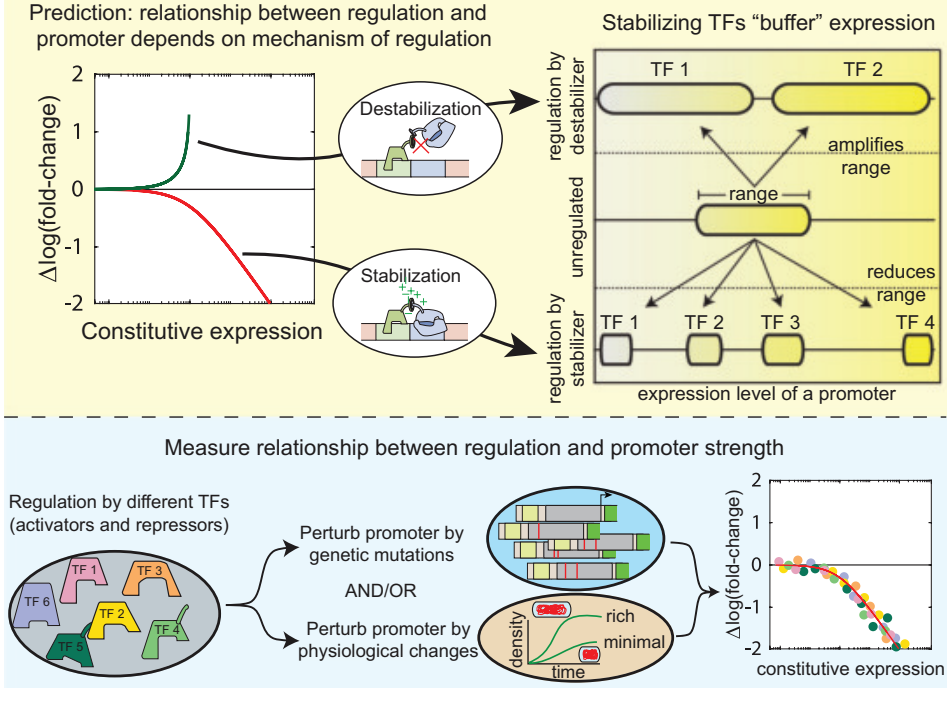

Mechanism of TF regulation. (Top) A general thermodynamic model predicts the relationship between fold change and the constitutive strength of the promoter regulated by a TF. The theory predicts two possible behaviors based on whether the TF has stabilizing (attractive or cooperative) or destabilizing (antagonistic or hindering) interactions with RNAP. TFs with destabilizing interactions are predicted to amplify the range of expression of a library of promoters, whereas TFs with stabilizing interactions would reduce that range. (Bottom) Experimental measurements of several TFs (both activators and repressors) on mutated libraries of promoters—in different media and with varying concentrations of polymerase—give a single relationship precisely aligned with that expected from TFs with stabilizing interactions.

RESEARCH ARTICLE SUMMARY

STRUCTURAL BIOLOGY

Structure and function of a huge photosystem I–fucoxanthin chlorophyll supercomplex from a coccolithophore

Lili Shen†, Fei Ren†, Yin-Chu Wang†, Zhenhua Li†, Mengyuan Zheng†, Xiaoyi Li, Wenzheng Fan, Yanyan Yang, Min Sang, Cheng Liu, Guangye Han, Song Qin, Jianhua Fan, Lijin Tian*, Tingyun Kuang, Jian-Ren Shen, Wenda Wang*

Full article and list of author affiliations: https://doi.org/10.1126/science.adv2132

INTRODUCTION: Photosystem I (PSI) is a crucial pigment-protein complex in thylakoid membranes and drives electron transfer for the fixation of carbon dioxide, which has almost 100% quantum efficiency in converting light energy into chemical energy. To make full use of light energy under different habitats, eukaryotic photosynthetic organisms use multiple types and numbers of light-harvesting complexes (LHCs) to collect light energy and transfer it to PSI reaction centers. Among them, Lhca serves as the light-harvesting antenna of PSI in green algae and land plants, whereas a number of Lhcr, Lhcf, or Lhcq proteins are found in red-lineage algae, including red algae, diatoms, cryptophytes, haptophytes, and dinoflagellates. These varying LHCs absorb light energy and mediate energy balance under different light conditions.

RATIONALE: The PSI core and reaction center are largely conserved across different lineages of photosynthetic organisms, but some PSI complexes of the red-lineage algae bind more than 20 LHC antenna subunits to expand cross sections for harvesting more light energy. In addition, diverse pigments [chlorophylls (Chls)] c and keto-carotenoids, such as fucoxanthins and peridinins] are contained in Lhcr, Lhcf, or Lhcq antennae, which function to harvest more blue-green (460 to 490 nm) and green (490 to 540 nm) light energy where seawater attenuates most of the blue and red light. Coccolithophores were a dominant group of red-lineage algae in the Cretaceous and are abundant in modern oceans. They contribute substantially to the global primary productivity and carbon and calcium cycles. The coccolithophore PSI-LHCI has complicated pigments and LHCI protein components, which confer it with the ability to adapt to changing light environments under water.

RESULTS: We purified a PSI-fucoxanthin chlorophyll a/c-binding protein (PSI-FCPI) supercomplex from the coccolithophore *Emiliania huxleyi* (Eh) and solved its structure by single-particle cryo–electron microscopy at a resolution of 2.79 Å. This monomeric supercomplex contains 12 PSI core subunits, a specific lumenal linker protein (EhLP), and 38 peripheral Eh-FCPI antennae, with 411 Chls a, 152 Chls c, 256 carotenoids, and a number of other ligands, which thus constitutes the largest PSI-antenna supercomplex known so far. Phylogenetic analysis indicated that 16 Lhcq-like Eh-FCPIs were specific to *E. huxleyi*, whereas 10 Lhcrs, 1 Lhcf, 1 RedCAP, and 10 Lhcq Eh-FCPIs were similar to either those in red algae or diatoms. The 38 Eh-FCPIs formed a radial arrangement of eight belt-like Eh-FCPI clusters around the PSI core. In addition, four Chl c species and four fucoxanthin derivatives were found in the structure, in addition to Chl a, diadinoxanthin, diatoxanthin, α-carotene, and β-carotene, which formed a complicated pigment network for light harvesting and energy transfer. We measured femtosecond transient absorption spectrograms and found that Eh-PSI-FCPI has an overall excitation trapping time of 96 to 120 ps, representing 95% quantum efficiency in this giant Eh-PSI-FCPI.

CONCLUSION: Our results reveal the organization of 38 FCPI antennae and a huge number of pigments that contribute to light harvesting and fast energy transfer in the Eh-PSI-FCPI. The 95% quantum efficiency of coccolithophore PSI-FCPI illustrates a highly efficient system in spite of a four to five times expansion of the light-harvesting cross section compared with PSI-LHCI of land plants. □

*Corresponding author. Email: wdwang@ibcas.ac.cn (W.W.); ltian@ibcas.ac.cn (L.T.)
†These authors contributed equally to this work. **Cite this article as L. Shen *et al.*, *Science* 389, eadv2132 (2025). DOI: 10.1126/science.adv2132**

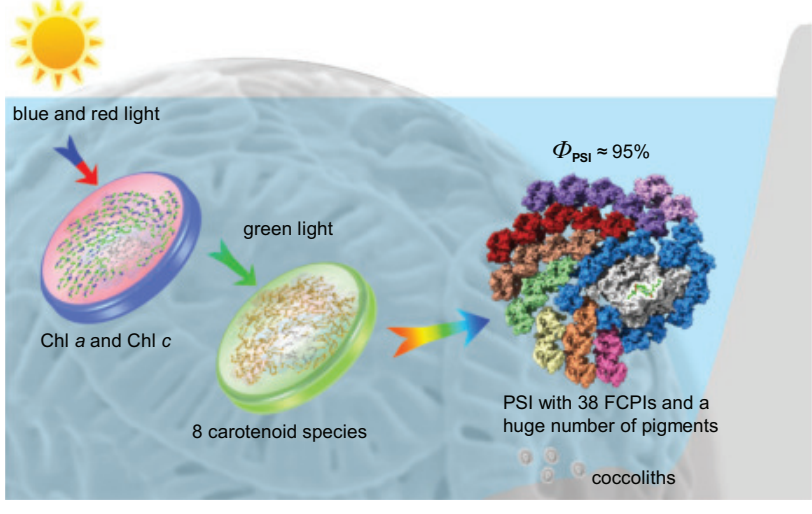

A coccolithophore PSI-FCPI supercomplex consisting of a large number of light-harvesting antennae and pigments. The Eh-PSI-FCPI contains 38 LHC antennae surrounding the PSI core, with a total of 819 pigments. Among them, Chl a, Chl c, and Fx (including their derivatives) enable different absorption ranges of sunlight under water. The whole system showed 95% quantum efficiency (Φ_{PSI}), illustrating its high efficiency of light-energy utilization.

RESEARCH ARTICLE SUMMARY

NEUROSCIENCE

Visual objects refine head direction coding

Dominique Siegenthaler, Henry Denny†, Sofía Skromne Carrasco†, Johanna Luise Mayer†, Daniel Levenstein, Adrien Peyrache*‡, Stuart Trenholm*‡, Émilie Macé*‡

Full article and list of author affiliations: https://doi.org/10.1126/science.adu9828

INTRODUCTION: In our day-to-day life, we use visual objects (e.g., a specific clock tower when walking around town, etc.) as spatial landmarks to help orientate ourselves as we make our way through the world. We can use visual objects as spatial landmarks because our brains dedicate considerable computational power toward parsing the world into objects. Moreover, our location in the world is processed by specialized cells such as place cells, grid cells, and head direction (HD) cells in the brain's spatial navigation system. However, much remains unknown about how visual objects modulate tuning properties of the neurons that encode spatial variables, partly because it is unclear how visual objects are processed in the rodent brain, where spatial navigation signals have been most extensively studied.

RATIONALE: To address this gap in knowledge, we reasoned that a brainwide activity screen in mice could identify visual object–preferring areas in an unbiased way. Using electrophysiology, we then characterized the spatial correlates of individual neurons in the areas responding to objects in freely moving mice.

RESULTS: Our brainwide screen based on functional ultrasound imaging revealed that spatial navigation–related areas, not visual cortical areas, tended to show a preference for visual objects. The postsubiculum, a hub of the HD system, exhibited the strongest object preference. In head-fixed conditions, we discovered that HD cells were differentially modulated by visual stimulation based on their preferred firing direction: HD cells pointing toward the visual stimulus were excited, whereas HD cells pointing away from the visual stimulus were inhibited. The same modulation was observed in freely moving conditions, when an object was displayed in the environment.

CONCLUSION: Visual objects refine the population encoding of HD in the postsubiculum by increasing the response of HD cells that code toward the object while simultaneously decreasing the firing rate of HD cells that code directions away from the object. As an analogy, imagine yourself wandering around a city with a compass (which, in our experiments, is the brain's HD system), and each time you look at a landmark (which, in our experiments, is an image of an object), the compass needle becomes more stable and thus more accurate. Together, these results provide insights into how the brain uses visual landmarks to dynamically enhance the encoding of spatial information about the world. □

*Corresponding author. Email: adrien.peyrache@mcgill.ca (A.P.); stuart.trenholm@mcgill.ca (S.T.); emilie.mace@med.uni-goettingen.de (E.M.) †These authors contributed equally to this work. ‡These authors contributed equally to this work. **Cite this article as** D. Siegenthaler *et al.*, *Science* **389**, eadu9828 (2025). DOI: 10.1126/science.adu9828

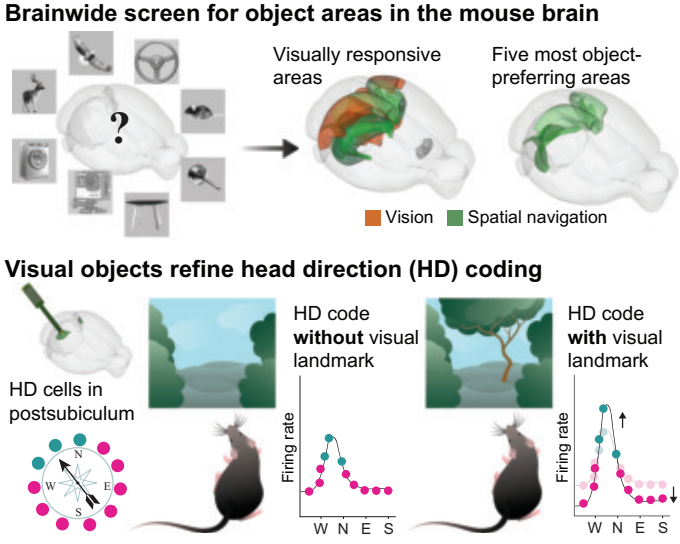

Visual objects sharpen the representation of head direction. Of all visually responsive regions, the most object-preferring areas belonged to the spatial navigation system. Electrophysiological analysis in one of the identified regions, the postsubiculum, indicated that when an animal faces a visual landmark, HD encoding is refined. W, west; N, north; E, east; S, south. [Three-dimensional brain images prepared with cocoframer © 2018 Allen Institute for Brain Science. Allen Brain Explorer]

RESEARCH ARTICLE SUMMARY

DEVELOPMENT

Oxytocin signaling regulates maternally directed behavior during early life

Daniel D. Zelmanoff, Rebecca Bornstein, Menachem Kaufman, Julien Dine†, Jonas Wietek‡, Anna Litvin, Shaked Abraham, Savanna Cohen, Ayelet Atzmon, Ido Porat, Ofer Yizhar*

Full article and list of author affiliations: https://doi.org/10.1126/science.ado5609

INTRODUCTION: Oxytocin is a brain hormone that plays a critical role in regulating social behavior. Although much research has focused on how oxytocin supports adult behaviors such as pair-bonding and caregiving, far less is known about how this system functions during early life. The early postnatal period is a time of critical social interactions between infants and caregivers, and disruptions during this period may contribute to developmental disorders. Notably, expression of the oxytocin receptor peaks during infancy in both humans and mice, suggesting that this period represents a critical window of heightened sensitivity to oxytocin signaling. However, technical challenges have limited the study of the oxytocin system during this sensitive time of brain development. As a result, the role of oxytocin in shaping social behavior during infancy remains poorly understood.

RATIONALE: We set out to investigate how oxytocin influences pup behavior during a brief separation from the mother and littermates and subsequent reunion. We focused on vocal communication, as rodent pups emit ultrasonic vocalizations that signal distress but may also reflect social motivation and need. We combined detailed behavioral analysis with fiber photometry, pharmacological intervention, and a novel optogenetic strategy built on wireless silencing of oxytocin neurons in freely behaving pups—a technical advance that overcomes prior limitations in studying brain circuits during early life.

RESULTS: Pups that were acutely separated from their mother and littermates displayed a substantial increase in vocalizations upon reunion, especially when in close proximity to their mother. The rate and type of vocalizations were modulated by nipple attachment behavior. We found that hypothalamic oxytocin neurons increased their activity upon separation, and that this activity was tightly linked with the emission of vocalizations. Blocking the oxytocin receptor in pups during separation reduced nipple attachment and altered the pattern of vocal behavior both during separation and reunion. For increased temporal precision, we developed a new optogenetic method using a highly light-sensitive, red-shifted inhibitory opsin (eOPN3). This allowed us to wirelessly silence oxytocin neurons in untethered pups. We found that silencing oxytocin neurons during separation disrupted vocal—but not nonvocal—behavior during both the separation and reunion.

CONCLUSION: Our findings reveal a specific role for oxytocin in shaping maternally directed behavior during infancy. We also introduce a noninvasive optogenetic approach for studying brain circuits in developing animals, opening new opportunities to investigate the neural mechanisms underlying early life social behavior. Our work emphasizes the need to gain a more nuanced understanding of oxytocin function and provides a technical platform for studying the social brain during its most formative stages. □

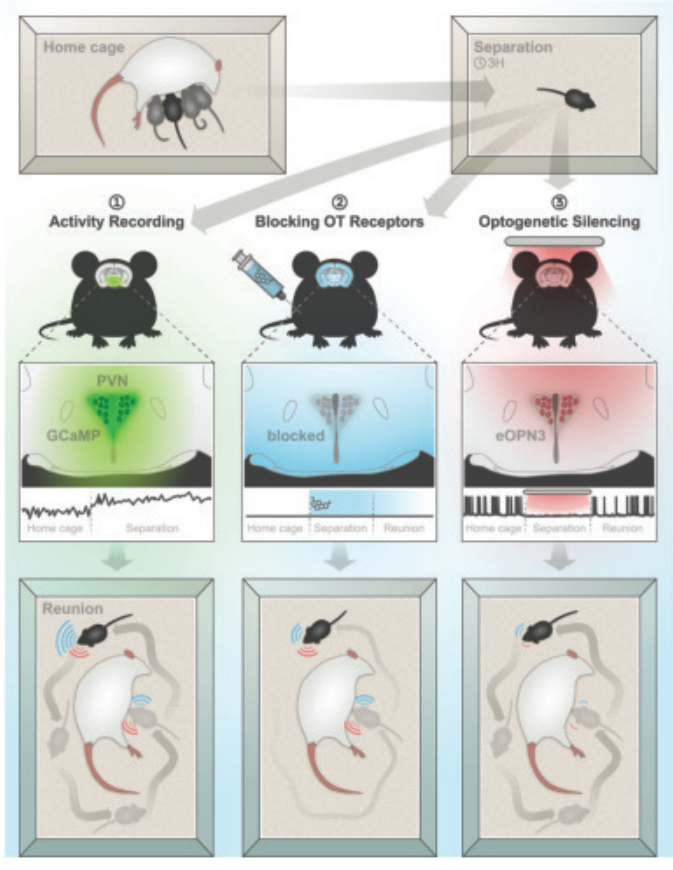

Oxytocin shapes infant behavior toward the mother. To explore the role of oxytocin in early life, we separated pups from their mother (top) and then reunited them while tracking vocal and nonvocal behaviors (bottom). Oxytocin cells in the pups' brain increased their activity upon separation (1), while blocking the oxytocin receptor (2) or optogenetic silencing of oxytocin neurons (3) altered the pattern of maternally directed behavior upon reunion, highlighting an important role for oxytocin during early life.

*Corresponding author. Email: ofer.yizhar@weizmann.ac.il †Present address: Boehringer Ingelheim Pharma GmbH & Co. KG, CNS Diseases, Biberach an der Riss, Germany. ‡Present address: Charité-Universitätsmedizin Berlin, corporate member of Freie Universität Berlin, and Humboldt-Universität zu Berlin, Neuroscience Research. **Cite this article as Daniel D. Zelmanoff *et al.*, *Science* 389, eado5609 (2025). DOI: 10.1126/science.ado5609**

SIGNAL TRANSDUCTION

Structural basis for LZTR1 recognition of RAS GTPases for degradation

Srisathiyanarayanan Dharmaiah[1]†, Daniel A. Bonsor[1]†, Stephanie P. Mo[2]†‡, Alvaro Fernandez-Cabrera[2], Albert H. Chan[1], Simon Messing[1], Matthew Drew[1], Martha Vega[2], Dwight V. Nissley[1], Dominic Esposito[1], Pau Castel[2]*, Dhirendra K. Simanshu[1]*

The RAS family of small guanosine triphosphatases (GTPases) are tightly regulated signaling molecules that are further modulated by ubiquitination and proteolysis. Leucine Zipper-like Transcription Regulator 1 (LZTR1), a substrate adapter of the Cullin-3 RING E3 ubiquitin ligase, binds specific RAS GTPases and promotes their ubiquitination and proteasomal degradation. We present structures of LZTR1 Kelch domains bound to RIT1, MRAS, and KRAS, revealing interfaces that govern RAS isoform selectivity and nucleotide specificity. Biochemical and structural analyses of disease-associated Kelch domain mutations revealed three types of alterations: impaired substrate interaction, loop destabilization, and blade-blade repulsion. In cellular and mouse models, mutations disrupting substrate binding phenocopied LZTR1 loss, underscoring its substrate specificity. These findings define RAS recognition mechanisms by LZTR1 and suggest a molecular glue strategy to degrade oncogenic KRAS.

The activation and inactivation of RAS guanosine triphosphatases (GTPases) are tightly regulated processes that involve cycling between the active, GTP-bound state and the inactive, guanosine diphosphate (GDP)–bound state (*1*). Guanine nucleotide exchange factors (GEFs) such as SOS catalyze GTP loading to promote the active conformation of RAS, enabling its interaction with effector proteins (*2*). These interactions drive critical downstream signaling pathways, including the mitogen-activated protein kinase (MAPK) (RAF-MEK-ERK) and phosphatidylinositol 3-kinase (PI3K) pathways, which control fundamental cellular processes such as proliferation and growth (*3*, *4*). Inactivation occurs through the slow intrinsic hydrolysis of GTP to GDP, a process accelerated in cells by GTPase-activating proteins (GAPs) such as neurofibromin (*5*). Dysregulation of this cycle, either through increased GTP loading or reduced GAP activity, results in aberrant RAS signaling, a hallmark of numerous human diseases, in particular cancer (*6*).

The substrate adapter protein Leucine Zipper-like Transcription Regulator 1 (LZTR1) regulates RAS protein abundance through ubiquitination and subsequent proteasomal degradation (*7*–*9*). The RAS GTPases RIT1 and MRAS and, to a lesser extent, the canonical RAS isoforms HRAS, KRAS, and NRAS, bind LZTR1 through its N-terminal Kelch domain (*7*–*9*) (Fig. 1A). Ubiquitin transfer occurs through the Cullin3-RING E3 ubiquitin ligase (CLR3) complex, which interacts with the C-terminal BTB (Broad complex, Tramtrack, and Bric-à-brac) and BACK (BTB and C-terminal Kelch) domains of LZTR1 (*7*–*10*). Pathogenic loss-of-function variants in *LZTR1* are associated with Noonan syndrome (NS), LZTR1-related schwannomatosis (SWN), and various human cancers and lead to RAS protein accumulation and dysregulated downstream signaling pathways (*11*–*14*).

[1]National Cancer Institute RAS Initiative, Cancer Research Technology Program, Frederick National Laboratory for Cancer Research, Frederick, MD, USA. [2]Department of Biochemistry and Molecular Pharmacology, NYU Grossman School of Medicine, New York, NY, USA. ***Corresponding author. Email: Pau.Castel@nyulangone.org (P.C.); Dhirendra.Simanshu@nih.gov (D.K.S.)** †These authors contributed equally to this work. ‡Present address: MRC Laboratory of Medical Sciences, London, UK.

Nucleotide- and isoform-specific recognition of RAS GTPases by LZTR1

To investigate the nucleotide state and isoform specificity of LZTR1, we used isothermal titration calorimetry (ITC) to quantify the binding affinities of the LZTR1 Kelch domain for RIT1, MRAS, and the canonical HRAS, KRAS, and NRAS proteins in the GDP-bound and the nonhydrolyzable GTP analog 5′-guanylyl imidodiphosphate (GMPPNP)–bound states (fig. S1A). All tested RAS GTPases bound LZTR1 exclusively in the GDP-bound form, with no detectable interaction in the GMPPNP-bound state (fig. S1, A and B). LZTR1 displayed stronger binding to GDP-bound RIT1 and MRAS [dissociation constant (K_D) ~4 to 5 μM] compared with the canonical RAS isoforms (K_D ~20 μM). These findings confirm the preferential recognition of LZTR1 for RIT1 and MRAS over the canonical RAS isoforms and highlight that subtle structural differences between GDP- and GTP-bound RAS isoforms contribute to this differential affinity.

Initial attempts to crystallize the LZTR1-RIT1 complex were unsuccessful, likely because of the presence of predicted disordered regions in the LZTR1 Kelch domain, including the first 50 residues and a 55-residue loop between the fifth and sixth Kelch motifs (fig. S1C). This disordered loop contains an RVxF motif, which is proposed to interact with the catalytic domain of protein phosphatase 1B (PP1CB) (*15*). However, ITC experiments revealed no detectable binding between LZTR1 and either PP1CA or PP1CB (fig. S1, B and D). This disordered loop is encoded by a single exon (exon 10) unique to mammals, indicating a recent evolutionary insertion. Its amino acid sequence is highly variable across mammals, with the RVxF motif conserved only in humans and certain great apes (fig. S1E).

To overcome the challenges posed by these disordered regions, we generated a truncated LZTR1 construct lacking the first 49 residues and the 55-residue loop [LZTR1(50-422, Δ331-382), referred hereafter as LZTR1]. This construct retained binding to GDP-bound RIT1, MRAS, HRAS, KRAS, and NRAS with affinities comparable to those of the full-length LZTR1 Kelch domain and showed no binding to GMPPNP-bound RAS proteins (Fig. 1B and fig. S2). The removed regions appeared to be dispensable for RAS binding and did not affect the selectivity of LZTR1 for GDP-bound RAS isoforms.

Crystal structures of LZTR1-RAS complexes

The structures of LZTR1 bound to GDP-loaded RIT1 and MRAS were determined at 2.95 and 2.80 Å, respectively (Fig. 1, C and D, and table S1). Attempts to crystallize the KRAS(GDP)-LZTR1 complex were unsuccessful because of its weaker affinity compared with RIT1 and MRAS. To improve KRAS affinity for LZTR1, we tested several KRAS mutants. Analyzing key interacting residues at the RIT1-LZTR1 interface (discussed later) revealed that KRAS mutations T35A/S (equivalent to T53 in RIT1) and the substitutions of E62 and H95 in KRAS to their equivalent residues in RIT1 enhanced KRAS binding to LZTR1 (fig. S3A). Specifically, the T35A and E62A mutations in KRAS increased its affinity for LZTR1 by threefold (K_D ~8 μM) and eightfold (K_D ~2 μM), respectively (Fig. 1F and fig. S3B). The KRAS-T35A/E62A double mutant (K_D ~2 μM) formed a stable complex with LZTR1 and crystallized, resulting in a structure at 3.30-Å resolution (Fig. 1G and table S1).

The overall structures of RIT1, MRAS, and KRAS bound to LZTR1 were highly similar, with superimpositions by the Cα atoms yielding low root mean square deviation (RMSD) values ranging from 0.52 to 0.65 Å (fig. S4A). All three RAS GTPases adopted the classic G-domain fold, consisting of six β-strands forming a single β-sheet surrounded by five α-helices. The LZTR1 Kelch domain was composed of six Kelch motifs, each containing four antiparallel β-strands. These motifs were circularized to form a β-propeller fold shaped like a truncated cone, with a central channel

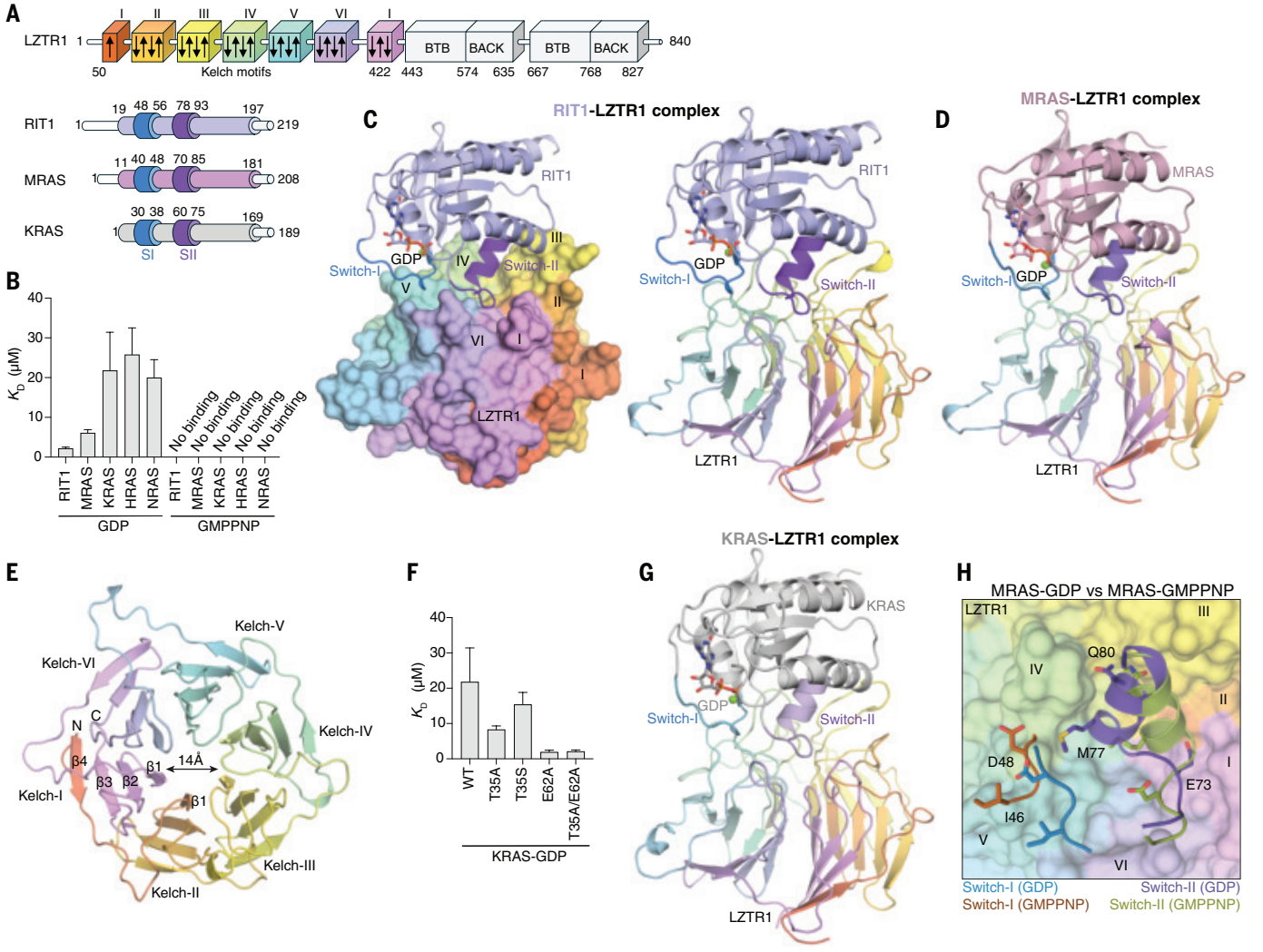

Fig. 1. Structural basis for LZTR1 interactions with GDP-bound RAS proteins. (**A**) Domain architecture of LZTR1 and the RAS GTPases RIT1, MRAS, and KRAS analyzed in this study. Biophysical and structural studies focused on the N-terminal Kelch domain of LZTR1. RIT1 and MRAS contain 11 and 10 additional N-terminal residues, respectively, compared with KRAS, requiring residue numbering adjustments to identify equivalent switch residues for comparison. (**B**) Bar graph comparing the binding affinities (K_D) of LZTR1 with RAS family members RIT1, MRAS, KRAS, HRAS, and NRAS in their GDP- and GMPPNP-bound forms. Error bar indicates errors of the fit. (**C**) Overall structure of RIT1(GDP) in complex with LZTR1 shown as a cartoon representation. (**D**) Overall structure of MRAS(GDP) in complex with LZTR1 shown as a cartoon representation. The individual Kelch motifs of LZTR1 and the switch regions of RIT1 and MRAS use the same color coding as in (A). (**E**) Top view of LZTR1 with Kelch motifs and blades numbered from the RIT1-LZTR1 structure. (**F**) Bar graph comparing the binding affinities of LZTR1 with wild-type KRAS and its T35A, E62A, and double-mutant (T35A/E62A) variants, highlighting the effects of these mutations on binding. Error bar indicates error of the fit. (**G**) Overall structure of KRAS-T35A/E62A(GDP) in complex with LZTR1 shown as a cartoon representation. (**H**) Structural superposition of MRAS-GMPPNP (PDB: 9B4R, cartoon representation) onto MRAS-GDP (cartoon representation) bound to LZTR1 (surface representation) highlighting the distinct conformations of the switch regions and elucidating the structural basis for LZTR1's specificity for GDP-bound MRAS.

connecting the two faces of the structure (Fig. 1, C and E). The channel is closed at the narrower end by residue N230 of the β-propeller but remains open at the wider end. The β-propeller is stabilized through a "Velcro" closure mechanism, common in other β-propeller proteins (*16*). The first Kelch motif of LZTR1 was formed by a β-strand from the N terminus and three β-strands from the C terminus (1+3 mechanism) (Fig. 1E). The β-propeller had a diameter of ~55 Å, a height of ~40 Å, and an average central channel diameter of ~14 Å (fig. S4B). To investigate the structural changes in RAS GTPases upon LZTR1 binding, we compared the free and LZTR1-bound structures of GDP-bound RIT1, KRAS, and MRAS. Although the switch-I region showed minimal conformational changes, the switch-II region underwent rearrangements upon LZTR1 binding, likely enhancing the structural complementarity and stability of the RAS-LZTR1 complex (fig. S4C).

To gain structural insight into the specificity of LZTR1 for GDP-bound RAS GTPases, we conducted a comparative analysis using GMPPNP-bound structures available for MRAS and KRAS. The presence of the γ-phosphate in these GTP analog–bound structures induced conformational changes in the switch-I and switch-II regions. These changes altered the spatial orientation and dynamics of the switch regions, rendering them incompatible with the binding interface required for interaction with LZTR1 (Fig. 1H and fig. S5A). This structural incompatibility underpins the strict preference of LZTR1 for the GDP-bound state of RAS GTPases.

Given that LZTR1 has the highest binding affinity for RIT1, we characterized the interaction interface using the RIT1-LZTR1 complex structure (details of the MRAS- and KRAS-LZTR1 interfaces are provided in fig. S5B). The interface included switch-I (residues 48 to 56) and switch-II (residues 78 to 93) of RIT1, burying ~2200 Å^2 of surface area and stabilizing the complex through 15 hydrogen bonds and four salt bridges by contacting all six Kelch motifs and occluding the central channel of LZTR1 (Fig. 2, A and B). Residues 51 to 56 of switch-I interacted with Kelch motifs IV to VI and

connecting loops, forming five hydrogen bonds and van der Waals (vdW) contacts (Fig. 2C), whereas switch-II engaged Kelch motifs I to IV, contributing 10 hydrogen bonds and additional contacts (Fig. 2, D and E). Alanine scanning of key RIT1 residues (I54, D56 in switch-I; E81, M85, and Q88 in switch-II) and LZTR1 residues (Y119, N143, N230, and R283) at the interface, in combination with ITC, pulldown, and degradation assays, confirmed their critical roles in complex formation (Fig. 2, F to K, and figs. S6 and S7).

RIT1-, MRAS-, and KRAS-LZTR1 complexes showed a conserved binding mode despite minor differences in interface residues among these RAS GTPases. The LZTR1-interacting residues in RIT1 were conserved in either MRAS or KRAS, resulting in similar contacts and buried surface area (Fig. 2, L to N). Structural and mutational analyses indicated that distinct binding affinities arose due to subtle variations in interacting residues and switch dynamics, highlighting the molecular interplay

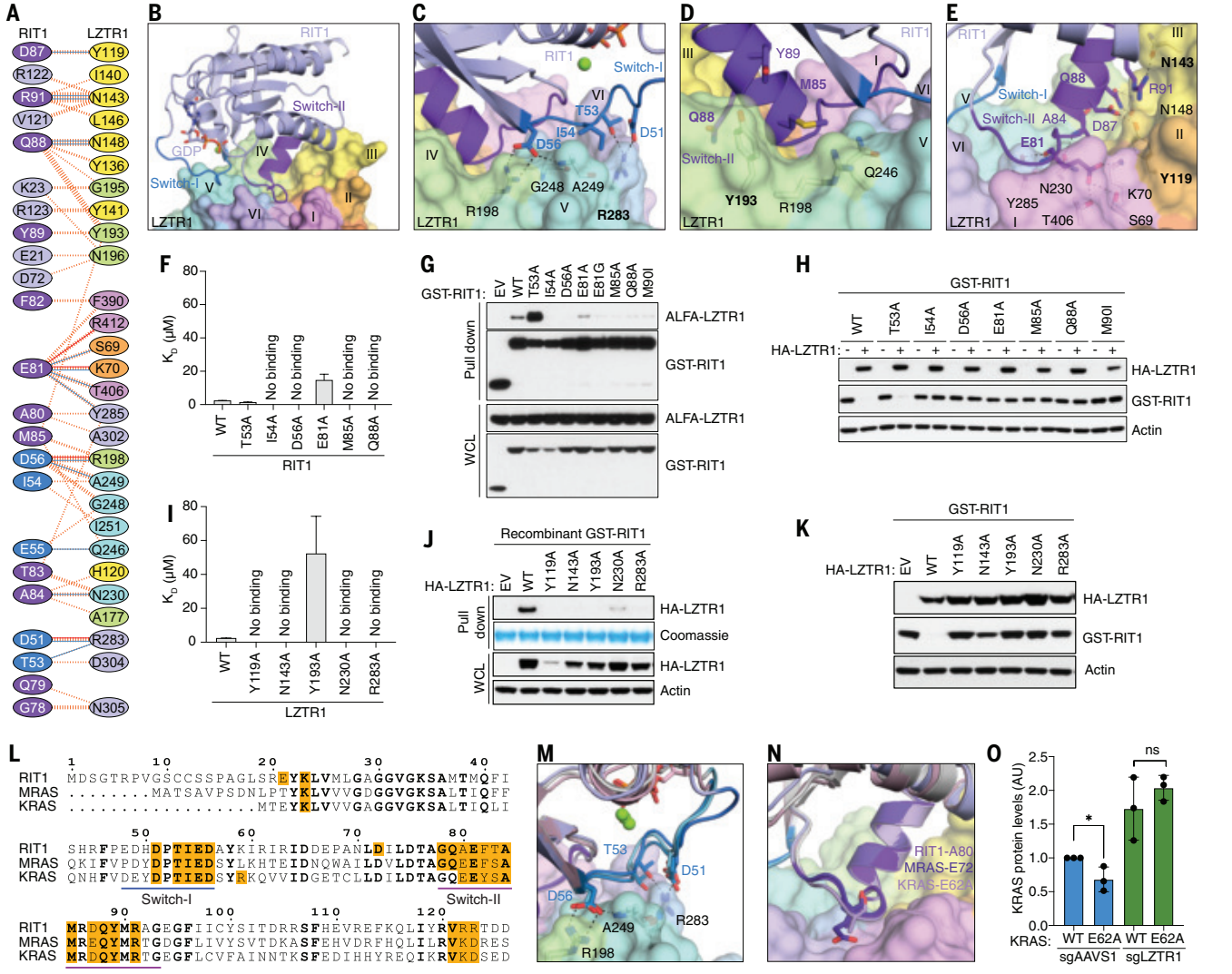

Fig. 2. Molecular basis of RIT1-LZTR1 interactions. (**A**) Schematic overview of the RIT1-LZTR1 interaction interface. The lines represent different types of interactions. Hydrogen bonds are shown in solid blue, salt bridges in solid red, and nonbonded contacts in striped orange, with the width of the striped lines proportional to the number of atomic contacts. (**B**) Enlarged view of the RIT1-LZTR1 complex showing the interaction interface, with Kelch motifs (surface) and RIT1 switch regions (cartoon) color-coded as in Fig. 1A. (**C**) Magnification of the interactions between the switch-I region of RIT1 (cartoon) and the Kelch IV and V motifs of LZTR1 (surface). (**D**) Detailed view of the α2-helix in the switch-II region of RIT1 (cartoon) interacting with the Kelch IV motif of LZTR1 (surface). (**E**) Interaction interface highlighting the switch-II region of RIT1 (cartoon) and the Kelch I, II, and III motifs of LZTR1 (surface). Hydrogen bonds and salt bridge interactions are depicted as dashed lines. (**F**) Bar graph showing the binding affinity (K_D) measured using ITC for point mutants of RIT1(GDP) interface residues with LZTR1. Error bar indicates error of the fit. Residues mutated to alanine are in bolded in (C) to (E). (**G**) Immunoblot of proteins in lysates and glutathione pulldowns from 293T LZTR1-ALFA cells ectopically expressing GST-fused RIT1 mutants. WCL, whole-cell lysates. (**H**) Immunoblot of indicated proteins from a cell-based degradation assay coexpressing GST-tagged RIT1 mutants and HA-LZTR1 in 293T cells. (**I**) Bar graph showing the binding affinity (K_D) measured using ITC for point mutants of LZTR1 interface residues with RIT1(GDP). Error bar indicates error of the fit. (**J**) Representative immunoblot and Coomassie staining of in vitro pulldown assays between recombinant GST-RIT1 and lysates from 293T cells ectopically expressing the indicated HA-LZTR1 mutations. (**K**) Immunoblot of indicated proteins from a cell-based degradation assay coexpressing GST-tagged RIT1 and indicated HA-LZTR1 mutations in 293T cells. (**L**) Sequence alignment of RIT1, MRAS, and KRAS, with LZTR1-interacting residues highlighted in brown. Fully conserved residues among the three GTPases are shown in bold, and residues within the switch regions are underlined below the alignment. EV, empty vector. (**M**) Structural superposition of RIT1, MRAS, and KRAS complexes with LZTR1, highlighting similarities and subtle differences in the conformations of switch-I. RAS GTPases are shown as cartoons, and LZTR1 is shown as a surface representation. (**N**) Structural superposition of RIT1, MRAS, and KRAS complexes with LZTR1, highlighting similarities and subtle differences in the conformations of switch-II. RAS GTPases are shown as cartoons, and LZTR1 is shown as a surface representation. (**O**) Quantification of KRAS protein levels in HEK293T-Flp-In cells stably expressing KRAS WT or E62A in the presence (sg*AAVS1*) or absence (sg*LZTR1*) of *LZTR1* ($n = 3$). Data were analyzed by Student's *t* test.

governing LZTR1 interactions. Key findings included enhanced LZTR1 binding by the equivalent RIT1-T53A and KRAS-T35A mutations. ^{31}P nuclear magnetic resonance studies showed that the T35A mutation in GTP-bound KRAS induced an alternative switch-I conformation (state 1), which disrupted effector binding (*17*–*19*). The KRAS-T35A mutation likely increases switch-I flexibility even in the GDP-bound state, resulting in enhanced LZTR1 binding. Additionally, residues distal to the interface, such as KRAS-H95E located near the switch-II region, appear to have important roles, because this mutation, mimicking RIT1, enhanced binding to LZTR1 likely by affecting switch-II dynamics (fig. S3A). The KRAS-E62A mutation, mimicking the corresponding residue in RIT1, resulted in increased binding to LZTR1 and degradation in cells (fig. S8). This reduction was reversed by knocking out *LZTR1*, which further confirms that higher affinity for LZTR1 leads to increased KRAS degradation (Fig. 2O and fig. S3A).

Role of disease-associated RIT1 and LZTR1 mutations

Several pathogenic *RIT1* variants have been identified in NS, a common RASopathy caused by hyperactivation of the RAS-mediated MAPK pathway, as well as in cancer (*20*, *21*). These variants are primarily located in the interswitch or switch-II regions (Fig. 3A). We tested their ability to bind LZTR1 and found that the F82L, T83P, and M90I mutations abolished binding (Fig. 3B and fig. S9). F82L and T83P disrupted critical vdW interactions with LZTR1, and M90I likely altered the position of nearby F82, indirectly impairing binding (Fig. 3A). By contrast, other RIT1 NS mutations, including A57G, Y89H, and Q79L (equivalent to KRAS Q61L), retained wild-type binding affinity for LZTR1 as measured by ITC. However, in cells, these mutations render RIT1 predominantly GTP-bound, likely due to increased nucleotide exchange rates and reduced intrinsic hydrolysis, thus preventing interaction with LZTR1 (*7*, *22*–*24*).

Several germline pathogenic *LZTR1* variants have been identified in individuals with NS or SWN. To understand the mechanisms underlying LZTR1 variant pathogenesis, we curated 25 Kelch domain missense variants associated with NS or SWN and screened them for their ability to bind recombinant RIT1 (or MRAS) and promote their degradation in cells (Fig. 3, C to F, and fig. S10). Of the 25 variants, 18 failed to bind RIT1 or MRAS and did not induce degradation (Fig. 3, E and F). Four variants (R267H, P281L, R294L, and R412C) showed reduced binding and partial RIT1 degradation, whereas three variants (A116V, R170Q, and E217A) retained RIT1 binding and promoted its degradation (Fig. 3, E and F). R170Q and E217A mutations likely cause splice-site defects leading to missplicing and nonsense-mediated mRNA decay. To further validate these findings, we analyzed five

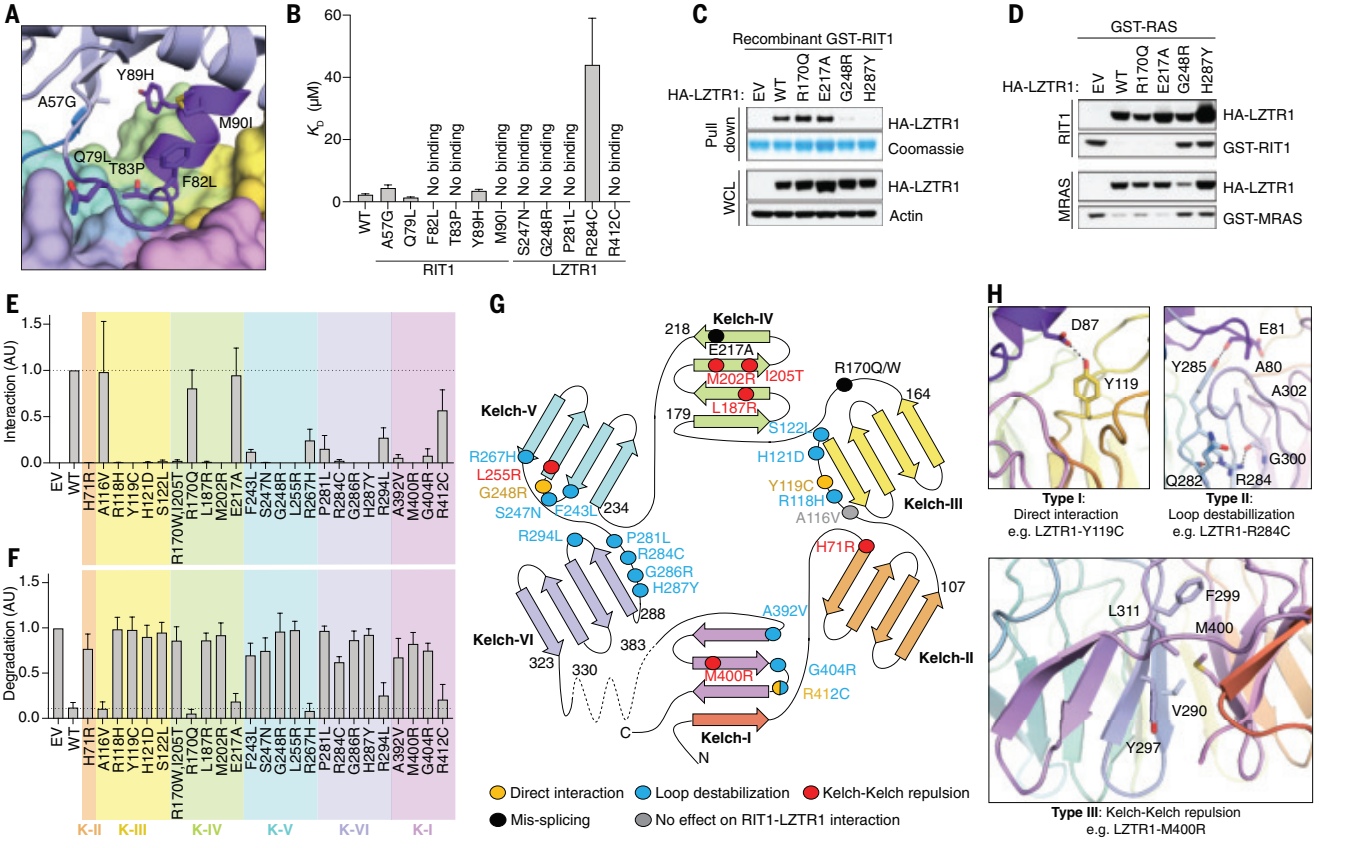

Fig. 3. Mechanistic insights into LZTR1 disease-associated variants. (**A**) Enlarged view of the RIT1-LZTR1 interaction interface showing the switch-II residues mutated in NS. (**B**) Bar graph showing the impact of disease-associated mutations in RIT1 and LZTR1 on their binding affinities. Error bar indicates error of the fit. (**C**) Representative immunoblot and Coomassie staining of in vitro pulldown assays used to assess the effects of disease-associated variants on RIT1 and MRAS binding. GST-RIT1 and lysates from 293T cells ectopically expressing the indicated HA-LZTR1 variants (two that lead to loss of function and two that show no effect in this assay are shown). (**D**) Immunoblot of the indicated proteins from a cell-based degradation assay used to assess the effects of LZTR1 disease-associated variants on RIT1 and MRAS degradation. Shown are 293T cells coexpressing GST-tagged RIT1 or MRAS and HA-LZTR1 variants (two that lead to loss of function and two that had no effect in this assay). (**E**) RIT1 interaction assay with the indicated HA-LZTR1 variants. Densiometric quantification and normalization to LZTR1 wild-type binding to recombinant GST-RIT1 were used to assess the effect of each variant ($n = 3$). AU, arbitrary units. Error bar indicates SEM. (**F**) In-cell RIT1 degradation assay with the indicated HA-LZTR1 variants. Densiometric quantification and normalization to GST-RIT1 coexpressed with EV were used to analyze the effect of each variant ($n = 3$). Error bar indicates SEM. (**G**) Schematic representation of loss-of-function mechanisms for LZTR1 mutations based on the LZTR1-RIT1 structure. (**H**) Enlarged view of the RIT1-LZTR1 complex illustrating the loss-of-function mechanisms of LZTR1 mutations. Type I mutations disrupt direct interactions with RIT1. Type II mutations destabilize Kelch loops essential for RIT1 binding. Type III mutations disrupt hydrophobic Kelch-Kelch interfaces, altering loop conformations required for RIT1 engagement.

LZTR1 mutations (S247N, G248R, P281L, R284C, and R412C) by ITC with recombinant proteins (Fig. 3B and fig. S11). Four variants showed no binding to RIT1, including P281L and R412C, which retained reduced binding in our cellular assay; R284C exhibited a reduced binding affinity.

Leveraging our LZTR1-RIT1 structure, we mapped these 25 missense mutations and identified three mechanistic types for their loss of function (Fig. 3G). Type I mutations directly disrupted LZTR1-RIT1 interactions by breaking hydrogen bonds or vdW contacts or by introducing steric clashes, as seen with Y119C, G248R, and R412C (Fig. 3H). Type II mutations indirectly disrupted RIT1 binding by destabilization of LZTR1 binding loop conformations. This disruption, exemplified by R284C, prevented proper engagement by destabilizing key loop interactions (Fig. 3H). Type III mutations introduced charged residues between the hydrophobic Kelch motifs and destabilized the Kelch domain, as seen with M400R (Fig. 3H).

The type 1 mutation G248R phenocopies LZTR1 loss

Among NS-associated LZTR1 variants, G248R is the most common and segregates in an autosomal-dominant manner (*11*). LZTR1-G248 is buried at the RIT1-binding interface, and substitution with a long arginine introduced steric clashes with RIT1-D56 (Fig. 4A). Therefore, we selected this type I variant for further characterization because it can serve as a proof-of-concept experimental model to assess the effects of disrupting the LZTR1-RIT1 interaction in vivo. We established isogenic knock-in cells containing this mutation either in heterozygosity (GR/+) or homozygosity (GR/GR). Time-course growth factor stimulation experiments with epidermal growth factor (EGF) showed increased MAPK signaling in both GR/GR and *LZTR1* knockout cells (Fig. 4, B and C). We further analyzed proteome changes in these cells using quantitative mass spectrometry. In GR/GR and knockout cells, RIT1 abundance was significantly increased; however, knockout cells also showed elevated levels of several other proteins (Fig. 4D, fig S12, and data S1). These findings show that in our cellular model, LZTR1-G248R failed to recognize and degrade its physiological substrate, RIT1.

In mice, *Lztr1* deletion causes embryonic lethality due to vascular defects, cardiac abnormalities, and liver apoptosis (*7*, *9*, *25*–*27*). Therefore, we assessed whether disruption of the LZTR1-RIT1 interaction by G248R would phenocopy LZTR1 deletion. We constructed a mouse allele that allows for the isogenic comparison of *Lztr1* loss ($Lztr1^{null}$) against the G248R mutation ($Lztr1^{G248R}$), which results from germline Cre recombination (fig. S13). We did not recover any homozygous $Lztr1^{null}$ mice

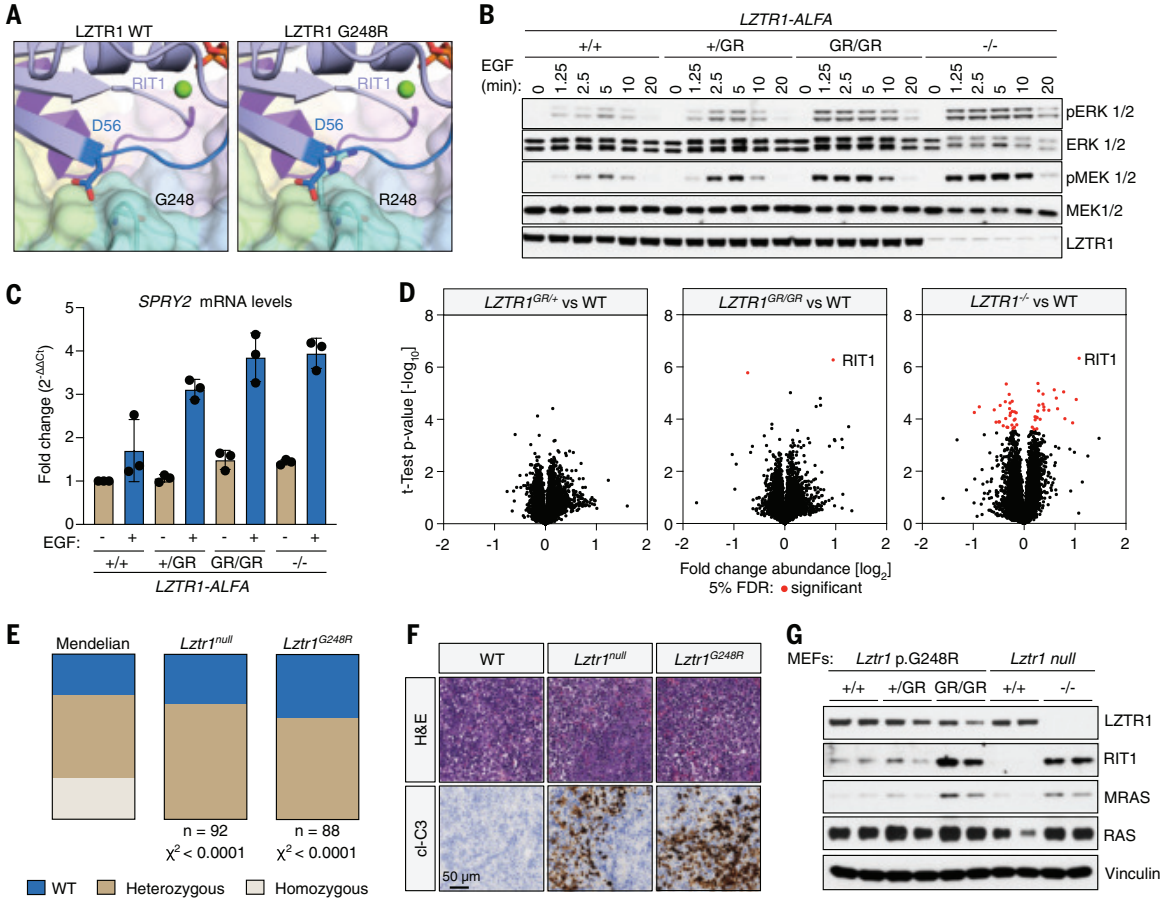

Fig. 4. The type I LZTR1 mutation G248R phenocopies LZTR1 loss in cells and mice. (**A**) Enlarged view of the RIT1-LZTR1 interface showing LZTR1 G248 (left) and its steric clash with RIT1 D56 upon mutation to arginine (right). (**B**) Immunoblot of the indicated proteins in lysates from 293T LZTR1-ALFA cells wild-type (+/+), heterozygous (+/GR), homozygous G248R (GR/GR), and knockout (−/−) LZTR1 treated for the indicated times with 20 ng/ml EGF. (**C**) *SPRY2* mRNA levels assessed by quantitative polymerase chain reaction in cells from (B), treated for 2 hours with or without EGF (20 ng/ml) ($n = 3$). (**D**) Volcano plot obtained from TMT-based quantitative proteomics in lysates from 293T LZTR1-ALFA isogenic cells described in (B). Highlighted in red are proteins that were significantly up-regulated or down-regulated, as defined by $q \leq 0.05$ [false discovery rate (FDR) of <5%]. The most significantly up-regulated protein in GR/GR and −/− cells, RIT1, is labeled. Source data are provided in the supplementary materials (data S1). (**E**) Percentages of obtained genotypes upon weaning (21 days of age) the offspring of indicated heterozygous mutant intercrosses, using $Lztr1^{G248R}$ ($n = 88$) and $Lztr1^{null}$ ($n = 92$) mice. Estimated Mendelian rates are shown and were used to calculate the indicated Chi-square statistics. (**F**) Representative images of hematoxylin & eosin (H&E) and cleaved caspase-3 (cl-C3) immunohistochemistry staining in livers from embryonic day 16.5 embryos with the indicated genotypes. (**G**) Immunoblot of indicated proteins in lysates from embryonic day 13.5 primary MEFs derived from individual embryos with the indicated genotypes.

because of embryonic lethality; isogenic *Lztr1*^{G248R} mice also died as embryos (Fig. 4E). Further examination revealed that both *Lztr1*^{null} and *Lztr1*^{G248R} embryos died at similar ages and from similar causes, exhibiting hemorrhagic defects and severe liver apoptosis, as confirmed by cleaved caspase 3 staining (Fig. 4F). We isolated primary mouse embryonic fibroblasts (MEFs) from both *Lztr1*^{G248R} and *Lztr1*^{null} embryos and confirmed that RIT1 and MRAS levels were up-regulated in homozygotes (Fig. 4G). These results demonstrate that disrupting the LZTR1-RIT1 interaction phenocopies LZTR1 loss in both cellular and mouse models (*28*), highlighting the critical role of RAS GTPases as primary substrates of the LZTR1-Cullin3-RING E3 ubiquitin ligase complex (CRL3^{LZTR1}).

Discussion

We provide structural insights into the mechanisms by which LZTR1 selectively recognizes RAS GTPases in their GDP-bound state. Other studies have identified different RAS GTPases as substrates of CRL3^{LZTR1}, but our biophysical analyses revealed that RIT1 and MRAS bind LZTR1 with higher affinity than do canonical RAS proteins. Given that RIT1 deletion rescues several phenotypes associated with LZTR1 loss (*28*), RIT1 likely serves as the main physiological substrate for CRL3^{LZTR1}. However, despite their weaker binding affinity, canonical RAS proteins may still be regulated by CRL3^{LZTR1} through other factors such as subcellular localization and local concentration. If small pools of GDP-bound KRAS are subject to LZTR1 regulation, then oncogenic mutations that shift KRAS toward the GTP-bound state would lead to increased protein abundance and signaling.

Our structural analysis of RAS-LZTR1 complexes uncovers a binding mode for GDP-bound RAS proteins that is distinct from previously described interactions involving GEFs, GAPs, and effectors. SOS (GEF) catalyzes nucleotide exchange by binding nucleotide-free RAS at the catalytic site, where its preferential interaction with RAS-GDP destabilizes GDP and promotes its release, rendering RAS nucleotide free (*29*). RAS complexes with SOS (allosteric site), GAPs, and effectors are typically characterized by GTP-dependent binding, where GTP binding remodels the switch-I and switch-II regions to create a unique interface for GTP-specific recognition.

LZTR1 provides an example of a binding partner that specifically recognizes and stabilizes GDP-bound RAS by forming extensive contacts with switch-I and switch-II motifs. This configuration is incompatible with GTP-bound RAS because of steric clashes, which explains the strict GDP selectivity of LZTR1. Rho GTPases also interact with ubiquitin ligase complexes such as CRL3^{KCTD13}, which selectively binds GDP-bound RHOA, but structural data are not yet available (*30*).

Our findings further elucidate the functional consequences of disease-associated *LZTR1* variants, highlighting their impact on RAS degradation. Loss-of-function mutations, including frame shifts, deletions, and splicing defects, are commonly observed. Missense variants, predominantly located in the Kelch domain, can be categorized into three mechanistic types on the basis of our structure-function analysis. However, whether these mutation types correlate with phenotypic features in humans will require further study. Mutated residues that are at the binding interface (type I), such as the common NS-related G248R variant, phenocopy the LZTR1-null allele. This shows that RAS GTPases are likely the main substrates responsible for the phenotypes seen in LZTR1 knockout cells and mice.

Given the advances in RAS therapeutics and emerging resistance mechanisms, protein-targeted degradation has become a promising strategy to combat RAS-driven diseases (*31*). In this context, our structural and mutational insights into the LZTR1-KRAS interaction provide a framework for rational drug design. Certain mutations that enhance KRAS-LZTR1 affinity highlight the interaction interface as a blueprint for developing molecular glues that stabilize the LZTR1-RAS complex, promoting selective degradation of RAS oncoproteins. Targeting GDP-bound oncogenic RAS may offer an effective strategy, because a reduction in overall RAS levels suppresses oncogenic signaling from its GTP-bound form. KRAS oncoproteins are still susceptible to cycling and nucleotide exchange (*32*, *33*) and may be targetable by degradation strategies that deplete the GDP-bound pool, thereby impairing their oncogenic potential.

REFERENCES AND NOTES

1. D. K. Simanshu, D. V. Nissley, F. McCormick, *Cell* **170**, 17–33 (2017).
2. A. Hennig, R. Markwart, M. A. Esparza-Franco, G. Ladds, I. Rubio, *Biol. Chem.* **396**, 831–848 (2015).
3. K. Rajalingam, R. Schreck, U. R. Rapp, S. Albert, *Biochim. Biophys. Acta* **1773**, 1177–1195 (2007).
4. A. M. Mozzarelli, D. K. Simanshu, P. Castel, *Mol. Cell* **84**, 3163–3164 (2024).
5. K. Scheffzek, G. Shivalingaiah, *Cold Spring Harb. Perspect. Med.* **9**, a031500 (2019).
6. J. L. Bos, H. Rehmann, A. Wittinghofer, *Cell* **129**, 865–877 (2007).
7. P. Castel *et al.*, *Science* **363**, 1226–1230 (2019).
8. J. W. Bigenzahn *et al.*, *Science* **362**, 1171–1177 (2018).
9. M. Steklov *et al.*, *Science* **362**, 1177–1182 (2018).
10. T. Abe *et al.*, *Cell Death Differ.* **27**, 1023–1035 (2020).
11. G. L. Yamamoto *et al.*, *J. Med. Genet.* **52**, 413–421 (2015).
12. V. Frattini *et al.*, *Nat. Genet.* **45**, 1141–1149 (2013).
13. A. Piotrowski *et al.*, *Nat. Genet.* **46**, 182–187 (2014).
14. J. J. Johnston *et al.*, *Genet. Med.* **20**, 1175–1185 (2018).
15. I. Umeki *et al.*, *Hum. Genet.* **138**, 21–35 (2019).
16. V. Fülöp, D. T. Jones, *Curr. Opin. Struct. Biol.* **9**, 715–721 (1999).
17. M. Spoerner *et al.*, *J. Biol. Chem.* **285**, 39768–39778 (2010).
18. M. Spoerner, C. Herrmann, I. R. Vetter, H. R. Kalbitzer, A. Wittinghofer, *Proc. Natl. Acad. Sci. U.S.A.* **98**, 4944–4949 (2001).
19. M. Araki *et al.*, *J. Biol. Chem.* **286**, 39644–39653 (2011).
20. Y. Aoki *et al.*, *Am. J. Hum. Genet.* **93**, 173–180 (2013).
21. A. H. Berger *et al.*, *Oncogene* **33**, 4418–4423 (2014).
22. H. Shao, K. Kadono-Okuda, B. S. Finlin, D. A. Andres, *Arch. Biochem. Biophys.* **371**, 207–219 (1999).
23. K. Sakabe *et al.*, *FEBS Lett.* **511**, 15–20 (2002).
24. Z. Fang *et al.*, *J. Biol. Chem.* **291**, 15641–15652 (2016).
25. R. N. Sewduth *et al.*, *Circ. Res.* **126**, 1379–1393 (2020).
26. T. Abe *et al.*, *JCI Insight* **9**, e182382 (2024).
27. S. Chen *et al.*, *Cancer Discov.* **12**, 2434–2453 (2022).
28. A. Cuevas-Navarro *et al.*, *eLife* **11**, e76495 (2022).
29. M. C. Burns *et al.*, *Proc. Natl. Acad. Sci. U.S.A.* **111**, 3401–3406 (2014).
30. Y. Chen *et al.*, *Mol. Cell* **35**, 841–855 (2009).
31. J. Popow *et al.*, *Science* **385**, 1338–1347 (2024).
32. J. J. Kwon *et al.*, bioRxiv, (2024).
33. P. Lito, M. Solomon, L. S. Li, R. Hansen, N. Rosen, *Science* **351**, 604–608 (2016).

ACKNOWLEDGMENTS

We thank W. Gillette, H. Ambrose, J. Cregger, J.-P. Denson, P. H. Frank, N. Granato-Guerrero, C. Grose, K. Hanson, B. Higgins, M. Hong, J. Hull, T. Lohneis, S. Mackay, J. Mehalko, A. Mitchell, S. Perkins, I. Poon, N. Ramakrishnan, K. Geis, J. A. Sánchez Hernández, M. Sherekar, M. Smith, K. Snead, T. Taylor, V. E. Wall, and S. R. T. Widmeyer for the production of protein reagents used in this work and T. Waybright for performing the nucleotide exchange analysis. **Funding:** This work is based upon research conducted at the NECAT beamlines, which are funded by the National Institute of General Medical Sciences of the National Institutes of Health (NIGMS/NIH grant P30 GM124165). The Eiger 16M detector on 24-ID-E is funded by the NIH Office of Research Infrastructure Programs [ORIP High-End Instrumentation (HEI) grant S10 OD021527]. This research used the resources of the Advanced Photon Source, a US Department of Energy (DOE) Office of Science User Facility operated for the DOE Office of Science by Argonne National Laboratory under contract no. DE-AC02-06CH11357, and was supported by an agreement between the Advanced Photon Source and the Diamond Light Source, the UK's national synchrotron science facility, located at the Harwell Science and Innovation Campus in Oxfordshire, where the work was performed under proposal AU34315-3 and by a grant from National Cancer Institute of the NIH (NCI grant R01 CA279171 to P.C.) and the Department of Defense Neurofibromatosis Research Program (grant HT94252310248 to S.M.). We thank the NYU Proteomics laboratory, which is supported in part by NYU Langone Health and the PerImutter Cancer Center support grant P30 CA016087 from NCI, for quantitative MS. This project was also funded in part with federal funds from the NCI/NIH (contract 75N91019D00024). The content of this publication does not necessarily reflect the views or policies of the Department of Health and Human Services, and the mention of trade names, commercial products, or organizations does not imply endorsement by the US Government. **Author contributions:** S.D., D.A.B., A.H.C., and D.K.S. performed structural and biophysical studies. S.P.M., A.F.-C., M.V., and P.C. conducted functional cellular and mouse experiments. S.M., M.D., and D.E. provided assistance with recombinant protein preparation. D.A.B., P.C., D.V.N., and D.K.S. conducted structural and functional analyses. P.C. and D.K.S. supervised the project. D.A.B., P.C., and D.K.S. wrote the manuscript with input from all authors. **Competing interests:** The authors declare no competing interests. **Data and materials availability:** The atomic coordinates and structure factors have been deposited into the Protein Data Bank and are available under accession numbers 9MEY [RIT1(GDP)-LZTR1 complex], 9MEZ [MRAS(GDP)-LZTR1 complex], 9MF0 [KRAS-T35A/E62A(GDP)-LZTR1 complex], and 9MF1 [RIT1(GDP)]. All data are available in the main text or the supplementary materials.

SUPPLEMENTARY MATERIALS

science.org/doi/10.1126/science.adv7088
Materials and Methods; Figs. S1 to S13; Table S1; References (*34*–*53*);
MDAR Reproducibility Checklist; Data S1

Submitted 3 January 2025; accepted 3 July 2025

10.1126/science.adv7088

ORGANOMETALLICS

A main-group metal carbonyl complex: Structure and isomerization to a carbene-stabilized tin atom

Maximilian Dietz, Andrey V. Protchenko, Agamemnon E. Crumpton, Surendar Karwasara, Matthew M. D. Roy, James Stewart-Moreno, Christiane Timmel, Simon Aldridge*

In contrast to transition elements, s- and p-block metal compounds that coordinate carbon monoxide (CO) under near-ambient conditions are elusive. Here, we report an isolable, crystalline main-group metal carbonyl complex and its isomerization to a carbene-stabilized metal atom. The stannylene $(Boryl)_2Sn$ [where Boryl is $B(NDippCH)_2$] coordinates CO reversibly, affording an isolable adduct below 0°C, which was characterized by x-ray crystallography. This complex rearranges at temperatures above 0°C to generate the stannavinylidene, (Boryl)(OBoryl)C=Sn, that is, a complex between the triplet carbene (Boryl)(OBoryl)C and monatomic Sn(0) in its electronic ground state.

Whereas molecules that feature tetravalent carbon represent the cornerstones of organic chemistry, divalent compounds such as carbenes (CR_2) and vinylidenes (CCR_2) are typically transient, highly reactive species (*1*). One key exception is the metastable compound carbon monoxide (CO), which is a critical feedstock for a wide range of industrial processes. Its interaction with transition metals is of primary importance to both large-scale extraction and purification processes (e.g., the Mond process) (*2*) and the catalytic production of commodity chemicals (e.g., carboxylic acids, esters, aldehydes, and hydrocarbon fuels) (*3*–*6*). A key factor that enables the interaction of CO with d-block metals is a frontier orbital manifold that promotes bonding in a synergistic fashion: σ donation from the lone pair of the CO molecule is accompanied by back-bonding, that is, the transfer of electron density from the metal into a higher energy π-symmetric orbital on the CO ligand. Stable transition metal carbonyl complexes typically involve substantial contributions from both bonding components (*7*).

Among compounds based on s- and p-block elements, the coordination of CO is much less common and is limited to lighter nonmetal or metalloid elements (B, C, Si, and P; Fig. 1) (*8*). Three-coordinate boranes can bind CO, provided that they are sufficiently Lewis acidic, with the CO molecule typically acting as a simple σ donor (e.g., **I**) (*9*–*20*). CO has also been used to trap highly reactive transient p-block species, such as in situ–generated silylenes and borylenes, in the form of adducts (e.g., **II** and **III**) (*21*–*24*). To date, however, the only isolable systems that can bind CO in the synergistic manner akin to that seen with transition metals are nonmetal boraallene, phosphinidene, and carbene systems (e.g., **IV** to **VI**), which make use of their ambiphilic (donor-acceptor) character and (in the latter case) carbon's distinctive capacity for C=C bond formation to bind CO in the form of a ketene (*25*–*28*). In stark contrast to their d-block counterparts, isolable main-group metal compounds that can coordinate CO are unknown, reflecting the weak nature of covalent bonding offered by s- and p-block cations (*29*).

Inorganic Chemistry Laboratory, Department of Chemistry, University of Oxford, South Parks Road, Oxford, UK. *Corresponding author. Email: simon.aldridge@chem.ox.ac.uk

An important challenge in designing a main-group metal system to bind CO is generating energy separation between the key frontier orbitals [typically the highest occupied molecular orbital (HOMO) and lowest unoccupied molecular orbital (LUMO)] that is wide enough for such a compound to be isolable yet narrow enough to permit chemically significant σ donation from (and π back-bonding to) the CO ligand (*8*). We have shown that the very strong σ donor properties of boryl ligands used within carbene-like p-block compounds can lead to a narrow HOMO-LUMO separation, owing to elevation of the HOMO. As such, diborylstannylene $(Boryl)_2Sn$ [**1**; where Boryl is $B(NDippCH)_2$ and Dipp is 2,6-$^{i}Pr_2$-C_6H_3 (^{i}Pr, isopropyl)], although stable at room temperature, has been shown to possess a narrow enough HOMO-LUMO energy separation to effect the activation of the H–H bond in dihydrogen (*30*, *31*).

In addition, here we show explicitly that **1** also possesses a low-lying LUMO, a feature that we hypothesized to be important in the binding of CO, given that σ donation is predicted to be the dominant component of main-group metal–carbonyl bonding (*32*). Accordingly, **1** reacts smoothly with potassium graphite in benzene in the presence of dibenzo-18-crown-6 to generate the room-temperature stable Sn(I) radical anion $[\mathbf{1}]^{\bullet-}$ (*33*). [K(dibenzo-18-crown-6)][**1**] has been characterized by x-ray crystallography and superconducting quantum interference device magnetometry in the solid state and by electron paramagnetic resonance (EPR) measurements in frozen solution (figs. S24 to S27 and S37), with the latter revealing occupancy by a single electron in a tin-centered orbital of predominantly $5p_z$ character (with 89.5% spin density at tin).

With this in mind, we surmised that the frontier orbital characteristics of **1** might be appropriate for the binding of CO at tin. Consistently, we show here that (i) **1** coordinates CO reversibly to give a structurally characterized main-group metal-carbonyl adduct of the type $(Boryl)_2Sn{\cdot}CO$, which is stable up to 0°C, and (ii) this system can transform CO into a carbene ligand capable of supporting a single metal atom without additional coligands.

Synthesis and characterization of a tin carbonyl complex

Exposure of a solution of **1** in hexane to excess CO (at –30°C and ~1 bar) leads to a rapid color change from deep green to red and quantitative conversion by multinuclear nuclear magnetic resonance (NMR) spectroscopy to a single new species, characterized by a symmetrical pattern of ^{1}H NMR signals (one Dipp CH; two Dipp CH_3 signals), a broad $^{13}C\{^{1}H\}$ NMR resonance at a chemical shift (δ_C) of 186.5 parts per million (ppm) and a ^{119}Sn resonance shifted upfield by ~5000 ppm compared to that of **1** (δ_{Sn} = –264 ppm compared with +4755 ppm) (*30*). Exposure to vacuum (~10^{-2} torr) leads to regeneration of **1**, thereby establishing the reversibility of CO coordination (Fig. 2A). The pattern of NMR

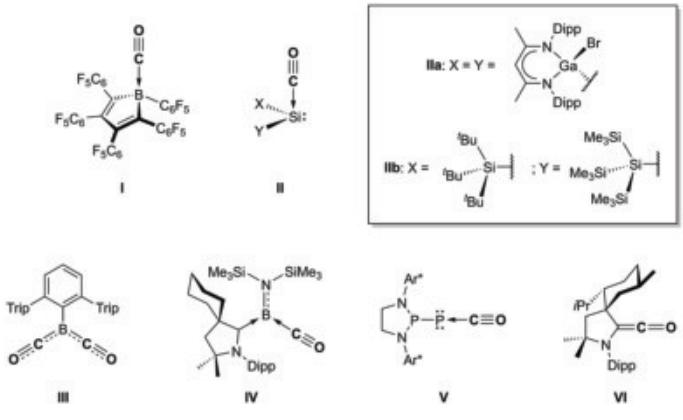

Fig. 1. Examples of existing carbonyl complexes of main-group elements relevant to the present study. Trip is 2,4,6-$^{i}Pr_3$-C_6H_2, and Ar* is 4-Me-2,6-$(CHAr_2)_2$-C_6H_2, where Ar is 4-^{t}Bu-C_6H_4. ^{t}Bu, *tert*-butyl.

signals is unchanged at temperatures up to 0°C, and the product $(Boryl)_2Sn{\cdot}CO$ (**2**) could be unambiguously characterized in the solid state by x-ray crystallography using crystals obtained from hexane at −30°C under a partial CO atmosphere (Fig. 2B).

Structural characterization of **2** shows that complexation involves relatively minor perturbations of both the CO and metal-containing fragments. The bond lengths and angles within the $(Boryl)_2Sn$ unit in **2** [d(Sn–B) = 2.291(2), 2.304(2) Å; ∠(B–Sn–B) = 118.1(1)°] are very similar to those found in **1** [2.285(7), 2.294(8) Å; 118.8(3)°] (*30*), and the CO bond length [1.123(3) Å] is not statistically distinct from that of free CO (1.128 Å) (*34*). The angle at carbon is slightly bent [∠(Sn–C–O) = 165.8(1)°], although quantum chemical calculations imply that the energetic penalty for bending within the range 150° to 180° is minimal (~1 kcal mol^{-1}; fig. S105). The orientation of the carbonyl ligand [∠(C–Sn–B) = 89.8(1), 91.3(1)°] implies donation of the CO lone pair into the LUMO of the $(Boryl)_2Sn$ unit, and the relatively long Sn–C bond [2.282(2) Å] compared with the sum of the respective covalent radii [1.39(4) + 0.69(1) Å] (*35*) presumably reflects, at least in part, the fact that this orbital is predominantly Sn $5p_z$ in character. This geometry is consistent with (i) the electronic structure of the radical anion $[\mathbf{1}]^{\bullet-}$, as revealed by EPR measurements, and (ii) the structure of the related ammonia adduct $\mathbf{1}{\cdot}NH_3$, which features a similar geometry and a relatively long bond to the donor atom [d(Sn–N) = 2.355(3) Å] (*31*).

Spectroscopically, infrared measurements on **2** reveal a strong band at 2016 cm^{-1}, which has been assigned by comparison with quantum chemical simulation (and with a band at 2070 cm^{-1} in the spectrum of the corresponding CNXyl adduct) to the CO stretching mode [figs. S28 and S31; Xyl is 2,6-Me_2-C_6H_3 (Me, methyl)]. This band can be compared with that of free CO (2143 cm^{-1}) and with those found at 1945 and 1908 cm^{-1} for the silicon carbonyl adducts **IIa** and **IIb**, respectively (*21*, *22*). These data imply substantially less n to π* back-bonding in the case of tin complex **2**, consistent with the observed reversible coordination of CO in **2**.

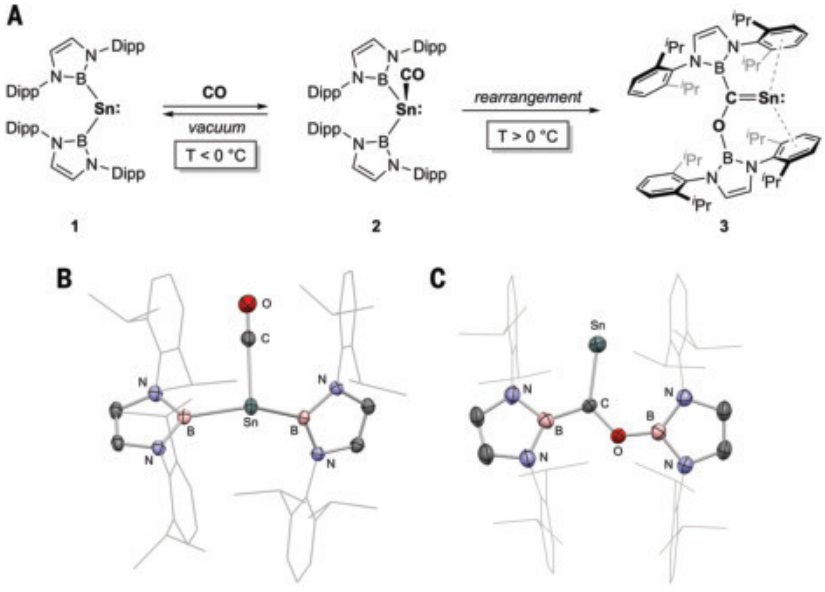

Fig. 2. Synthesis and structural characterization of compounds 2 and 3. (**A**) Synthesis and onward reactivity of tin carbonyl complex **2**. (**B**) Molecular structure of **2** in the solid state as determined by x-ray crystallography. Hydrogen atoms are omitted, and Dipp groups are shown in wireframe format for clarity; thermal ellipsoids are drawn at the 50% probability level. Key bond lengths (Å) and angles (°) are as follows: Sn–C 2.282(2), C–O 1.123(3), Sn–B 2.291(2), 2.304(2), C–Sn–B 89.8(1), 91.3(1), Sn–C–O 165.8(1), and B–Sn–B 118.1(1). (**C**) Molecular structure of **3** in the solid state as determined by x-ray crystallography. Hydrogen atoms and the second disorder component are omitted, and Dipp groups are shown in wireframe format for clarity; thermal ellipsoids are drawn at the 50% probability level. Key bond lengths (Å) and angles (°) are as follows: Sn–C 2.096(3), B–O 1.361(5), C–O 1.419(4), C–B 1.550(5), B–C–O 114.9(3), B–C–Sn 115.9(2), and O–C–Sn 129.2(2).

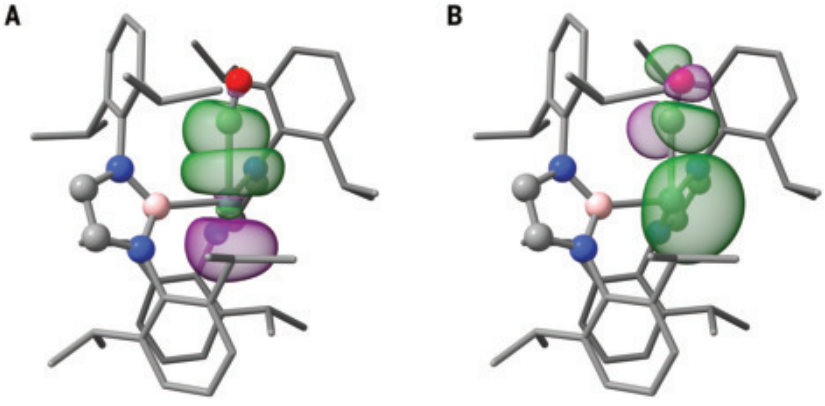

Fig. 3. NBO SOPT analysis for 2. (**A**) Electron donation from NBO 72 (CO σ donor orbital) into NBO 230 (Sn vacant orbital), with an interaction energy of 183.4 kcal mol^{-1}. (**B**) Electron donation from NBO 70 (Sn lone pair) into NBO 234 (CO π* system), with an interaction energy of 13.8 kcal mol^{-1} (a second n to π* back-bonding component involving the orthogonal CO π* orbital accounts for an additional 3.9 kcal mol^{-1}; see fig. S93). Green and purple overlay indicates the relative phases of the respective orbitals [isovalue: 0.05 arbitrary units (a.u.)].

Theoretical analyses

We further investigated the electronic structure of **2** by density functional theory (DFT) calculations (using the r2SCAN-3c composite method), which reproduced well the experimentally determined geometry and elucidated the nature of the metal-ligand interaction. The Wiberg bond index of 0.81 calculated for the Sn–C linkage is consistent with the (long) bond length determined crystallographically (and with relatively little π character), whereas that determined for the C–O bond is 2.14. Positive natural atomic charges were evaluated for the tin, carbon, and both boron centers (+0.36, +0.53, +0.50, and +0.51, respectively), with the carbonyl oxygen bearing a charge of −0.48. Quantum theory of atoms in molecules analysis revealed a bond critical point between Sn and C, with an associated electron density $\rho(r)$ of 0.510 e $Å^{-3}$ [Laplacian, $\nabla^2\rho(r) = +9.724$ e $Å^{-5}$]; the corresponding data for the C–O bond are 3.32 e $Å^{-3}$ and +17.887 e $Å^{-5}$, respectively (fig. S61). Comparison of these data with those reported for silicon compound **IIb** [e.g., $\rho(r)$ = 0.68 and 3.13 e $Å^{-3}$ for the Si–C and C–O bonds, respectively] is also reflective of less significant back-bonding for the tin complex (*22*). Consistently, although the HOMO of **2** has Sn–C π-bonding character and the LUMO corresponds to the corresponding π* orbital, these orbitals are noticeably polarized toward the tin and CO components, respectively (figs. S63 and S64). Second-order perturbation theory (SOPT) within natural bond orbital (NBO) analysis was used to quantify the primary orbital interactions between singlet $(Boryl)_2Sn$ and CO fragments. This approach identifies σ electron donation from a lone pair orbital at C to a lone valency orbital centered on Sn (possessing 97% p character) as contributing 183.4 kcal mol^{-1} to the overall interaction energy (Fig. 3A); electron donation from the Sn lone pair

to the CO π* system (n to π* back-bonding) accounts for only 17.7 kcal mol^{-1} (Fig. 3B and fig. S93). The overall free energy of binding of the CO molecule to **1** was calculated to be close to thermoneutral at −30°C (−0.1 kcal mol^{-1}) and marginally endergonic at room temperature (+0.9 kcal mol^{-1}), consistent with the experimentally observed reversible binding at 0°C and below (fig. S44) (*9*).

Rearrangement to a carbene-stabilized tin center

At temperatures above 0°C (in the absence of excess CO) (*36*), **2** rearranges to give a lower-symmetry compound featuring inequivalent boryl substituents, as shown by ^{1}H and ^{11}B NMR spectroscopy (e.g., distinct ^{11}B NMR signals at δ_B = 31.7 and 21.8 ppm). The product (**3**) could be crystallized from hexane as dark green plates, and its structure in the solid state was determined crystallographically (Fig. 2C). The molecular structure features a single tin atom bound to the carbon atom of a (Boryl)(BorylO)C unit through a short tin-carbon bond. The Sn–C distance [2.096(3) Å] is much shorter than that of typical single bonds, falling within the range of compounds described as having tin-carbon multiple bond character [e.g., 2.082(6) Å for a recently reported stannyne] (*37*). The ^{119}Sn-^{13}C coupling constant (748 Hz) also supports a model featuring tin-carbon multiple bonding. The tin center also engages in longer contacts with the ipso carbons of the diisopropylphenyl substituents of both the boryl and boryloxy groups [with Sn···C distances of 2.864(4) and 2.911(7) Å, respectively]. The positioning of the tin center between the aromatic π systems of two arene rings presumably underpins the high-field ^{119}Sn NMR signal measured for **3** (δ_{Sn} = +1651 ppm, compare with +4755 ppm for **1**) (*30*). Based on connectivity, **3** can therefore be viewed as a tin analog of vinylidene (:C=CH$_2$), [(*38*); see also (*39*)] or as a tin atom stabilized by a single boryl(boryloxy)carbene ligand. Although a range of elemental dimers, E$_2$, ligated by a pair of carbene ligands have been reported (including examples for which E is Si, Ge, and Sn) (*40*–*42*), mononuclear systems of this type are, to our knowledge, unknown for any metal.

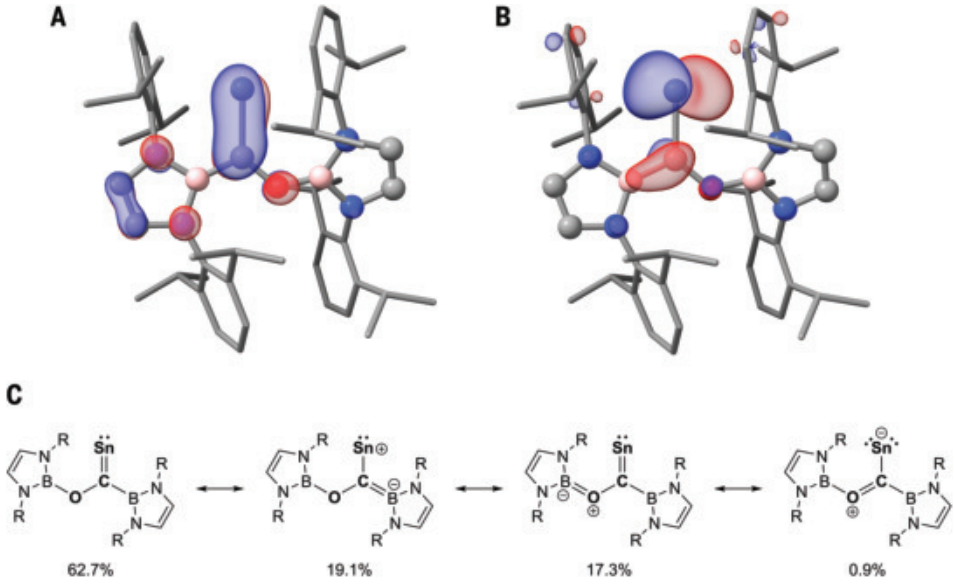

Fig. 4. Calculated orbitals and Lewis structures. (**A**) HOMO and (**B**) LUMO for **3**. (**C**) Predominant contributing resonance structures for **3** calculated by NRT. Blue and red overlay indicates the relative phases of the respective orbitals [isovalue: 0.05 arbitrary units (a.u.)].

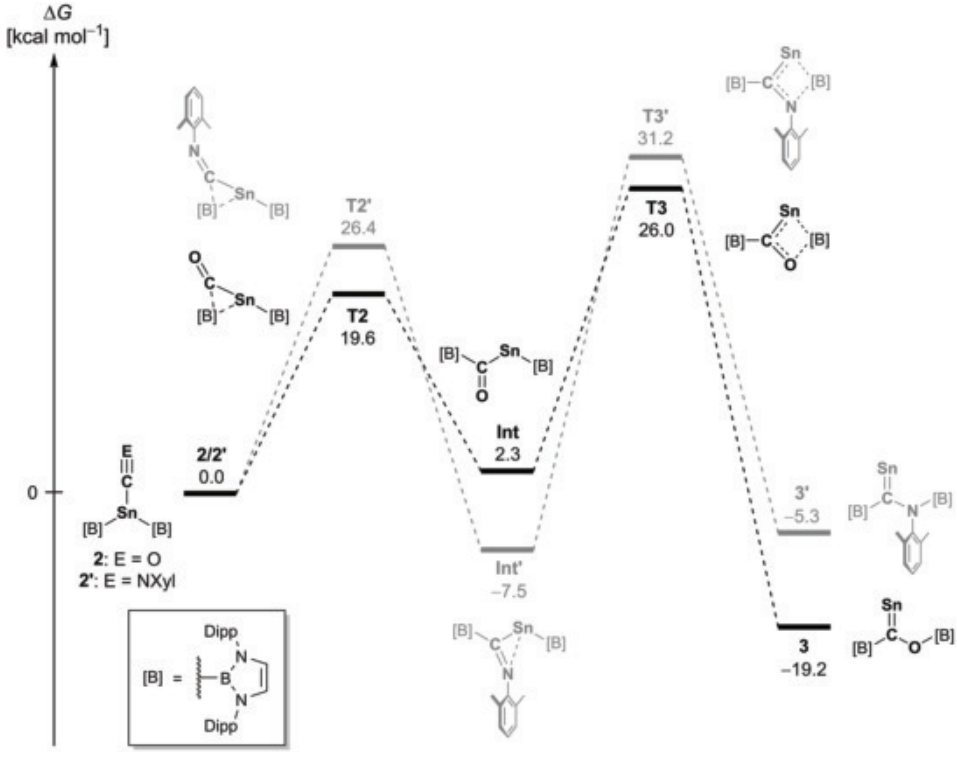

Fig. 5. DFT-calculated mechanism for the conversion of 2 to 3. Corresponding transformations originating from the isonitrile adduct (Boryl)$_2$Sn·CNXyl (**2'**) are shown in gray.

A description of the electronic structure of **3** based on a Sn=C double bond formed between a triplet carbene and a tin atom in its triplet (^{3}P) ground state is supported by a range of quantum chemical techniques. As such (i) the HOMO and LUMO show Sn=C π/π* character, respectively (Fig. 4, A and B); (ii) natural resonance theory (NRT) calculations show that the predominant resonance structures (totaling ~80%) are those featuring a Sn=C double bond (Fig. 4C); (iii) electron localization function analysis reveals two basins of electron density (containing 1.63 and 1.67 electrons), to which the contributions from the tin and carbon centers in each case are ~25% (Sn) and 75% (C) (fig. S60); and (iv) fragmentation of the Sn=C bond by the extended transition state–natural orbital for chemical valence approach reveals homolytic cleavage into triplet fragments to be the lowest-energy bond scission pathway (by ~40 kcal mol^{-1}; table S4), that is, akin to a classical Schrock carbene (*43*).

Finally, we probed the mechanism for the conversion of **2** into ***3*** by a combination of experimental and quantum chemical approaches. The lowest-energy pathway defined computationally (Fig. 5 and fig. S44) occurs through fundamental steps that are directly analogous to classical transition metal carbonyl chemistry.

After CO coordination, carbonyl adduct **2** undergoes a migratory insertion process involving one tin-bound boryl ligand to give boraacyl intermediate **Int** [via a transition state **T2** at a Gibbs free energy ($\Delta G^{\ddagger}$) of 19.6 kcal mol^{-1}]. Boraacyl compounds have precedent as isolable compounds in coordination chemistry (*44*, *45*), but in this case, onward conversion to stannavinylidene ***3*** is facile. In this step, B–O bond formation involving the remaining tin-bound boryl ligand occurs via a four-membered transition state and a local barrier height of 23.7 kcal mol^{-1}. The two steps leading to the conversion of **2** into ***3*** mimic classical Fischer carbene synthesis, for example, of $(OC)_5WC(Me)(OMe)$ from $W(CO)_6$, which occurs through sequential reactions of the CO ligand with nucleophilic and electrophilic carbon-containing reagents [(*46*); see also (*47*)]. In the case of main-group carbene complex ***3***, analogous processes involve nucleophilic then electrophilic transfer of the boron-containing ligands to C and O, respectively. Although we were unable to isolate bora(boraacyl) intermediate **Int**, the related chemistry carried out with xylyl isonitrile can be shown experimentally to proceed from the corresponding adduct $(Boryl)_2Sn{\cdot}CNXyl$ (**2′**) (*48*) to yield the analogous insertion compound (Boryl)Sn[C(NXyl)(Boryl)] (**Int′**) over 16 hours at room temperature. In this case, **Int′** could be isolated and characterized crystallographically (figs. S42 and S43), thereby providing further corroboration for the mechanistic pathway proposed for CO. In the case of the isonitrile system, onward conversion of **Int′** to yield a species analogous to ***3*** is calculated to be both endergonic and subject to a prohibitively high activation barrier through transition state **T3′**; consistently, no experimental evidence is found for the onward conversion of **Int′** to ***3′***, even under forcing conditions.

More than 150 years after the first report of a tractable d-block metal carbonyl complex (*49*), we report the synthesis of an isolable complex of this key ligand with a main-group metal. The subsequent rearrangement of $(Boryl)_2Sn{\cdot}CO$ demonstrates that such a system can access fundamental steps central to classical transition metal chemistry, in this case, to give a metal atom stabilized by a single carbene ligand.

REFERENCES AND NOTES

1. D. Bourissou, O. Guerret, F. P. Gabbaï, G. Bertrand, *Chem. Rev.* **100**, 39–92 (2000).
2. L. Mond, C. Langer, F. Quincke, *J. Chem. Soc. Trans.* **57**, 749–753 (1890).
3. J.-B. Peng, H.-Q. Geng, X.-F. Wu, *Chem* **5**, 526–552 (2019).
4. M. Beller, Ed., *Catalytic Carbonylation Reactions*, *Topics in Organometallic Chemistry*, vol. 18 (Springer, 2006).
5. F. Fischer, H. Tropsch, *Ber. Dtsch. Chem. Ges. B* **59**, 830–831 (1926).
6. A. Y. Khodakov, W. Chu, P. Fongarland, *Chem. Rev.* **107**, 1692–1744 (2007).
7. A. Diefenbach, F. M. Bickelhaupt, G. Frenking, *J. Am. Chem. Soc.* **122**, 6449–6458 (2000).
8. S. Fujimori, S. Inoue, *J. Am. Chem. Soc.* **144**, 2034–2050 (2022).
9. A. B. Burg, H. I. Schlesinger, *J. Am. Chem. Soc.* **59**, 780–787 (1937).
10. J. R. Spielman, A. B. Burg, *Inorg. Chem.* **2**, 1139–1145 (1963).
11. W. H. Knoth, *J. Am. Chem. Soc.* **89**, 4850–4852 (1967).
12. H. Jacobsen *et al.*, *Organometallics* **18**, 1724–1735 (1999).
13. J. C. Jeffery, N. C. Norman, J. A. J. Pardoe, P. L. Timms, *Chem. Commun.* **2000**, 2367–2368 (2000).
14. M. Finze *et al.*, *J. Am. Chem. Soc.* **124**, 15385–15398 (2002).
15. M. Gerken, G. Pawelke, E. Bernhardt, H. Willner, *Chemistry* **16**, 7527–7536 (2010).
16. A. Fukazawa *et al.*, *Chem. Sci.* **3**, 1814–1818 (2012).
17. H. Wang, L. Wu, Z. Lin, Z. Xie, *J. Am. Chem. Soc.* **139**, 13680–13683 (2017).
18. C. Chen *et al.*, *Angew. Chem. Int. Ed.* **59**, 21460–21464 (2020).
19. T. Heitkemper, C. P. Sindlinger, *Chemistry* **26**, 11684–11689 (2020).
20. A. E. Crumpton, C. McManus, S. Aldridge, *Angew. Chem. Int. Ed.* **64**, e202501774 (2025).
21. C. Ganesamoorthy *et al.*, *Nat. Chem.* **12**, 608–614 (2020).
22. D. Reiter, R. Holzner, A. Porzelt, P. Frisch, S. Inoue, *Nat. Chem.* **12**, 1131–1135 (2020).
23. H. Braunschweig *et al.*, *Nature* **522**, 327–330 (2015).
24. H. Braunschweig *et al.*, *J. Am. Chem. Soc.* **139**, 1802–1805 (2017).
25. F. Dahcheh, D. Martin, D. W. Stephan, G. Bertrand, *Angew. Chem. Int. Ed.* **53**, 13159–13163 (2014).
26. M. M. Hansmann, R. Jazzar, G. Bertrand, *J. Am. Chem. Soc.* **138**, 8356–8359 (2016).
27. V. Lavallo, Y. Canac, B. Donnadieu, W. W. Schoeller, G. Bertrand, *Angew. Chem. Int. Ed.* **45**, 3488–3491 (2006).
28. T. W. Hudnall, C. W. Bielawski, *J. Am. Chem. Soc.* **131**, 16039–16041 (2009).
29. X. Wu *et al.*, *Science* **361**, 912–916 (2018).
30. A. V. Protchenko *et al.*, *J. Am. Chem. Soc.* **134**, 6500–6503 (2012).
31. A. V. Protchenko *et al.*, *J. Am. Chem. Soc.* **138**, 4555–4564 (2016).
32. A. J. Lupinetti, G. Frenking, S. H. Strauss, *Angew. Chem. Int. Ed.* **37**, 2113–2116 (1998).
33. L. F. Lim *et al.*, *Angew. Chem. Int. Ed.* **61**, e202201248 (2022).
34. R. Gilliam, C. M. Johnson, W. Gordy, *Phys. Rev.* **78**, 140–144 (1950).
35. B. Cordero *et al.*, *Dalton Trans.* **2008**, 2832–2838 (2008).
36. In the presence of excess CO, an alternative product of composition $[(Boryl)_2Sn(CO)_3]_2$ is formed from **3** through CC homologation and boryl group migration, which has been investigated spectroscopically, crystallographically, and computationally (see figs. S38 and S41).
37. X.-F. Wang *et al.*, *Nat. Chem.* **16**, 1673–1679 (2024).
38. P. J. Stang, *Chem. Rev.* **78**, 383–405 (1978).
39. A. Rit, J. Campos, H. Niu, S. Aldridge, *Nat. Chem.* **8**, 1022–1026 (2016).
40. Y. Wang *et al.*, *Science* **321**, 1069–1071 (2008).
41. A. Sidiropoulos, C. Jones, A. Stasch, S. Klein, G. Frenking, *Angew. Chem. Int. Ed.* **48**, 9701–9704 (2009).
42. C. Jones, A. Sidiropoulos, N. Holzmann, G. Frenking, A. Stasch, *Chem. Commun.* **48**, 9855–9857 (2012).
43. W. A. Nugent, J. M. Mayer, *Metal Ligand Multiple Bonds* (Wiley-Blackwell, 1988).
44. R. Frank *et al.*, *J. Am. Chem. Soc.* **136**, 15730–15741 (2014).
45. R. Frank *et al.*, *Angew. Chem. Int. Ed.* **54**, 9586–9590 (2015).
46. E. O. Fischer, A. Maasböl, *Angew. Chem. Int. Ed.* **3**, 580–581 (1964).
47. M. Härterich *et al.*, *Nat. Commun.* **14**, 2764 (2023).
48. H. Grützmacher, S. Freitag, R. Herbst-Irmer, G. Sheldrick, *Angew. Chem. Int. Ed.* **31**, 437–438 (1992).
49. P. Schützenberger, *Bulletin de la Société Chimique de Paris* **10**, 188–192 (1868).

ACKNOWLEDGMENTS

Funding: This work was funded by Alexander von Humboldt Stiftung (Feodor Lynen Fellowship to M.D.) and the Engineering and Physical Sciences Research Council [Inorganic Chemistry for Future Manufacturing (OxICFM) CDT – EP/S023828/1]. **Author contributions:** Conceptualization: S.A.; Investigation: M.D., A.V.P., A.E.C., S.K., M.M.D.R., J.S.-M.; Visualization: M.D., A.E.C., S.A.; Supervision: S.A., C.T.; Writing – original draft: S.A.; Writing – review & editing: S.A., M.D., A.E.C. **Competing interests:** The authors declare that they have no competing interests. **Data and materials availability:** Crystallographic information files (CIFs) relating to the x-ray crystal structures are available free of charge from the Cambridge Crystallographic Data Centre (CCDC), deposition numbers 2434774 to 2434779. All other data are available in the main text or the supplementary materials.

SUPPLEMENTARY MATERIALS

science.org/doi/10.1126/science.ady0247
Materials and Methods; Supplementary Text; Figs. S1 to S106; Tables S1 to S4; References (*50*–*91*); Data S1

Submitted 9 April 2025; accepted 10 July 2025

10.1126/science.ady0247

ULTRACOLD GASES

Directly observing replica symmetry breaking in a vector quantum-optical spin glass

Ronen M. Kroeze[1,2], Brendan P. Marsh[2,3], David Atri Schuller[2,3], Henry S. Hunt[1,2], Alexander N. Bourzutschky[1,2], Michael Winer[4], Sarang Gopalakrishnan[5], Jonathan Keeling[6], Benjamin L. Lev[1,2,3*]

Spin glasses are quintessential examples of complex matter. Although their ordering lacks complete theoretical understanding, abstract models of spin glasses inform problems in other fields, such as combinatorial optimization and artificial intelligence—where they form a mathematical basis for neural network computing. We demonstrate the ability to realize a spin glass of a distinct driven-dissipative and vector form. By microscopically visualizing its glassy spin states, the technique allows us to directly measure replica symmetry breaking and the resulting ultrametric hierarchical structure. Ultrametricity is known to be emergent in models of evolution, protein folding, and climate change; this work shows it to be directly observable in a physically realized system.

Infinite-range spin glasses are described by the Parisi solutions to the equilibrium Sherrington-Kirkpatrick (SK) model (*1*–*3*). This theoretical treatment predicts a rugged free-energy landscape across the high-dimensional spin configuration space. Ergodicity is broken owing to quenched disorder and geometric frustration among the spins: When cooled, exact system copies may relax into distinct regions or states. These copies—called replicas—can, under dynamical evolution, result in nonidentical, yet highly correlated, spin configurations, even when ignoring a global spin flip; this is called replica symmetry breaking (RSB). A comparison of spin configurations reveals a correlation structure known as "ultrametric." Ultrametricity means that when considering the distance between these configurations—quantified by their "overlap," the degree to which patterns of spins between any two replicas match—one finds that these distances are not compatible with any standard geometry. Rather, they form a hierarchy manifest as a family tree. This structure emerges below the critical temperature T_c separating the SK spin glass from the paramagnet (*4*) and has broad relevance to complex systems (*2*, *5*).

We engineered a driven-dissipative experimental system that enables visualization of the ultrametric structure of a glassy system. To do so, we simultaneously created a spin glass and microscopically studied its spin structure using a multimode cavity. We measured spin correlations from steady-state images and found that nonthermal distributions arise, which adds to the rich nonequilibrium phenomena already found in glasses, such as aging (*2*, *6*). This extends spin glass physics beyond the simulation of known equilibrium models by creating an intrinsically driven-dissipative nonequilibrium glass.

Spin frustration and disorder have been separately realized in controllable systems using trapped ions (*7*, *8*) and cavity-coupled atoms (*9*). We simultaneously achieved both using multimode cavity quantum electrodynamics (QED), as suggested in (*10*–*14*) and discussed further in (*15*–*17*). RSB has been reported in nonlinear optical devices such as random lasers (*18*–*22*). However, these devices lack microscopic disorder control and individual spin readout. In such devices, only indirect measurements of the spin correlations emerging from RSB are possible, precluding any direct demonstration of ultrametricity. [Incipient glassiness has also been reported in networks of superconducting circuits (*23*, *24*).]

Experimental protocol

Figure 1A illustrates the confocal multimode cavity QED system; the apparatus is discussed in detail in the supplementary materials (*25*). Briefly, a pair of mirrors, separated by a distance equal to their radius of curvature, confine many electromagnetic modes at nearly the same frequency; the cavity light acts both to provide site-resolved imaging of the spin states and to create photon-mediated, infinite-range interactions among spins (*26*). An array of optical tweezer traps place $n = 8$ ultracold gases of ^{87}Rb atoms at different locations $\mathbf{r}_i$ within the cavity midplane $z = 0$ (*25*). Physically, the spins are motional states of the atomic gases, and each gas serves as one of the n vertices of the spin network. Each vertex contains $N = 2.3(1) \times 10^5$ atoms within a radius $\sigma_A \approx 4$ μm centered at $\mathbf{r}_i$.

A standing-wave transverse pump at wavelength $\lambda = 780$ nm and oriented along $\hat{x}$ scatters photons off the atoms in each vertex and into a superposition of cavity modes that is peaked at the vertices (*13*, *26*). A key experimental control is the power of the pump field, proportional to the Rabi rate squared (Ω^2), and the rate at which it linearly increases through the superradiant threshold of a Hepp-Lieb-Dicke transition (*27*). At threshold, the atoms in each vertex i spontaneously break translation symmetry by spatially ordering into a density wave along $\hat{z}$. The atoms choose a spatial phase θ_i that maximizes the local field amplitude at the vertex's position. However, the field of the confocal cavity is not perfectly localized and has a weaker, long-distance tail that is quasi-random in space (*13*, *28*, *29*). When there are two vertices in the cavity, the nonlocal, long-range part of the field associated with vertex 1 explicitly breaks the translational symmetry for vertex 2 and vice versa. This leads to an interaction J_{12} between the symmetry-breaking phases of the two vertices, depending on the spatial position between the vertices (*28*, *29*)—extending to many vertices directly follows. Thus, another set of experimental control parameters involve the placement $\mathbf{r}_i$ of the vertices within the cavity.

Because the phases θ_i lie on a circle, we modeled each as an *XY*-vector spin. The connection to a vector spin model is made by writing the photon-mediated interaction energy E_{int} in terms of collective spin components $S_i^x = \cos\theta_i$ and $S_i^y = \sin\theta_i$

$$E_{\text{int}} = -\sum_{i,j=1}^{n} \left[J_{ij} \left(S_i^x S_j^x - S_i^y S_j^y \right) + K_{ij} \left(S_i^x S_j^y + S_i^y S_j^x \right) \right] \quad (1)$$

where the coupling $J_{ij} \approx J_0 \cos R_{ij}$, $J_0 \equiv N^2 g_0^2 \Omega^2 / \left(8\Delta_A^2 |\Delta_C|\right)$, and $R_{ij} \equiv 2\mathbf{r}_i \cdot \mathbf{r}_j / w_0^2$. Equation 1 applies in the far-detuned limit, where the pump is red-detuned by $\Delta_C = -2\pi \cdot 60$ MHz from the near-degenerate cavity resonances; both cavity and pump are $\Delta_A = -2\pi \cdot 97.3$ GHz from the atomic resonance. The waist w_0 of the cavity's fundamental mode is 35 μm, and g_0 is the single-atom coupling strength to this mode. The $K_{ij} \approx \left(4\sigma_A^2 / w_0^2\right) J_0 R_{ij} \sin R_{ij}$ coupling term arises from the finite extent of each of the vertices in the imperfect confocal cavity. The total system energy is that of a transverse-field vector spin model with a transverse field strength proportional to E_r, the atomic recoil energy, which is $h \times 3.7$ kHz, where h is Planck's constant; see section II (*25*) for the full quantum Hamiltonian description.

The multimode single-atom cooperativity, defined in the dispersive limit, is $C_{mm} = 110$ (*26*). Thus, the intracavity field mediates strong atomic interactions, and the cavity's large effective numerical aperture allows us to holographically image the intracavity field at $z = 0$ with a resolution of 1.7 μm (*26*). This is smaller than the width σ_A of each vertex. Figure 1C presents an example image taken at a pump power 25% above threshold, well within the spin-ordered phase.

[1]Department of Physics, Stanford University, Stanford, CA, USA. [2]E. L. Ginzton Laboratory, Stanford University, Stanford, CA, USA. [3]Department of Applied Physics, Stanford University, Stanford, CA, USA. [4]Joint Quantum Institute, Department of Physics, University of Maryland, College Park, MD, USA. [5]Department of Electrical and Computer Engineering, Princeton University, Princeton, NJ, USA. [6]SUPA, School of Physics and Astronomy, University of St Andrews, St Andrews, UK. ***Corresponding author. Email: benlev@stanford.edu**

Ordered states of the vector spin model

We now discuss the nonequilibrium steady-state phase portrait realized by Eq. 1 and shown in Fig. 1D. At small pump strength Ω, the system is in a normal (i.e., paramagnetic) phase that weakly scatters incoherent light into the cavity. Superradiant scattering ensues at large pumping strength, and the spins order either as a ferromagnet or spin glass depending on the values of J_{ij}. For K_{ij} sufficiently smaller than J_{ij}, as is the case here, Eq. 1 favors an x- (y-)ferromagnet when all $J_{ij} > 0$ (< 0) or a spin glass when J_{ij} values are disordered. By "disordered," we mean J_{ij} values that are both randomly signed and of random magnitude between $\pm J_0/N = \pm 2\pi \cdot 2.0(1)$ kHz.

Ferromagnets differ from paramagnets and spin glasses in their nonzero magnetization order parameter $m^{\mu} = \frac{1}{n}\sum_{i=1}^{n}\langle S_i^{\mu}\rangle$, where $\langle\cdot\rangle$ indicates time average and, for the n vector spins, we define $\mu \in \{x, y\}$. Distinguishing between the paramagnet and spin glass requires another order parameter, the Edwards-Anderson spin overlap $q_{\mathrm{EA}}^{\mu\nu} = \frac{1}{n}\sum_{i=1}^{n}\langle S_i^{\mu}\rangle\langle S_i^{\nu}\rangle$ (*30*). This overlap is always zero for a paramagnet but is nonzero for the ferromagnet and spin glass because of their frozen spin order. The $q_{\mathrm{EA}}^{\mu\nu}$ order parameter may be extended to account for overlaps among replicas through $q_{\alpha\beta}^{\mu\nu} = \frac{1}{n}\sum_{i=1}^{n}\langle S_i^{\alpha,\mu}\rangle\langle S_i^{\beta,\nu}\rangle$, where α and β are replica indices (*3*). We focus on two linear combinations of this overlap: $Q_{\alpha\beta} \equiv q_{\alpha\beta}^{xx} + q_{\alpha\beta}^{yy}$ and $R_{\alpha\beta} \equiv q_{\alpha\beta}^{yy} - q_{\alpha\beta}^{xx}$.

Before we present measurements of spin-overlap distributions, we discuss how these overlaps distinguish different phases. For an XY-vector ferromagnet, the spin-overlap distribution lies on the boundary of the square spanned by the allowed values of the overlap matrices, $|Q_{\alpha\beta}| \le Q_{\alpha\alpha}$ and $|R_{\alpha\beta}| \le |R_{\alpha\alpha}|$. Both $Q_{\alpha\alpha}$ and $|R_{\alpha\alpha}| = 1$ near $T = 0$ and in the measurements presented below. By contrast, a spin glass that exhibits RSB has nonzero overlaps in the interior of this square. This is the signature manifestation of RSB (*3*): Even for identical initial conditions, thermal (or quantum) fluctuations during spin ordering drive replicas into distinct, energetically disconnected regions of the rugged free-energy landscape. This breaks ergodicity, yielding many non-spin-flip-symmetric states that may be accessible to different replicas. Each real-time spin trajectory obtainable from cavity emission is equivalent to replica time evolution (*14*). The order that emerges from RSB is the ultrametric structure of overlap distances $D_{\alpha\beta} = 1 - |Q_{\alpha\beta}|$ (*31*, *32*). Mathematically, this implies that the $D_{\alpha\beta}$ satisfy the strong triangle inequality, $D_{\alpha\gamma} \le \max\{D_{\alpha\beta}, D_{\beta\gamma}\}$, among any triple of replicas, thereby imposing a family-tree structure.

We now discuss the existence of RSB in the aforementioned vector spin model before presenting direct experimental evidence for it. We will then return to discuss differences arising from the driven-dissipative version we experimentally studied. First, we performed parallel-tempering Monte Carlo (PTMC) simulations (*33*, *34*) based on Eq. 1 that capture the equilibrium properties of the model at varying system sizes. As shown in fig. S12, this yields a phase diagram with RSB at low temperature similar to that of the SK spin glass model held in equilibrium. The existence of RSB is further supported by an analytical replica analysis of the equilibrium version of the vector model; see section VI (*25*). We provide the replica symmetric solution and show that it becomes unstable below a critical temperature T_c. This reveals RSB, and full RSB is found directly below T_c.

Benchmarking with ferromagnetic order

Figure 2, A and D, presents reconstructed images showing x- and y-ferromagnets, respectively; hereafter, we refer to these as xFM and yFM. Repeating the experiment with identical positions allowed us to compile a set of 900 replicas. We constructed the magnetization and spin-overlap distributions shown in Fig. 2, B, C, E, and F. These exhibit the expected near-maximal magnetization and overlap "goalposts" of ferromagnets at $q_{\alpha\beta}^{xx} = \pm 1$ $\left(q_{\alpha\beta}^{yy} = \pm 1\right)$ for xFM (yFM). The slight tilt of the yFM magnetization as well as the nonmaximal $q_{\alpha\beta}^{yy}$ are caused by the K term (*25*). We measured the energy distributions of the xFM and yFM states and found them to be deep within the ordered phase; see section IX and fig. S21 (*25*).

Observation of replica symmetry breaking

We then created a spin glass by moving the vertices to realize disordered J matrices. Figure 3, A to D, shows four distinct replicas of the same glassy J matrix. These exemplify the multitude of configurations accessible within the glassy rugged landscape. The spin-overlap distributions in Fig. 3, E to H, are compiled from 100 experimental

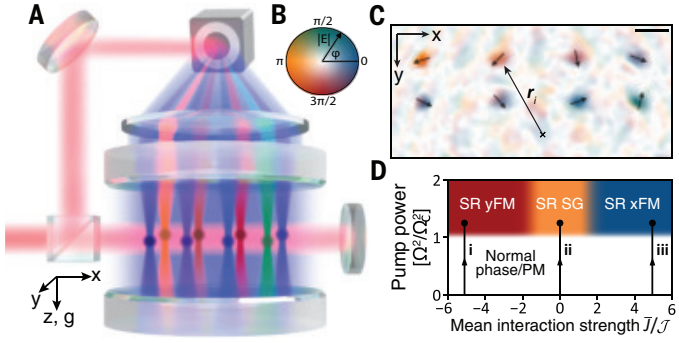

Fig. 1. Experimental system and spin detection. (**A**) Sketch of the confocal multimode cavity QED apparatus. Atomic gases ($n = 8$ colored balls) at vertex positions $\mathbf{r}_i$ from the center of the cavity midplane. The network vertices are pumped with a transverse field (red) and scatter light into local (multicolored) and nonlocal (light blue) components of the cavity field. Neither the mirror-image field components at $-\mathbf{r}_i$ nor the lasers trapping the atomic gases are shown. A portion of the pump mixes with cavity emission and illuminates a camera for holographic imaging; the analysis required to account for optical aberrations and spin-angle inhomogeneities is discussed in the supplementary materials (*25*). (**B**) Color map for electric fields, where opacity indicates its amplitude $|E|$ and hue indicates phase φ. (**C**) Example of a reconstructed hologram of cavity emission for a coupled network of eight atomic gases. The eight colored spots are the local fields coupled to each gas. The arrows here and in subsequent figures indicate the spin vector direction θ derived from the electric field phase φ. The scale bar length here and in subsequent figures is $w_0 =$ 35 μm. (**D**) Sketch of the nonequilibrium steady-state phase diagram of the vector spin model. Superradiance (SR) occurs as the pump strength Ω exceeds a threshold Ω_c above the normal, paramagnetic (PM) phase. SR is accompanied by the ordering of spins into the spin glass (SG) or ferromagnetic (FM) states along y or x. The particular state depends on the ratio of $\bar{J}$, the mean of the interaction strengths J_{ij}, and $\mathcal{J}$, their standard deviation divided by $\sqrt{n}$. Figure 2 plots data corresponding to the experimental pump power ramp along arrows i and iii. Figures 3 and 4 relate to the ramp along arrow ii, which can vary within ~0.4 of zero.

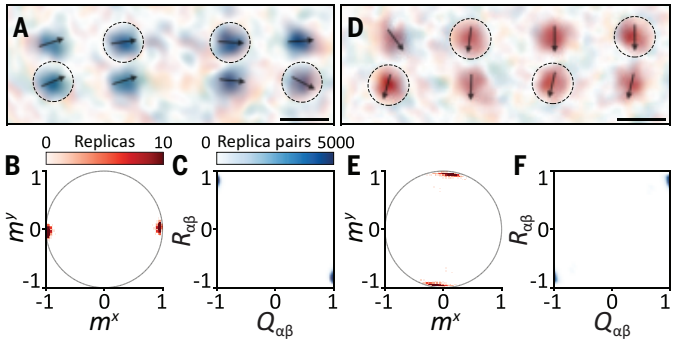

Fig. 2. Demonstration of two ferromagnetic states. (**A** to **C**) Data in support of an xFM state arising from vertices positioned to realize an effective $J_{ij} > 0$ network. (A) Representative reconstructed image showing a cavity field with vertex phases of a spin configuration ordered along $\hat{x}$. A local π gauge rotation was applied to the vertices indicated by dashed circles (*25*). (B) Magnetization distribution m^{μ}. (C) Distribution of overlap components $Q_{\alpha\beta}$ and $R_{\alpha\beta}$ between pairs of replicas. (**D** to **F**) As in (A) to (C), but for an effective $J_{ij} < 0$ network realizing a yFM state.

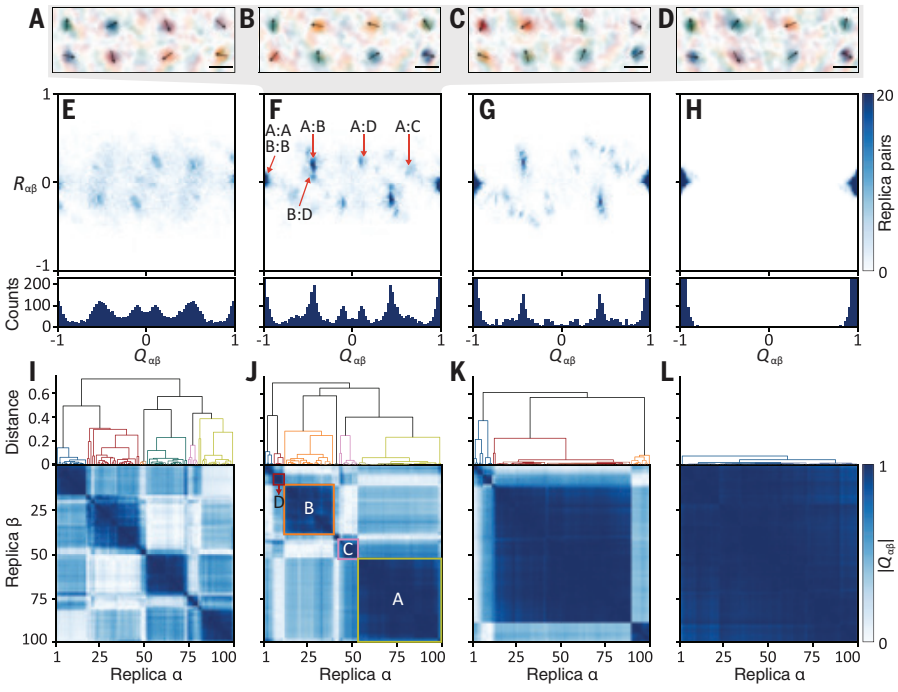

Fig. 3. Spin-overlap distributions and ultrametric correlations of the vector spin glass versus ramp rate. (**A** to **D**) Reconstructed images of the four most commonly found spin configurations for the same representative disordered J_{ij}. These spin states are found in 45, 26, 9, and 5% of the 100 total experimental replicas, respectively. (**E** to **H**) (Top row) Overlap distributions versus ramp rate for the same disordered J_{ij}. The rate of increase of the pump lattice depth is, in E_r/ms: (E) 1100, (F) 45, (G) 23, and (H) 11. The mean energies $\langle E_{\text{int}} \rangle$ of these states, normalized by the ground-state energy $|E_{\text{gs}}|$, are: (E) −0.75(1), (F) −0.84(1), (G) −0.88(1), and (H) −0.926(4). The particular replica pairs from (A) to (D) contributing to each major peak are also indicated in (F). The peaks are denoted α:β using the panel tags A, B, C, and D as replica labels. (Bottom row) The 1D marginal distributions—that is, histograms of the number of replica pairs at each value of $Q_{\alpha\beta}$. (**I** to **L**) Hierarchically clustered $|Q_{\alpha\beta}|$ matrices with family-tree–like dendrograms are shown for each ramp rate. The states in (A) to (D) are contained in the four distinct clusters outlined with squares in (J). The squares are color coded to match the associated branch of the family-tree–like dendrogram drawn along the top. The distance of each branch is calculated from the average of overlaps within the limb below it. Color coding is used for families below a distance of 0.4, which corresponds to emergent, near-kin clusters with spin configurations separated by approximately two spin flips.

replicas each but are taken with different pump power ramp rates. The rate used for Fig. 3F is the same as that used for the images in Fig. 3, A to D, and the ferromagnetic data in Fig. 2. This ramp rate is sufficiently slow to observe overlap peaks at $Q_{\alpha\beta} = \pm 1$, in addition to multiple $\alpha \neq \beta$ peaks in the distribution's interior. This structure is consistent with the presence of RSB.

A ramp rate increase of more than 24× blurred these peaks while reducing the overlap goalposts, as seen in Fig. 3E. Presumably, more Landau-Zener transitions lead to a glass with higher mean energy $\langle E_{\text{int}} \rangle$ that explores more configurations in the rugged landscape. (We have not been able to ramp fast enough to image the paramagnet.) Conversely, slowing the ramp by a factor of two created sharper, more sparse overlap peaks, as shown in Fig. 3G. Because we have a finite-sized system, RSB disappears when further slowing the ramp, producing distributions with lower $\langle E_{\text{int}} \rangle$. As shown in Fig. 3H, the ground-state spin configuration dominates the distribution when $\langle E_{\text{int}} \rangle$ drops below the first excited state.

Evidence for ultrametricity

Next, we provide evidence for nascent ultrametric structure in the $Q_{\alpha\beta}$. Hierarchical clustering was performed to iteratively combine the replicas into groups that minimize the average distance $1 - |Q_{\alpha\beta}|$ within those groups (*35*). This allows for the visualization of ultrametric relationships as block-diagonal structures in $|Q_{\alpha\beta}|$ (*31*) and is shown in Fig. 3, I to L; see (*36*) for the leaf-sorting algorithm. For example, Fig. 3I shows at least six clusters. Off-diagonal rectangles of lighter shade provide evidence for multistep RSB structure; the three distinct shades indicate that at least three states contribute to the spin glass order (*2*, *37*). (The clustering hierarchy becomes trivial for the slow-ramp case in Fig. 3L.)

Ultrametric structure is also shown above the $|Q_{\alpha\beta}|$ matrices. Replicas are the leaves at the lowest generation level. The overlap between two replicas is approximately the value of the distance of the topmost branch connecting them. A quantitative analysis based on the strong triangle inequality (*38*) is presented in section XI and fig. S24 (*25*).

Exploration of quenched disorder

Figure 4, B to D, shows overlap distributions for three additional realizations of disordered J matrices. They differ both from each other and from the overlap in Fig. 3F (reproduced in Fig. 4A), demonstrating the strong dependence of spin overlaps on disorder realization, as expected. Although the purpose of the experiment was not to simulate the equilibrium SK model, it was instructive to compare the experimental overlaps with those of the intrinsically equilibrium-based PTMC simulations of the SK model presented in section V and fig. S13 (*25*). We find that there is no simulated temperature at which all experimentally found features of RSB also appear in the PTMC simulations, presumably because it cannot capture the experiment's driven-dissipative dynamics (*25*). Although all peaks are reproduced at high temperature, they are blurred owing to thermal fluctuations. Moreover, overlap peaks are sharper at low temperature, and some are missing because they arise from higher-energy configurations.

Seeking closer theory-experiment correspondence, we compared our experimental overlap distributions in Fig. 4, A to D, to a different simulation method, one that accounts for the driven-dissipative effect of the superradiant phase transition. That is, we numerically calculated the dynamics using a stochastic unraveling of the Lindblad master equation under a mean-field approximation that uses the same pump ramp schedule as the experiment (*25*). These trajectory simulations use the J and K matrices derived from experimental observations for each disorder realization, as explained in sections IV and VII (*25*). The results appear in Fig. 4, F to H; some are in qualitative agreement with the experimental ensemble, but others, such as in Fig. 4I, are far off. These simulations also do not fully capture the experimental spin glass overlaps. Noise in the coupling matrices does not qualitatively change this assessment (*25*). Future theoretical work will be needed to better understand the full many-body dynamics of the driven-dissipative spin glass realized in our apparatus.

Measuring the Parisi order parameter

Specific disorder details cease to play a role in the large system-size limit of nonglassy systems. By contrast, the values of $q_{\alpha\beta}^{\mu\nu}$ are different for different disorder realizations of the J matrices, implying a lack

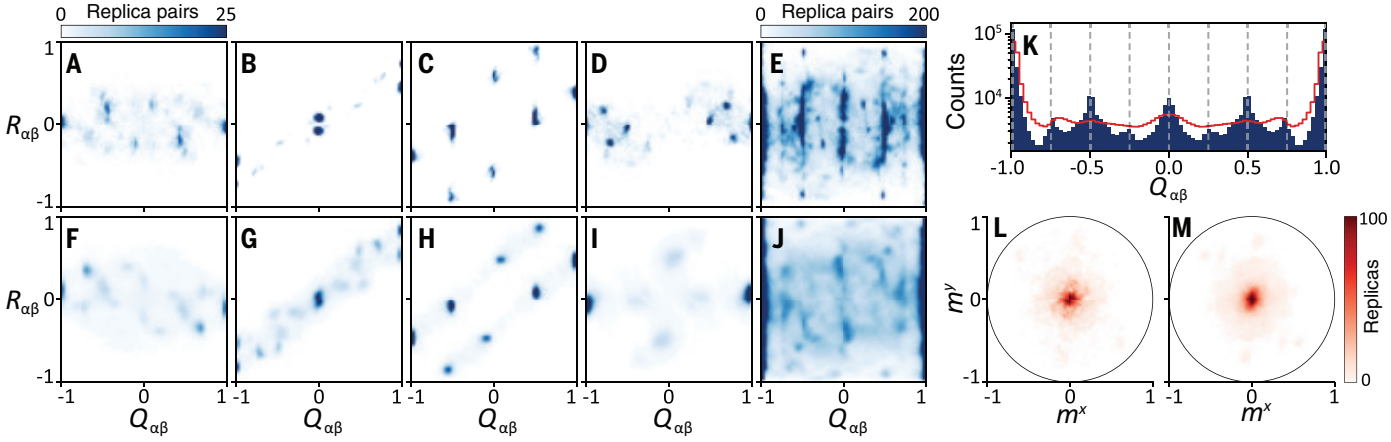

Fig. 4. Comparison of experimental and simulated spin overlaps and Parisi order parameters. (**A** to **D**) Each of these experimental overlap distributions is realized by moving the vertices to different sets of positions that realize four different disorder realizations of the *J* matrix. Individual overlaps are derived from 100 experimental replicas and share the same color scale. (**E**) The experimental Parisi order parameter distribution formed by averaging 123 overlap distributions, each with a different disordered *J* matrix; see fig. S27 for all distributions. (**F** to **I**) Numerical simulations using a mean-field trajectory technique with experimentally measured *J* and *K*s in (A) to (D). (**J**) Numerical simulation of the Parisi order parameter distribution using *J* matrices calculated from observed positions. For (F) to (J), see section VII (*25*) for simulation details. (**K**) 1D marginal histogram of the Parisi order parameter distribution in (E). Dashed lines indicate allowed overlap values for a binarized (Ising) eight-spin system. The red trace is the 1D marginal histogram from (J). (**L**) Experimental and (**M**) numerical magnetization distributions averaged over the same experimental ensemble as above.

of self-averaging. A quantity that is independent of microscopic disorder details appears if one takes the disorder average $\left\langle q_{\alpha\beta}^{\mu\nu} \right\rangle_J$ over all *J*-matrix realizations. This is the Parisi order parameter (*3*, *39*–*41*), which exhibits a smooth distribution of $Q_{\alpha\beta}$ between the $\pm Q_{\alpha\alpha}$ goalposts and whose shape would be determined by temperature via the Gibbs measure for equilibrium spin glasses (*2*).

To measure the Parisi order parameter, we averaged the experimental overlap distributions in Fig. 4, A to D, plus 119 others (each compiled from 100 experimental replicas). The result is shown in Fig. 4E; see sections VIII and X (*25*) for assessment of ensemble randomness and convergence. The one-dimensional (1D) marginal distribution in Fig. 4K exhibits continuous support between the overlap goalposts, similar to that known from solutions to the equilibrium SK Ising spin glass (*2*, *25*). However, we observe several peaks between the goalposts rather than a smooth distribution. Overlaid on the plot are $n + 1 = 9$ equally spaced vertical dashed lines set at the allowed overlap-value locations that would be found in an Ising network of $n = 8$ vertices. That the peaks in the data match these positions suggests that the vector spins are weakly binarized along the *Q* quadrature. This may arise from an unidentified easy-axis anisotropy; see section II.E (*25*) for discussion.

The Parisi order parameter from the mean-field trajectory simulations is shown in Fig. 4J. It reproduces some of this striped behavior, as is clear from the marginal shown in red in Fig. 4K. The PTMC simulation results in fig. S13 (*25*) are even less similar to the experimental data. As with the overlap distributions, it seems that neither an equilibrium (PTMC) nor a nonequilibrium (mean-field trajectory) simulation method faithfully reproduces all details of the experimental Parisi order parameter distribution. There could be some transient entanglement at threshold that governs aspects of spins organization in a way not captured by the mean-field theory; indeed, entanglement has been shown to play such a role in spin-1/2 glasses (*14*).

A spin glass should also have zero average magnetization. The experimental disorder-averaged vector magnetization is shown in Fig. 4L and is centered around $\mathbf{m} = 0$, as expected. It is similar to the simulation in Fig. 4M.

Discussion and outlook

That clear signatures of RSB and ultrametricity can be experimentally observed in a frustrated spin network as small as $n = 8$ is surprising. This fact is supported by finite-size scaling simulations of both equilibrium and nonequilibrium models; see figs. S10, S11, S19, S20, S25, and S26 (*25*). Nevertheless, the apparatus will not be limited to this system size: Optical tweezers can now realize arrays of thousands of atom traps (*42*), and incorporating this technology should enlarge the spin glass by orders of magnitude. Sending light directly through the multimode cavity mirrors will allow individual spin sites to be addressed. This will enable the recall of associative memories stored in the spin glass (*10*, *43*–*48*), or the local addressing of spins for microscopically imaging the spatiotemporal response of spins and their domains, a capability not yet experimentally achieved.

Other types of driven-dissipative spin glasses can be realized using this system. Nonconfocal multimode cavities (*29*) can realize Ising spin models (*49*), and short-range interactions (*50*) are possible through a marginally more sophisticated transverse pumping scheme (*51*). The latter will enable the experimental exploration of non-mean-field spin glasses, where the theoretical determination of whether some form of RSB describes their order remains an important unresolved problem in statistical physics (*2*, *52*). Finally, inducing Rydberg blockade (*53*, *54*) in each of the spin network vertices can realize effective spin-1/2 degrees of freedom while preserving high light-matter coupling strength (*14*). Glassy quantum spin dynamics would then be accessible to microscopic experimental observation and would provide access to novel quantum states and dynamics (*11*, *14*, *15*, *55*–*57*) that may find application in quantum neuromorphic computational devices (*58*, *59*).

REFERENCES AND NOTES

1. D. Sherrington, S. Kirkpatrick, *Phys. Rev. Lett.* **35**, 1792–1796 (1975).
2. D. L. Stein, C. M. Newman, *Spin Glasses and Complexity*, *Primers in Complex Systems* (Princeton Univ. Press, 2013).
3. P. Charbonneau *et al.*, *Spin Glass Theory and Far Beyond* (World Scientific, 2023).
4. M. Mezard, G. Parisi, M. Virasoro, *Spin Glass Theory And Beyond: An Introduction To The Replica Method And Its Applications*, vol. 9 of *World Scientific Lecture Notes in Physics* (World Scientific, 1987).
5. G. Parisi, *Rev. Mod. Phys.* **95**, 030501 (2023).
6. K. H. Fischer, J. A. Hertz, *Spin Glasses* (Cambridge Univ. Press, 1991).
7. K. Kim *et al.*, *Nature* **465**, 590–593 (2010).
8. R. Islam *et al.*, *Science* **340**, 583–587 (2013).
9. N. Sauerwein *et al.*, *Nat. Phys.* **19**, 1128–1134 (2023).
10. B. P. Marsh *et al.*, *Phys. Rev. X* **11**, 021048 (2021).
11. S. Gopalakrishnan, B. L. Lev, P. M. Goldbart, *Phys. Rev. Lett.* **107**, 277201 (2011).

12. S. Gopalakrishnan, B. L. Lev, P. M. Goldbart, *Philos. Mag.* **92**, 353–361 (2012).
13. V. D. Vaidya *et al.*, *Phys. Rev. X* **8**, 011002 (2018).
14. B. P. Marsh *et al.*, *Phys. Rev. X* **14**, 011026 (2024).
15. P. Strack, S. Sachdev, *Phys. Rev. Lett.* **107**, 277202 (2011).
16. P. Rotondo, E. Tesio, S. Caracciolo, *Phys. Rev. B* **91**, 014415 (2015).
17. V. Erba, M. Pastore, P. Rotondo, *Phys. Rev. Lett.* **126**, 183601 (2021).
18. N. Ghofraniha *et al.*, *Nat. Commun.* **6**, 6058 (2015).
19. A. S. L. Gomes *et al.*, *Sci. Rep.* **6**, 27987 (2016).
20. D. Pierangeli *et al.*, *Nat. Commun.* **8**, 1501 (2017).
21. F. Antenucci, C. Conti, A. Crisanti, L. Leuzzi, *Phys. Rev. Lett.* **114**, 043901 (2015).
22. J. Niedda, G. Gradenigo, L. Leuzzi, G. Parisi, *SciPost Phys.* **14**, 144 (2023).
23. R. Harris *et al.*, *Science* **361**, 162–165 (2018).
24. A. D. King *et al.*, *Nature* **617**, 61–66 (2023).
25. See supplementary materials for experimental details and numerical simulations.
26. R. M. Kroeze, B. P. Marsh, K.-Y. Lin, J. Keeling, B. L. Lev, *PRX Quantum* **4**, 020326 (2023).
27. F. Mivehvar, F. Piazza, T. Donner, H. Ritsch, *Adv. Phys.* **70**, 1–153 (2021).
28. Y. Guo, R. M. Kroeze, V. D. Vaidya, J. Keeling, B. L. Lev, *Phys. Rev. Lett.* **122**, 193601 (2019).
29. Y. Guo *et al.*, *Phys. Rev. A* **99**, 053818 (2019).
30. S. F. Edwards, P. W. Anderson, *J. Phys. F Met. Phys.* **5**, 965–974 (1975).
31. R. Rammal, G. Toulouse, M. A. Virasoro, *Rev. Mod. Phys.* **58**, 765–788 (1986).
32. M. Mézard, G. Parisi, N. Sourlas, G. Toulouse, M. Virasoro, *Phys. Rev. Lett.* **52**, 1156–1159 (1984).
33. R. H. Swendsen, J.-S. Wang, *Phys. Rev. Lett.* **57**, 2607–2609 (1986).
34. K. Hukushima, K. Nemoto, *J. Phys. Soc. Jpn.* **65**, 1604–1608 (1996).
35. F. Murtagh, P. Contreras, *Wiley Interdiscip. Rev. Data Min. Knowl. Discov.* **2**, 86–97 (2012).
36. Z. Bar-Joseph, D. K. Gifford, T. S. Jaakkola, *Bioinformatics* **17** (suppl. 1), S22–S29 (2001).
37. G. Parisi, *J. Phys. A Math. Gen.* **13**, L115–L121 (1980).
38. H. G. Katzgraber, A. K. Hartmann, *Phys. Rev. Lett.* **102**, 037207 (2009).
39. D. Elderfield, D. Sherrington, *J. Phys. C Solid State Phys.* **17**, 5595–5603 (1984).
40. J. R. L. de Almeida, R. C. Jones, J. M. Kosterlitz, D. J. Thouless, *J. Phys. C Solid State Phys.* **11**, L871–L875 (1978).
41. G. Toulouse, M. Gabay, *J. Physique Lett.* **42**, 103–106 (1981).
42. H. J. Manetsch *et al.*, arXiv:2403.12021 [quant-ph] (2025).
43. J. J. Hopfield, *Proc. Natl. Acad. Sci. U.S.A.* **79**, 2554–2558 (1982).
44. J. J. Hopfield, D. W. Tank, *Science* **233**, 625–633 (1986).
45. D. J. Amit, *Modeling Brain Function: The World of Attractor Neural Networks* (Cambridge Univ. Press, 1989).
46. J. Hertz, A. Krogh, R. Palmer, *Introduction to the Theory of Neural Computation* (Avalon Publishing, 1991).
47. Y. Bahri *et al.*, *Annu. Rev. Condens. Matter Phys.* **11**, 501–528 (2020).
48. Y. Guo *et al.*, *Nature* **599**, 211–215 (2021).
49. B. P. Marsh *et al.*, arXiv:2505.22658 [quant-ph] (2025).
50. M. A. Ruderman, C. Kittel, *Phys. Rev.* **96**, 99–102 (1954).
51. R. M. Kroeze, thesis, Department of Physics, Stanford University (2023).
52. P. Contucci, C. Giardinà, *Perspectives on Spin Glasses* (Cambridge Univ. Press, 2013).
53. T. Peyronel *et al.*, *Nature* **488**, 57–60 (2012).
54. N. Jia *et al.*, *Nat. Phys.* **14**, 550–554 (2018).
55. H. Hosseinabadi, D. E. Chang, J. Marino, *Phys. Rev. Res.* **6**, 043314 (2024).
56. M. Tikhanovskaya, S. Sachdev, R. Samajdar, *PRX Quantum* **5**, 020313 (2024).
57. J. Lang, S. Sachdev, S. Diehl, *SciPost Phys.* **17**, 160 (2024).
58. F. Barahona, *J. Phys. A Math. Gen.* **15**, 3241–3253 (1982).
59. A. Lucas, *Front. Phys.* **2**, 5 (2014).
60. R. M. Kroeze *et al.*, Replication data for: Directly observing replica symmetry breaking in a quantum-optical vector spin glass, version 10.0, Harvard Dataverse (2025); https://doi.org/10.7910/DVN/JFKKFQ.

ACKNOWLEDGMENTS

We thank S. Ganguli and H. Katzgraber for discussions and Z. Zhang for experimental assistance. **Funding:** We are grateful for funding support from the Army Research Office (grant W911NF2210261), NTT Research, and the Q-NEXT DOE National Quantum Information Science Research Center (partial support of D.A.S. and B.L.L.). J.K. and S.G. were supported in part by the International Centre for Theoretical Sciences (ICTS) through participation in the "Periodically and quasi-periodically driven complex systems" program (code: ICTS/pdcs2023/6). B.P.M. acknowledges funding from the Stanford QFARM Initiative and an NSF Graduate Research Fellowship. A.N.B. and M.W. acknowledge support from a Stanford Graduate Fellowship and a Joint Quantum Institute Fellowship, respectively. A portion of the computing for this project was performed using the Stanford Sherlock cluster. **Author contributions:** R.M.K., B.P.M., D.A.S., H.S.H., and B.L.L. carried out the experiments. R.M.K., B.P.M., D.A.S., H.S.H., and A.N.B. carried out the numerical simulations, and M.W. did the replica calculations. S.G., J.K., and B.L.L. conceived of the project, and B.L.L. oversaw the work. All authors were involved in the analysis of the results and contributed to writing the paper. **Competing interests:** The authors declare that they have no competing interests. **Data and materials availability:** Primary data generated in the current study and the code used to generate it are publicly available in the Harvard Dataverse Repository (*60*).

SUPPLEMENTARY MATERIALS

science.org/doi/10.1126/science.adu7710
Supplementary Text; Figs. S1 to S27; References (*61–89*)

Submitted 20 November 2024; accepted 22 July 2025; published online 14 August 2025
10.1126/science.adu7710

BIOELECTRONICS

Drop-printing with dynamic stress release for conformal wrap of bioelectronic interfaces

An Li[1]†, Wenjianlong Zhou[2]†, Huizeng Li[1]*†, Wei Fang[3]†, Yifei Luo[4]†, Zheng Li[5], Qingrong Zhang[5], Quan Liu[1,6], Qin Xu[2], Luanluan Xue[1,6], Kaixuan Li[1], Renxuan Yuan[1,6], Wanling Liu[1,6], Wang Jia[2]*, Xiaodong Chen[4,7]*, Yanlin Song[1,6]*

Bioelectronic interfaces demonstrate promising applications in health monitoring, medical treatment, and augmented reality. However, conformally wrapping these film devices onto three-dimensional surfaces often leads to stress-induced damage. We propose a "drop-printing" strategy that enables damage-free film transfer using a droplet. The droplet acts as a lubricating layer between the film and the target surface, facilitating local sliding during shape-adaptive deformation. This mechanism prevents in-plane film stretching and reduces stress concentration. Even nonstretchable and fragile films can be intactly and accurately wrapped onto delicate surfaces, such as microscale microorganisms and optical fibers. Two-micrometer-thick silicon films, without any stretchable engineering, can form conformal neural-electronic interfaces by being drop-printed on nerves and brain tissue. The interfaces achieve light-controlled in vivo neuromodulation with high spatiotemporal resolution.

Bioelectronic interfaces have been proven as a promising platform for applications including high-fidelity physiological monitoring, real-time prosthetic control, and long-term rehabilitation assistance (*1*–*5*). These electronic interfaces, typically <50 μm thick, are fabricated on planar substrates (*6*–*8*) and then wrapped on three-dimensional (3D) objects during operation (*9*–*11*). Conformal wrapping of the films requires localized stretching, bending, and compression, which can damage the fragile metal- or silicon-based components within the film devices (*12*, *13*). Several strategies have been proposed to achieve conformal wrapping of bioelectronic interfaces, such as designing nonstretchable materials into intricate structures (*14*–*16*) or replacing them with stretchable organic materials (*17*–*19*). However, these approaches often introduce additional design, processing procedures, and molecular or phase engineering challenges, complicating the design and fabrication of bioelectronic interfaces and compromising device performance (*20*, *21*). Achieving damage-free wrapping of nonstretchable films onto 3D objects will effectively streamline these processes, but it remains challenging.

The difficulty lies in stress accumulation during the deformation of nonstretchable films, which leads to rupture when the fracture strain is exceeded. Therefore, damage-free wrapping of nonstretchable films can be achieved if we can effectively manage and release the intrafilm stress. In nature, biofilms such as the stratum corneum resist mechanical failure through a "slide" mechanism (*22*, *23*). Despite a low elongation limit (~10%), it accommodates skin deformation up to 100% strain by sliding laterally over the underlying tissue (Fig. 1B), achieving a 2D-to-3D deformation through local wrinkling rather than stretching (*24*–*26*). Because bending generates ~10^6 times less stress than stretching (fig. S1 and supplementary text, section 1), this sliding strategy can quickly release the stress and effectively prevent film damage.

Inspired by the natural mechanism, we propose a "drop-printing" approach to conformally wrap films, whether stretchable or nonstretchable, onto arbitrarily shaped objects, without damaging the films or target surfaces (movie S1). Our method uses droplets to transfer and complete the wrapping process, creating a lubricating layer between the film and the target surface. The liquid layer not only generates capillary forces that drive conformal deformation but also facilitates local sliding during shape-adaptive deformation. This sliding behavior prevents the film from stretching, thereby effectively reducing mechanical stress during deformation. By precisely controlling the three-phase contact line (TCL) behavior, we prevent the film's overall movement and enhance positional accuracy.

Dynamic stress release during film deformation by drop-printing

The drop-printing process for film devices involves using a droplet to pick up the film device (fig. S2), moving it to the substrate, releasing the droplet for printing, and wrapping the film onto the target surface (Fig. 1A). Unlike the conventional soft stamp transfer method that induces severe stress concentration, drop-printing enables dynamic stress release through a skin-inspired sliding mechanism (Fig. 1B). After printing, the droplet spontaneously permeates the microstructures on the target surface, forming a liquid layer that separates the film from the surface. This interfacial fluid acts as a lubricating layer that generates capillary pressure to assist deformation (*27*) and reduces solid-solid friction to low viscous drag (~10^{-9} N). As shown in Fig. 1C, the boundary of a gold (Au) film drop-printed on a microstructured surface demonstrates an obvious sliding during the deformation process. This allows the film to conformally wrap by forming localized wrinkles rather than experiencing in-plane stretching, thereby effectively reducing internal stress accumulation (*28*, *29*). We performed numerical simulations comparing the stress evolution of films wrapped onto highly curved surfaces using drop-printing and the conventional method (Fig. 1D and movie S2). In both cases, stress arises as the film deforms from a planar shape to a 3D contour. However, in drop-printing, this stress is dynamically released via sliding over the lubricating liquid, resulting in a rapid reduction in intrafilm stress, whereas the conventional method causes critical stress accumulation owing to the lack of stress-release pathways (Fig. 1E and fig. S3). Detailed comparisons with established film transfer methods are provided in fig. S4 and supplementary text, section 2.

The stress regulation capability of the drop-printing is demonstrated by using a patterned 150-nm-thick Au film, which is extremely sensitive to mechanical stress and can rupture from even a light air blow (fig. S5). When drop-printed on a 3D surface, the ultrathin Au pattern conformally adheres to the target surface without any surface modification (Fig. 1F). Scanning electron microscope images confirm that the cross lines of the pattern remain fully intact, whereas the same film transferred with conventional method exhibits notable fragmentation (Fig. 1G, fig. S6, and movie S3). This nondestructive conformal wrapping allows the unstretchable Au film to stably adhere to the substrate underwater for >2 weeks (fig. S7) and remain intact under repeated cycles of finger bending and straightening

[1]Key Laboratory of Green Printing, CAS Research/Education Center for Excellence in Molecular Sciences, Institute of Chemistry, Chinese Academy of Sciences, Beijing, China. [2]Department of Neurosurgery, Beijing Tiantan Hospital, National Center for Neurological Disorders, Capital Medical University, Beijing, China. [3]Department of Mechanics, Tianjin University, Tianjin, China. [4]Institute of Materials Research and Engineering (IMRE), Agency for Science, Technology and Research (A*STAR), Singapore, Republic of Singapore. [5]Institute of Burn Research, Chongqing Key Laboratory of Wound Repair and Tissue Regeneration, Southwest Hospital & State Key Lab of Trauma and Chemical Poisoning, Army Medical University (Third Military Medical University), Chongqing, China. [6]University of Chinese Academy of Sciences, Beijing, China. [7]Innovative Center for Flexible Devices (iFLEX), Max Planck-NTU Joint Lab for Artificial Senses, School of Materials Science and Engineering, Nanyang Technological University, Singapore, Republic of Singapore. ***Corresponding author. Email: ylsong@iccas.ac.cn (Y.S.); chenxd@ntu.edu.sg (X.C.); jwttyy@126.com (W.J.); lihz@iccas.ac.cn (H.L.)** †These authors contributed equally to this work.

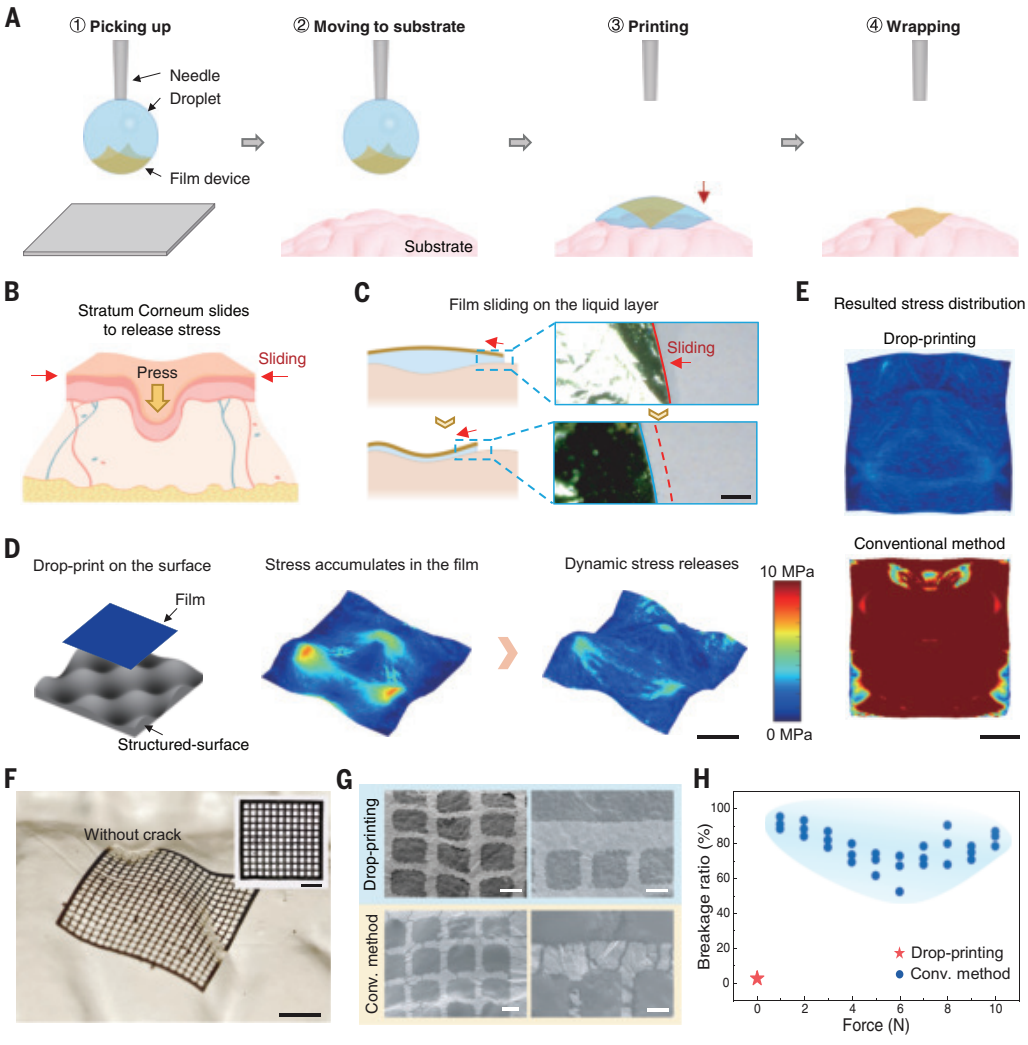

Fig. 1. Stress-regulated film transfer via drop-printing. (**A**) Scheme of the drop-printing process. (**B**) Stress release through transverse sliding of stratum corneum under external force. (**C**) Solid-liquid interface formation enables localized sliding during drop-printing. Scale bar, 200 μm. (**D**) Dynamic stress release during the film conformal deformation. Scale bar, 500 μm. (**E**) Uniform stress distribution achieved by drop-printing versus stress concentration in conventional soft stamp transfer method. Scale bar, 500 μm. (**F**) Optical image of a patterned Au film with a thickness of 150 nm drop-printed on an uneven surface. Scale bar, 1 mm. The inset shows a drop-printed Au film in a transmission mode. Scale bar, 1 mm. (**G**) Comparison of Au films transferred by drop-printing and conventional method. Scale bars: 140 μm, 120 μm, 160 μm, 130 μm, from upper left to lower right, respectively. (**H**) Summary of applied forces and resulting film integrity for drop-printing and conventional soft stamp transfer method. The data for the soft stamp transfer method were collected by applying varying pressures during the transfer process.

(fig. S8). In addition, drop-printing is a contact-free strategy, applying only a transient droplet impact force (~2 mN for ~10 ms) on the substrate (fig. S9), much smaller than the several-newton force applied for seconds in conventional methods (fig. S10). This indicates that the film is very gently placed in the drop-printing process and then spontaneously achieves nondestructive wrapping of the film. A quantitative comparison of the applied force and the breakage ratio across different transfer methods (Fig. 1H) further highlights the notable advantage of drop-printing (the statistical method of evaluating breakage ratios is detailed in fig. S11). These results conclude that drop-printing is a general method for wrapping films on air-exposed solid surfaces. It is broadly applicable to both stretchable [e.g., polydimethylsiloxane (PDMS)] and nonstretchable (e.g., metals, silicon) films of varying sizes (50 μm to 3 cm) and target substrates with a wide modulus range (5 kPa to 100 GPa) and radii of curvature (>10 μm) (fig. S12). It also offers high positional precision, as demonstrated by drop-printing a 7 × 7 Au film array on a scallop shell (at a spacing of 2.5 mm) with accurate alignment across complex convex and concave features (fig. S13).

Mechanism of droplet control for drop-printing

Controlling droplet behavior on the target surface is crucial for accurate transfer and conformal wrapping. When the droplet picks up the film, capillary force between the film and the needle drives the film to the upper surface of the droplet (fig. S14) (*30*). Upon release, the droplet impacts the target surface and spreads into a spherical cap (Fig. 2, A and B) (*31*), with the film floating on the liquid surface (fig. S15). As the droplet evaporates, capillary attraction at the TCL causes the film to randomly shift, leading to unpredictable deviations D (defined as the distance between the film center and the target center after drying) (Fig. 2C and movie S4). Further investigation concludes that the film movement will be restricted by the TCL (movie S4), suggesting that the location of the film can be regulated by adjusting the size of the TCL, thereby improving the positional accuracy (fig. S16). Numerical simulations demonstrate that optimal alignment occurs when the TCL serves as the circumscribed circle of the film (fig. S17).

To elucidate the parameters governing TCL size, we performed a theoretical analysis. Considering the low impact velocity (<1 $m \cdot s^{-1}$)

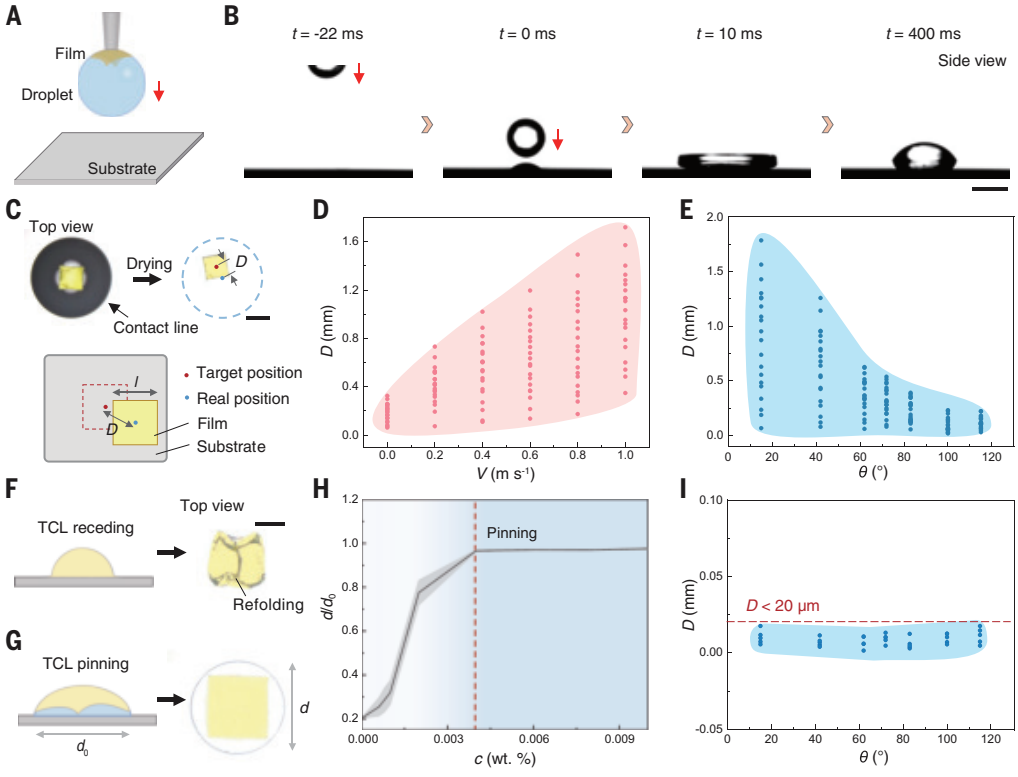

Fig. 2. Controlling the TCL behavior during drop-printing. (**A** and **B**) Dynamic evolution of droplet impact on a solid surface in the drop-printing process. Scale bar, 2 mm. (**C**) Mechanism of the positional deviation in drop-printed film. After impact on the solid surface, a TCL forms around the droplet. The internal flows of the evaporating droplet cause the film to move randomly within the range of the TCL, resulting in positional deviation. Scale bar, 1 mm. (**D**) Effect of droplet impact speed on the positional deviation of the drop-printed film. (**E**) Effect of substrate contact angle on the positional deviation of the drop-printed film. (**F** and **G**) Morphologies of drop-printed films with receding TCL (F) or pinning TCL (G). Scale bar, 500 μm. (**H**) Effect of the concentration of gelatin on the TCL pinning behavior. Shaded areas indicate standard deviations, calculated from five independent experiments. (**I**) Positional deviation of the drop-printed film can be reduced to <20 μm by regulation of TCL behavior.

and small viscosity (<2 mPa·s) of the droplet (supplementary text, section 3, and fig. S18), it is reasonable to assume an energy balance between the preimpact and maximum spreading states (*31*); this yields the relation $We + 12 = \left(\frac{d_0}{2R}\right)^2\left[3\left(1-\cos\theta_e\right)+4\frac{We}{\sqrt{Re}}\right]$. This equation indicates that the TCL diameter d_0 is positively correlated with the droplet impact velocity V and the radius R and negatively correlated with the equilibrium contact angle θ_e (where the Weber number $We = \rho V^2 R/\gamma$ and the Reynolds number $Re = \rho VR/\eta$, with γ and η as the surface tension and dynamic viscosity of the droplet, respectively) (*32*). Experimental results support this analysis: For fixed droplet size, lower impact velocity and larger contact angle lead to smaller film deviation (Fig. 2, D and E). The detailed theoretical analysis is shown in supplementary text, section 4. Therefore, when the droplet impact velocity is reduced to zero, the optimal droplet radius to generate an ideal-sized TCL (matching the film's circumscribed circle) is given by $R = \frac{\sqrt{2}}{4} l\left[\frac{\sin^3\theta_e}{2(1-\cos\theta_e)(2-\cos\theta_e-\cos^2\theta_e)}\right]^{-1/3}$, where l is the side length of the film. The droplet size required to locate the 1-mm film on surfaces with different contact angles is shown in fig. S19. The agreement between the experimental data (brown dots) and the theoretical results (green line) demonstrates the validity of the proposed model.

To ensure conformal wrapping, TCL receding during evaporation must be prevented, as it can cause the film refolding (Fig. 2F, fig. S20, and movie S5). To address this, we introduce additives to the droplets that will accumulate at the TCL (by capillary and Marangoni flows), thereby inducing a receding-to-pinning transition (Fig. 2G) (*33*). Adding trace amounts of gelatin [0.004 weight % (wt %)] does not alter the contact angle (fig. S21) and impact dynamics (fig. S22) but effectively pins the TCL throughout the drying process (Fig. 2H). This is attributed to the hydrophilic functional groups on gelatin molecules, which interact with the polar groups on the substrate, thereby stabilizing the contact line. This strategy is broadly applicable across surfaces with a wide range of contact angles (fig. S23). Gelatin is not the only suitable additive. Selection criteria for other candidates are summarized in supplementary text, section 5, and fig. S24. Using this method, we achieve highly accurate film placement with deviations <20 μm for 1-mm films (Fig. 2I and fig. S25), outperforming existing methods (fig. S26). Furthermore, film picking and wrapping are essential steps in the drop-printing. These two processes are driven by capillary forces between the film and the liquid, which have been demonstrated effective for film transfer (*34*) and conformal deformation (*35*) in bioelectronic interfaces. The underlying mechanisms are theoretically analyzed in supplementary text, section 6, and fig. S27.

General demonstrations of drop-printing

The drop-printing approach enables damage-free wrapping and high-precision transfer of various films, demonstrating a wide range of applications. For instance, nanometer-thick films can be conformally wrapped onto small biological structures. As shown in Fig. 3A, Au films were successfully drop-printed onto the surfaces of five randomly distributed paramecia (fig. S28), which are extremely pressure-sensitive (*36*). The magnified view (Fig. 3B) reveals that the films form conformal, metalized "armors" without causing damage, demonstrating potential applications in bioreactors, microimaging, and intelligent sensing (*37*–*39*). Similarly, an Au film is drop-printed onto a 10-μm-diameter dandelion fiber (Fig. 3C). The droplet reflows around the fiber, enabling conformal wrapping on its high-curvature surface. The fiber is not required to separate from the dandelion, and its entire structure remains intact throughout the drop-printing process (inset, Fig. 3C). Moreover, this technique enables the transfer of objects with diverse materials and geometries. Demonstrations include a SiO_2 microsphere (20-μm diameter) positioned on the tip of a thumbtack (Fig. 3D), graphene nanosheet wrapped around optical fibers (Fig. 3E), fragile 400-nm-thick Si film wrapped onto a 500-μm-diameter glass tube (Fig. 3F), and Au film wrapped on microstructured substrates conforming to reentrant geometries (Fig. 3G). Beyond small films, drop-printing also facilitates the wrapping of large-area films, as demonstrated by an Au pattern (3-cm side length, 150 nm thick) coated onto a skin surface (fig. S29). A systematic study of the transferable film limitations, including film wettability (fig. S30), thickness (fig. S31), size (fig. S32), weight, and the roughness of the target substrate (fig. S33), is provided in supplementary text, section 7.

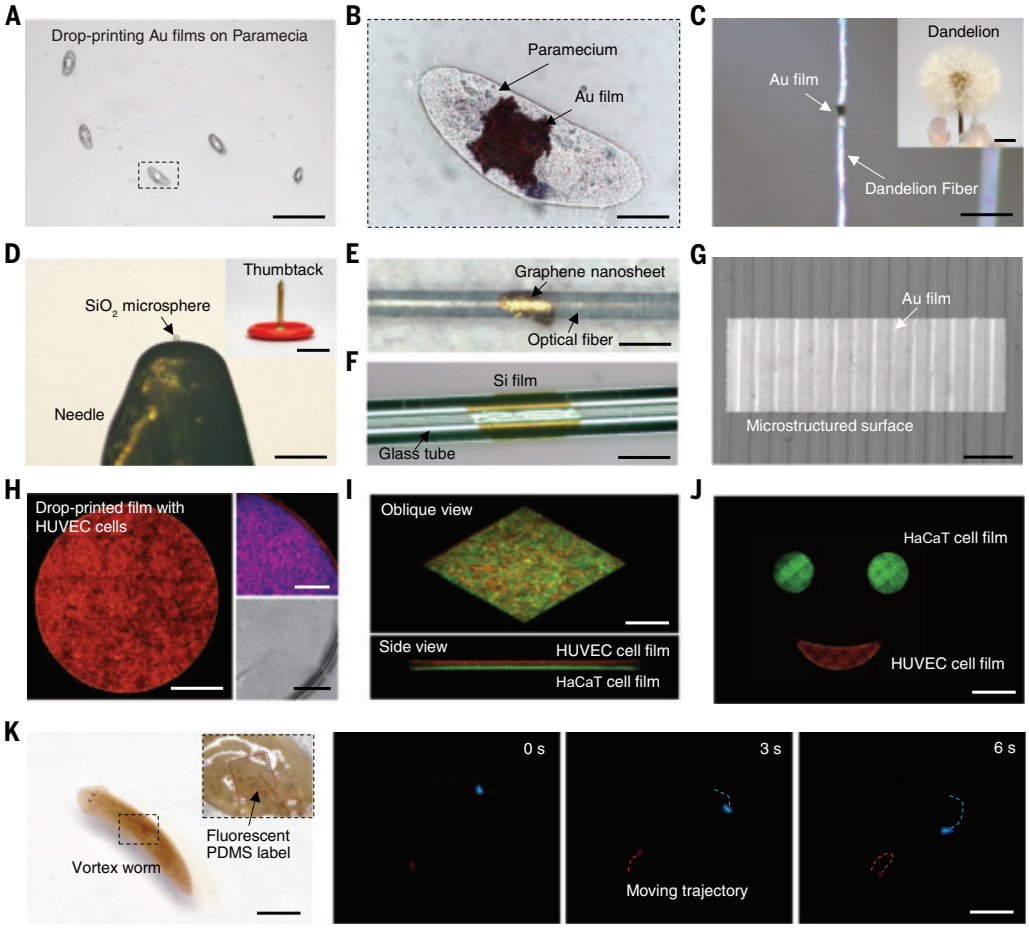

Fig. 3. General demonstration of drop-printing. (**A** to **C**) Precise and nondestructive wrapping of ultrathin films onto small biological surfaces. (A) Wrapping Au films on randomly dispersed paramecia. Scale bar, 500 μm. (B) Enlarged image of the paramecium marked as the black box in (A). Scale bar, 50 μm. (C) Wrapping Au film on a single fiber of dandelion without damaging its structure. Scale bar, 50 μm. The inset is an image of the dandelion after film transfer. Scale bar, 1 cm. (**D** to **G**) Drop-printing of various materials with different topologies on curved surfaces. (D) Placing a SiO_2 microsphere on the tip of a thumbtack. Scale bar, 200 μm. Scale bar of the inset image is 1 cm. (E) Wrapping of graphene nanosheets onto the surface of a multimode optical fiber. Scale bar, 50 μm. (F) Wrapping silicon film around the outside of the glass tube. Scale bar, 500 μm. (G) Drop-printing Au film on microstructured surfaces with protrusion and reentrant features. Scale bar, 500 μm. (**H** to **K**) Customized droplet composition for special film wrapping. (H) to (J) Drop-printing of the cell-coated films with PBS droplets. (H) Stained images of human umbilical vein endothelial cell (HUVEC) film drop-printed on the surface of the hydrogel. The left is an immunofluorescence image of HUVEC (red, F-actin), the upper right is an immunofluorescence image of HUVEC (blue, 4′,6-diamidino-2-phenylindole; red, F-actin), and the lower right is a phase contrast image of HUVEC. Scale bar of the left image is 500 μm. Scale bars of the right images are 100 μm. (I) Images of two stacked cell films. Scale bar, 500 μm. (J) Smile face made of cell films that were stained different colors. Scale bar, 2 mm. (K) Adding polydopamine to droplets for bioadhesion of film. The fluorescent film can be firmly fixed on the back of the planarian, enabling the tracking of the planarian in the dark. Scale bars: 3 mm (left), 5 mm (right).

Drop-printing also allows for customization through simple adjustments to droplet composition. For instance, transferring cell films is challenging because of mechanical stress and osmotic imbalances (*40*). With phosphate-buffered saline (PBS) droplets to transfer parylene films seeded with stem cells, the cells can distribute evenly on the target surface without structural collapse (Fig. 3H). These cell films can be stacked (Fig. 3I) or aligned into precise patterns (Fig. 3J), with tunable intercellular spacing via cell-substrate adhesion control (fig. S34). Furthermore, the type and concentration of additives within the droplet can be tuned to modulate interfacial interactions, unlocking functional capabilities. For instance, polydopamine-containing droplets enhance the adhesion of fluorescent PDMS tags to soft-bodied worms, enabling long-term trajectory tracking under ultraviolet light (Fig. 3K and movie S6). Increasing the gelatin concentration to 0.05 wt % facilitates its aggregation at the film-substrate interface, enhancing the adhesion of Au film to the substrate from 0.0023 to 0.06 $N \cdot m^{-1}$ (fig. S35), and polyvinyl alcohol serves as an acid-stable alternative additive, enabling a strong and stable adhesion even under conditions with a pH of 1 (fig. S36). In addition, drop-printing requires minimal specialized equipment and can be performed with basic tools such as pipettes or micropipettes (fig. S37).

Neuromodulation by drop-printed bioelectronic interfaces

We also demonstrate the application of drop-printed semiconductor films as high-performance bioelectronic interfaces for neuromodulation (*41*). Optoelectrical nerve stimulation has gained attention in neurological research and clinical medicine because of its minimal invasiveness, wireless control, and absence of genetic modification (*42*–*44*). Si heterojunction films (SiHFs) are commonly used because of their ability to generate photoinduced potentials that induce cation accumulation and trigger action potentials (Fig. 4A and fig. S38) (*45*–*48*). Typically, reducing thickness increases the

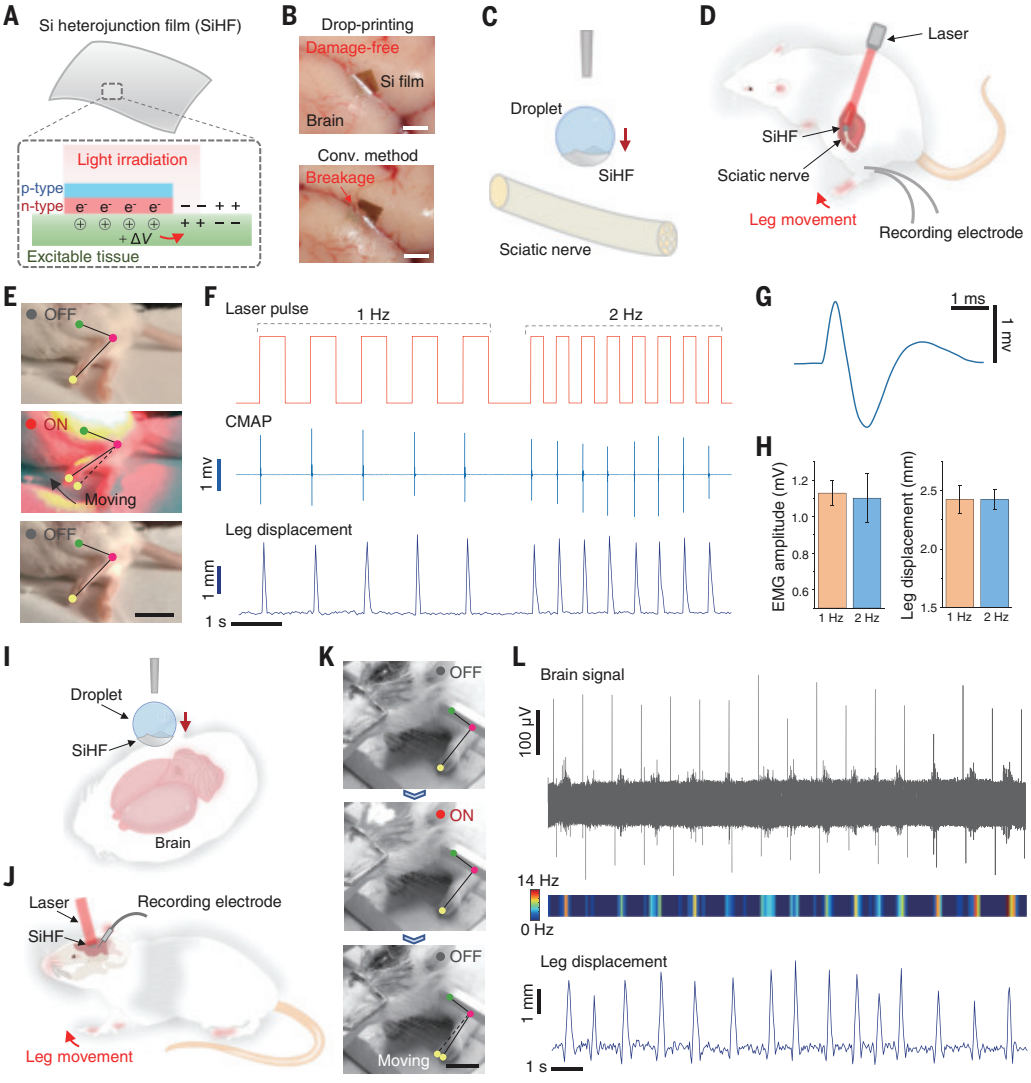

Fig. 4. In vivo optoelectrical neuromodulation by drop-printed SiHF. (**A**) Mechanisms of optoelectrical neuromodulation. Light irradiation across the SiHF generates an electric field, causing cation accumulation and neuronal depolarization. (**B**) Si films transferred on a pig brain through drop-printing and the conventional method. Scale bars: 2 μm. Drop-printing effectively releases stress and prevents the film from breaking during 2D-3D deformation. (**C**) Scheme of drop-printing SiHF on the sciatic nerve in mice. (**D**) Schematic diagram of sciatic nerve stimulating and recording in mice. (**E**) Images before (up) and after (down) photostimulation showing hindlimb movement. Scale bar, 5 mm. (**F**) Synchronized images of the optical signal, electromyogram (EMG) signals, and amplitude of hindlimb movement. (**G**) Individual CMAP signals recorded by optoelectrical stimulation. (**H**) Amplitudes of CMAP signal and leg movement at different laser frequencies. Error bars represent standard deviations calculated from the data shown in (F). At 1 Hz, the EMG amplitude was 1.13 ± 0.07 mV, and leg displacement was 2.43 ± 0.12 mm; at 2 Hz, the EMG amplitude was 1.10 ± 0.13 mV, and leg displacement was 2.43 ± 0.09 mm. (**I** to **L**) In vivo brain stimulation by drop-printing SiHF. (I) SiHF drop-printing on the surface of rat brain. (J) Schematic diagram of brain stimulating and recording in the rat. (K) Movement of rat left forelimb before and after light stimulation. Scale bar, 5 mm. (L) Synchronized images of brain electrophysiological signals and amplitude of forelimb movement.

flexibility of SiHFs but weakens mechanical strength, increasing the fracture risk during the transfer and wrap processes. Although processing SiHFs into stretchable structures and encapsulating them with polymer can mitigate this issue, it introduces additional fabrication complexity and biocompatibility concerns. Conversely, through drop-printing, SiHFs can be directly wrapped on tissues and form conformal bioelectronic interfaces without any stretchable engineering.

In Fig. 4B, we compare silicon films (400 nm thick) transferred onto a pig brain using different methods. Drop-printing dynamically releases stress within the silicon film, allowing it to be precisely, conformally, and nondestructively wrapped onto the brain surface. By contrast, the conventional pressing method causes the fragile film to break. We further demonstrate the neuromodulation performance of the nerve-silicon interfaces. With PBS droplets, SiHF was drop-printed onto the nerve of a mouse (Fig. 4C), followed by near-infrared (653 nm, ~1 $W \cdot cm^{-2}$) laser irradiation. Infrared thermal imaging confirms that the photothermal effect of the film did not influence neural activity (fig. S39). A camera and a recording electrode are used to capture hindlimb movements and compound muscle action potentials (CMAPs) (Fig. 4D). As shown in Fig. 4E and movie S7, the light instantaneously triggers hindlimb movement (~2-mm amplitude). The synchronized laser pulse, CMAP signals, and hindlimb movements shown in Fig. 4F evidence successful nerve stimulation by the SiHF (*47*). An enlarged individual stimulated CMAP signal is shown in Fig. 4G. Statistical results of CMAP signals and leg movements at

different laser frequencies show comparable amplitudes, demonstrating the excellent performance of the drop-printed device (Fig. 4H).

Brain activity can also be regulated by the drop-printed nerve-electronic interface. We drop-print SiHF on the right M1 region of a rat's brain (Fig. 4I) and use a camera and a recording electrode to capture left-forelimb movements and brain activity signals (Fig. 4J). Upon stimulation with 1-Hz pulsed near-infrared light (653 nm), the rat exhibits regular left-forelimb movements (Fig. 4K and movie S8), accompanied by distinct neural spikes (fig. S40) interspersed between optoelectrical artifacts of ~300 μV (Fig. 4L), indicating successful evoking of brain activity. The consistency of the heatmap of neural responses with the forelimb movements further confirms the correlation between light irradiation and forelimb movements (*45*, *48*).

In summary, we demonstrated a drop-printing strategy, achieving high-precision, damage-free, and conformal wrapping of bioelectronic interfaces. We revealed that the lubricant-induced sliding effect, coupled with the capillary-induced deformation, enables dynamic stress release and effectively avoids the destructive stress concentration during the conformal deformation process. By matching the droplet impact dynamics and film morphology, we proposed the drop-printing control mechanism and realized micrometer-scale positional accuracy. This allowed us to wrap diverse, fragile films on the microscale, pressure-sensitive, and high-curvature objects, and even microorganisms. On this basis, we demonstrated neural-electronic interfaces on animal tissues and achieved in vivo photo-induced neuromodulation.

REFERENCES AND NOTES

1. D. H. Kim *et al.*, *Science* **333**, 838–843 (2011).
2. S. Park *et al.*, *Nature* **561**, 516–521 (2018).
3. X. Yu *et al.*, *Nature* **575**, 473–479 (2019).
4. D. Zhong *et al.*, *Nature* **627**, 313–320 (2024).
5. S. Zhou *et al.*, *Nature* **629**, 810–818 (2024).
6. C. B. Cooper *et al.*, *Science* **380**, 935–941 (2023).
7. Y. Kim *et al.*, *Science* **377**, 859–864 (2022).
8. Z. Jiang *et al.*, *Nat. Electron.* **5**, 784–793 (2022).
9. H. Yuk, J. Wu, X. Zhao, *Nat. Rev. Mater.* **7**, 935–952 (2022).
10. Z. Xue *et al.*, *Sci. Adv.* **8**, eabm6922 (2022).
11. Z. Yan *et al.*, *Science* **375**, 852–859 (2022).
12. K. Sim *et al.*, *Nat. Electron.* **2**, 471–479 (2019).
13. Y. Shin *et al.*, *Nat. Mater.* **23**, 1411–1420 (2024).
14. D. H. Kim *et al.*, *Science* **320**, 507–511 (2008).
15. J. A. Rogers, T. Someya, Y. Huang, *Science* **327**, 1603–1607 (2010).
16. X. Cheng *et al.*, *Science* **379**, 1225–1232 (2023).
17. J. Xu *et al.*, *Science* **355**, 59–64 (2017).
18. P. Li *et al.*, *Science* **384**, 557–563 (2024).
19. Y. Dai *et al.*, *Science* **386**, 431–439 (2024).
20. Y.-K. Lee *et al.*, *Sci. Adv.* **6**, eaax6212 (2020).
21. J. Hure, B. Roman, J. Bico, *Phys. Rev. Lett.* **106**, 174301 (2011).
22. A. Pissarenko, M. A. Meyers, *Prog. Mater. Sci.* **110**, 100634 (2020).
23. F. H. Silver, L. M. Siperko, G. P. Seehra, *Skin Res. Technol.* **9**, 3–23 (2003).
24. N. Bowden, S. Brittain, A. G. Evans, J. W. Hutchinson, G. M. Whitesides, *Nature* **393**, 146–149 (1998).
25. J. Huang *et al.*, *Science* **317**, 650–653 (2007).
26. R. D. Schroll *et al.*, *Phys. Rev. Lett.* **111**, 014301 (2013).
27. J. Bico, É. Reyssat, B. Roman, *Annu. Rev. Fluid Mech.* **50**, 629–659 (2018).
28. D. Kumar, J. D. Paulsen, T. P. Russell, N. Menon, *Science* **359**, 775–778 (2018).
29. J. D. Paulsen *et al.*, *Nat. Mater.* **14**, 1206–1209 (2015).
30. G. Xie *et al.*, *Nat. Chem.* **14**, 208–215 (2022).
31. C. Josserand, S. T. Thoroddsen, *Annu. Rev. Fluid Mech.* **48**, 365–391 (2016).
32. D. C. Vadillo, A. Soucemarianadin, C. Delattre, D. C. D. Roux, *Phys. Fluids* **21**, 122002 (2009).
33. J. H. Snoeijer, B. Andreotti, *Annu. Rev. Fluid Mech.* **45**, 269–292 (2013).
34. H. Li, Z. Wang, Y. Cao, Y. Chen, X. Feng, *ACS Appl. Mater. Interfaces* **13**, 1612–1619 (2021).
35. B. L. Borgne *et al.*, *Adv. Mater. Technol.* **4**, 1800600 (2019).
36. C. Campillo *et al.*, *New J. Phys.* **14**, 125016 (2012).
37. R. F. Fakhrullin, Y. M. Lvov, *ACS Nano* **6**, 4557–4564 (2012).
38. R. B. Song *et al.*, *Angew. Chem. Int. Ed.* **129**, 10652–10656 (2017).
39. H. K. Baca *et al.*, *Science* **313**, 337–341 (2006).
40. J. A. Park *et al.*, *Adv. Mater.* **35**, e2204390 (2023).
41. J. A. Rogers, M. G. Lagally, R. G. Nuzzo, *Nature* **477**, 45–53 (2011).
42. Y. Jiang, B. Tian, *Nat. Rev. Mater.* **3**, 473–490 (2018).
43. K. L. Montgomery *et al.*, *Nat. Methods* **12**, 969–974 (2015).
44. M. Silverå Ejneby *et al.*, *Nat. Biomed. Eng.* **6**, 741–753 (2022).
45. Y. Jiang *et al.*, *Nat. Biomed. Eng.* **2**, 508–521 (2018).
46. P. Li *et al.*, *Nature* **626**, 990–998 (2024).
47. A. Prominski *et al.*, *Nat. Mater.* **21**, 647–655 (2022).
48. Y. Huang *et al.*, *Nat. Biomed. Eng.* **7**, 486–498 (2023).

ACKNOWLEDGMENTS

We thank X. Sheng and X. Fu from Tsinghua University, Z. Fan from the Institute of Semiconductors Chinese Academy of Sciences, and Y. Zhang from Peking University for the valuable discussions. **Funding:** This work was supported by the National Natural Science Foundation of China (nos. 52321006 and T2394484 to Y.S., 22272182 and 52293473 to H.L., 82402429 to W.Z., 12202248 to W.F., and 82372528 to Z.L.), the National Key R&D Program of China (nos. 2023YFE0111500 to Y.S. and 2024YFF1502800 to W.J.), the China Postdoctoral Science Foundation (nos. 2023M733554 and 2024T170940 to A.L.), the Youth Innovation Promotion Association of CAS (no. 2023039 to H.L.), and the Beijing Nova Program (nos. 20230484291 and 20240484643 to H.L.). **Author contributions:** Y.S., X.C., W.J., H.L., and A.L. guided the whole research project. A.L., Y.S., and H.L. conceived the research. A.L. performed the experiments. W.F. performed numerical calculations. Z.L. performed cell experiments. A.L., W.Z., and Q.X. performed animal experiments. A.L., H.L., Y.L., and Y.S. wrote the manuscript with input from all authors. All authors participated in drafting the manuscript and interpreting the data. **Competing interests:** The authors declare that they have no competing interests. **Data and materials availability:** All data are available in the manuscript or the supplementary material.

SUPPLEMENTARY MATERIALS

science.org/doi/10.1126/science.adw6854
Materials and Methods; Supplementary Text; Figs. S1 to S43; Tables S1 and S2; References (*49*–*55*); MDAR Reproducibility Checklist; Movies S1 to S8

Submitted 12 February 2025; resubmitted 17 June 2025; accepted 14 July 2025

10.1126/science.adw6854

INSECT DECLINES

Genomic signatures indicate biodiversity loss in an endemic island ant fauna

Cong Liu[1,2,3]*, Eli Sarnat[1], Jo Ann Tan[4], Julia Janicki[1], John Deyrup[1], Masako Ogasawara[1], Miquel L. Grau[4], Lijun Qiu[4], Francisco Hita Garcia[1,5], Georg Fischer[1], Akanisi Caginitoba[6], Nitish Narula[1], Clive T. Darwell[1], Yasuhiro Kubota[2], Naomi E. Pierce[3], Alexander S. Mikheyev[4,7]*†, Evan P. Economo[1,8]*†

Insect populations have declined worldwide, but the extent and drivers of these declines are debated. Most studies rely on field surveys performed in the past century, leaving gaps in our understanding of longer-term trends. Using a "community genomics" approach, we estimated community assembly over millions of years and more recent demographic trends of ant species in the Fijian archipelago. We found that 79% of endemic species are in decline, starting after the arrival of humans approximately 3000 years ago and accelerating in the past 300 years, whereas recent arrivals are expanding. The primary correlate of population decline among endemic species was found to be sensitivity to habitat disturbance. This study demonstrates the value of contemporary collections for estimating long-term community trends and highlights the vulnerability of endemic island species to anthropogenic change.

Insects and other arthropods comprise much of the animal diversity on the planet (*1*). They are a critical component of terrestrial environments, providing ecosystem services including pollination, biological controls, decomposition, and nutrient cycling (*2*). However, recent reports of substantial declines in insect abundance, biomass, and diversity have raised global alarm over the "insect apocalypse" (*3*–*15*). These declines have been attributed to several potential causes, including habitat loss and degradation (*11*), agricultural intensification (*16*), climate change (*17*, *18*), insecticide use (*19*), and light pollution (*20*), but their nature and extent are still hotly debated and it is far from clear that they are a general phenomenon (*13*). Furthermore, many studies have suggested that the Anthropocene has accelerated change, favoring winners and losers rather than general directional declines (*7*). However, although humans have been affecting the planet for thousands of years, studies evaluating evidence for insect declines have been based either on records collected over the past few decades (*7*) or are from museum collections that are at most a few centuries old (*21*, *22*). This narrows the scope of our knowledge and understanding to well-sampled areas and recent timescales. Evaluating trends over longer timescales in regions of the globe critical for conservation would illuminate a broader picture of insect declines across human history and complement more recent studies based on direct observations. An analysis spanning thousands of years should provide additional insight into the mechanisms at play by separating short-term or recent drivers from those that have been acting over decades and centuries.

Recent advances in genomic techniques offer a deeper time window into historical population and community trends (*23*). These developments can provide insights into insects' demographic responses to historical human activities and other phenomena without collections or observations that span the time frame of interest. Although some anthropogenic effects such as increased pesticide use and anthropogenic climate change are recent, others such as deforestation and land use change are relatively old. For example, pollen cores from islands suggest that the plant community change accelerated after the arrival of humans but well before the industrial age (*24*). Whether historical human activity substantially shaped present-day insect populations is important for understanding the evolutionary and geographic context of winners and losers in the Anthropocene.

Here, we used the ant community of the Fijian archipelago as a model system with which to evaluate long-term population and community trends and their biogeographic, ecological, and historical context. To do this, we used a community genomics approach (i.e., inferring patterns and processes using genomic data across a community of species) applied to contemporary collections. Ants are key players in most terrestrial ecosystems in terms of abundance, richness, and function (*25*), and they have served as reliable indicator taxa for a diversity of other organisms (*26*). Remote island systems are home to some of the most fascinating but geographically restricted and threatened lineages on the planet (*27*–*29*). The Fijian archipelago is a biodiversity hotspot harboring a high number of endemic ant species (*30*), many of which have evolved through localized radiations (*31*–*34*). If human activities have been causing declines of insect populations in Europe and other continents (*13*), then the decline may be much more pronounced on remote islands such as Fiji, where species evolving in isolation are thought to be more vulnerable. Moreover, the consequences of human impacts on islands often unfold rapidly and have caused many documented extinctions during settlement history (*35*). Therefore, island systems provide a good model for evaluating long-term trends and the impacts of human activities to shed light on present-day insect declines.

Fiji was settled by Lapita migrations ~3000 years ago (ka) (*36*–*38*), and slash-and-burn (Swidden) agriculture in Fiji dates to ~1.8 ka (*38*). After the initial contact with Europeans in the 17th century, Fiji was connected to global commerce networks. By the 19th century, the expansion of commercial agriculture accelerated human population growth and associated land use change. Since that time, a large number of species have arrived in Fiji from around the globe (*39*). In many terrestrial ecosystems, especially islands, introduced ants have caused detrimental ecological impacts on native biodiversity (*40*–*43*). We aimed to correlate these changes in land use over the course of human settlement and increases in globalization with ant population size changes to identify (i) whether there is evidence of widespread declines and (ii) how habitat affinities, specifically elevation and disturbance tolerance, allow species to "win or lose" in the new ecological regime.

Results and discussion

We applied high-throughput museumomic sequencing [a restriction site–associated DNA sequencing (RADseq) protocol] to specimens collected more than a decade ago as part of a biodiversity inventory (*30*). This approach of reduced representation sequencing was chosen to meet the challenges of unlocking information from museum collections from diverse tropical environments. These challenges include that: (i) the DNA is often degraded and fragmented; (ii) the

[1]Biodiversity and Biocomplexity Unit, Okinawa Institute of Science and Technology Graduate University, Onna, Okinawa, Japan. [2]Faculty of Science, University of the Ryukyus, Nishihara, Okinawa, Japan. [3]Department of Organismic and Evolutional Biology, Museum of Comparative Zoology, Harvard University, Cambridge, MA, USA. [4]Ecology and Evolution Unit, Okinawa Institute of Science and Technology Graduate University, Onna, Okinawa, Japan. [5]Center for Integrative Biodiversity Discovery, Museum für Naturkunde, Berlin, Germany. [6]Wildlife Conservation Society, Suva, Fiji. [7]Research School of Biology, Australian National University, Canberra, Australian Capital Territory, Australia. [8]Department of Entomology, University of Maryland, College Park, MD, USA. ***Corresponding author. Email: cong.liu0514@gmail.com (C.L.); alexander.mikheyev@anu.edu.au (A.S.M.); economo@umd.edu (E.P.E.)** †These authors contributed equally to this work.

species and their boundaries are incompletely described, thus requiring clarification through the process of sequencing across the community; and (iii) there is a need to sample across geographic space to capture biogeographic and population genetic signals. The latter two issues require an approach that scales to many individuals. We sequenced 4132 specimens from 144 ant species and 40 genera. Because species boundaries for many Fijian ant taxa are based on morphological analysis (*30*), we first analyzed the population structure of putative species to confirm species boundaries before proceeding to the population genetics analysis. Although most were confirmed, we split several species complexes into multiple species based on the totality of genetic and post hoc morphological analysis. Conversely, we lumped several previously identified morpho species into a single species when genetic data indicated no significant differentiation. In total, we confirmed 127 species for subsequent analyses (see the materials and methods). We then reconstructed a phylogeny and the colonization history of these lineages to provide evolutionary and biogeographic context for more recent changes. Our phylogenomic analysis revealed that the Fijian ant community was assembled through at least 65 colonization events. First, 26 lineages colonized Fiji naturally and led to the evolution of 88 endemic species. The high level of endemism was the result of colonizations that occurred millions of years ago followed by both in situ radiation (cladogenesis) and divergence from mainland relatives (anagenesis) (Fig. 1A). This is consistent with previous studies showing that the high endemism of several ant genera in Fiji was generated by postcolonization radiations (*31*–*34*). Second, a further 23 colonizations occurred by widespread species native to the Pacific region. This group is likely a mixture of species that colonized Fiji naturally and others that were brought more recently by human movements within the region. Finally, at least 16 non-native species were brought by humans from outside of the Pacific region (Fig. 1A and figs. S1 and S2) after Fiji was connected to global commerce networks.

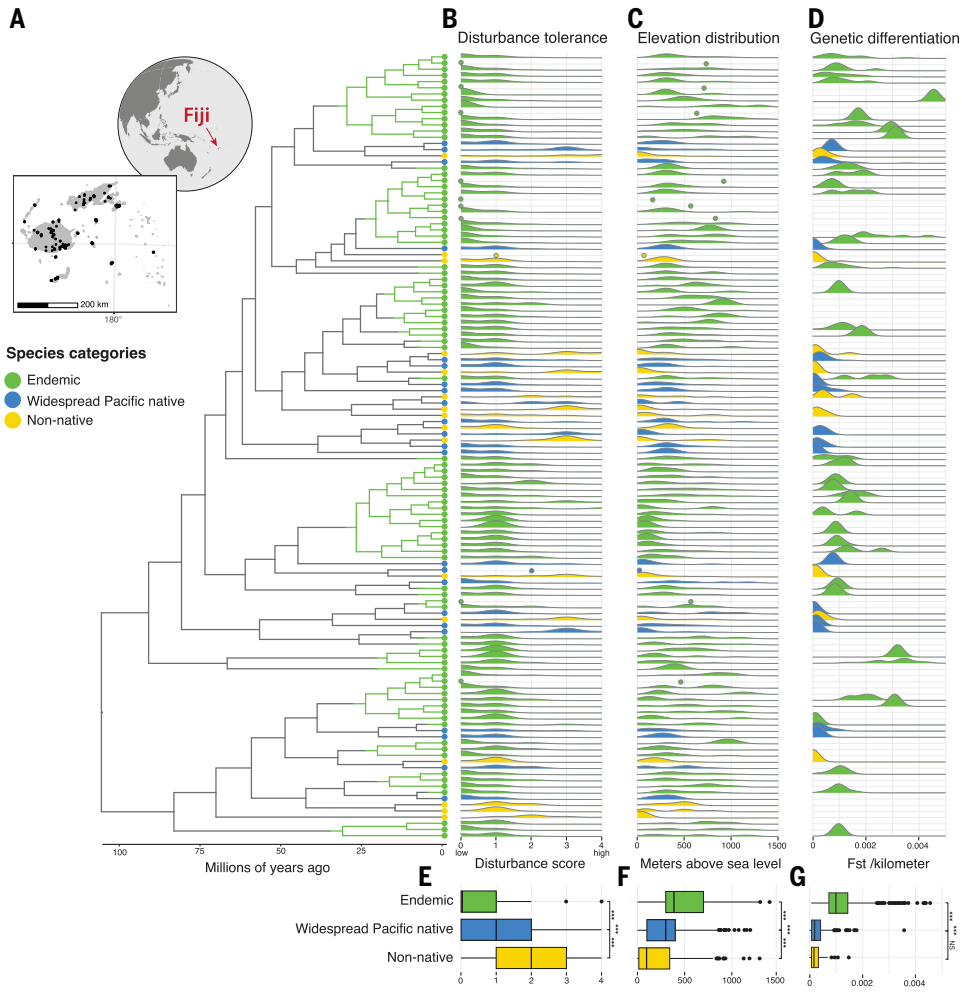

Fig. 1. Three types of ant species in the Fijian archipelago. (**A**) The ant community of Fiji is composed of 88 endemic species derived from 26 colonizations (endemic lineages and clades are shaded green), along with 23 species native to the region and widespread in the Pacific and 16 species non-native to the region arriving after European colonization (fig. S2 and data S8). (**B** and **C**) Density distribution of ecological data for each species indicating that habitat distribution is highly correlated with endemism status. Non-native species and widespread Pacific natives tend to be found in more disturbed habitats found at lower elevations (e.g., urban environments and agricultural plantations), whereas natives are found in less disturbed habitats (e.g., closed canopy primary or secondary forests) that tend to be found at higher elevations. (**D**) Populations of endemic species show higher levels of population genetic structure compared with non-native species or widespread Pacific natives, thus indicating lower levels of gene flow. The distance used in the F_{st}/kilometer calculation represents the closest linear distance between the sampling sites of the pairwise populations being compared. Note that not all species have sufficient sampling for estimating population differentiation. (**E** to **G**) Marginal summaries corresponding to plots (B) to (D) highlighting population-level trends colored by ant species type. These data indicate that the mode of colonization is associated with distinct ecological differences, with more recent arrivals found in marginal habitats associated with anthropogenic disturbance, whereas endemics are restricted to more isolated habitats in the island interiors. Statistical differences for panels (E) to (G) were assessed using posterior distributions from a Bayesian phylogenetic regression model, which accounts for phylogenetic relationships as a random effect. Significant differences between species types are indicated by ***$P < 0.001$; NS, nonsignificant differences ($P > 0.05$).

To examine the population trends of these species, we used demographic modeling (*44*) to characterize changes in effective population size (N_e) for each of the 240 geographic ant populations belonging to 72 species. We found that 79% of endemic species are in decline (Fig. 2A). By contrast, we detected substantial population expansions in both widespread Pacific species and non-native species that occurred rapidly over the past four centuries, with no declines detected in these groups (Fig. 2, B and C). We also found that the reductions in endemic species begin after the arrival of humans ~3000 years ago in Fiji and continued until the present, with most declines concentrated in the previous few hundred years. This coincides with European contact and subsequent colonization, the rise of industrial agriculture, and the arrival of alien species through global trade (Fig. 2A).

The ecological distribution of species across the Fijian landscape offers insights into the divergent patterns of population change. Overall, endemic species are mostly limited to higher elevation, where more

intact habitats are still found (Figs. 1, B, C, E, and F, and 3). They also have greater geographic population differentiation across the Fijian archipelago, suggesting lower gene flow between populations (Fig. 1, D and G). In particular, the endemic species are often confined to upland primary forest, with limited dispersal potential to other habitats. By contrast, nonendemic species are often distributed in the lowland marginal habitats across the whole archipelago (*33*, *34*, *45*). Population trends are strongly correlated with habitat disturbance, because species found in more disturbed lowland habitats typically show population expansion, whereas those now found in more intact upland habitats are declining (Fig. 3). Although most of the endemic species are declining, the few that are increasing are associated with more disturbed habitats (Fig. 3).

Previous work on Melanesian ants interpreted the widespread and endemic species as stages of range expansion, speciation, and

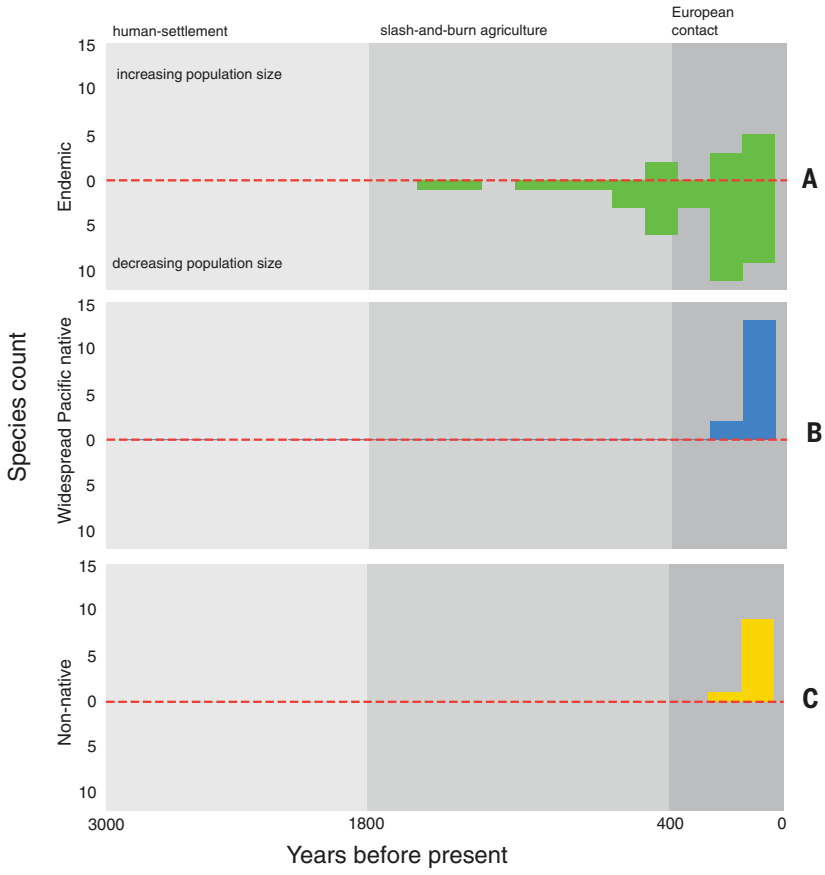

Fig. 2. Ant population size changes are associated with endemism status and the history of human colonization. The first human settlements in Fiji date back to the earliest Lapita colonization ~3000 years ago, with inland settlement occurring ~2500 years ago (*36*–*38*). Slash-and-burn (Swidden) agriculture became widespread ~1800 years ago, leading to significant landcover changes in the archipelago (*38*). Europeans first arrived in the 17th century, and more active colonization commenced in the early 19th century. (**A**) Coalescent reconstruction showing that native ant population declines began soon after the widespread adoption of slash-and-burn agriculture, although they greatly increased in frequency after European colonization, a time associated with the human population growing by more than an order of magnitude. Whereas most endemic species declined, a small number have shown net increases in population size in the past few hundred years. (**B** and **C**) By contrast, no widespread Pacific natives or non-native ants show population declines, but all show signs of recent population expansion. Extant endemic species are experiencing a cryptic population decline, which has increased with the intensity of anthropogenic pressure.

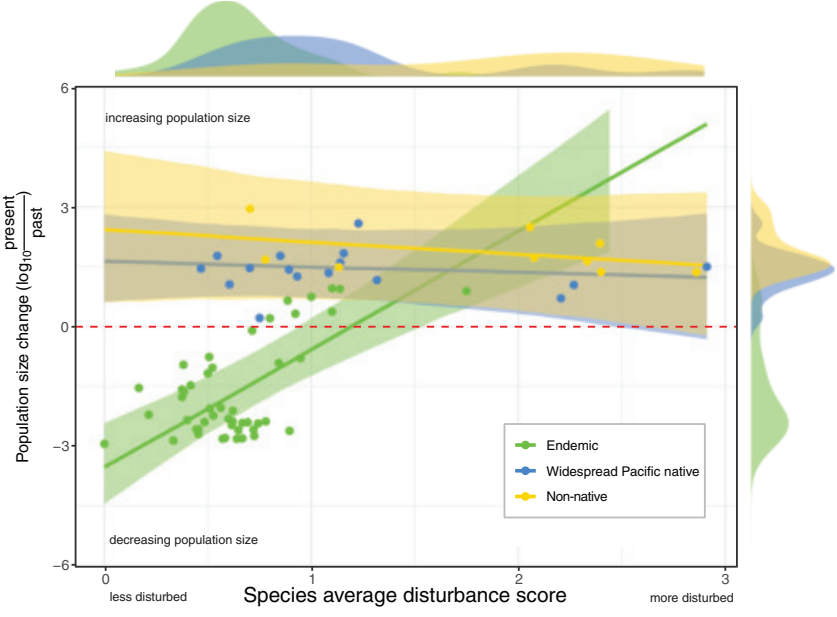

Fig. 3. Endemic population declines are associated with tolerance of disturbed habitats. Bayesian phylogenetic generalized linear mixed model results for population change and the interaction of endemism category and disturbance tolerance. The line indicates the model prediction, and shading is the posterior 95% confidence interval. Marginal distributions are shown on the axes. Historical changes in species average population size are strongly correlated with endemism class, but disturbance tolerance only predicts change for endemic species, and elevation was not significant for any endemism classes. Full posteriors can be seen in fig. S8.

contraction associated with ecological shifts from more marginal habitats to interior primary habitats (i.e., the taxon cycle hypothesis) (*45*, *46*). Regardless of whether this cyclical interpretation is correct, a common theme in island biogeography is the idea that endemic species on islands evolve ecological syndromes (e.g., reduced dispersal ability and reduced defense against enemies) that make them more sensitive to habitat changes and to the impacts of new arrivals (*28*). Furthermore, the vulnerability of insular biotas is underscored by the fact that most documented extinctions (mostly of vertebrates) are from island systems (*43*, *47*). Our results, which are based on contemporary museum collections, show that endemic island insects may also be particularly vulnerable. They are also conservative in their estimation of declines in that they will miss species that have already gone extinct or reached extremely low abundances that caused them to be undetected by surveys.

Conclusions

Recent global attention on insect declines has highlighted how little we know about their long-term trends, especially in tropical regions. Our community genomics approach using museum samples opens a new pathway to the study of insect population and community trends on longer timescales that can complement field monitoring of short-term dynamics. Moreover, it underscores the enduring value and increasing utility of biodiversity collections. Our results suggest that most endemic ant species of the Fijian archipelago have declined since the arrival of humans, whereas species that are tolerant of or adapted to human-dominant habitats, including all widely distributed and alien species, are expanding. If such dynamics occur across geographies, then this will increase global biotic homogenization. Although it is possible that the vulnerability of geographically restricted species may be to some degree a feature of islands, this likely represents a more general phenomenon as mainland habitats become more fragmented and island-like. Small-ranged species on the mainland may have characteristics that make them prone to decline, but future work is needed to test this hypothesis. More generally, these results underscore how ecological and biogeographic context mediates patterns of change, producing "winners" and "losers" as different species become more or less tolerant of Anthropocene environments, respectively. Moreover, it highlights how a singular focus on total biomass or abundance could mask the wholesale collapse of important elements of a community. Our study provides an approach for examining insect decline over much longer timescales, and the results are alarming.

REFERENCES AND NOTES

1. N. E. Stork, *Annu. Rev. Entomol.* **63**, 31–45 (2018).
2. E. O. Wilson, *Conserv. Biol.* **1**, 344–346 (1987).
3. L. M. Casey, H. Rebelo, E. Rotheray, D. Goulson, *Divers. Distrib.* **21**, 864–875 (2015).
4. R. Fox, *Insect Conserv. Divers.* **6**, 5–19 (2013).
5. C. A. Hallmann *et al.*, *PLOS ONE* **12**, e0185809 (2017).
6. C. A. Hallmann, A. Ssymank, M. Sorg, H. de Kroon, E. Jongejans, *Proc. Natl. Acad. Sci. U.S.A.* **118**, e2002554117 (2021).
7. G. A. Montgomery *et al.*, *Biol. Conserv.* **241**, 108327 (2020).
8. G. D. Powney *et al.*, *Nat. Commun.* **10**, 1018 (2019).
9. D. M. Salcido, M. L. Forister, H. Garcia Lopez, L. A. Dyer, *Sci. Rep.* **10**, 422 (2020).
10. F. Sánchez-Bayo, K. A. G. Wyckhuys, *Biol. Conserv.* **232**, 8–27 (2019).
11. S. Seibold *et al.*, *Nature* **574**, 671–674 (2019).
12. R. van Klink *et al.*, *Science* **368**, 417–420 (2020).
13. D. L. Wagner, *Annu. Rev. Entomol.* **65**, 457–480 (2020).
14. D. L. Wagner, R. Fox, D. M. Salcido, L. A. Dyer, *Proc. Natl. Acad. Sci. U.S.A.* **118**, e2002549117 (2021).
15. M. S. Warren *et al.*, *Proc. Natl. Acad. Sci. U.S.A.* **118**, e2002551117 (2021).
16. P. H. Raven, D. L. Wagner, *Proc. Natl. Acad. Sci. U.S.A.* **118**, e2002548117 (2021).
17. M. L. Forister *et al.*, *Science* **371**, 1042–1045 (2021).
18. T. D. Schowalter, M. Pandey, S. J. Presley, M. R. Willig, J. K. Zimmerman, *Proc. Natl. Acad. Sci. U.S.A.* **118**, e2002556117 (2021).
19. J. Lämsä, E. Kuusela, J. Tuomi, S. Juntunen, P. C. Watts, *Proc. Biol. Sci.* **285**, 20180506 (2018).
20. E. Knop *et al.*, *Nature* **548**, 206–209 (2017).
21. J. C. Habel *et al.*, *Conserv. Biol.* **30**, 754–762 (2016).
22. P. Soroye, T. Newbold, J. Kerr, *Science* **367**, 685–688 (2020).
23. A. C. Beichman, E. Huerta-Sanchez, K. E. Lohmueller, *Annu. Rev. Ecol. Evol. Syst.* **49**, 433–456 (2018).
24. S. Nogué *et al.*, *Science* **372**, 488–491 (2021).
25. B. Hölldobler, E. O. Wilson, *The Ants* (Harvard Univ. Press, 1990).
26. M. Kaspari, J. D. Majer, in *Ants: Standard Methods for Measuring and Monitoring Biodiversity* (Smithsonian Institution Press, 2000), pp. 89–98.
27. J. C. Russell, C. Kueffer, *Annu. Rev. Environ. Resour.* **44**, 31–60 (2019).
28. R. J. Whittaker, J. M. Fernández-Palacios, T. J. Matthews, M. K. Borregaard, K. A. Triantis, *Science* **357**, eaam8326 (2017).
29. R. G. Gillespie, G. K. Roderick, *Annu. Rev. Entomol.* **47**, 595–632 (2002).
30. E. M. Sarnat, E. P. Economo, *The Ants of Fiji* (Univ. of California Press, ed. 1, 2012).
31. A. Lucky, E. M. Sarnat, *J. Biogeogr.* **37**, 624–634 (2010).
32. E. M. Sarnat, C. S. Moreau, *Mol. Ecol.* **20**, 114–130 (2011).
33. C. T. Darwell *et al.*, *Mol. Ecol.* **29**, 1611–1627 (2020).
34. C. Liu *et al.*, *Evolution* **74**, 1082–1097 (2020).
35. J. R. Wood *et al.*, *Environ. Conserv.* **44**, 348–358 (2017).
36. G. Clark, A. Anderson, in *The Early Prehistory of Fiji*, G. Clark, A. Anderson, Eds. (Australian National Univ. Press, 2009); pp. 407–437; https://press-files.anu.edu.au/downloads/press/p49471/pdf/161.pdf.
37. P. D. Nunn *et al.*, *Archaeol. Ocean.* **39**, 139–143 (2004).
38. C. I. Roos, J. S. Field, J. V. Dudgeon, *J. Ethnobiol.* **36**, 535–553 (2016).
39. A. Naikatini *et al.*, *Pac. Sci.* **71**, 241–255 (2017).
40. D. J. O'Dowd, P. T. Green, P. S. Lake, *Ecol. Lett.* **6**, 812–817 (2003).
41. P. D. Krushelnycky, R. G. Gillespie, *Ecol. Appl.* **18**, 1547–1562 (2008).
42. P. D. Krushelnycky, R. G. Gillespie, *Biol. Invasions* **12**, 643–655 (2010).
43. D. L. Wagner, R. G. Van Driesche, *Annu. Rev. Entomol.* **55**, 547–568 (2010).
44. R. N. Gutenkunst, R. D. Hernandez, S. H. Williamson, C. D. Bustamante, *PLOS Genet.* **5**, e1000695 (2009).
45. E. P. Economo, E. M. Sarnat, *Am. Nat.* **180**, E1–E16 (2012).
46. E. O. Wilson, *Am. Nat.* **95**, 169–193 (1961).
47. C. N. Johnson *et al.*, *Science* **356**, 270–275 (2017).
48. C. Liu, Code archive for Fijian Ant Community Genomics, Zenodo (2025); https://doi.org/10.5281/zenodo.16877570.

ACKNOWLEDGMENTS

We thank the Okinawa Institute of Science and Technology Graduate University (OIST) DNA Sequencing Section and Scientific Computing and Support Section for assistance with sequencing and HPC, respectively. **Funding:** This work was supported by subsidy funding to OIST and by the Japan Society for the Promotion of Science (Kakenhi grants 17K15180 to E.P.E., 18K14768 to F.H.G., and 16J00372 to C.L) E.P.E. and Y.K. were partially supported by a grant from the Environment Research and Technology Development Fund (JPMEERF20234G01) from the Japan Ministry of Environment. C.L was supported by an E. O. Wilson Biodiversity Postdoctoral Fellowship from the Museum of Comparative Zoology, Harvard University. **Author contributions:** C.L., A.S.M., and E.P.E. conceived the study. A.S.M. and E.P.E. supervised the study. E.S., A.C., and E.P.E. collected the ant specimens. E.S., E.P.E, F.H.G., and G.F. identified the ant species. J.A.T. and L.Q. conducted the laboratory work and RADseq sequencing. J.J., J.D., M.O., M.L.G., and N.N. managed the specimens and database. C.L., M.L.G., and N.N. designed the initial bioinformatics pipelines. C.L. ran the bioinformatics pipelines. C.L., A.S.M., and E.P.E. performed the analyses. C.L., C.T.D., Y.K., N.E.P., A.S.M., and E.P.E. discussed the results. C.L., A.S.M., and E.P.E. drafted the manuscript, with contributions from all authors. Funding was acquired by A.S.M. and E.P.E. **Competing interests:** The authors declare no competing interests. **Data and materials availability:** All sequence data have been submitted to the National Center for Biotechnology Information under BioProject PRJNA1131011. All ecological data can be found in the supplementary materials. All code is available in a Zenodo archive (*48*).

SUPPLEMENTARY MATERIALS

science.org/doi/10.1126/science.ads3004
Materials and Methods; Figs. S1 to S9; References; MDAR Reproducibility Checklist; Data S1 to S7

Submitted 7 August 2024; resubmitted 21 March 2025; accepted 10 July 2025
10.1126/science.ads3004

WILDFIRES

Fire Heat Affects the Impacts of Wildfires on Air Pollution in the United States

Qihan Ma[1,2]†, Linyi Wei[2,3]†, Yong Wang[1,2]*, Guang J. Zhang[4], Xinlin Zhou[5], Bin Wang[6,7]

Conventional wisdom suggests that wildfires in the western United States (WUS) degrade air quality nationwide as a result of aerosol emissions and eastward transport. However, we found that heat produced by wildfires, a commonly neglected effect, can reduce fine particle concentrations ($PM_{2.5}$) in the eastern United States (EUS) by an amount comparable to the increases in the WUS during the fire season. This phenomenon arises from fire heat–induced convection in the WUS and subsequent downstream meteorological changes distant from fires. Enhanced wet deposition and weakened eastward transport of fire aerosols lower $PM_{2.5}$ levels in the EUS. Therefore, neglecting the effect of fire heat on $PM_{2.5}$ pollution leads to an overestimate of 1200 additional premature deaths and 3.3 billion USD in economic losses, particularly in the densely populated EUS.

In recent decades, with increased climate warming the occurrence frequency, average area burned, and duration of wildfires in the western United States (WUS) have increased considerably, frequently setting new records (*1*–*3*). These fires, which predominantly occur in temperate forests and adjacent savannas (fig. S1), produce abundant aerosols and gaseous pollutants (*4*–*6*), posing threats to ecosystems, infrastructure, and public health (*7*–*9*). In particular, fire aerosols can severely degrade air quality not only near fire activity but also in remote downwind regions as a result of long-range transport (*10*). The interactions between fire aerosols and weather can further amplify air pollution exposure (*11*, *12*). Fire-sourced air pollution has led to thousands of premature deaths annually in the US (*13*–*15*). These understandings of the impacts of fire aerosols have been widely used to guide air quality control and fire management practices (*16*–*18*). However, in addition to aerosol emissions, fires also release a tremendous amount of heat (*19*–*21*), the effects of which are relatively underexplored. In the fire-prone areas of the WUS, a broad expanse of burned areas is often monitored from July to September (hereafter defined as the fire season), with a considerable amount of monthly fire heat flux of up to 126 W/m^2 (fig. S2). Such a huge energy source can alter local air temperature and atmospheric stability, triggering strong convection (*22*–*25*). These changes may subsequently influence atmospheric circulation, further affecting weather far from the fire regions (*26*, *27*). Therefore, in addition to fire aerosols, fire heat can also play a key role in modulating climate.

Air pollution from extensive industrial and anthropogenic activities—especially fine particulate matter <2.5 micrometers in diameter ($PM_{2.5}$)—has been a persistent hazard in the eastern United States (EUS) over recent decades (*28*–*30*). During the fire season, $PM_{2.5}$ concentrations in the EUS can be elevated by the eastward transport of smoke from extreme wildfires in the WUS. This is presupposed as a matter of course in most observational studies (*31*–*33*). Nonetheless, given that $PM_{2.5}$ concentrations are intricately tied to local atmospheric conditions (*34*, *35*), detectable smoke and/or resulting $PM_{2.5}$ increases in the EUS do not always follow extreme wildfires in the WUS. Fire heat can affect large-scale atmospheric features (*26*, *27*), and the fact that these changes may affect air pollution in distant regions has not been fully acknowledged. In modeling the effects of fires on $PM_{2.5}$ concentrations, most regional and global climate models incorporate fire aerosols only and neglect fire heat (*36*, *37*). Although these models consistently suggest that transcontinental fire aerosols exacerbate air pollution, some recent studies have noted that the simulated $PM_{2.5}$ concentrations in the EUS are overestimated (*27*, *38*). As such, the actual impacts of wildfires in the WUS on $PM_{2.5}$ air pollution in the EUS may not be as straightforward as envisioned.

We used observation and reanalysis data to reveal that during extreme wildfire events (EWEs) in the WUS, $PM_{2.5}$ concentrations in the EUS decrease by an amount comparable to the increase observed in the WUS. This was verified by model simulations in the National Center for Atmospheric Research (NCAR) Community Earth System Model version 1.2.1 (CESM1.2.1) utilizing observed daily fire aerosols and heat from the Global Fire Emissions Database version 4.1s (GFED4.1s). We found that the substantial heat released by fires can initiate intense local convection, which indirectly influences atmospheric circulation and subsequent cloud and precipitation processes in the EUS, ultimately contributing to $PM_{2.5}$ reductions. Combined with the effects of fire aerosols, the contrasting $PM_{2.5}$ changes in the WUS and EUS reduce disparities in $PM_{2.5}$ air pollution. Given the higher population density in the EUS, neglecting the effect of fire heat leads to an overestimation of the national socioeconomic impacts of fires, including premature mortality and economic losses.

Observed reductions in $PM_{2.5}$ over the EUS

To identify and refine the signal of wildfire impacts on air pollution in observations as much as possible, we conducted a composite analysis of in situ $PM_{2.5}$ measurements during EWEs. To define EWEs, we first used GFED4.1s fire data with a 0.25°×0.25° resolution to obtain burned areas and dry matter emissions under different types of fires (*39*). Second, we estimated daily fire heat, including sensible heat and latent heat, based on the dry matter emissions (materials and methods). We then aggregated the burned areas (ΣBA_{wus}) and fire heat (ΣQ_{wus}) across all grid points within the fire-prone areas of the WUS (fig. S2). An event was classified as an EWE if both ΣBA_{wus} and ΣQ_{wus} exceeded the 90th percentile and the fire lasted for at least 3 days (materials and methods). To harmonize different available periods across multiple datasets, all analyses were performed on data for the 2005 to 2015 fire seasons. In total, 10 EWEs were identified. We computed the difference in the $PM_{2.5}$ concentrations ($\Delta PM_{2.5}$) between each EWE and the fire-season mean in the same year rather than that for 2005 to 2015, which largely excluded the effects of other factors such as air pollution control policies and interannual variabilities in $PM_{2.5}$.

The $\Delta PM_{2.5}$ averaged over all EWEs in the US exhibited a dipole pattern, with a positive regional average of 2.86 $\mu g/m^3$ for all sites in the WUS and a comparable negative value of −1.71 $\mu g/m^3$ for all sites in the EUS (Fig. 1A). Compared with the 2005 to 2015 fire seasons, the probability density functions of $\Delta PM_{2.5}$ during EWEs in the WUS and EUS shifted towards larger positive and negative anomalies, respectively (Fig. 1, B and C). The observed aerosol optical depth also exhibited a sharp increase in the WUS but decreased in the EUS (fig. S3). According to the Hazard Mapping System smoke product (*40*), during the 10 EWEs, smoke plumes originating in the WUS were observable over the EUS (fig. S4), which is consistent with previous findings (*30*–*33*). However, most smoke plumes covered only a small fraction

[1]Shanghai Key Laboratory of Ocean-land-atmosphere Boundary Dynamics and Climate Change, Department of Atmospheric and Oceanic Sciences, Fudan University, Shanghai, China. [2]Department of Earth System Science, Ministry of Education Key Laboratory for Earth System Modeling, Institute for Global Change Studies, Tsinghua University, Beijing, China. [3]Key Lab of Loess Science, Institute of Earth Environment, Chinese Academy of Sciences, Xi'an, China. [4]Scripps Institution of Oceanography, La Jolla, CA, USA. [5]Lakefield College School, Lakefield, ON, Canada. [6]State Key Laboratory of Earth System Numerical Modeling and Application, Institute of Atmospheric Physics, Chinese Academy of Sciences, Beijing, China. [7]College of Marine Sciences, University of Chinese Academy of Sciences, Beijing, China. ***Corresponding author. Email: yongw@fudan.edu.cn (Y.W.)** †These authors contributed equally to this work.

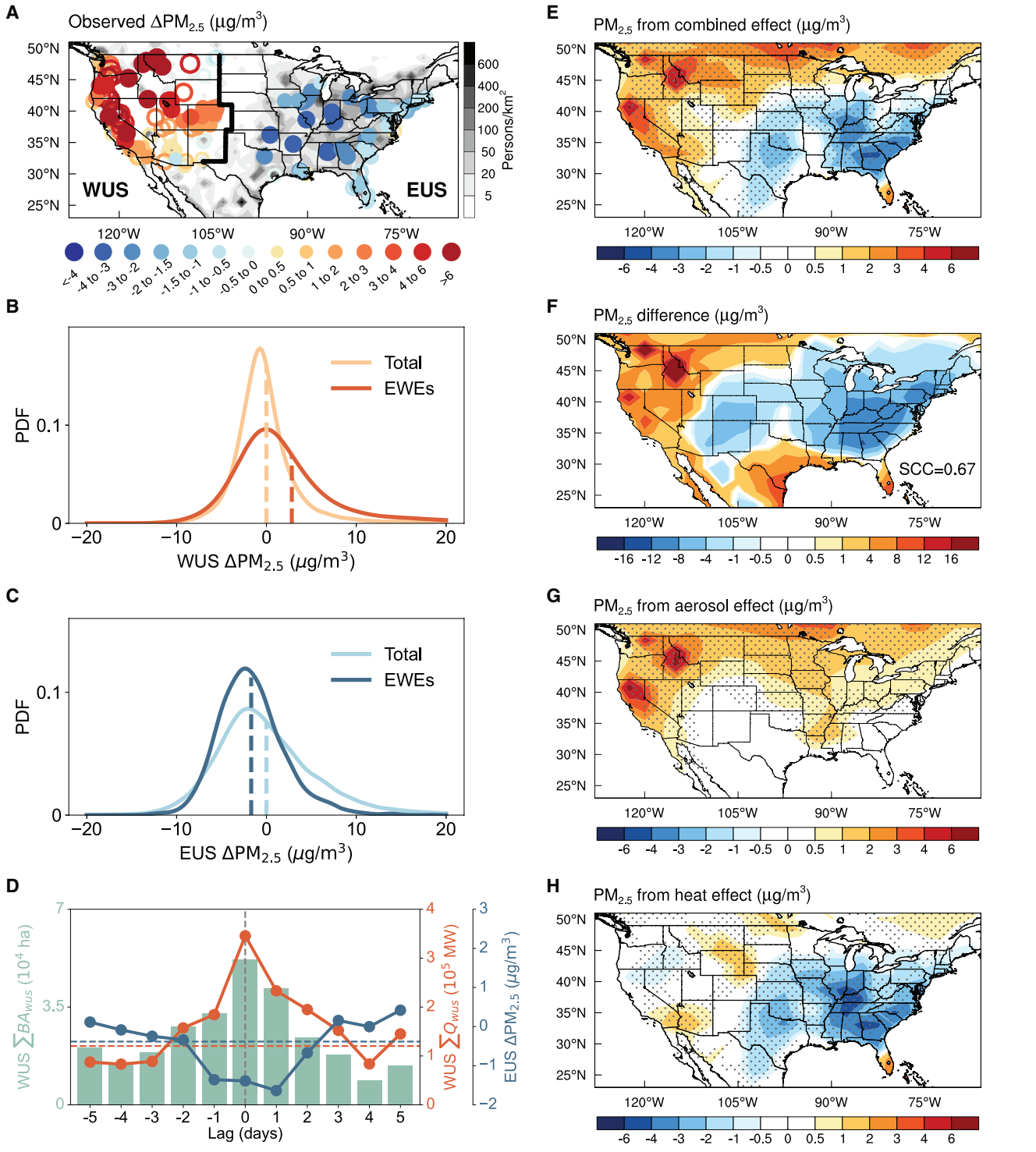

Fig. 1. Observed and simulated $PM_{2.5}$ concentration anomalies in the US. (**A**) Observed mean $\Delta PM_{2.5}$ (circles) for all EWE days and population density (shaded gray areas). The sites that exceed the 90% confidence level in the Wilcoxon signed-rank test are denoted by solid circles; the remaining sites are denoted by open circles. The thicker black line divides the US into eastern and western parts. (**B** and **C**) Probability density functions (PDFs) of observed daily $\Delta PM_{2.5}$ for all EWE days and the 2005 to 2015 fire seasons in the WUS and EUS, respectively. The dashed lines denote means. (**D**) Lead-lag composite analysis for daily mean both ΣBA_{wus} and ΣQ_{wus} in the fire-prone areas of the WUS and the median of observed daily mean $\Delta PM_{2.5}$ across all sites in the EUS around EWEs. The day with the largest ΣQ_{wus} is indicated by the gray dashed line in the middle (day 0). The blue and red horizontal dashed lines are the mean values for the 5 days that precede day 0. (**E**) Spatial distribution of the anomalous $PM_{2.5}$ concentrations induced by both fire aerosols and heat during the 2005 to 2015 fire seasons. (**F**) Spatial distribution of the average of $PM_{2.5}$ concentration differences between three datasets (MERRA-2, CAMS, and USHAP) and the NoFireA_NoFireH experiment during the 2005 to 2015 fire seasons. The spatial correlation coefficient (SCC) for the US corresponding to (E) is noted. (**G**) Same as (E) but for fire aerosols. (**H**) Same as (E) but for fire heat. The gray dots in (E), (G), and (H) denote areas exceeding the 95% confidence level according to the Student's *t*-test.

of the EUS. $PM_{2.5}$ air pollution in the EUS did not worsen but instead decreased at most sites. In particular, for the case of 18 to 26 August, 2015, despite the occurrence of severe fire-induced air pollution in the WUS and strong transcontinental smoke transport covering the entire EUS with smoke plumes, $PM_{2.5}$ concentrations in the EUS exhibited a substantial decline. Around the occurrence times of extreme wildfires, $\Delta PM_{2.5}$ in the EUS began to decline approximately 1 to 2 days after ΣQ_{wus} started to increase (Fig. 1D). We found that $\Delta PM_{2.5}$ in the EUS plummeted to the minimum value one day after the peak ΣQ_{wus}. Given that the studied extreme wildfires released substantial amounts of heat, the reduction in $PM_{2.5}$ concentrations in the EUS suggests that fire heat likely has a first-order but contrasting effect on $PM_{2.5}$ air pollution compared with the considerable release of fire aerosols.

These features are consistent across different datasets, including the Modern-Era Retrospective analysis for Research and Applications version 2 (MERRA-2), Copernicus Atmosphere Monitoring Service Reanalysis (CAMS), and US high-resolution air pollutants (USHAP) products (fig. S5). In addition, the composite results are retained when different percentiles are employed to define EWEs (fig. S6). However, despite the composite analysis of observations and reanalysis data, attributing the dipole pattern of $\Delta PM_{2.5}$ to wildfires remains challenging. Therefore, we performed simulations using a global climate model (GCM) to identify the contributing factors.

Evidence from model simulations

We used CESM1.2.1 to comprehensively investigate the impacts of wildfires in the WUS on the climate during the fire season. In addition to daily fire aerosols, we introduced daily fire heat into CESM1.2.1 (materials and methods). Three simulations were conducted: one with neither fire aerosols nor heat (NoFireA_NoFireH), one with fire aerosols only (FireA_NoFireH), and one with both fire aerosols and heat (FireA_FireH). The CESM modeling meteorological fields and $PM_{2.5}$ concentrations in the US have been validated against observation and reanalysis data (figs. S7 to S9; materials and methods).

We found that the distribution of the differences in simulated $PM_{2.5}$ concentrations during the fire season between FireA_FireH and NoFireA_NoFireH (Fig. 1E) resembles that of the observations (Fig. 1A), exhibiting comparable contrasts: an average of 1.71 $\mu g/m^3$ in the WUS and −1.21 $\mu g/m^3$ in the EUS. Additionally, we calculated the average of the differences in $PM_{2.5}$ concentrations from MERRA-2, CAMS, and USHAP relative to the NoFireA_NoFireH experiment (see Fig. 1F and fig. S10 for individual differences). These differences likely contain wildfire-induced $PM_{2.5}$ patterns as these datasets capture the combined effects of fire aerosols and heat on $PM_{2.5}$ concentrations (materials and methods), which are absent in the NoFireA_NoFireH experiment (*41*). Figure 1F also reveals a dipole pattern for $PM_{2.5}$ changes, with particularly pronounced negative anomalies in the EUS. Overall, there is a large degree of similarity between panels E and F in Fig. 1, with a spatial correlation coefficient of 0.67 for the US. These results demonstrate that wildfires in the WUS are a plausible source of the dipole pattern in $PM_{2.5}$ changes.

Subsequently, we separated the impacts of wildfires on $PM_{2.5}$ air pollution into those caused by fire aerosols and fire heat. As previous studies have noted (*37*, *42*), fire aerosols result in an inverted U-shaped pattern of positive $PM_{2.5}$ anomalies across the US. This pattern is shaped by the prevailing westerlies, which transport fire smoke from the WUS and Canada (Fig. 1G). The elevated $PM_{2.5}$ concentrations are dominated by primary organic matter (fig. S11). By contrast, fire heat serves to mitigate $PM_{2.5}$ concentrations in the EUS (Fig. 1H), primarily by diminishing secondary organic aerosols and sulfate (fig. S12). In the EUS, the negative $PM_{2.5}$ anomalies caused by fire heat outweigh the positive anomalies caused by fire aerosols several times over.

Attributed to anomalous easterlies and enhanced rainfall

Given the dominant role of fire heat in alleviating $PM_{2.5}$ air pollution over the EUS, with a 1 to 2 day lag we strongly suspected that fire heat alters weather systems and associated large-scale atmospheric circulations. As shown in Fig. 2A, fire heat from wildfires in the WUS considerably increases local convective available potential energy (CAPE). The elevated CAPE in the WUS intensifies convection, characterized by increased convective precipitation during fires (Fig. 2B). We noted that the CAPE also increases considerably in the EUS, with a magnitude comparable to that in the WUS (Fig. 2A). However, during the WUS fire season, wildfires in the EUS are infrequent, and the amount of heat they release is one order of magnitude less than that released in the WUS (fig. S2). This suggests that it is unlikely that local fires

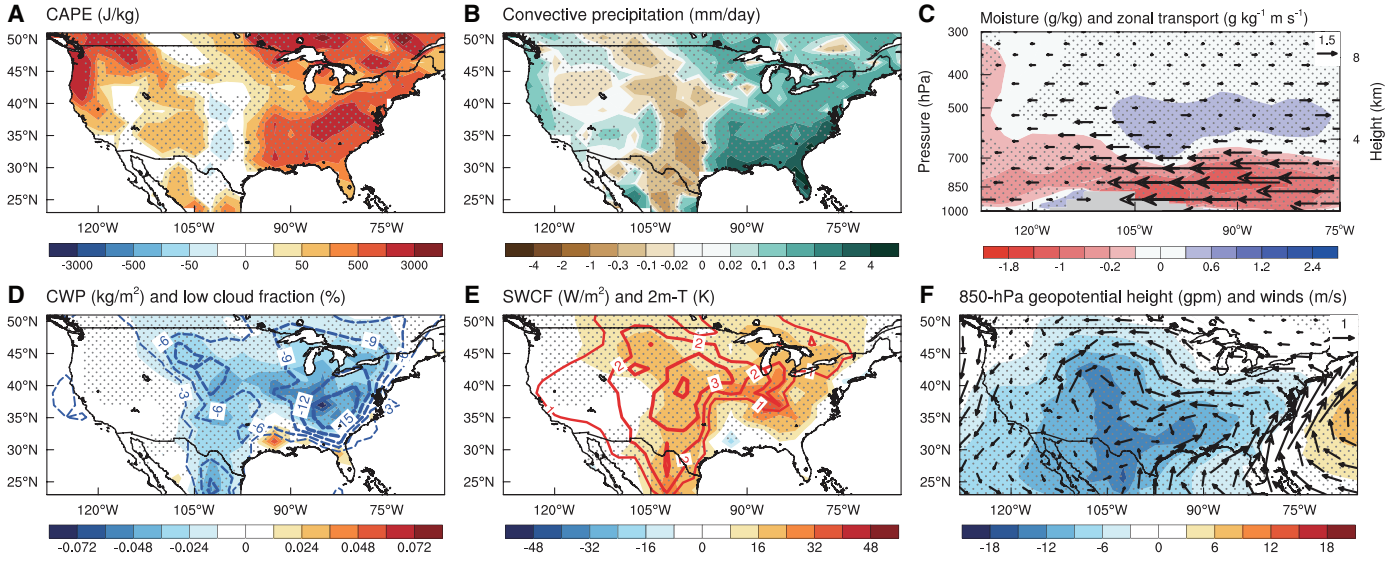

Fig. 2. Simulations of meteorological changes induced by fire heat in the WUS during the 2005 to 2015 fire seasons. (**A**) CAPE. (**B**) Convective precipitation. (**C**) Meridional mean (averaged over 30°N to 50°N) moisture (shaded areas) and zonal moisture transport (vectors). (**D**) Total cloud water path (shaded areas) and low cloud fraction (contour). (**E**) Net shortwave cloud radiative forcing at the surface (shaded areas) and 2-m air temperature (contour). (**F**) 850-hPa geopotential height superposed by the 850-hPa winds (vectors). The gray dots denote areas exceeding the 95% confidence level according to the Student's *t*-test.

are the primary cause of the increased CAPE over the EUS. Thus, there should be other factors, which are analyzed below.

Atmospheric water vapor in the central US during the fire season partially originates from the eastward transport of water vapor from the Pacific (fig. S8). Because of increased convective precipitation in the WUS, much of the water vapor is consumed in advance (Fig. 2C). To investigate changes in zonal moisture transport, we decomposed them into components induced by circulation and moisture changes, respectively. We noted that the enhanced westerlies from the WUS to the central US are consistent with previous findings based on the Weather Research and Forecasting model with Chemistry (WRF-Chem) simulations (*26*), which increases moisture transport (fig. S13). However, the drier atmosphere in the WUS dominates negative changes in zonal moisture flux (Fig. 2C and fig. S13), leading to reduced moisture flux convergence over the central US (fig. S14). Consequently, precipitation over the central US is suppressed (Fig. 2B and fig. S14). In addition, the column-integrated liquid water and low clouds diminish over the central US (Fig. 2D). This enhances net shortwave cloud radiation at the surface, which dominates the warming of the lower atmosphere and leads to negative low-level pressure anomalies (Fig. 2, E and F). The associated cyclonic circulation then produces anomalous easterlies across the central US and the EUS, suppressing onshore moisture transport from the Gulf of Mexico (Fig. 2C and fig. S8). This further exacerbates atmospheric drying over the central US, inhibiting moisture flux convergence and precipitation despite the ascending motion in response to near-surface warming (fig. S14). However, the anomalous cyclonic circulation in the EUS, as well as the local humid climate, leads to large-scale moisture flux convergence and ascending motion, resulting in increased CAPE and increased convective precipitation (Fig. 2F and fig. S14). Furthermore, we performed a composite analysis of precipitation, moisture, large-scale circulation, cloud water, and cloud radiative forcing during EWEs from observation and reanalysis data. The anomalies during EWEs resemble the simulated changes induced by fire heat, especially for the increased precipitation and the anomalous cyclone, along with easterly over the EUS (fig. S15). These consistent patterns further suggest that the domino effects across the US are triggered by fire heat from the WUS.

The increased convective precipitation in the EUS dominates the total precipitation increase, efficiently removing atmospheric $PM_{2.5}$ over the EUS (figs. S16 and S17). More convective precipitation also results in fewer large-scale stratiform clouds, thereby suppressing aqueous-phase sulfate formation, which further contributes to a decrease in aerosol pollution (fig. S16). Additionally, owing to anomalous easterlies over the EUS, the transport of smoke-related $PM_{2.5}$ from the fire-prone areas of the WUS and Canada is mitigated (fig. S16). Overall, the combined effects of these three factors alleviate $PM_{2.5}$ air pollution in the EUS.

Reduced $PM_{2.5}$-related mortality and economic losses nationwide

The combined effects of fire aerosols and heat decrease the disparities in $PM_{2.5}$ exposure across the US, which is measured by the Gini index (Fig. 3A; materials and methods). The mitigation of $PM_{2.5}$ disparities—particularly

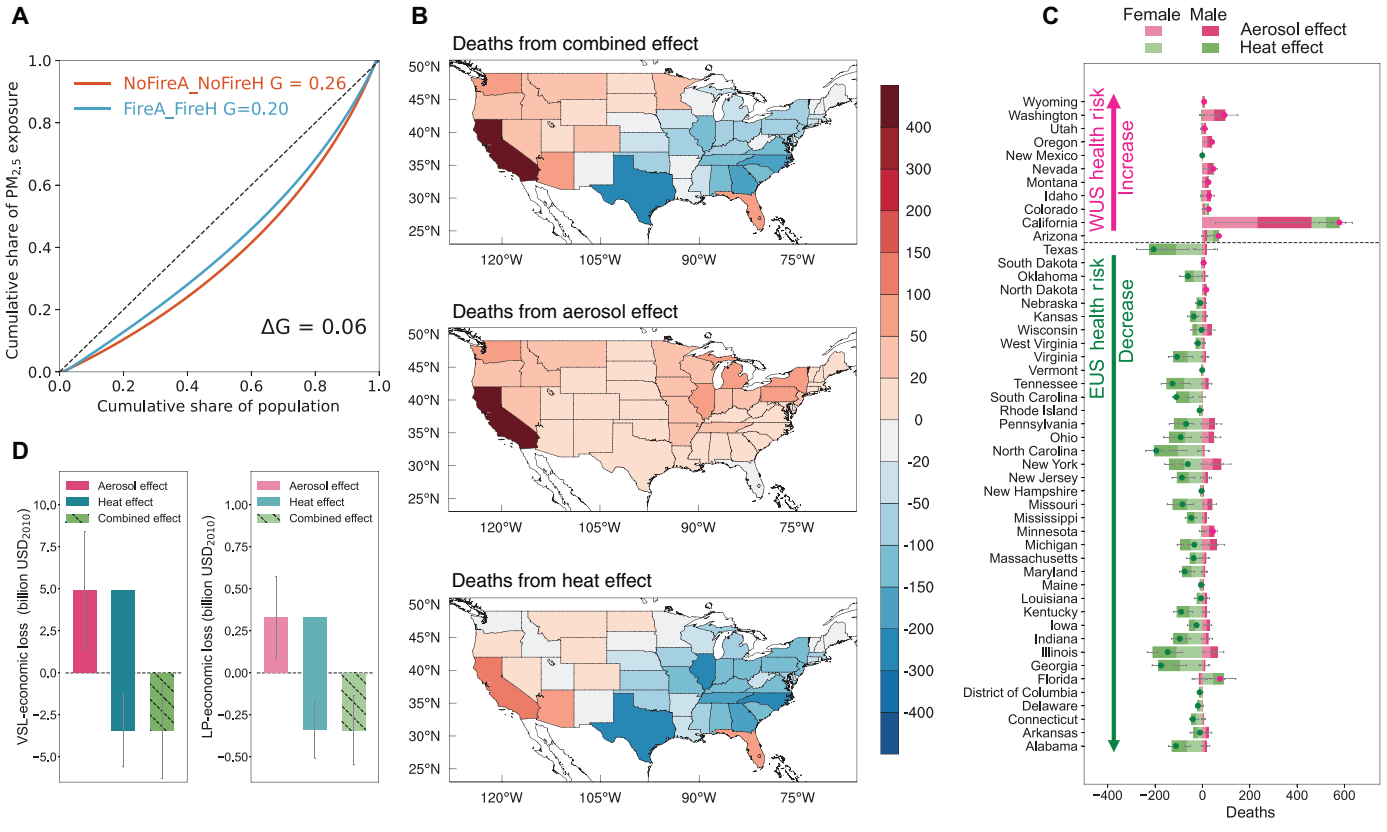

Fig. 3. $PM_{2.5}$ exposure inequality and health and economic consequences related to fire aerosols and heat in the US. (**A**) Lorenz curves underlying the $PM_{2.5}$ exposure inequality without (red) and with (blue) the effects of fires in the US. The individual Gini indexes and their difference ($\Delta G = 0.06$) are noted. (**B**) $PM_{2.5}$-related premature deaths from the combined effects of fire aerosols and heat (top); from only the effect of fire aerosols (middle); and from only the effect of fire heat (bottom). (**C**) Premature deaths among different states (excluding AK and HI) and the District of Columbia in the US caused by fire aerosols (pink) and heat (green). The effects for females and males are shown by the light and dark colors, respectively. Their combined deaths are denoted by pink dots (increases) and green dots (decreases). The gray dashed line divides the US into the WUS and the EUS. (**D**) Exacerbation and mitigation of health-economic losses caused by fire aerosols (pink), heat (blue), and their combination (green). US dollars (USD) are benchmarked to 2010. The gray error bars in (C) and (D) represent the uncertainties denoted by the standard deviation.

those due to decreased $PM_{2.5}$ concentrations in the more densely populated EUS—implies potentially unforeseen reductions to $PM_{2.5}$-related premature mortality and associated economic losses (Fig. 3). To quantify these, the global exposure mortality model (GEMM) was applied to estimate the premature mortality linked to fire-altered $PM_{2.5}$ during the fire season (*43*, *44*). Specifically, increased $PM_{2.5}$ concentrations from fire aerosols only increase health risks, causing more than 1500 premature deaths in the US (Fig. 3, B and C). This effect is particularly pronounced in CA, one of the most fire-prone states, where an increase in $PM_{2.5}$ concentrations to >5 μg/m^3 contributes to approximately 500 premature deaths. Considering only fire heat, the number of premature deaths is increased by about 200 in the WUS whereas 2900 premature deaths are alleviated in the EUS, resulting in a decrease of 2700 premature deaths nationwide. Consequently, the combined effects of fire aerosols and heat lead to a net reduction of 1200 premature deaths in the US.

The economic costs due to premature deaths from fires were also estimated through losses of the statistical value of life (VSL) and labor productivity (LP), which are separated into economic losses from fire aerosols and benefits from fire heat (Fig. 3D). The US economy faces challenges with 5 billion USD for VSL and 0.3 billion USD for LP due to the increased health risk posed by fire aerosols. By contrast, the substantial decrease in premature mortality due to fire heat leads to a notable reduction in health-economic losses, amounting to 8 billion USD for the VSL and 0.6 billion USD for the LP. The combined effects of fire aerosols and heat contribute to ~3 (0.3) billion USD in health-economic benefits for the VSL (LP), indicating that fire heat substantially mitigates health-economic losses in the US.

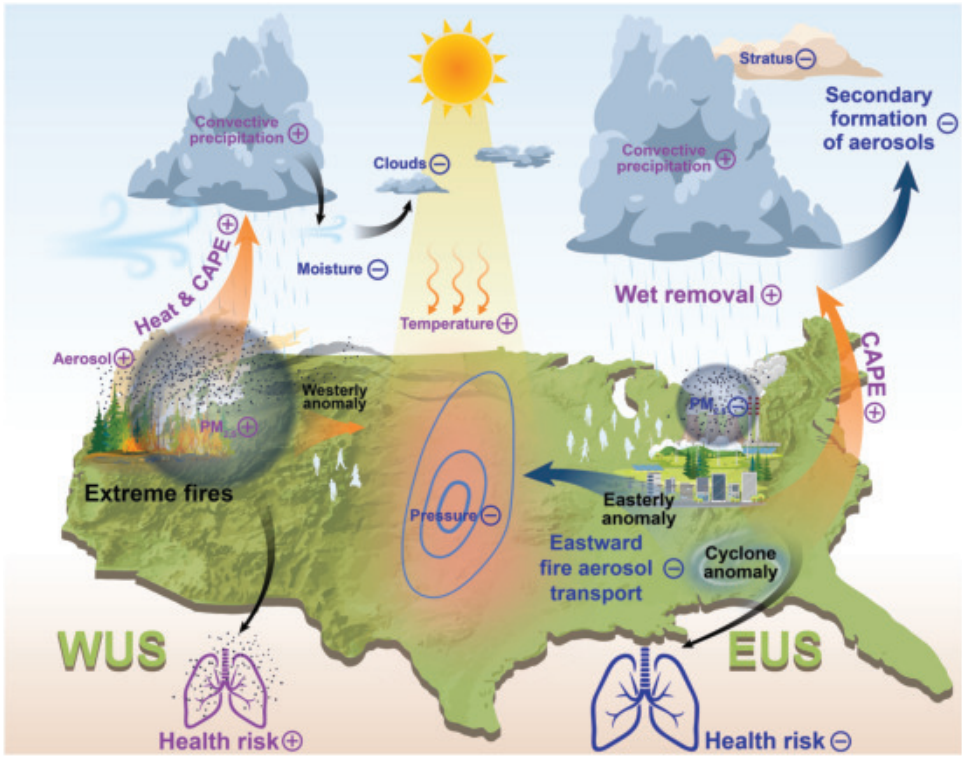

Fig. 4. Schematic diagram illustrating how fire heat in the WUS influences $PM_{2.5}$ air pollution in the EUS. Extreme fires in the WUS release heat that triggers convection, which reduces moisture transport from the WUS to the central US although westerlies are enhanced. The resulting dryer and warmer central US features low-level pressure anomalies, inducing anomalous easterlies and promoting convective precipitation over the EUS. As a result, $PM_{2.5}$ air pollution and associated health risks in the EUS are alleviated. It should be noted that the $PM_{2.5}$ air pollution and health consequences in this figure include the contribution of fire aerosols.

Discussion

Although the localized effects of fire heat in the WUS are recognized (*24*, *25*), the transcontinental influence of fire heat remains largely underappreciated. In this study, we present historical evidence from observation and reanalysis data showing that $PM_{2.5}$ concentrations decreased in the EUS during extreme wildfires in the WUS. We used model simulations to demonstrate that fire heat plays a key role in driving this effect during the fire season, extending beyond extreme wildfires (Fig. 1 and fig. S18). This reduction is due to the fire heat-induced convection over the WUS, which subsequently alters weather and atmospheric circulations downstream (Fig. 4). As a response, increased wet deposition through convective precipitation and reduced secondary aerosol formation occur in the EUS, effectively mitigating local $PM_{2.5}$ concentrations. Prevailing winds that typically transport wildfire smoke from the WUS are also suppressed by the easterly anomalies across the central US and the EUS. These domino effects triggered by fire heat in the WUS are well-depicted by wave activity analysis (fig. S19). Under the combined impacts of both fire heat and aerosols, disparities in $PM_{2.5}$ air pollution between more polluted and less polluted areas declined. Neglecting the effects of fire heat would lead to an overestimate of 1200 additional premature deaths and 3.3 billion USD in economic losses nationwide. US environmental policies for promoting environmental justice and reducing disparities should further consider the regional heterogeneity of air pollution caused by fire heat.

Despite the improvement of air quality over the EUS due to fire heat, air pollution in the WUS is exacerbated by fire aerosols, which pose a major threat public health and the economy. Moreover, the extreme wildfires in the WUS disrupt the local ecosystem and alter the landscape, potentially causing ecological shifts (*45*, *46*). These negative effects are profound and targeted interventions should still be implemented (*47*). The differential impacts of wildfires necessitate the more appropriate allocation of resources and policy intensity for fire management and regional pollution control. With greening in a warming world, the accumulation of fuels will lead to increased fire heat release when wildfires occur. It is imperative to consider fire heat in the Earth system when conducting comprehensive climate simulations and wildfire risk assessments.

We are aware of some limitations in our results. The coarse grid spacing used in GCMs such as CESM1.2.1 means that convection and its interaction with aerosols are highly parameterized, which introduces a variety of compromises in model simulations. To avoid some of those compromises, we repeated a subset of our evaluation using a more realistic model configuration with fewer approximations to convection and cloud processes. Specifically, we incorporated fire heat into a state-of-the-art superparameterized CESM (SP-CESM). The SP-CESM embeds cloud-resolving models (CRMs) at a 4-km resolution to explicitly resolve convection globally and to comprehensively treat interactions between convection and aerosols at the expense of approximately two orders of magnitude greater resources compared with the conventional

CESM (materials and methods). Overall, the SP-CESM results are consistent with those of the CESM, despite the weakened impacts of fire heat (figs. S20 to S22). In addition to the GCM, because of limited observations the daily fire heat applied in the GCM may underestimate fire heat-induced strong convection by averaging out the subdaily variations, which could diminish the subsequent domino effects.

REFERENCES AND NOTES

1. V. Iglesias, J. K. Balch, W. R. Travis, *Sci. Adv.* **8**, eabc0020 (2022).
2. P. E. Dennison, S. C. Brewer, J. D. Arnold, M. A. Moritz, *Geophys. Res. Lett.* **41**, 2928–2933 (2014).
3. C. X. Cunningham, G. J. Williamson, D. M. J. S. Bowman, *Nat. Ecol. Evol.* **8**, 1420–1425 (2024).
4. L. Liang, S. Liang, Z. Zeng, *Innovation* **5**, 100631 (2024).
5. Y. Xie, M. Lin, L. W. Horowitz, *Geophys. Res. Lett.* **47**, 47 (2020).
6. B. Zheng *et al.*, *Sci. Adv.* **7**, eabh2646 (2021).
7. X. Yue, N. Unger, *Nat. Commun.* **9**, 5413 (2018).
8. D. M. J. S. Bowman *et al.*, *Nat. Ecol. Evol.* **1**, 0058 (2017).
9. A. Modaresi Rad *et al.*, *Nat. Sustain.* **6**, 1343–1351 (2023).
10. S. J. Brey, M. Ruminski, S. A. Atwood, E. V. Fischer, *Atmos. Chem. Phys.* **18**, 1745–1761 (2018).
11. A. K. Kochanski *et al.*, *J. Geophys. Res. Atmos.* **124**, 9099–9116 (2019).
12. X. Huang *et al.*, *Science* **379**, 457–461 (2023).
13. N. Fann *et al.*, *Sci. Total Environ.* **610-611**, 802–809 (2018).
14. K. O'Dell *et al.*, *GeoHealth* **5**, e2021GH000457 (2021).
15. J. Wei *et al.*, *Lancet Planet. Health* **7**, e963–e975 (2023).
16. R. Xu *et al.*, *Nature* **621**, 521–529 (2023).
17. C. D. McClure, D. A. Jaffe, *Proc. Natl. Acad. Sci. U.S.A.* **115**, 7901–7906 (2018).
18. M. Burke *et al.*, *Nature* **622**, 761–766 (2023).
19. C. B. Clements, B. E. Potter, S. Zhong, *Int. J. Wildland Fire* **15**, 299 (2006).
20. X. Silvani, F. Morandini, *Fire Saf. J.* **44**, 279–285 (2009).
21. R. L. Kremens, M. B. Dickinson, A. S. Bova, *Int. J. Wildland Fire* **21**, 722 (2012).
22. J. Trentmann *et al.*, *Atmos. Chem. Phys.* **6**, 5247–5260 (2006).
23. S. Strada, C. Mari, J.-B. Filippi, F. Bosseur, *Atmos. Environ.* **51**, 234–249 (2012).
24. G. Kablick III *et al.*, *J. Geophys. Res. Atmos.* **123**, 123 (2018).
25. Y. Zhang, J. Fan, T. Logan, Z. Li, C. R. Homeyer, *Geophys. Res. Lett.* **46**, 10082–10093 (2019).
26. Y. Zhang *et al.*, *Proc. Natl. Acad. Sci. U.S.A.* **119**, e2207329119 (2022).
27. X. Lin, J. Fan, Y. Zhang, Z. J. Hou, *Adv. Atmos. Sci.* **41**, 1450–1462 (2024).
28. B. L. Boys *et al.*, *Environ. Sci. Technol.* **48**, 11109–11118 (2014).
29. EPA, "Our Nation's Air" (2018); https://gispub.epa.gov/air/trendsreport/2018/.
30. Y. Zhang *et al.*, *Atmos. Chem. Phys.* **18**, 15003–15016 (2018).
31. R. O. Saunders, D. W. Waugh, *Atmos. Environ.* **117**, 259–270 (2015).
32. M. J. Gunsch *et al.*, *Atmos. Chem. Phys.* **18**, 3701–3715 (2018).
33. Y. Li *et al.*, *Geophys. Res. Lett.* **48**, 48 (2021).
34. D. J. Jacob, D. A. Winner, *Atmos. Environ.* **43**, 51–63 (2009).
35. A. P. K. Tai, L. J. Mickley, D. J. Jacob, *Atmos. Environ.* **44**, 3976–3984 (2010).
36. I. S. Albores *et al.*, *Atmos. Environ.* **294**, 119436 (2023).
37. C. Sarangi *et al.*, *Atmos. Chem. Phys.* **23**, 1769–1783 (2023).
38. Y. Liu *et al.*, *Atmos. Chem. Phys.* **21**, 8003–8021 (2021).
39. G. R. van der Werf *et al.*, *Earth Syst. Sci. Data* **9**, 697–720 (2017).
40. NOAA, "Hazard Mapping System Fire and Smoke Product" (NOAA, 2025); https://www.ospo.noaa.gov/Products/land/hms.html#about.
41. X. Huang, A. Ding, *Sci. Bull.* **66**, 1917–1924 (2021).
42. A. S. Kaulfus, U. Nair, D. Jaffe, S. A. Christopher, S. Goodrick, *Environ. Sci. Technol.* **51**, 11731–11741 (2017).
43. R. Burnett *et al.*, *Proc. Natl. Acad. Sci. U.S.A.* **115**, 9592–9597 (2018).
44. H. Yin *et al.*, *Lancet Planet. Health* **5**, e356–e367 (2021).
45. M. Riches, T. C. Berg, M. P. Vermeuel, D. B. Millet, D. K. Farmer, *Geophys. Res. Lett.* **51**, e2023GL106667 (2024).
46. J. E. Halofsky, D. L. Peterson, B. J. Harvey, *Fire Ecol.* **16**, 4 (2020).
47. S. Zhou, R. Xu, G. Chen, P. Yu, Y. Guo, *Innov. Med.* **1**, 100024 (2023).
48. J. Wei, J. Wang, Z. Li, US High $PM_{2.5}$: Daily Seamless 1 km Ground-Level $PM_{2.5}$ Dataset for the United States (2000–Present), Version 1 (Zenodo, 2025); https://zenodo.org/doi/10.5281/zenodo.7884640.

ACKNOWLEDGMENTS

We thank the working groups and authors involved in the GFED fire dataset retrieval and public availability. We thank the National Aeronautics and Space Administration (NASA), the National Oceanic and Atmospheric Administration (NOAA), and the US Environmental Protection Agency (EPA) for making the reanalysis and observation data available. We also thank the GBD and the ILOSTAT organizations for providing detailed datasets on health and labor and making them publicly available. We would like to express our heartfelt thanks to Y. Han at the Scripps Institution of Oceanography for incorporating fire heat into the SP-CESM; H. Yin at the University of British Columbia; L. Lian at Lanzhou University for their suggestions on assessing the impacts of fires on health and the economy; and Z. Li at the University of Maryland for his helpful discussions. This research initiative originated at Tsinghua University and we would like to formally acknowledge the critical support extended through Tsinghua's research platform. **Funding:** This work was funded by the following: National Key Research and Development Program of China grant 2022YFF0802002, National Natural Science Foundation of China grant 41975126, and Office of Biological and Environmental Research of the US Department of Energy Atmospheric System Research Program Interagency Agreement grant DE-SC0022064. **Author contributions:** Conceptualization: Y.W. Methodology: Q.M., L.W., and Y.W. Investigation: Q.M. and L.W. Visualization: Q.M. and L.W. Funding acquisition: Y.W. Project administration: Y.W. Supervision: Y.W. Writing – original draft: Q.M., L.W., and Y.W. Writing – review & editing: G.J., X.Z., and B.W. **Competing interests:** The authors declare that they have no competing interests. **Data and materials availability:** The GFED4.1s dataset is available at https://www.geo.vu.nl/~gwerf/GFED/GFED4/. The $PM_{2.5}$ data from the Environmental Protection Agency (EPA) Air Quality System (AQS) and Interagency Monitoring of Protected Visual Environments (IMPROVE) network are available at https://aqs.epa.gov/aqsweb/airdata/download_files.html and https://vista.cira.colostate.edu/Improve/, respectively. The National Oceanic and Atmospheric Administration hazard mapping system (HMS) smoke products are available at http://www.ospo.noaa.gov/products/land/hms.html. The Modern-Era Retrospective analysis for Research and Applications version 2 (MERRA-2) aerosol diagnostics (tavg1_2d_aer_Nx), meteorology diagnostics (tavg1_2d_slv_Nx), and aerosol optical depth (inst3_2d_gas_Nx) are available at https://goldsmr4.gesdisc.eosdis.nasa.gov/data/MERRA2/. The Copernicus Atmospheric Monitoring Service (CAMS) global reanalysis dataset is available at https://ads.atmosphere.copernicus.eu/cdsapp#!/dataset/cams-global-reanalysis-eac4. The US high-resolution air pollutants (USHAP) dataset is available at https://zenodo.org/doi/10.5281/zenodo.7884640. (*48*) The Moderate Resolution Imaging Spectroradiometer (MODIS) atmosphere daily global product (MYD08_D3) for aerosol optical depth is available at https://atmosphere-imager.gsfc.nasa.gov/products/daily. The European Center for Medium-Range Weather Forecasts (ECMWF) fifth-generation atmospheric reanalysis (ERA5) data are available at https://cds.climate.copernicus.eu/datasets. The Tropical Rainfall Measuring Mission (TRMM) 3B42-V7 daily product is available at https://gpm.nasa.gov/missions/trmm. The Multi-source Weighted Ensemble Precipitation (MSWEP) product is available at https://www.gloh2o.org/mswep/. The Level 3 product of Clouds and the Earth's Radiant Energy System (CERES) Synoptic TOA and Surface Fluxes and Clouds (SYN1deg Level 3) dataset is available at https://ceres.larc.nasa.gov/data/. The Gridded Population of the World, version 4 (GPW v4) dataset is available at https://sedac.ciesin.columbia.edu/data/collection/gpw-v4/. Detailed population data for each US state is available from the United States Census Bureau (USCB) at https://www2.census.gov/programs-surveys/popest/technical-documentation/methodology/modified-race-summary-file-method/mrsf2010.pdf. The health metrics from the 2019 Global Burden of Disease (GBD) study can be accessed at https://vizhub.healthdata.org/gbd-results/. The labor data products from the International Labour Organization (ILOSTAT) are available at https://ilostat.ilo.org/data/.

SUPPLEMENTARY MATERIALS

science.org/doi/10.1126/science.ads1957
Materials and Methods; Figs. S1 to S23; Tables S1 to S2; References (*49–113*)

Submitted 2 August 2024; accepted 16 July 2025

10.1126/science.ads1957

CHEMICAL KINETICS

Microcanonical kinetics of water-mediated proton transfer in microhydrated 4-aminobenzoic acid

Abhijit Rana, Payten A. Harville, Thien Khuu, Mark A. Johnson*

Isolated cluster systems can help to elucidate the molecular level description of water-mediated proton transfer. Protonation of neutral 4-aminobenzoic acid (4ABA) occurs at the acid (*O*-protomer) and amine (*N*-protomer) functionalities, yielding two distinct species with relative energies dependent on the degree of hydration. Here, we measured the rates of intramolecular proton transfer in $4ABAH^+{\cdot}(H_2O)_6$ ions upon protomer-selective vibrational excitation of initially cold (6 K) cluster ions isolated in a cryogenic ion trap. Interconversion rates were observed on the microsecond time scale. These results quantify the kinetics of proton transfers in the context of a closed, finite system at well-defined internal energies and therefore provide experimental benchmarks for theoretical efforts that are being developed to treat relatively slow, highly cooperative solvent-mediated chemical processes.

The migration of excess protons through hydrogen-bonded networks lies at the heart of electrical charge conduction in natural processes (e.g., mammalian vision) (*1*–*3*) and in engineered devices (e.g., fuel cells and batteries) (*4*–*6*). In aqueous media, this process is generally thought to occur through a sequential proton-relay mechanism introduced by Grotthuss in 1809 and refined in many simulations (*7*–*11*) of protons in water and experimental measurements using ultrafast vibrational spectroscopy (*2*, *12*–*14*) and x-ray absorption (*15*). Here, we addressed how a precisely determined number of water molecules act to transfer protons between two sites on an organic scaffold, 4-aminobenzoic acid (4ABA) (*8*, *16*–*19*). In isolation, protonation of neutral 4ABA to form $4ABAH^+$ occurs at the acid (*O*-protomer or "***O***") and amine (*N*-protomer or "***N***") functionalities, with the calculated structures presented in Fig. 1A (*17*, *20*–*23*).

The relative energies of the two $4ABAH^+$ protomers strongly depend on the degree of hydration. Specifically, although ***N*** is energetically favored in aqueous solution, ***O*** lies lower in energy as an isolated ion (*17*, *20*–*24*). Hydration-induced conversion from ***O*** to ***N*** has been reported using ion mobility and IR spectroscopy (*16*–*18*). Another study used a "dual ion trap" scheme to control the protomer distribution under microhydration and concluded that the onset for proton transfer from ***O*** to ***N*** occurs at $n = 5$ (*16*, *25*). Most recently (*26*), however, interconversion was observed with an onset at $n = 3$, consistent with a molecular dynamics simulation of the kinetics (*8*). That experimental result was obtained using a variation on the method pioneered by Zwier and Rizzo (*27*, *28*) in which cold $4ABAH^+{\cdot}(H_2O)_n$ clusters were excited by a protomer-selective, pulsed infrared (IR) laser excitation and then quenched back to the trap temperature (without loss of H_2O). Shifts in the protomer distribution were then extracted by analyzing sharp bands in the infrared multiphoton dissociation (IRMPD) spectra of the cold ions. Theoretical predictions are not yet converged regarding the relative energies of the ***N*** and ***O*** hydrates (*8*, *16*–*19*), but agree in the overall expectation than they lie close in energy with ***N*** becoming favored at $n = 6$ by ~0.5 kcal/mol (*16*, *18*). Near the energetic tipping point for size-dependent interconversion, the transfer can occur at an internal energy below that required to dissociate a water molecule (*29*). This type of selective optical IR excitation enables direct measurements of the time scales involved in the long-range, multistep process of solvent-mediated proton transfer in an isolated, finite system at a precisely determined internal energy. We describe an experimental approach to measure these kinetics in the mass-selected $4ABAH^+{\cdot}(H_2O)_6$ cluster ion starting from well-defined initial structures by exploiting recent developments in cryogenic mass spectrometry combined with laser spectroscopy (*27*–*29*).

Preparation and spectroscopic characterization of $4ABAH^+{\cdot}(H_2O)_6$ isomers

The experimental approach is shown schematically in Fig. 1B and described in detail in the supplementary materials. Briefly, hydrated $4ABAH^+$ cations, $4ABAH^+{\cdot}(H_2O)_n$, are generated by electrospray ionization, followed by condensation of water vapor in a radiofrequency (RF) octopole ion trap held at 77 K (*30*, *31*). A packet of these clusters is then transferred to a cryogenic (6 K) three-dimensional (3D) ion trap (Paul), where they are cooled by a pulse of He buffer gas (*32*). The target ion, $4ABAH^+{\cdot}(H_2O)_6$, is isolated by operating the Paul trap in mass-selective mode (*33*, *34*). This is accomplished by applying a low-voltage (~2 V) RF pulse to one of the endcaps of the trap to resonantly excite and remove all other ions based on driving their secular frequencies during the initial 65 ms of the 100-ms (10-Hz) experimental cycle. The IR-pump/ultraviolet (UV)–probe (5-ns pulse width) lasers are introduced into the trap 15 ms after the end of the mass-selection RF burst. The time delay, Δt, between the IR and UV lasers is varied over the range of 0 to 20 μs.

The differing degrees of electron delocalization adopted by the two protomers result in substantially different electronic absorptions (*35*), as illustrated by the UV photofragmentation spectra of the cryogenically cooled D_2-tagged ions displayed in Fig. 1A (*26*). Specifically, the ***N*** spectrum consists of a well-defined vibrational progression with a band origin at ~272 nm, which is similar to that displayed by protonated aniline (*36*). This band system corresponds to the usual π-π* excitation centered on the benzene ring. Conversely, the UV spectrum of the planar *O*-protomer also displays a long vibrational progression but with a band origin at ~350 nm, indicating that the *p* orbitals on the NH_2 and $COOH_2^+$ groups share in the resonance delocalization of the electrons on the ring. This scenario creates the opportunity to efficiently monitor the population of ***O*** in a mixed ensemble of protomers by following the photofragment yield generated by excitation of the ion packet in the 290- to 350-nm range. However, selective detection of the ***O*** population in an ensemble of $4ABAH^+{\cdot}(H_2O)_n$ clusters requires understanding how the intrinsic absorptions evolve with increasing solvation. Figure S4 presents the cluster size dependence of the UV absorption bands displayed by the cold $\boldsymbol{O}{\cdot}(H_2O)_{n=0\text{-}6}$ and $\boldsymbol{N}{\cdot}(H_2O)_{n=0,1}$ protomers. The ***O*** series displays a solvatochromic blue shift with addition of each water molecule, whereas the overall band envelope remains similarly broad. The band origin in the $\boldsymbol{N}{\cdot}H_2O$ spectrum, however, appears very close to that observed for the bare ***N*** ion with a marked decrease in intensity upon addition of only one water molecule. The latter behavior is consistent with the substantial suppression of the ~272-nm band in 4ABA at low pH in aqueous solution (*37*).

The ability to selectively fragment the $\boldsymbol{O}{\cdot}(H_2O)_n$ population in a mixed ensemble is useful because it allows for isolation of the $\boldsymbol{O}{\cdot}(H_2O)_6$ vibrational spectrum at low temperature. This is accomplished by monitoring the IRMPD spectrum of the $4ABAH^+{\cdot}(H_2O)_6$ ions that is modulated by photoexcitation of the 6 K ion packet at 296 nm, thus depleting the ***O*** contribution to the spectrum. The details

Sterling Chemistry Laboratory, Yale University, New Haven, CT, USA. *Corresponding author. Email: mark.johnson@yale.edu

of this measurement are presented in the supplementary materials, sections S1.f and S4. The full-range UV absorption spectrum of ***O***·$(H_2O)_6$, used to guide bleach wavelength selection, is provided in fig. S5. The IRMPD spectra of the two cold $n = 6$ protomers are presented in Fig. 2, A and B. These patterns confirm the bands assigned earlier (*17*) to the bound NH groups of ***N*** near 3100 cm^{-1} $[v^b_{NH}(N)]$ and the bound OH groups associated with the ***O*** isomer near 3300 cm^{-1} $[v^b_{OH}(O)]$, whereas the envelope near 3400 cm^{-1} and the free OH bands near 3700 cm^{-1} are common to both species. The 4ABAH$^+$·$(H_2O)_6$ spectrum in the fingerprint region was obtained by D_2 tagging (for details, see the supplementary materials, section S1f) and confirms the presence of the acid C=O stretch at 1743 cm^{-1} arising from ***N***, which is not modulated upon bleaching at 296 nm (fig. S9B). This establishes that UV bleach near 300 nm is not associated with the hydrated ***N***. Note that the ***O*** spectrum (Fig. 2A) displays the characteristic strong bands arising from the symmetric and asymmetric stretches of the nonbonded, neutral NH_2 group, indicating that the water molecules in the cold *O*-protomer do not interact with the NH_2 group (*23*).

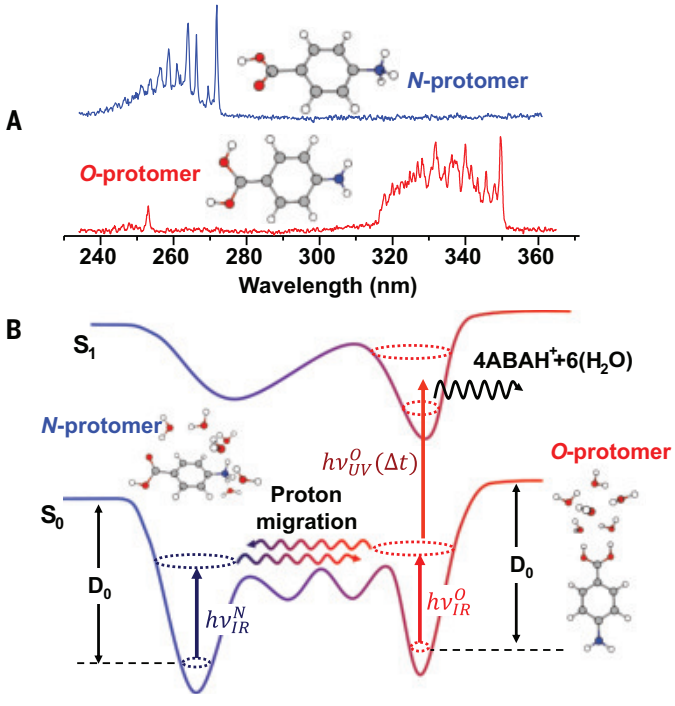

Fig. 1. Protonation motifs of 4ABAH$^+$. (**A**) UV photofragmentation spectra of the two protomers adopted by D_2-tagged, 4ABAH$^+$: ***N*** (detected by loss of D_2 and NH_3) and ***O*** (detected by loss of D_2 and H_2O). (**B**) Schematic diagram showing how isotopomer-selective vibrational excitation of the cold, locally stable clusters enables time-resolved measurements of the ***O***·$(H_2O)_6$ population by monitoring its strongly red-shifted UV absorption band in the 290- to 350-nm range.

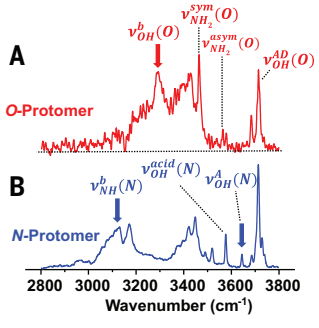

Fig. 2. Protomer-selective IRMPD spectra for 4ABAH$^+$·$(H_2O)_6$ cooled in an ion trap at 6 K. (**A**) Isolation of ***O***·$(H_2O)_6$ by recording the modulated IRMPD signal (loss of one water molecule) by *O*-specific UV photodissociation at 296 nm. (**B**) isolation of the ***N***·$(H_2O)_6$ spectrum by removing the contribution of ***O***·$(H_2O)_6$ from the overall IRMPD spectrum (see the supplementary materials, section S4 and fig. S6). Arrows indicate the transitions used for protomer-selective vibrational excitation.

The fact that the vibrational spectra of the cold protomers yield mutually exclusive vibrational bands creates the opportunity to selectively excite one or the other to trigger intracluster chemical transformations. This is accomplished by reducing the IR excitation laser power to suppress multiphoton induced dissociation. In addition, when the overall proton-transfer (PT) reaction is nearly isoenergetic, the solvent-mediated rearrangements occur without solvent evaporation, thus allowing large amplitude motions to occur in the context of a finite system in isolation and at a well-defined internal energy. This protomer-selective excitation scheme raises the interesting question of the hierarchy of relaxation processes that occur in the cluster. For example, it is expected that anharmonic coupling between (nominal) $v = 1$ OH and NH vibrational levels and background intermolecular modes leads to efficient randomization of the vibrational energy (*38*–*40*). This process is indeed at play in a typical vibrational predissociation "tagging" experiment. The situation is less clear, however, regarding the time scale of large amplitude motion through a tight transition state in the rugged landscape of the potential energy surface associated with water-mediated proton transfer. Clarifying the kinetics of this process was the goal of this study.

Time-resolved kinetics of proton migration in 4ABAH$^+$·$(H_2O)_6$

The state of the $n = 6$ cluster immediately after vibrational excitation of ***O***·$(H_2O)_6$ can be assessed by monitoring the population in vibrationally excited levels, which is encoded in the vibrational hot bands (absorptions to red of the sharp onset in the cold vibronic band envelope). Figure 3A compares the spectra of cold $n = 6$ with that 20 ns after vibrational excitation, and indeed diffuse absorption appears on the low-energy side of the sharp band origin at 312 nm in the cold spectrum (green). The time evolution of this envelope is critical because it reveals whether the hot ***O***·$(H_2O)_6$ species undergoes spectroscopically observable deformations as the water network relaxes from its initial structure. The hot-band absorption is indeed time dependent on the microsecond time scale, as evidenced by the spectra displayed in Fig. 3A. The overall shape remains essentially intact as the intensity decreases. This indicates that the average structure *O* solvent shell is persistent. The intensity of the 310-nm band is enhanced by vibrational excitation and was used to monitor the time-dependent changes in the ground state population. The fractional change in intensity is plotted in Fig. 3B and is observed to decrease substantially in a few microseconds. This intensity reduction is consistent with the conversion of the vibrationally hot *O*-protomer into the *N*-protomer. This conclusion was confirmed using the method described previously (*26*), in which we monitored vibrationally driven changes in the IRMPD spectra after collisionally cooling the vibrationally excited clusters back to the trap temperature, a process that occurs on a much slower (~5-ms) time scale (*29*). The results of this vibrationally driven interconversion followed by vibrational relaxation are displayed in fig. S8A. To determine the time scale for interconversion immediately after excitation of the $v^b_{OH}(O)$ band, we monitored absorbance at 310 nm with the result displayed in Fig. 3B. The decay follows a single-exponential form with a characteristic time constant of 2.1 ± 0.1 μs. Notably, the decay reaches an asymptotic value higher than the initial absorption before IR excitation, confirming that some of the vibrationally hot ***O***·$(H_2O)_6$ population persists when steady state is achieved. The observed asymptote is a lower limit because the points on the plot in Fig. 3B represent the IR laser on-off difference in UV absorption, which applies to the case where the net displacement of population from $v = 0$ to 1 is negligible.

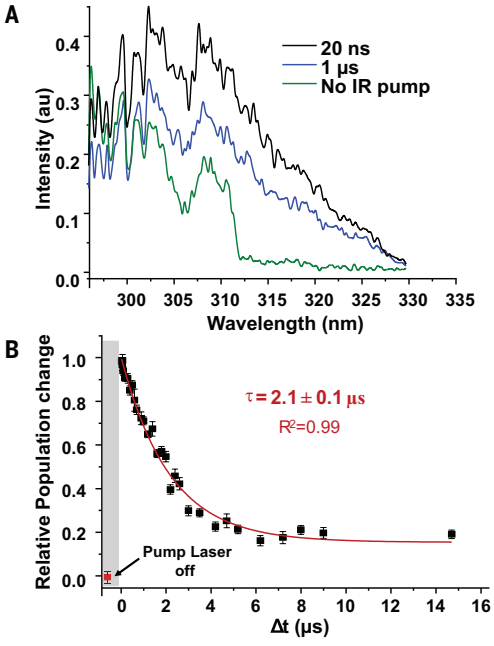

Fig. 3. Proton migration kinetics after *O*-protomer excitation. (**A**) UV photofragmentation spectrum of cold $\boldsymbol{O}\cdot(H_2O)_6$ (green) compared with that collected 20 ns (black) and 1 μs (blue) after *O*-selective IR excitation at 3290 cm^{-1} [$v^b_{OH}(O)$; arrow in Fig. 2A]. The green trace in (A) is reproduced as panel (J) in fig. S4. (**B**) Plot showing time-dependent vibrational hot-band absorption at 310 nm as a function of the time delay, Δt, between IR pump laser (3290 cm^{-1}, *O*-specific) and UV probe laser (310 nm, *O*-specific). The decay curve (red) is fit to a single exponential decay with a time constant of 2.1 ± 0.1 μs. The SD shown as error bars in the kinetics plots (typically about ±0.015) is derived by averaging ~750 data points for each measurement.

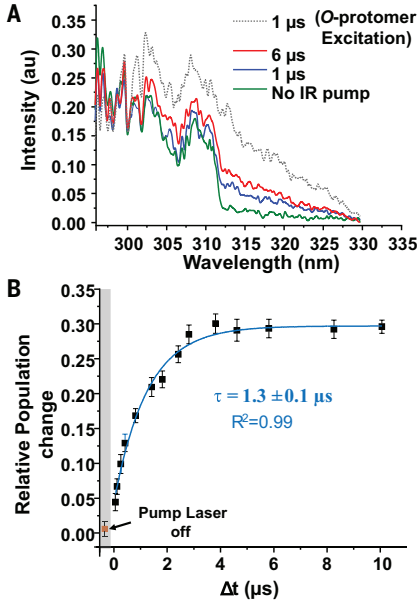

Fig. 4. Proton migration kinetics after *N*-protomer excitation. (**A**) UV photofragmentation spectrum of cold $\boldsymbol{O}\cdot(H_2O)_6$ compared with the UV spectrum collected 1 μs (blue) and 6 μs (red) after *N*-selective IR excitation at 3110 cm^{-1} [$v^b_{NH}(N)$; arrow in Fig. 2B]. UV photofragmentation spectrum collected 1 μs after *O*-specific IR excitation (as discussed in Fig. 3A) is compared in dotted gray. (**B**) Plot showing time-dependent vibrational hot-band absorption at 310 nm as a function of the time delay, Δt, between IR pump laser (3110 cm^{-1}, *N*-specific) and UV probe laser (310 nm, *O*-specific). The overall rise curve is fit to a single exponential decay (blue) with a time constant of 1.3 ± 0.1 μs. Each error bar in the kinetics plots reflects the SD from averaging ~750 data points for each time point.

It is also possible to vibrationally activate $\boldsymbol{N}\cdot(H_2O)_6$ to establish whether the characteristic $\boldsymbol{O}\cdot(H_2O)_6$ UV band is recovered, signaling transfer of the proton back to the acid carbonyl. Figure 4A displays the UV photofragmentation spectrum 1 and 6 μs after vibrational excitation of $\boldsymbol{N}\cdot(H_2O)_6$ with the $v^b_{NH}(N)$ transition (blue arrow at 3110 cm^{-1} in Fig. 2B). The excited $\boldsymbol{N}\cdot(H_2O)_6$ clusters indeed display absorption in the hot-band region quite similar to that observed promptly after $\boldsymbol{O}\cdot(H_2O)_6$ excitation (dotted gray trace in Fig. 4A). In contrast to the behavior upon vibrational excitation of $\boldsymbol{O}\cdot(H_2O)_6$, the hot bands are absent right after vibrational excitation of $\boldsymbol{N}$ but grow in over a few microseconds. Figure 4B displays the time dependence of the UV absorption at 310 nm. The UV absorption follows single-exponential kinetics with a time constant of 1.3 ± 0.1 μs, close to that displayed by the excited *O*-protomer. Similar results were obtained when probing in the hot-band region at 315 nm, as illustrated in fig. S11. The two time constants are distinguishable within error limits, however, such that the $\boldsymbol{N}\cdot(H_2O)_6 \rightarrow \boldsymbol{O}\cdot(H_2O)_6$ rate is 40% faster than that corresponding to $\boldsymbol{O}\cdot(H_2O)_6 \rightarrow \boldsymbol{N}\cdot(H_2O)_6$. In the case where relaxation occurs to the same equilibrium state, for example, the characteristic decay time is given by $1/(k_r + k_f)$, where k_r and k_f are the internal energy-dependent forward and reverse rate coefficients (*41*, *42*). One possibility for the observed difference in rates is that the internal energy above the global minimum is dependent on both infrared photon energy and overall reaction thermochemistry. To evaluate the internal energy dependence of the interconversion rate, we extended the pump-probe study to determine the internal energy dependence of the relaxation rate starting from the $\boldsymbol{N}$ configuration. This is possible because selective excitation of $\boldsymbol{N}\cdot(H_2O)_6$ can be achieved by pumping the higher energy band at 3645 cm^{-1} [$v^A_{OH}(N)$, blue arrow in Fig. 2B]. The time evolution of the $\boldsymbol{O}$-UV absorption is displayed in fig. S10, this time with a faster single exponential time constant of 0.9 μs, consistent with faster interconversion at higher energy upon excitation with a single IR photon. Classical MD simulations performed at 350 K indicated proton migration on the 100-ps time scale (*8*). Therefore, the much slower reaction times observed here likely reflect the lower internal energy (3400 cm^{-1} excitation yields an internal energy corresponding to average energy of a thermal ensemble at ~250 K; see the supplementary materials, section S8), accuracy of the potential energy landscape, and nuclear quantum effects.

These results establish the time scales of the highly cooperative mechanics at play in solvent-driven chemistry in the context of finite, isolated systems with well-defined internal energies and starting structures. This in turn provides an important benchmark for theoretical methods under development to address the complexity of the regime, ubiquitous in solution chemistry, in which solvents, reactants, and products play equivalent roles at the molecular level.

REFERENCES AND NOTES

1. E. Freier, S. Wolf, K. Gerwert, *Proc. Natl. Acad. Sci. U.S.A.* **108**, 11435–11439 (2011).
2. Z. Chen *et al.*, *J. Am. Chem. Soc.* **145**, 3394–3400 (2023).
3. J. Ono, C. Okada, H. Nakai, *Chemphyschem* **23**, e202200109 (2022).
4. M. Saito, K. Hayamizu, T. Okada, *J. Phys. Chem. B* **109**, 3112–3119 (2005).
5. Y. Lin *et al.*, *Angew. Chem. Int. Ed.* **62**, e202218745 (2023).
6. Z. Song *et al.*, *Angew. Chem. Int. Ed.* **62**, e202219136 (2023).
7. R. Tripathi, L. Durán Caballero, R. Pérez de Tudela, C. Hölzl, D. Marx, *ACS Omega* **6**, 12676–12683 (2021).
8. P. R. Batista, T. C. Penna, L. C. Ducati, T. C. Correra, *Phys. Chem. Chem. Phys.* **23**, 19659–19672 (2021).
9. S. Yan, B. Wang, H. Lin, *J. Chem. Theory Comput.* **19**, 448–459 (2023).
10. R. Jinnouchi, S. Minami, F. Karsai, C. Verdi, G. Kresse, *J. Phys. Chem. Lett.* **14**, 3581–3588 (2023).
11. R. J. Wei *et al.*, *Photosynth. Res.* **156**, 101–112 (2023).
12. M. Thämer, L. De Marco, K. Ramasesha, A. Mandal, A. Tokmakoff, *Science* **350**, 78–82 (2015).
13. S. Woutersen, H. J. Bakker, *Phys. Rev. Lett.* **96**, 138305 (2006).
14. F. Dahms, B. P. Fingerhut, E. T. J. Nibbering, E. Pines, T. Elsaesser, *Science* **357**, 491–495 (2017).
15. M. Ekimova *et al.*, *Angew. Chem. Int. Ed.* **61**, e202211066 (2022).

16. K. Akasaka *et al.*, *Phys. Chem. Chem. Phys.* **25**, 4481–4488 (2023).
17. T. M. Chang, J. S. Prell, E. R. Warrick, E. R. Williams, *J. Am. Chem. Soc.* **134**, 15805–15813 (2012).
18. M. J. Hebert, D. H. Russell, *J. Phys. Chem. B* **124**, 2081–2087 (2020).
19. T. Khuu, S. J. Stropoli, K. Greis, N. Yang, M. A. Johnson, *J. Chem. Phys.* **157**, 131102 (2022).
20. X. X. Zhang, J. L. Oscarson, R. M. Izatt, P. C. Schuck, D. Li, *J. Phys. Chem. B* **104**, 8598–8605 (2000).
21. Z. Tian, S. R. Kass, *Angew. Chem. Int. Ed.* **48**, 1321–1323 (2009).
22. J. Seo *et al.*, *Phys. Chem. Chem. Phys.* **18**, 25474–25482 (2016).
23. T. Khuu, N. Yang, M. A. Johnson, *Int. J. Mass Spectrom.* **457**, 116427 (2020).
24. A. L. Patrick, A. P. Cismesia, L. F. Tesler, N. C. Polfer, *Int. J. Mass Spectrom.* **418**, 148–155 (2017).
25. K. Hirata, K. Akasaka, O. Dopfer, S. I. Ishiuchi, M. Fujii, *Chem. Sci.* **15**, 2725–2730 (2024).
26. A. Rana *et al.*, *J. Phys. Chem. Lett.* **16**, 5252–5257 (2025).
27. C. P. Harrilal *et al.*, *J. Phys. Chem. A* **122**, 2096–2107 (2018).
28. C. Seaiby, A. V. Zabuga, A. Svendsen, T. R. Rizzo, *J. Chem. Phys.* **144**, 014304 (2016).
29. T. Khuu *et al.*, *J. Am. Soc. Mass Spectrom.* **34**, 737–744 (2023).
30. B. M. Marsh, J. M. Voss, E. Garand, *J. Chem. Phys.* **143**, 204201 (2015).
31. E. M. Duffy, J. M. Voss, E. Garand, *J. Phys. Chem. A* **121**, 5468–5474 (2017).
32. X.-B. Wang, L.-S. Wang, *Rev. Sci. Instrum.* **79**, 073108 (2008).
33. H. Kang, G. Féraud, C. Dedonder-Lardeux, C. Jouvet, *J. Phys. Chem. Lett.* **5**, 2760–2764 (2014).
34. R. E. March, *J. Mass Spectrom.* **32**, 351–369 (1997).
35. E. Matthews, C. E. H. Dessent, *Phys. Chem. Chem. Phys.* **19**, 17434–17440 (2017).
36. Y. Inokuchi *et al.*, *Phys. Chem. Chem. Phys.* **17**, 25925–25934 (2015).
37. W. D. Kumler, L. A. Strait, *J. Am. Chem. Soc.* **65**, 2349–2354 (1943).
38. D. J. Nesbitt, R. W. Field, *J. Phys. Chem.* **100**, 12735–12756 (1996).
39. Y. Yamada, J.-i. Okano, N. Mikami, T. Ebata, *Chem. Phys. Lett.* **432**, 421–425 (2006).
40. J. M. Smith, X. Zhang, J. L. Knee, *J. Chem. Phys.* **99**, 2550–2559 (1993).
41. M. Eigen, *Nobel Lecture* **11**, 1963–1979 (1967).
42. C. Bernasconi, *Relaxation Kinetics* (Academic Press, 2012).
43. A. Rana, P. A. Harville, T. Khuu, M. Johnson, Data for: Microcanonical kinetics of water-mediated proton transfer in microhydrated 4-aminobenzoic acid, Dryad (2025); https://doi.org/10.5061/dryad.547d7wmkw.
44. M. J. Frisch *et al.*, "Gaussian 09 revision A.1" (Gaussian, 2009).

ACKNOWLEDGMENTS

We thank E. Perez for his help in the early stages of obtaining the UV spectra and S. J. Stropoli and S. C. Edington for their assistance in developing the scheme for measuring the isomer-specific IRMPD spectra. **Funding:** This work was supported by the Department of Energy, Condensed Phase and Interfacial Molecular Science (CPIMS grant DE-SC0021012 to M.A.J. for our work on the speciation and transport of hydrated protons); the Air Force Office of Scientific Research (AFOSR MURI grant 62742085-204669 to M.A.J. for our work on microhydration of protonated organic acids); a John C. Tully Graduate Research Fellowship in Chemistry at Yale University (P.A.H.); and the National Institutes of Health (Biophysical Training grant 5T32GM008283-32 to T.K.). **Author contributions:** Conceptualization: M.A.J.; Funding acquisition: M.A.J.; Investigation: A.R., P.A.H., T.K.; Methodology: A.R., P.A.H., T.K., M.J.; Project administration: M.A.J.; Supervision: M.A.J.; Visualization: A.R., P.A.H.; Writing – original draft: M.A.J., A.R.; Writing – review & editing: M.A.J., P.A.H., A.R. **Competing interests:** The authors declare no competing interests. **Data and materials availability:** Data underlying the reported spectra and kinetics plots have been deposited in Dryad (*43*). **License information:** Copyright © 2025 the authors, some rights reserved; exclusive licensee American Association for the Advancement of Science. No claim to original US government works. https://www.science.org/about/science-licenses-journal-article-reuse

SUPPLEMENTARY MATERIALS

science.org/doi/10.1126/science.ady1723
Materials and Methods; Supplementary Text; Figs S1 to S12; Reference (*44*)

Submitted 14 April 2025; accepted 14 July 2025

10.1126/science.ady1723

SPECIATION

Rapid establishment of species barriers in plants compared with that in animals

François Monnet[1,2,3], Zoé Postel[1], Pascal Touzet[1], Christelle Fraïsse[1], Yves Van de Peer[2,3,4,5], Xavier Vekemans[1], Camille Roux[1]*

Speciation, the process by which new reproductively isolated species emerge from ancestral populations, results from the gradual accumulation of barriers to gene flow within genomes. To date, the notion that interspecific genetic exchange (introgression) occurs more frequently between plant species than animals has gained a strong footing in scientific discourse. By examining the dynamics of gene flow across a continuum of divergence in both kingdoms, we observed the opposite relationship: Plants experience less introgression than animals at the same level of genetic divergence, suggesting that species barriers are established more rapidly in plants. This pattern raises questions about which differences in microevolutionary processes between plants and animals influence the dynamics of reproductive isolation establishment at the macroevolutionary scale.

Introgression, the genetic exchange between populations or between speciating lineages, has long been recognized as an important evolutionary process (*1*). The number of genetic novelties brought by introgression in a population can exceed the contribution of mutation alone, thus increasing both neutral and selected diversity, which can be the source of major evolutionary advances (*2*). One consequence of such introgression events is the facilitation of the spread on a large scale (geographical and/or phylogenetic) of mutations that were originally locally beneficial (*3*). However, genetic exchange across the phylogenetic tree of life is not unrestricted. It is gradually interrupted by specific mutations, known as species barriers, that reduce hybrid fitness and progressively accumulate in the genome as evolutionary lineages diverge (*4*). These genetic barriers to gene flow contribute to reproductive isolation by either reducing hybrid production or diminishing hybrid fitness. The consequences of reproductive isolation can therefore be captured through the long-term effect of these genetic barriers as a localized reduction of introgression in the genomes, which provides a powerful quantitative metric applicable to any organism (*5*). Thus, the genomes of speciating lineages go through a transitional stage, the so-called "semi-isolated species" stage, during which they form mosaics of genomic regions: some remain permeable to gene flow, whereas others become tightly linked to barriers (*6*). The consideration of this "semi-isolated" status is key to better understanding the dynamics of the speciation process: i) When does the transition from populations to semi-isolated species occur, and ii) at what level of molecular divergence do species become fully reproductively isolated?

Historically, reproductive isolation has been studied using complementary approaches. From an "organismal" perspective, it is evaluated using controlled crosses that measure reductions in hybrid viability or fertility, typically over one or two generations (*5*). By contrast, the "genetic" approach infers reduction in gene flow between populations over extended evolutionary periods based on the molecular signatures left by reproductive isolation in their genomes (*5*). Although organismal studies offer valuable insights into isolating mechanisms and the genomic architecture of reproductive isolation—such as the number of loci involved, their individual phenotypic effects, and the extent of genetic interactions—they have inherent limitations in detecting species barriers as they occur in nature (*7*). To overcome these limitations and investigate the dynamics of reproductive isolation, we examined patterns of gene flow in natural populations, where introgression leaves detectable genomic signatures. Metrics such as the fixation index (F_{ST}) (*8*) and derivatives of the ABBA-BABA test (*9*, *10*) are widely used to assess whether divergence occurred under strict allopatry. However, they cannot estimate the timing of gene flow. Recent computational methods have made it possible to explicitly test evolutionary scenarios, including ongoing gene flow, and account for the effect of semipermeable species barriers (*11*–*13*). Applied to 61 pairs of animal taxa across a continuum of molecular divergence, these methods revealed frequent introgression of up to 2% net divergence (*14*) and outstanding cases of gene flow between lineages 14 times more divergent than humans and chimpanzees (*15*).

Whether the dynamics of species barrier formation follow universal patterns across kingdoms remains unknown. In the early 2000s, a landmark study comparing hybridization rates in plants and animals based on taxonomic records reported higher average frequencies in plants (*16*), in agreement with older assertions on the subject (*2*, *17*, *18*), but this was contradicted by an analysis that used phenotypic rather than taxonomic evidence and found higher crossability in animals (*19*). Since these two studies, few attempts have been made to directly compare plants and animals in this context (*20*). These early approaches were restricted to the occurrence of hybridization, largely based on morphological species, and lacked information on molecular divergence or introgression. As a result, they could not assess how gene flow decays with molecular divergence, a key component of speciation dynamics (*4*). This limitation can now be overcome by using genomic data, which enables the delineation of genetic clusters and the quantification of both divergence and effective gene flow across the genome (*5*, *21*). In this study, we adopted a comparative genomic approach that integrates datasets across taxa within a unified statistical framework to explicitly test whether the dynamics of gene flow reduction differ between plants and animals at comparable levels of divergence.

Results

The present investigation examines the decrease in ongoing gene flow between closely related lineages as a function of their genetic divergence and compares this dynamic across two phylogenetic kingdoms: plants and animals. For this purpose, we empirically explored a continuum of genetic divergence represented by 61 animal pairs and 280 plant pairs. Genomic data from each pair allowed the quantification of molecular patterns of polymorphism and divergence by measuring a combination of 39 summary statistics commonly used in population genetics along with the joint site frequency spectrum (jSFS). Analysis of simulated datasets provided evidence that our approach is more powerful than phylogenetic methods for detecting introgression (*22*) (supplementary materials A.4). For each dataset, we then applied an approximate Bayesian computation framework [ABC; (*11*)] to assess whether the observed set of summary statistics was better reproduced by scenarios of speciation with or without ongoing migration. The same ABC methodology for demographic inferences was used for both the animal dataset [analyzed in (*14*)] and the newly compiled plant dataset. The plant dataset was produced from publicly available sequencing reads covering 25 genera spanning the plant phylogeny (212 pairs of eudicots, 45 of monocots, 21 of gymnosperms, 1 lycophyte, and 1 magnoliid;

[1]Université de Lille, CNRS, UMR 8198 - Evo-Eco-Paleo, Lille, France. [2]Department of Plant Biotechnology and Bioinformatics, Ghent University, Ghent, Belgium. [3]VIB-UGent Center for Plant Systems Biology, Ghent, Belgium. [4]Department of Biochemistry, Genetics and Microbiology, University of Pretoria, Pretoria, South Africa. [5]College of Horticulture, Academy for Advanced Interdisciplinary Studies, Nanjing Agricultural University, Nanjing, China.
***Corresponding author. Email: camille.roux@cnrs.fr**

table S1). These pairs were selected without a preconceived idea about their speciation mode (supplementary materials A.2). The posterior probability of models with ongoing migration, as estimated by the ABC framework, was used to classify each pair as either isolated (isolation status) or still exchanging genes (migration status) along a continuum of divergence (Fig. 1A). This approach allowed for a direct comparison of speciation dynamics between plants and animals.

In contrast to qualitative expectations described in earlier studies (*16*), our findings suggest that genetic exchange ceases more rapidly in plants than in animals at lower levels of genetic divergence. This is characterized by a swifter transition in plants from population pairs that are best supported by migration models to those that are best described by isolation models ($P < 1 \times 10^{-4}$; Fig. 1A and table S2). Therefore, by fitting a generalized linear model for the migration or isolation status to the plant and animal datasets as a function of the net molecular divergence, we determined that the probability that two plant lineages are connected by gene flow falls below 50% at a net divergence of ≈0.3% [95% confidence interval (CI) (0.26%, 0.36%)]. By contrast, this inflection point in animals occurs at higher levels of divergence close to 1.5% [95% CI (1.1%, 2.7%); Fig. 1A and table S2]. This pattern remains robust after accounting for potential methodological and biological biases (supplementary materials A.6),

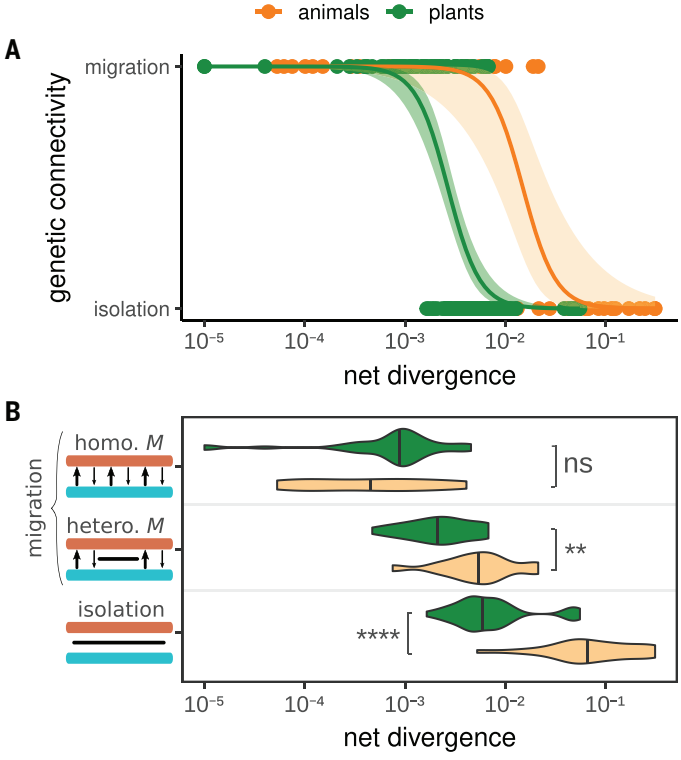

Fig. 1. Genomic patterns of introgression along a divergence continuum in plants versus animals. Average genomic divergence and migration or isolation status were estimated for 280 plant pairs (green) and 61 animal pairs (orange) using ABC (*11*, *14*). (**A**) Each point represents a plant (green) or animal (orange) pair, plotted according to its average genomic net divergence on the *x* axis and its best-supported model on the *y* axis (ongoing migration versus isolation). Curves show logistic regressions fitted separately for plants and animals. (**B**) Net divergence distributions for plant (green) and animal (orange) pairs under genomically homogeneous migration (homo. *M*), genomically heterogeneous migration (hetero. *M*), or isolation models. Bars along the *y* axis represent homologous chromosomes (blue, brown), gene flow (arrows), or barriers (black bars). Statistical significance (Mann–Whitney U test): ns, not significant ($P > 0.05$); *$P \leq 0.05$; **$P \leq 0.01$; ***$P \leq 0.001$; ****$P \leq 0.0001$.

including sequencing technology (table S3), unequal taxonomic sampling (fig. S1), and geographic distance (fig. S2). Within plants, speciation dynamics do not appear to be driven by growth form, as no significant difference was detected between trees and herbs using a similar comparative approach (fig. S3 and table S4). Likewise, we found no evidence that variation in selfing rates, whether estimated from published methods (*23*), custom approaches (*24*), or approximated from phenotypic data (*25*), influences the dynamics of gene flow cessation within plants across the range of selfing rates represented in our dataset (supplementary materials A.7.2, fig. S4, and table S4).

To further explore the build-up dynamics of species barriers within plant and animal genomes, we focused on species pairs supported by ongoing gene flow and examined the genomic distribution of introgression. Within the range of speciation scenarios considered, the rate of gene flow can be uniform across the genome (i.e., homogeneous), or it can vary locally from one genomic region to another (i.e., heterogeneous; see fig. S5) when barrier genes establish between the diverging species (*6*). The ABC framework described above allowed us to classify animal and plant pairs as experiencing either genomically homogeneous or heterogeneous introgression (*26*). We found that plants transition more quickly from having no barriers to having semipermeable barriers, with this shift occurring at a net divergence of ≈0.2% (compared with ≈0.6% in animals; Fig. 1B). These findings demonstrate that, in plants, both the onset of the species barriers that generate genomic heterogeneity of introgression rates as well as the establishment of complete isolation between species manifest at relatively lower levels of divergence than in animals. This suggests that the speciation process may require fewer mutations in plants than in animals for reproductive isolation to be both initiated and completed, a conclusion consistent with previous experimental crosses unraveling the genomic architecture of reproductive isolation in plants (*27*–*29*).

Lastly, we compared the temporal dynamics of gene flow during divergence in plants versus animals. We specifically examined whether ongoing gene flow is more often explained by continuous migration initiated since the subdivision of the ancestral population (as illustrated in Fig. 2) or by secondary contact following an initial period of geographic isolation and divergence. This model comparison using ABC was restricted to pairs for which we previously found a strong statistical support for ongoing gene flow. Our analysis shows that plants and animals differ in their primary mode of historical divergence, specifically in the extent of gene flow during the initial generations after the lineage split. Among animals, most cases of ongoing gene flow are best explained by models of continuous migration since the subdivision of the ancestral population (≈80%; Fig. 2), indicating that gene flow tends to occur more steadily over time. By contrast, plant lineages more frequently exhibit patterns indicative of secondary contact following an initial phase of allopatry (≈52%; Fig. 2). This result aligns with Richard Abbott's synthesis suggesting that secondary contact predominates in plant hybrid zones (*30*).

Discussion

The historical literature on hybridization defined hybrids as the offspring of crosses between individuals from genetic lineages, "which are distinguishable on the basis of one or more heritable characters" (*31*). Within this conceptual framework, examinations of numerous wild species on the basis of morphological and taxonomic records have historically supported the assumption that plants are more prone to hybridize than animals (*2*, *16*, *18*), although this result has been questioned by analyses using phenotypic criteria that found higher crossability in animals (*19*). However, the advent of molecular markers to measure genetic differentiation in the early 2000s provided results challenging morphological studies. Molecular data revealed that plants often show higher F_{ST} values within species than animals (*32*, *33*), indicating that gene flow at the intraspecific level is

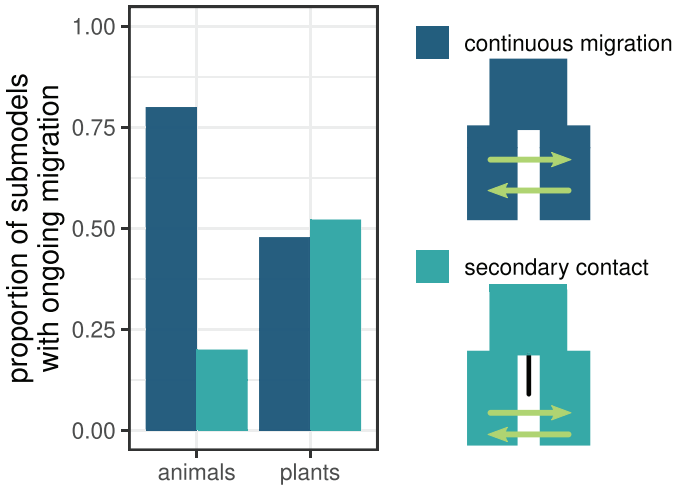

Fig. 2. Temporal models of ongoing migration in plants and animals. Among the 69 plant pairs and 30 animal pairs that were strongly supported under models with ongoing gene flow by our ABC approach, we further distinguished between alternative temporal models. For each of these supported pairs, we compared submodels of continuous migration (dark blue) and secondary contact (light blue) and report their relative proportions within each kingdom.

generally more restricted in plants. Moreover, Morjan and Rieseberg (*32*) showed that this difference between kingdoms persists regardless of the mating system (from outcrossing to selfing) as well as across various geographical scales (local, regional, or biregional ranges). Our methodological approach focused on genetic clusters that varied in both their degrees of pairwise divergence and connectivity through gene flow (fig. S8). By explicitly modeling the divergence history between lineages and genome-wide heterogeneity of gene flow, we were able to capture the genomic effect of species barriers. This framework helped reconcile an apparent contradiction—that morphology-based studies of reproductive isolation suggest more frequent hybridization events in plants than in animals (*16*) [although this view was challenged by Rieseberg *et al.* (*19*)] —whereas molecular data revealed greater genetic differentiation within plant species (*32*). Indeed, our explicit comparisons of ongoing migration models support the idea that scenarios of secondary contact are particularly frequent among the surveyed lineages in plants (*30*) relative to closely related animal species that tend to experience gene flow more continuously over time. Secondary contact scenarios imply an initial period of allopatry, which can drive divergence of sister lineages across molecular and morphological markers. Such a historical context may thus engender the misconception that plants undergo hybridization events more frequently than animals, simply because these events are more conspicuous in plants, as introgression happens more often between morphologically distinct lineages due to prior isolation. Conversely, the overall contribution of introgression to animal gene pools may be overlooked when species are delimited by morphology because much of it occurs between lineages lacking clear visible differences, regardless of their level of genomic divergence. However, we strongly emphasize that our findings should not be interpreted as evidence that speciation in animals frequently occurs in the presence of gene flow. Rather, the absence of ongoing gene flow inferred in our study serves as a proxy for reproductive isolation, reflecting the effect of barriers that, on average, accumulate more slowly across animal genomes.

The long-standing hypothesis that plants may experience more frequent hybridization at the population or species level than animals has also been difficult to reconcile with observations from both micro- and macroevolutionary scales:

(i) At the experimental level, quantitative genetic studies suggest potential differences in the genomic architecture of reproductive isolation between plants and animals. In plants, reproductive barriers may often involve relatively simpler genetic architectures, typically governed by a small number of loci with large effects (*27*–*29*, *34*). Moreover, it has been proposed that speciation genes may be subject to different evolutionary constraints in plants and animals (*35*). The growing number of speciation genes identified across diverse clades (*36*) will facilitate future empirical tests of whether average effect sizes differ between plants and animals and whether speciation genes indeed evolve under weaker selective constraints in plants. In parallel with these studies, measurements of postzygotic isolation in interspecific crosses indicate that a greater proportion of phenotypically defined species correspond to reproductively independent lineages in plants (around 70%) than in animals (~40%) (*19*).

(ii) At the phylogenetic scale, estimates of diversification rates suggest that plant lineages, on average, give rise to new lineages more rapidly than both vertebrates and invertebrates, as reflected in their higher estimated speciation rates (*37*, *38*).

The observed contrast in the accumulation of reproductive isolation between plants and animals may reflect underlying differences in the genetic architecture of reproductive barriers and/or differences in selective constraints acting on these barriers. Although our analysis focuses on population- or species-level processes, it raises the possibility that such microevolutionary differences could partly underlie the higher speciation rates often inferred in plants. Clarifying this connection will require future efforts combining comparative population genomics and macroevolutionary analyses.

Speciation dynamics clearly do not follow a universal molecular clock, although certain molecular constraints inevitably make the process irreversible once a critical level of divergence is reached (*4*, *16*). The rarity of hybrid zones in plants has recently received renewed attention (*30*), raising a new question: What genomic properties of plants facilitate the emergence of reproductive isolation between lineages after relatively few genetic changes? The evolution of reproductive barriers is shaped by ecological, genetic, geographical, and cytological factors, among others. Although our comparative population genomics approach reveals a notable contrast between plants and animals, it cannot alone unravel the underlying mechanisms driving this difference. Advancing our understanding of why reproductive isolation appears to accumulate more rapidly in plants will require integrative approaches, combining genomic, ecological, and developmental insights across diverse biological systems and evolutionary timescales (*39*, *40*).

REFERENCES AND NOTES

1. R. Abbott *et al.*, *J. Evol. Biol.* **26**, 229–246 (2013).
2. G. L. Stebbins, *Proc. Am. Philos. Soc.* **103**, 231–251 (1959).
3. M. Slatkin, in *Population genetics and ecology* (Elsevier, 1976), pp. 767–780.
4. M. R. Brown *et al.*, *Proc. Natl. Acad. Sci. U.S.A.* **120**, e2220261120 (2023).
5. A. M. Westram, S. Stankowski, P. Surendranadh, N. Barton, *J. Evol. Biol.* **35**, 1143–1164 (2022).
6. C.-I. Wu, *J. Evol. Biol.* **14**, 851–865 (2001).
7. M. E. Frayer, B. A. Payseur, *Evolution* **78**, 1025–1038 (2024).
8. S. Wright, *Ann. Eugen.* **15**, 323–354 (1951).
9. S. H. Martin, J. W. Davey, C. D. Jiggins, *Mol. Biol. Evol.* **32**, 244–257 (2015).
10. A. J. Dagilis *et al.*, *Evol. Lett.* **6**, 344–357 (2022).
11. C. Fraïsse *et al.*, *Mol. Ecol. Resour.* **21**, 2629–2644 (2021).
12. D. R. Laetsch *et al.*, *PLOS Genet.* **19**, e1010999 (2023).
13. V. C. Sousa, M. Carneiro, N. Ferrand, J. Hey, *Genetics* **194**, 211–233 (2013).
14. C. Roux *et al.*, *PLOS Biol.* **14**, e2000234 (2016).
15. C. Fraïsse *et al.*, *Peer Community J.* **2**, e54 (2022).
16. J. Mallet, *Trends Ecol. Evol.* **20**, 229–237 (2005).
17. L. Gottlieb, *Am. Nat.* **123**, 681–709 (1984).
18. E. Mayr, *Animal species and evolution* (Harvard Univ. Press, 1963).
19. L. H. Rieseberg, T. E. Wood, E. J. Baack, *Nature* **440**, 524–527 (2006).
20. S. Wang, J. E. Mank, D. Ortiz-Barrientos, L. H. Rieseberg, *Mol. Ecol.* 10.1111/mec.70004 (2025).

21. N. Galtier, *Evol. Appl.* **12**, 657–663 (2019).
22. N. B. Edelman *et al.*, *Science* **366**, 594–599 (2019).
23. M. A. Stoffel *et al.*, *Methods Ecol. Evol.* **7**, 1331–1339 (2016).
24. C. Roux, popgenomics/selfing_ML: selfing_ML, Zenodo (2025); https://doi.org/10.5281/zenodo.15296403.
25. A. J. Helmstetter *et al.*, Pollination and mating traits underlie diverse reproductive strategies in flowering plants. bioRxiv 2024.02.26.582019 [Preprint] (2024); https://doi.org/10.1101/2024.02.26.582019.
26. C. Roux, G. Tsagkogeorga, N. Bierne, N. Galtier, *Mol. Biol. Evol.* **30**, 1574–1587 (2013).
27. L. C. Moyle, E. B. Graham, *Genetics* **169**, 355–373 (2005).
28. L. C. Moyle, T. Nakazato, *Genetics* **179**, 1437–1453 (2008).
29. A. L. Sweigart, L. Fishman, J. H. Willis, *Genetics* **172**, 2465–2479 (2006).
30. R. J. Abbott, *J. Syst. Evol.* **55**, 238–258 (2017).
31. R. G. Harrison, *Oxf. Surv. Evol. Biol.* **7**, 69–128 (1990).
32. C. L. Morjan, L. H. Rieseberg, *Mol. Ecol.* **13**, 1341–1356 (2004).
33. R. Frankham, C. J. Bradshaw, B. W. Brook, *Biol. Conserv.* **170**, 56–63 (2014).
34. M. P. Zuellig, A. L. Sweigart, *Evolution* **72**, 2394–2405 (2018).
35. L. H. Rieseberg, B. K. Blackman, *Ann. Bot. (Lond.)* **106**, 439–455 (2010).
36. M. E. Frayer, N. V. Robles, M. J. R. Barrera, J. M. Coughlan, M. Schumer, The molecular evolutionary basis of species formation revisited. EcoEvoRxiv [Preprint] (2025); https://doi.org/10.32942/X2CP9B.
37. J. P. Scholl, J. J. Wiens, *Proc. Biol. Sci.* **283**, 20161334 (2016).
38. H. Morlon *et al.*, *Annu. Rev. Ecol. Evol. Syst.* **55**, 1–21 (2024).
39. D. I. Bolnick *et al.*, *Evolution* **77**, 318–328 (2023).
40. S. Stankowski *et al.*, *Evol. J. Linn. Soc.* **3**, kzae001 (2024).
41. F. Monnet *et al.*, Rapid establishment of species barriers in plants compared to animals, Zenodo (2025); https://zenodo.org/records/15288584.
42. F. Monnet, Ladarwall/Greenworld: Main release, Zenodo (2025); https://doi.org/10.5281/zenodo.15881247.

ACKNOWLEDGMENTS

We are grateful to the Institut Français de Bioinformatique (IFB; ANR-11-INBS-0013), thanks to whom bioinformatics analyses and demographic inferences have been carried out. The authors would like to thank H. Morlon, B. Van Boxlaer, S. Glémin, J. Pannell, and M. Lascoux for their constructive feedback. **Funding:** This work was supported by University of Lille (grant I-SITE ULNE – Ghent University). The French State under the France-2030 program and the Initiative of Excellence of the University of Lille are acknowledged for the funding and support granted to the R-CDP-24-002-PIE project. Y.V.d.P. acknowledges funding from the European Research Council (ERC) under the European Union's Horizon 2020 research and innovation program (grant no. 833522) and from Ghent University (Methusalem funding, BOF. MET.2021.0005.01). **Author contributions:** F.M.: data curation, formal analysis, investigation, visualization, writing; Z.P.: data curation; P.T.: resources, data curation, supervision; C.F.: methodology, writing; Y.V.d.P.: funding acquisition, supervision, writing; dX.V. funding acquisition, supervision, writing; C.R.: funding acquisition, conceptualization, methodology, supervision, coding, investigation, visualization, writing. **Competing interests:** The authors declare that they have no competing interests. **Data and materials availability:** All data described in the manuscript or the supplementary materials are available. The assembled datasets, the list of references used for mapping, and the results of demographic inference are deposited in Zenodo (*41*). Scripts for bioinformatic treatment of raw sequencing data and estimate of selfing rates are also available from Zenodo (*24*, *42*).

SUPPLEMENTARY MATERIALS

science.org/doi/10.1126/science.adl2356
Materials and Methods; Figs. S1 to S14; Tables S1 to S4; References (*43*–*102*); MDAR Reproducibility Checklist

Submitted 16 October 2023; resubmitted 22 December 2024; accepted 24 July 2025

10.1126/science.adl2356

HABITAT FRAGMENTATION

Fragmentation increased in over half of global forests from 2000 to 2020

Yibiao Zou[1]*, Thomas W. Crowther[1,2], Gabriel Reuben Smith[1], Haozhi Ma[3], Lidong Mo[1,4], Lalasia Bialic-Murphy[1], Peter Potapov[5,6], Klementyna A. Gawecka[7,8], Chi Xu[9], Pablo J. Negret[10,11], Thomas Lauber[1], Zhaofei Wu[1,3,12], Dominic Rebindaine[1], Constantin M. Zohner[1]

Habitat fragmentation, in which contiguous forests are broken into smaller, isolated patches, threatens biodiversity by disrupting species movement, shrinking populations, and altering ecosystem dynamics. Past assessments suggested declining global fragmentation, but they relied on structure-based metrics that overlook ecological connectivity. We analyzed global forest fragmentation from 2000 to 2020 using complementary metrics that captured patch connectivity, aggregation, and structure. Connectivity-based metrics revealed that 51 to 67% of forests globally—and 58 to 80% of tropical forests—became more fragmented, which is nearly twice the rate suggested by traditional structure-focused methods (30 to 35%). Aggregation-focused metrics confirmed increases in 57 to 83% of forests. Human activities such as agriculture and logging drive this change. Yet protected tropical areas saw up to an 82% reduction in fragmentation, underscoring the potential of targeted conservation.

Forests are essential to global biodiversity and climate regulation (*1*–*6*). Yet human activities increasingly threaten them, not only by reducing forest area but also by fragmenting forests into smaller, isolated patches (*7*–*10*). This process, known as habitat fragmentation (hereafter "fragmentation"), reduces species richness and carbon storage (*11*–*13*). Its importance, particularly regarding ecological connectivity and integrity, is emphasized in global policy frameworks such as the Aichi Target 11 and the Kunming-Montreal Global Biodiversity Framework (*14*, *15*). Accurately quantifying fragmentation is critical not only to understand its global extent but also to identify high-risk regions and guide conservation efforts.

Fragmentation arises through multiple pathways: Patches may shrink, split, vanish, stretch into complex shapes, or grow more distant (Fig. 1, A to E). These changes often co-occur, as in ongoing Amazon deforestation (Fig. 1F and fig. S2), and affect biodiversity through three main mechanisms (*16*–*21*). First, new edges change microclimates and disturbance regimes, often making forests warmer and drier (*22*, *23*). Second, shrinking core areas threaten species that are dependent on large, intact habitats (*11*). Third, increased patch isolation disrupts connectivity and reduces movement, often leading to long-term population declines (*24*–*26*). Although edge effects vary, losses of core habitat and connectivity consistently harm forest specialists (*11*, *17*).

To assess these impacts, researchers use a range of landscape metrics (*27*–*32*), broadly categorized into structure, aggregation, and connectivity (*7*, *11*). Structure-focused metrics quantify habitat subdivision—including patch number, size, and edge length—but often neglect the habitat extent and spatial arrangement (*7*). Aggregation-focused metrics assess how clustered patches are but may also overlook overall extent. Connectivity-focused metrics incorporate both patch area and spatial configuration, offering a more ecologically relevant perspective. Because each captures different aspects of fragmentation, selecting ecologically meaningful metrics is critical to accurately track progress toward conservation goals (*27*, *33*).

Connectivity- and aggregation-focused studies suggest that fragmentation has increased in recent decades, particularly in the tropics (*34*–*36*). For example, Hansen *et al.* found consistent tropical forest patch loss from 2001 to 2018, with smaller patches disappearing fastest (*35*). Edge habitat also expanded from 2000 to 2010, increasing exposure to disturbances (*36*). However, global assessments that used structure-focused metrics reported declining fragmentation in 75% of forests from 2000 to 2020 (*7*) despite a net forest loss of 101 Mha (*37*). This discrepancy arises because structure metrics define fragmentation by patch number and size, interpreting fewer, larger patches as reduced fragmentation (Fig. 1, C and F), even when ecologically critical patches are lost (*7*, *33*, *38*, *39*). Such losses reduce connectivity and harm species that depend on stepping-stone habitats for dispersal and persistence (*11*, *13*, *19*).

In conservation biology, debate persists over whether habitat configuration (Fig. 1A) or total area plays a greater role in shaping biodiversity (*13*, *17*–*19*). Structure-focused metrics are valuable for isolating the effects of fragmentation per se—that is, changes in patch structure without habitat loss (*11*, *19*). However, they often overlook critical aspects such as connectivity and aggregation, which limits their ability to capture how landscape change affects species movement, resource access, and population viability (*7*, *11*, *13*). As such, they can misrepresent fragmentation trends over time. A comprehensive global assessment must therefore integrate connectivity- and aggregation-focused metrics to fully reflect fragmentation's ecological impacts and its drivers.

We quantified global forest fragmentation from 2000 to 2020 using a comprehensive set of metrics that represent habitat connectivity, aggregation, and structure (Table 1, Fig. 1, and fig. S1). We calculated nine widely used fragmentation metrics (*7*, *27*–*30*, *32*), grouped into three categories on the basis of their ecological focus. Connectivity metrics included total core forest area (TCA), largest patch index (LPI), and landscape division index [LDI; probability that two randomly placed individuals occur in the same forest patch (*29*)]. Aggregation metrics included aggregation index (AI), percentage of like adjacency (PLADJ), and mean Euclidean nearest-neighbor distance among patches (ENN). Structural metrics included mean patch area (MPA), edge density (ED), and number of patches (NP) (detailed descriptions are provided in Table 1 and table S1). To capture broader fragmentation trends, we synthesized these into three composite indices: the connectivity-based fragmentation index (CFI), the aggregation-based fragmentation index (AFI) (*27*–*30*, *32*), and the structure-based fragmentation index [SFI, formerly termed the forest fragmentation index (FFI) in Ma *et al.* (*7*)]. We first established how each metric responds to hypothetical and real-world landscape changes, demonstrating their ecological relevance. We then applied them to high-resolution (30 m) global forest cover data (*37*) to map trends in fragmentation, identify key drivers (*8*), and evaluate the effectiveness of protected areas in mitigating fragmentation.

[1]Institute of Integrative Biology, ETH Zurich (Swiss Federal Institute of Technology), Zurich, Switzerland. [2]Oath, The Presidio of San Francisco, San Francisco, CA, USA. [3]Swiss Federal Institute for Forest, Snow and Landscape Research WSL, Birmensdorf, Switzerland. [4]Department of Plant Biology and Ecology, College of Life Sciences, Nankai University, Tianjin, China. [5]World Resources Institute, Washington, DC, USA. [6]Department of Geographical Sciences, University of Maryland, College Park, MD, USA. [7]Department of Evolutionary Biology and Environmental Studies, University of Zurich, Zurich, Switzerland. [8]UK Centre for Ecology and Hydrology, Bush Estate, Penicuik, UK. [9]School of Life Sciences, Nanjing University, Nanjing, China. [10]Wyss Academy for Nature, Centre for Development and the Environment, Institute of Geography, University of Bern, Bern, Switzerland. [11]Hawkesbury Institute for the Environment, Western Sydney University, Richmond, Australia. [12]College of Water Sciences, Beijing Normal University, Beijing, China. ***Corresponding author. Email: yibiao.zou@usys.ethz.ch**

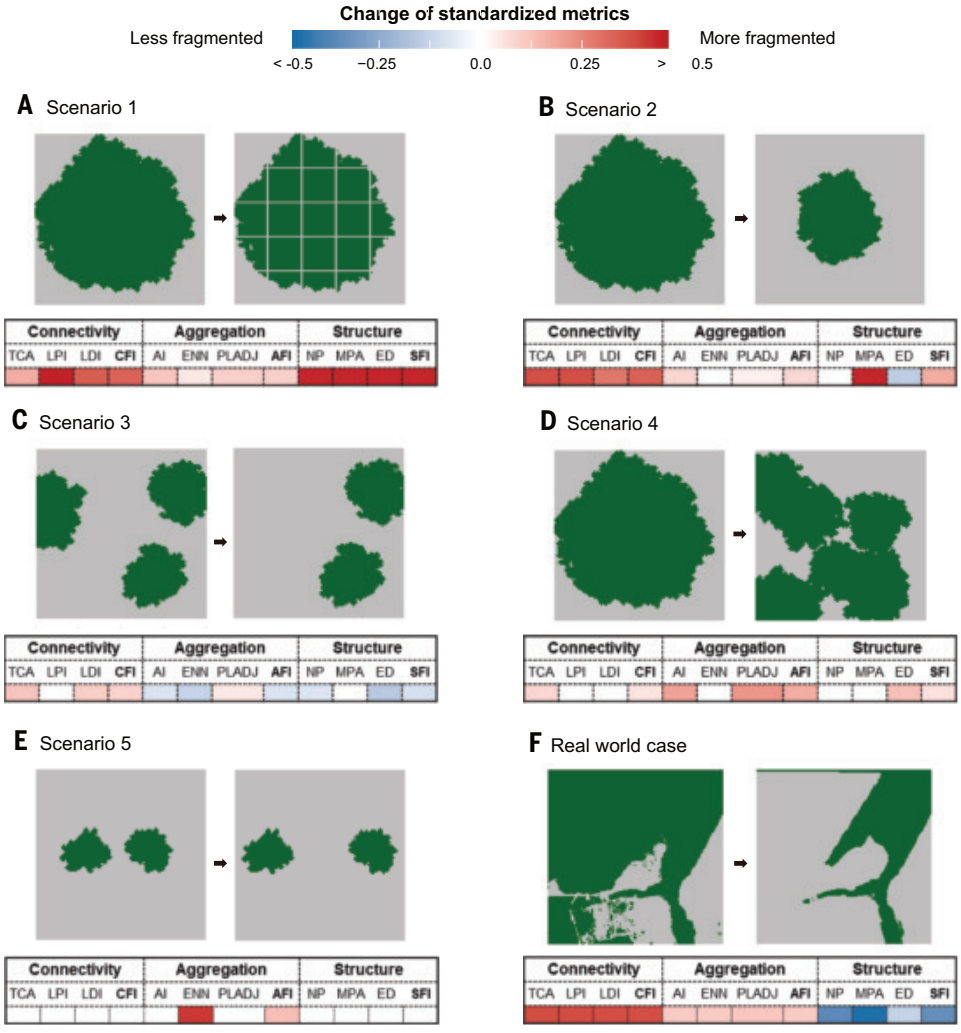

Fig. 1. Responses of fragmentation metrics to simulated and observed landscape change scenarios. (**A**) Transition from a single forest patch with 60% canopy cover to multiple smaller patches with minimal cover loss. (**B**) Reduction of a single forest patch from 60 to 20% cover. (**C**) Removal of one of three equally sized forest patches. (**D**) Transformation of a circular patch with 60% cover into an irregular shape with the same coverage but a longer perimeter. (**E**) Increased distance between two previously proximate patches. (**F**) Observed deforestation in an Amazon forest site from (left) 2000 (72% cover) to (right) 2020 (26% cover). Similar patterns occur in other sites (fig. S2). Our analysis shows that scenarios 2 and 3 are the most prevalent globally, affecting 18 and 46% of forests experiencing cover loss, respectively (fig. S3). Although scenarios 4 and 5 are hypothetical and may not frequently occur in real forested landscapes, they help to illustrate how aggregation-focused metrics respond to changes in patch shape and distance compared with connectivity- and structure-focused metrics. For each scenario, changes were assessed by using 12 normalized fragmentation metrics (scaled from 0 to 1) (Table 1 and table S1), categorized into three groups: connectivity-focused, aggregation-focused, and structure-focused metrics. Positive values indicate increased fragmentation. Red indicates a fragmentation increase, blue indicates a decrease, and white indicates no change, with darker shades representing greater magnitude. The CFI, AFI, and SFI, which represent integrated indices for connectivity, aggregation, and structure, are highlighted in bold.

Results

Fragmentation metrics respond differently to landscape change

Fragmentation metrics responded differently depending on the type of landscape alteration (Fig. 1). All metric groups detected increased fragmentation when forest patches were subdivided without substantial forest loss, with structure-focused metrics showing the strongest response to patch division (Fig. 1A). By contrast, connectivity-focused metrics consistently indicated increased fragmentation in scenarios that involved shrinking patches (Fig. 1B), the disappearance of patches (Fig. 1C), and real-world deforestation (Fig. 1F). In these cases, structure-focused metrics often suggested reduced fragmentation, highlighting their insensitivity to losses in habitat connectivity. Aggregation-focused metrics were especially responsive to increases in patch shape complexity (Fig. 1D) and patch distance (Fig. 1E) but indicated reduced fragmentation when patches disappeared (Fig. 1C), resulting in variable outcomes in real-world scenarios (Fig. 1F and fig. S2). Only the aggregation-focused ENN and the composite AFI detected increased fragmentation when patch separation increased without loss of area (Fig. 1E), underscoring their particular sensitivity to spatial configuration.

To quantify how these fragmentation dimensions manifest globally, we conducted a principal components analysis (PCA) on all individual and composite metrics. We also incorporated metapopulation capacity (MPC)—a measure of functional connectivity that reflects a landscape's ability to support species persistence (*25*, *31*). The PCA biplot revealed three statistically distinct metric clusters [multivariate analysis of variance (MANOVA) P value < 0.001], corresponding to habitat connectivity, aggregation, and structure (Fig. 2A). Connectivity-focused metrics aligned closely with MPC, confirming their strength in capturing functional connectivity and ecologically meaningful fragmentation (Fig. 2A and fig. S10C). This underscores the importance of incorporating connectivity-based approaches in global fragmentation assessments to better understand biodiversity impacts and conservation priorities.

Trends of global fragmentation from 2000 to 2020

To quantify global forest fragmentation trends, we assessed the proportion of forest area that showed increased fragmentation from 2000 to 2020 at multiple spatial resolutions (5, 10, 20, and 40 km). We used three composite indices—CFI, AFI, and SFI—to capture trends globally and across major forest biomes (tropical, temperate, and boreal). The results reveal stark differences among metric types. The CFI indicates that depending on grid size, 51 to 67% of forests globally (Fig. 2C), and 58 to 80% of tropical forests (Fig. 2D), have become more fragmented. Similarly, the AFI suggests that 57 to 83% of global forests became more fragmented, reflecting declines in spatial proximity and ecological connectivity, both of which are crucial for species movement and habitat continuity. By contrast, the SFI suggests that only 30 to 35% of forests worldwide became more fragmented over the same period (Fig. 2C), which aligns with earlier findings (*7*). This discrepancy arises because the SFI interprets the loss of small or connecting patches as reduced fragmentation because of SFI's focus on patch number and size rather than ecological connectivity.

Table 1. Overview of landscape-level fragmentation metrics.

	Metric	Full name	Description	Reference
	Canopy cover	Forest cover percentage	The percentage of the landscape covered by forests	McGarigal *et al*. (*27*)
Connectivity-focused	TCA	Total core area	The sum of core areas of all patches belonging to forests. A cell is defined as core area if all of its neighboring cells are forests.	McGarigal *et al*. (*27*)
	LPI	Largest patch index	The percentage of the landscape covered by the corresponding largest patch of forest	McGarigal *et al*. (*27*)
	LDI	Landscape division index	The probability that two randomly selected cells are not located in the same patch of forest	Jaeger (*29*)
	CFI	Connectivity-based fragmentation index	Synthetic metric integrating TCA, LPI, and LDI	This paper
Aggregation-focused	AI	Aggregation index	The number of like adjacencies divided by the theoretical maximum possible number of like adjacencies for forest cells	He *et al*. (*30*)
	PLADJ	Percentage of like adjacency	The number of adjacencies between forest cells divided by the number of adjacencies between forest and nonforest cells	McGarigal *et al*. (*27*)
	ENN	Mean of Euclidean nearest-neighbor distance	The mean Euclidean distance to the nearest neighboring patch for each forest patch	McGarigal *et al*. (*27*)
	AFI	Aggregation-based fragmentation index	Synthetic metric integrating AI, PLADJ, and ENN	This paper
Structure-focused	NP	Number of patches	Number of distinct forest patches	McGarigal *et al*. (*27*)
	MPA	Mean patch area	The mean of all patch areas belonging to forests	McGarigal *et al*. (*27*)
	ED	Edge density	The length sum of all edges of forest divided by the landscape area (in our study, the landscape area is the grid cell area)	McGarigal *et al*. (*27*)
	SFI	Structure-based fragmentation index	Synthetic metric integrating NP, MPA, and ED. This index was called FFI in Ma *et al*. (*7*).	Ma *et al*. (*7*)
Functional connectivity	MPC	Metapopulation capacity	A relative measure of the ability of a spatially explicit landscape to support long-term species persistence based on connectivity and area of habitat	Hanski and Ovaskainen (*31*)

Fragmentation estimates from the CFI and AFI were scale-dependent, with higher fragmentation detected at coarser resolutions (10 to 40 km) (Fig. 2, C and D). This reflects the edge-driven nature of fragmentation: As grid size increases, fewer cells fall within intact cores, increasing the apparent fragmentation rate. By contrast, the SFI remained largely scale-insensitive, even indicating slight declines in fragmentation at larger scales (Fig. 2, C and D).

To examine how fragmentation metrics respond to deforestation, we related each composite metric to forest cover at a 5-km resolution for the years 2000 (Fig. 2B) and 2020 (fig. S5). CFI and AFI values declined with increasing forest cover, aligning with ecological expectations that larger, contiguous forests are less fragmented (*11*). By contrast, the SFI indicated reduced fragmentation in areas with both low and high forest cover, thus equating severe deforestation with reduced fragmentation and highlighting its limitations in capturing deforestation-driven fragmentation. Spatial analysis confirms that these discrepancies between metrics are most pronounced across the pantropical regions (fig. S9), where deforestation is severe (*8*, *35*).

Drivers of forest fragmentation

Forest fragmentation and cover loss arise from various processes that can be broadly classified into permanent conversion and temporary disturbances (*8*). Permanent conversion includes commodity-driven deforestation (such as mining and energy development) and urban expansion, resulting in lasting land-use change. Temporary disturbances such as shifting agriculture (agricultural conversion followed by abandonment), forestry (clearcutting or selective logging), and wildfires often allow for forest regrowth over time.

To quantify the contribution of these drivers, we integrated data from the Global Forest Watch dataset (*8*), which maps primary deforestation drivers from 2000 to 2023 (Fig. 3). Results were consistent with earlier assessments (*8*) from 2000 to 2015 (figs. S12 and S13), confirming the growing influence of anthropogenic disturbance, especially shifting agriculture, commodity-driven deforestation, and forestry. We used the CFI at 5-km resolution, the finest available for this analysis and the subsequent assessment of protected areas because it best aligned with ecological indicators of fragmentation (Fig. 2, A and B, and fig. S10).

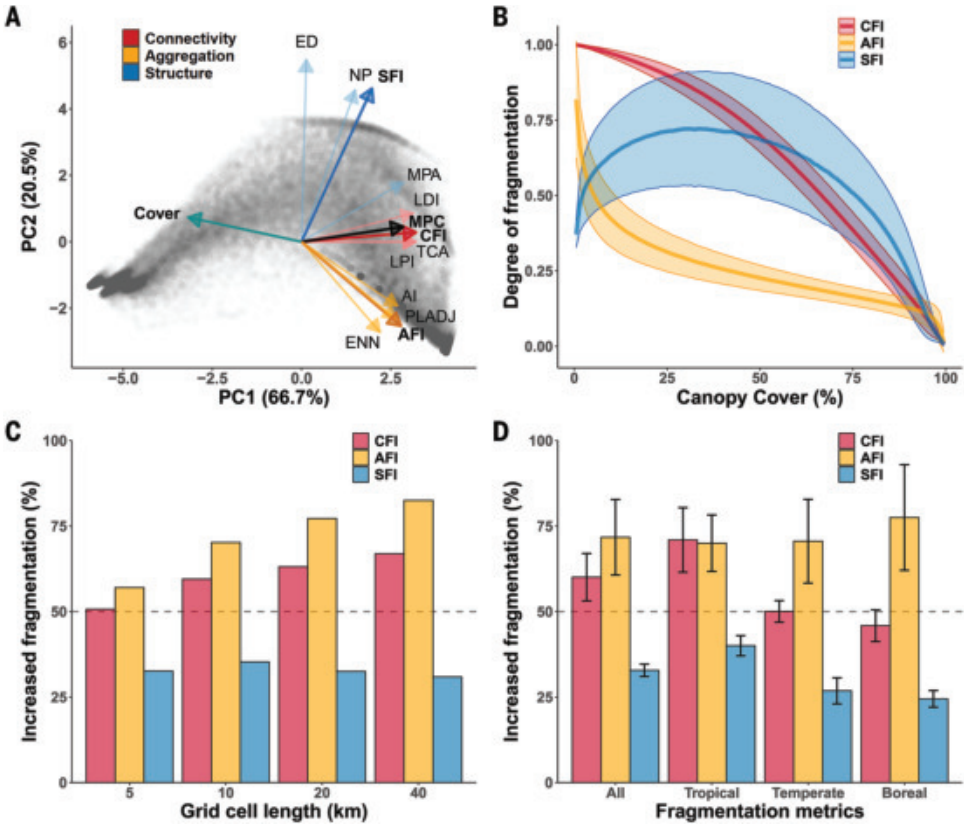

Fig. 2. Classification and analysis of fragmentation metrics. (**A**) Major axes of forest fragmentation: PCA biplot showing the distribution of various fragmentation metrics applied to a 10% random sample of all grid cells (forest cover > 0) for the year 2000. Metrics are color-coded according to their focus: connectivity-focused in red, aggregation-focused in orange, and structure-focused in blue. The integrated indices—CFI, AFI, and SFI [formerly termed FFI from Ma *et al*. (*7*)]—are highlighted in darker shades within their groups. Forest cover (dark cyan) is also included. A pairwise MANOVA confirms significant differences among loadings of these three groups ($P < 0.001$), indicating distinct clustering. The MPC (black), a critical metric for functional connectivity, aligns closely with connectivity-focused metrics. PCA biplots on the 12 fragmentation metrics across all grid cells in both years 2000 and 2020 are provided in fig. S3. (**B**) Relationship between the observed fragmentation degree (based on the CFI, AFI, and SFI) and canopy cover for all analyzed forest grid cells in the year 2000. Solid lines indicate mean fragmentation values; the shaded areas indicate mean ± SD. (**C**) Proportion of global forest grid cell areas with increased fragmentation between 2000 and 2020 at different grid cell scales, based on the CFI, AFI, and SFI. (**D**) Proportion of forest grid cell areas with increased fragmentation (mean ± SD, over different grid cell scales) between 2000 and 2020 across global forest grid cells and in different forest biomes, based on the CFI, AFI, and SFI. (C) and (D) include only forest grid cells with forest cover >30% in 2000. Results remained consistent across different forest cover thresholds used to define forest grid cells (fig. S17).

Globally, shifting agriculture (37% of grids with increased fragmentation) and forestry (34%) were the dominant drivers of increased fragmentation (Fig. 3), followed by wildfires and commodity-driven deforestation (both 14%). In the tropics, fragmentation was overwhelmingly driven by shifting agriculture (61%), whereas temperate forests were mainly affected by forestry (81%). In boreal regions, wildfires (62%) and forestry (38%) were the primary drivers. Permanent conversions from commodity-driven deforestation and urbanization accounted for <15% of fragmentation globally. Identifying these region-specific drivers is essential for designing targeted and effective conservation strategies.

Fragmentation status within and outside protected areas

To examine how protection status influences forest fragmentation, we integrated data from the World Database on Protected Areas (*40*). Area-based protection remains a cornerstone of biodiversity conservation (*41*, *42*), and previous studies have suggested that protected tropical forests face fewer human disturbances (*43*). However, whether this translates into reduced fragmentation rates over time remains unclear.

We classified 5-km forest grid cells into protected and nonprotected categories and applied a matching approach to control for environmental and socioeconomic differences (figs. S14 to S16) (*42*, *44*–*46*). Fragmentation trends from 2000 to 2020 were analyzed across four categories: strictly protected, protected, matched nonprotected, and all nonprotected. Given distinct fragmentation drivers, tropical and nontropical forests were analyzed separately.

In the tropics, fragmentation increased in all categories but remained significantly lower in protected areas. Strictly protected areas experienced 82% less fragmentation than matched nonprotected areas, whereas less strictly protected areas saw a 45% reduction (Fig. 4A). These patterns align with reduced human activity: Shifting agriculture was 59 and 16% lower in strictly and less strictly protected areas, respectively, whereas forestry was 10 and 58% lower (Fig. 4B). These results highlight the effectiveness and importance of tropical protected areas in limiting human-driven fragmentation and underscore the urgent need to expand protection across tropical regions in line with international conservation targets, including Aichi Target 11 and the "30x30" goal of the Kunming-Montreal Global Biodiversity Framework (*14*, *15*).

By contrast, nontropical forests showed slightly higher fragmentation in strictly protected areas compared with nonprotected ones (Fig. 4C), alongside a 63% increase in forestry activity (Fig. 4D). This may reflect inconsistencies in how protection status is defined across jurisdictions, with some areas that allow logging still classified as strictly protected (*43*, *47*).

Discussion

A recent study that used structure-focused metrics suggested that 75% of the world's forests are becoming less fragmented as patch counts decline with forest loss (Fig. 1F) (*7*). Although this conclusion is mathematically valid, our analysis incorporating connectivity and aggregation reveals the opposite: Most forests, especially in the tropics, have become more fragmented over the past two decades. These findings align with prior studies that have shown increasing fragmentation in the tropics, with declining cover, more edge habitats, and reduced core areas (*34*–*36*). This trend holds across varying forest cover thresholds that are used to define forest grid cells (fig. S17) and is primarily driven by declining connectivity and aggregation.

The divergences among fragmentation metrics highlight the importance of assessing not only forest areas but also the spatial arrangement of patches to evaluate changes in landscape integrity (*11*, *12*). Structure-focused metrics, such as the SFI, capture a distinct and

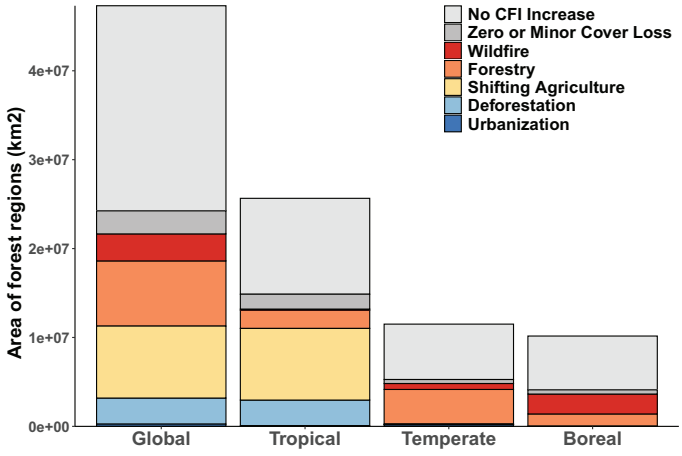

Fig. 3. Drivers of forest fragmentation trends (2000 to 2020) across biomes. Total area of forest regions [grid cells with >30% canopy cover at 2.5 arc min (~5 km) resolution, the finest resolution available] affected by different fragmentation drivers at global and biome scales. "No CFI increase" represents forest regions where fragmentation levels have remained stable or decreased. "Zero or minor cover loss" includes areas where fragmentation slightly increased because of an unknown cause but with minor or no forest cover loss. All other categories represent regions with increased fragmentation driven by specific factors, including (i) "Wildfire," where forest burning occurred without subsequent human conversion or agricultural activity; (ii) "Forestry," representing large-scale harvesting within managed forests with signs of regrowth; (iii) "Shifting agriculture," referring to small- to medium-scale forest conversion for agriculture, later abandoned and followed by forest regrowth; (iv) "Deforestation," characterized by permanent forest loss due to commodity-driven activities such as agriculture, mining, or energy infrastructure; and (v) "Urbanization," where forests have been converted for urban expansion. The drivers are arranged from (top) Wildfire to (bottom) Urbanization to reflect the increasing degree of irreversible forest loss.

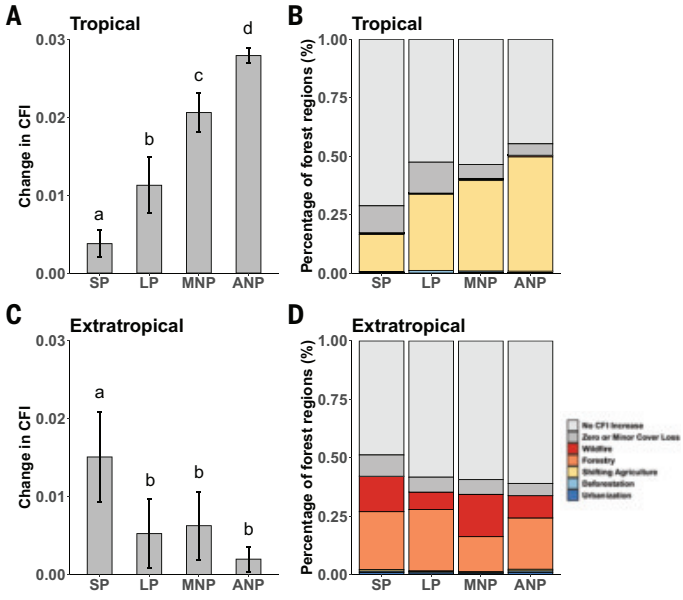

Fig. 4. Forest fragmentation trends (2000 to 2020) inside and outside protected areas. (**A** and **C**) Changes in the degree of fragmentation (indicated with the CFI, mean ± 3 SE) across forest grid cells [at 2.5 arc min (~5 km) resolution] in strictly protected areas (SP), less strictly protected areas (LP), matched nonprotected areas (MNP), and all nonprotected areas (ANP) in (A) tropical and (C) extratropical forests. Kruskal-Wallis and post hoc Mann-Whitney *U* tests (tables S4 and S5) show that (A) in tropical forests, fragmentation levels significantly differ across all protection categories ($P < 0.001$), whereas (C) in extratropical forests, only the "strictly protected" group is significantly different from all other groups ($P < 0.05$). (**B** and **D**) Proportions of forest regions experiencing fragmentation owing to different drivers across different protection categories in (B) tropical and (D) extratropical regions. "No CFI increase" represents areas where fragmentation levels have remained stable or decreased. "Zero or minor cover loss" includes areas where fragmentation slightly increased because of an unknown cause but with minor or no forest cover loss. All other categories represent regions with increased fragmentation driven by specific factors such as forestry, shifting agriculture, deforestation, or urbanization. To address spatial autocorrelation, we only included forest grid cells at least 40 km apart.

meaningful dimension of fragmentation related to patch size, number, and edge complexity (Fig. 2A). They are especially valuable for isolating fragmentation per se from habitat loss (*11*, *17*–*19*) and for comparing sites with similar forest cover but differing patch structures (*13*). However, they reflect only one of three critical axes—structure, aggregation, and connectivity (Fig. 2A)—and can yield misleading results when forest cover changes alongside fragmentation, whether over time or across space. For example, they may indicate reduced fragmentation when patch numbers decline, even as habitat loss degrades connectivity and ecosystem function (Fig. 1C).

By contrast, connectivity- and aggregation-focused metrics offer a more ecologically meaningful perspective for detecting and interpreting fragmentation over time. They show stronger alignment with key ecological indicators such as MPC and net primary productivity (fig. S10) and directly reflect functional landscape properties that affect biodiversity persistence (*25*, *31*). The strong correlation between the CFI and MPC suggests that the CFI offers a computationally efficient proxy for ecological connectivity.

These differences among fragmentation metrics underscore the need for ecologically meaningful indicators in conservation planning (*11*, *19*). For example, both the CFI and AFI detect increased fragmentation across pantropical regions, which is consistent with high deforestation rates (*42*), and reveal 82 and 79% less fragmentation in strictly protected areas compared with matched nonprotected ones, respectively (Fig. 4A and fig. S18). These reductions were largely driven by declines in agricultural activity (Fig. 4B). By contrast, the SFI suggests declining fragmentation both within and outside tropical protected areas (fig. S18), illustrating how reliance on structure-based metrics alone can obscure ecological degradation and potentially mislead conservation efforts. To fully evaluate forest fragmentation and its ecological consequences, all three dimensions—structure, aggregation, and connectivity—must be considered in tandem. However, metrics that capture connectivity and aggregation offer greater ecological relevance for understanding functional landscape change and guiding effective conservation.

Given the ecological relevance of connectivity-focused metrics, we used the CFI to assess the primary drivers of fragmentation and the effectiveness of protected areas across forest biomes. Our analysis shows that permanent forest conversion accounts for only 15% of global connectivity-focused fragmentation, and wildfires—intensified by climate change—contribute another 14% (Fig. 3). The remaining 71% was primarily driven by agricultural and forestry activities that can often represent temporary transitions, highlighting opportunities for restoration (*3*, *8*). Protected areas mitigate these impacts, although their effectiveness varies by biome. Tropical forests benefit most, with reduced fragmentation primarily because of lower agricultural encroachment. By contrast, temperate and boreal forests show slight

increases in fragmentation within protected areas, mainly driven by ongoing forestry. These patterns underscore the need for biome-specific conservation strategies that reflect distinct regional pressures.

Although our study provides important insights into global forest fragmentation and its ecological implications, several limitations may affect the accuracy of our estimates. Landsat-derived data likely underestimate fragmentation by failing to detect narrow barriers, such as roads <30 m wide (*48*, *49*). Additionally, this forest cover product does not distinguish between natural forests and agroforestry, potentially underestimating natural forest loss (*37*). Conversely, using a 5-m height threshold to define forests may not fully capture restoration trends, as degraded forests with slow regrowth below this height remain undetected (*37*).

Our study reveals widespread declines in forest ecological integrity over the past two decades, driven largely by human activity. The stark divergence among fragmentation metrics underscores the urgent need for ecologically relevant tools to accurately assess and address these changes. As human pressures on nature intensify, such tools will be essential for guiding effective conservation and reversing global trends in fragmentation and biodiversity loss.

REFERENCES AND NOTES

1. G. B. Bonan, *Science* **320**, 1444–1449 (2008).
2. Y. Pan *et al.*, *Science* **333**, 988–993 (2011).
3. L. Mo *et al.*, *Nature* **624**, 92–101 (2023).
4. H. Ma *et al.*, *Nat. Plants* **9**, 1795–1809 (2023).
5. Y. Zou *et al.*, *Nat. Commun.* **15**, 4658 (2024).
6. Z. Wu *et al.*, *New Phytol.* **240**, 1421–1432 (2023).
7. J. Ma, J. Li, W. Wu, J. Liu, *Nat. Commun.* **14**, 3752 (2023).
8. P. G. Curtis, C. M. Slay, N. L. Harris, A. Tyukavina, M. C. Hansen, *Science* **361**, 1108–1111 (2018).
9. W. F. Laurance, G. B. Williamson, *Conserv. Biol.* **15**, 1529–1535 (2001).
10. A. C. Staver, S. Archibald, S. A. Levin, *Science* **334**, 230–232 (2011).
11. N. M. Haddad *et al.*, *Sci. Adv.* **1**, e1500052 (2015).
12. M. Pfeifer *et al.*, *Nature* **551**, 187–191 (2017).
13. T. Gonçalves-Souza *et al.*, *Nature* **640**, 702–706 (2025).
14. Convention on Biological Diversity, "Aichi Target 11" [United Nations Environment Programe (UNEP), 2010].
15. Intergovernmental Science-Policy Platform on Biodiversity and Ecosystem Services (IPBES), "Kunming-Montreal Global Biodiversity Framework" (UNEP, 2019).
16. L. Fahrig, *Annu. Rev. Ecol. Evol. Syst.* **34**, 487–515 (2003).
17. L. Fahrig, *Glob. Ecol. Biogeogr.* **28**, 33–41 (2019).
18. L. Fahrig *et al.*, *Biol. Conserv.* **230**, 179–186 (2019).
19. R. J. Fletcher Jr. *et al.*, *Biol. Conserv.* **226**, 9–15 (2018).
20. A. E. Martin, L. Fahrig, *Ecology* **99**, 2058–2066 (2018).
21. F. Riva, L. Fahrig, *Conserv. Lett.* **15**, e12881 (2022).
22. J. Rybicki, N. Abrego, O. Ovaskainen, *Ecol. Lett.* **23**, 506–517 (2020).
23. J. N. G. Willmer, T. Püttker, J. A. Prevedello, *Biol. Conserv.* **272**, 109654 (2022).
24. J. Oehri, S. L. R. Wood, E. Touratier, B. Leung, A. Gonzalez, *Biodivers. Conserv.* **33**, 4043–4071 (2024).
25. I. Hanski *et al.*, *Nat. Commun.* **8**, 14504 (2017).
26. M. Beger *et al.*, *Trends Ecol. Evol.* **37**, 1079–1091 (2022).
27. K. S. McGarigal, S. Cushman, M. Neel, E. Ene, FRAGSTATS: Spatial pattern analysis program for categorical maps (2002).
28. N. H. Schumaker, *Ecology* **77**, 1210–1225 (1996).
29. J. A. G. Jaeger, *Landsc. Ecol.* **15**, 115–130 (2000).
30. H. S. He, B. E. DeZonia, D. J. Mladenoff, *Landsc. Ecol.* **15**, 591–601 (2000).
31. I. Hanski, O. Ovaskainen, *Nature* **404**, 755–758 (2000).
32. D. R. Patton, *Wildl. Soc. Bull.* **3**, 171–173 (1975).
33. H. Li, J. Wu, *Landsc. Ecol.* **19**, 389–399 (2004).
34. F. Taubert *et al.*, *Nature* **554**, 519–522 (2018).
35. M. C. Hansen *et al.*, *Sci. Adv.* **6**, eaax8574 (2020).
36. R. Fischer *et al.*, *Sci. Adv.* **7**, eabg7012 (2021).
37. P. Potapov *et al.*, *Front. Remote Sens.* **3**, 856903 (2022).
38. L. Tischendorf, *Landsc. Ecol.* **16**, 235–254 (2001).
39. L. Tischendorf, L. Fahrig, *Oikos* **90**, 7–19 (2000).
40. UNEP-WCMC, IUCN, Protected Planet: The World Database on Protected Areas (WDPA) (2023); www.protectedplanet.net.
41. E. Dinerstein *et al.*, *Bioscience* **67**, 534–545 (2017).
42. J. S. Sze, L. R. Carrasco, D. Childs, D. P. Edwards, *Nat. Sustain.* **5**, 123–130 (2022).
43. J. Geldmann, A. Manica, N. D. Burgess, L. Coad, A. Balmford, *Proc. Natl. Acad. Sci. U.S.A.* **116**, 23209–23215 (2019).
44. P. J. Ferraro, M. M. Hanauer, K. R. E. Sims, *Proc. Natl. Acad. Sci. U.S.A.* **108**, 13913–13918 (2011).
45. V. Graham *et al.*, *Sci. Rep.* **11**, 23760 (2021).
46. P. J. Negret *et al.*, *Conserv. Biol.* **34**, 1452–1462 (2020).
47. J. Geldmann *et al.*, *Biol. Conserv.* **191**, 692–699 (2015).
48. B. Slagter *et al.*, *Remote Sens. Environ.* **315**, 114380 (2024).
49. J. E. Engert *et al.*, *Nature* **629**, 370–375 (2024).
50. Y. Zou, Yibiaozou/Global_ForestFRAG: Global fragmentation trends during 2000-2020. Zenodo (2025); https://doi.org/10.5281/zenodo.14883322.
51. Y. Zou, Global fragmentation trends during 2000-2020. Zenodo (2025); https://doi.org/10.5281/zenodo.15703795.

ACKNOWLEDGMENTS

We thank all the members of the Crowther lab team, including those not listed as coauthors of the study, for their incredible support. **Funding:** This work was supported by grants from the Ambizione Fellowship program (PZ00P3_193646 to C.M.Z.), Bernina Foundation and DOB Ecology (to T.W.C.), Ambizione Fellowship program (PZ00P3_216194 to G.R.S.), and Marie Skłodowska-Curie Actions Postdoctoral Fellowship (EP/Z000831/1 to K.A.G.).
Author contributions: Y.Z., C.M.Z., and T.W.C. conceived, developed, and wrote the paper. Y.Z. performed the analyses. All authors reviewed and provided input on the manuscript.
Competing interests: The authors declare that they have no competing interests. **Data and materials availability:** All data used in this study are from open-source databases and referenced in the paper. Code is available at https://github.com/Yibiaozou/Global_ForestFRAG and Zenodo (*50*). Major dataset and outcome maps of fragmentation metrics are also available at Zenodo (*51*).

SUPPLEMENTARY MATERIALS

science.org/doi/10.1126/science.adr6450
Materials and Methods; Figs. S1 to S23; Tables S1 to S5; References (*52*–*76*); MDAR Reproducibility Checklist

Submitted 11 July 2024; resubmitted 19 February 2025; accepted 14 July 2025
10.1126/science.adr6450

My lucky detour

Henry C. Henson

I still remember the first morning I biked to university in Copenhagen, the February air reddening my cheeks. I was thrilled to be on an exchange semester overseas, but I saw it as just a detour from my imagined career path. I didn't realize I was already pedaling toward a different life—one that would make me reassess how to achieve a fulfilling research career. I grew up in the United States with a clear sense of what a "successful" science career should look like. I might not have admitted it openly, but I believed that the right pedigree—a well-known university, a prestigious Ph.D. program, a respected adviser—was what determined whether someone would be taken seriously as a scientist.

But everything changed during my time as an undergraduate in Denmark. Here, I fell in love. First with the country. The cobbled streets. The bike lanes. The quiet confidence of a society that seemed to trust its institutions. Later, with a man I met by chance—who will soon be my husband. A Fulbright grant allowed me to return to Denmark after my exchange. The official goal was to broaden my academic horizons and learn new scientific skills. But unofficially it was a chance to see whether this relationship might become something lasting.

As the months passed, the idea of returning to the U.S. to pursue a "big name" Ph.D. program felt less compelling. I began to seriously consider staying in Denmark for a doctoral position that would allow me to build a life with someone I loved.

I found myself fixating on how this choice might look on a CV. Would colleagues back home see a Danish Ph.D. as a step down? Would I be taken less seriously without North American training? Would I regret prioritizing my personal life over a more conventional path? In hindsight, these anxieties seem ludicrous. But at the time, they felt very real. In the end, I chose to stay.

The adjustment wasn't always easy. It can be hard for a foreigner to live in Denmark, where many friendships are formed early in life and social circles can be slow to open. But I had my relationship to lean on, and gradually I built a community.

As I started my academic life here, Danish culture began to transform my mindset. Danish society is guided by *Janteloven*, an unwritten code that says you are no better than anyone else. Growing up, I would have said I believed in this ideal. But subconsciously I probably felt otherwise. In the U.S., an unspoken hierarchy is attached to certain professions. Scientists and doctors often enjoy a higher social standing than, say, electricians. In Denmark, this distinction is far less pronounced.

The same ideals pervade academia. There is no Danish university that is considered "better" than others, and prestige plays a smaller role in people's decisions. Even within universities, there is very little hierarchy. Everyone addresses each other by first name, and talking to a senior professor feels like chatting with a colleague.

In Denmark, I also discovered a new type of work culture: one that insists on work-life balance, expects people to leave the office at a reasonable hour, and treats evenings and weekends as personal time. In the U.S., long hours are worn like badges of honor. But after my time in Denmark, that way of life no longer appeals to me. I feel fortunate to work in a place where I have more space for hobbies, relationships, and simply living.

Gradually, I have come to adopt the Danish perspective. I now see that the value of a scientific career isn't measured only by the institution on your diploma, but by whether your work feels meaningful, whether you're growing as a researcher, and whether you can sustain the curiosity that brought you into science in the first place. I now question why I ever felt a degree from Denmark would somehow be worth less than one from North America.

I still sometimes wonder how my life might have unfolded had I returned to the U.S. I might have gained more recognizable credentials. But I would have missed the chance to build a life here, to invest in a relationship with someone I love, and to discover a work culture that aligns with my values. For me, staying in Denmark has brought not just a different way to approach science, but also a sense of belonging I didn't know I was missing. □

Henry C. Henson is a Ph.D. student at Aarhus University.

ILLUSTRATION: ROBERT NEUBECKER

Apply for the BII and Science Translational Medicine **Prize for Innovations in Women's Health**

BII Science Translational Medicine — Prize for Innovations in Women's Health

The prize seeks to recognize researchers who have developed innovative advances with translational potential to impact women's health.

BioInnovation Institute (BII) and Science Translational Medicine introduce a new annual prize to celebrate scientists whose research has advanced translation and innovation to address high unmet medical needs in the underserved fields of women's health.

The winner will have their essay published in Science Translational Medicine, will receive a cash reward of $25,000, and be invited to BII headquarters in Copenhagen, Denmark, for the grand award ceremony.

Contributions within any area of women's health will be considered. These include:

- Female specific conditions;
- Reproductive health;
- Conditions that affect females and males differently.

Deadline
November 1, 2025
bii.dk/community/prizes

BII BioInnovation Institute

Science Translational Medicine